Compact High Repetition Rate Mid-infrared Solid-state Lasers

Fiona Elizabeth Thorburn MPhys (Hons.)

Submitted for the degree of Doctor of Philosophy

Institute of Photonics and Quantum Sciences

School of Engineering and Physical Sciences

Heriot-Watt University

September 2019

Abstract

The work in this thesis focuses on the development of novel mid-infrared laser sources which are compact, robust and suitable for the generation of ultrafast pulses with GHz pulse repetition frequencies. The motivation behind the work is to overcome the challenges associated with many of the mid-infrared ultrafast sources used at present.

The novel laser gain medium Erbium doped Gallium Lanthanum Sulphide glass has been explored for use as a compact mid-infrared emission source. Ultrafast Laser Inscription was utilised to inscribe waveguides and under pumping conditions the waveguides emitted fluorescence at ~ 2.73 μm. The fluorescence intensity increased with increasing dopant concentration. The propagation loss of these waveguides was measured to be ~ 1.83 dBcm^{-1} and an IR waveguide amplifier was demonstrated exhibiting a maximum gain of 5.4 dBcm^{-1} at 1538 nm. These results indicate ways in which the cavity should be optimised for mid-infrared lasing operation.

High repetition rate pulse generation from a Holmium doped YAG waveguide laser has been investigated using a graphene based saturable absorber. Depressed cladding waveguides were fabricated with Ultrafast Laser Inscription; these were subsequently employed in a compact quasi-monolithic laser resonator. Initially the laser operated in the CW regime resulting in a maximum laser output power of 1.78 W with a slope efficiency of 16% at 2.09 μm. In pulsed operation the laser generated pulses in a Q-switched modelocked regime with an average output power of 170 mW and slope efficiency of 6.8%. The modelocked pulses were emitted with a high pulse repetition rate of 5.9 GHz.

A room temperature Kerr-lens modelocked Chromium doped Zinc Selenide laser emitting sub-40-fs mid-infrared pulses is presented. The active crystal in this laser has been treated by hot isostatic pressing. Ultrafast pulses were generated with a pulse duration of 37 fs centred at 2388 nm. The laser emitted stable modelocked pulses at a repetition rate of 182 MHz with a maximum average output power of 144 mW. This is the shortest pulse width demonstrated to date from polycrystalline Cr:ZnSe indicating that hot isostatic pressing is beneficial for the generation of mid-infrared ultrafast pulses in Transition metal doped II – VI semiconductors.

Acknowledgements

First and foremost I would like to thank my supervisor, Professor Ajoy Kar. Without doubt, this would not have been possible without his continual support and words of encouragement throughout the course of my PhD. I am truly grateful for the opportunities and guidance he has provided for me.

I also thank the UK Engineering and Physical Sciences Research Council (EPSRC) for providing my studentship and EOARD for their continued funding for this work.

I thank all previous members of the Nonlinear Optics Group who welcomed me so kindly. In particular I must thank Adam Lancaster for taking the time to train me in ULI, mid-IR waveguide characterisation and many essential lab skills.

I also express great gratitude to Gary Cook and Sean McDaniel at the Air Force Research Laboratory in the Wright-Patterson Air Force Base, Ohio, USA. I thank Sean for teaching me so much time during his short visit to Heriot Watt, and for providing me with many waveguides and samples. I thank you both for the countless photonics discussions, without this invaluable help and advice much of this work could not have been completed.

I also express great thanks to Gianluca Galzerano for allowing us the opportunity to collaborate with his group. Thank you to Yuchen Wang and Gianluca for all your teachings, patience and to the entire group for giving me such a warm welcome to Milano.

Sincere thanks to Richard McCracken for sharing with me his vast knowledge and expertise in all things related to modelocking.

Thanks also goes to Ali and Martin in the Heriot-Watt Mechanical Workshop, who despite being so busy, always found time to help us out and provide components to the highest standard which have been essential to our work.

My wonderful friends outside of University deserve a huge thank you for offering so many words of encouragement and advice, as well as much needed distractions; great days/nights, holidays, countless laughs and adventures. Special mention must go to Ruth, Tasha, Mike, Kalin and Carrie – Thank you all for keeping me going!

My parents have sacrificed so much to provide me with every opportunity and support throughout my life, I am eternally thankful. I would not have been able to achieve any of this without you both; I hope I have done you proud thus far. I must also give special mention to Johanna Thorburn, it is difficult to express how grateful and fortunate I feel to call you not only a sister, but a truly wonderful and special friend, thank you for always being there.

I extend my special thanks to my Godmother May Angus and close family friend Maureen Stevenson for providing a wonderful support system. Thanks to all my other family and friends. I am lucky that there are too many to list them all!

Finally, I express my most heartfelt gratitude to my fiancé Matthew Stephen Fleming for his endless patience, encouragement, advice and love. Your belief in me is unwavering, for this I am eternally grateful. I am truly blessed to have you in my life.

Research Thesis Submission

Name*:*	Fiona Elizabeth Thorburn		
School:	School of Engineering and Physical Sciences		
Version: *(i.e. First, Resubmission, Final)*	Final	Degree Sought:	PhD

Declaration

In accordance with the appropriate regulations I hereby submit my thesis and I declare that:

1. The thesis embodies the results of my own work and has been composed by myself
2. Where appropriate, I have made acknowledgement of the work of others
3. The thesis is the correct version for submission and is the same version as any electronic versions submitted*.
4. My thesis for the award referred to, deposited in the Heriot-Watt University Library, should be made available for loan or photocopying and be available via the Institutional Repository, subject to such conditions as the Librarian may require
5. I understand that as a student of the University I am required to abide by the Regulations of the University and to conform to its discipline.
6. I confirm that the thesis has been verified against plagiarism via an approved plagiarism detection application e.g. Turnitin.

ONLY for submissions including published works

7. Where the thesis contains published outputs under Regulation 6 (9.1.2) or Regulation 43 (9) these are accompanied by a critical review which accurately describes my contribution to the research and, for multi-author outputs, a signed declaration indicating the contribution of each author (complete)
8. Inclusion of published outputs under Regulation 6 (9.1.2) or Regulation 43 (9) shall not constitute plagiarism.

* *Please note that it is the responsibility of the candidate to ensure that the correct version of the thesis is submitted.*

Signature of Candidate*:*		Date:	

Submission

Submitted By *(name in capitals):*	FIONA ELIZABETH THORBURN
Signature of Individual Submitting:	
Date Submitted:	

For Completion in the Student Service Centre (SSC)

Limited Access	Requested	Yes		No		Approved	Yes		No	
*E-thesis Submitted (**mandatory for final theses)***										
Received in the SSC by *(name in capitals):*						Date:				

Inclusion of Published Works

Declaration

This thesis contains one or more multi-author published works. In accordance with Regulation 6 (9.1.2) I hereby declare that the contributions of each author to these publications is as follows:

Citation details	N/A
Author 1	
Author 2	
Signature:	
Date:	

Citation details	
Author 1	
Author 2	
Signature:	
Date:	

Citation details	
Author 1	
Author 2	
Signature:	
Date:	

Contents

List of Tables

List of Figures

List of Abbreviations

ABS – Astigmatic Beam Shaping

AFRL – Air Force Research Laboratory

AI – Avalanche Ionisation

AM – Amplitude Modulation

AOM – Acousto-optic Modulator

AR – Anti-reflection

CW – Continuous Wave

DBR – Distributed Bragg Reflector

EDFA – Erbium doped Fibre Amplifier

EM – Electromagnetic

EOM – Electro-optic Modulator

ESA – Excited State Absorption

FCA – Free Carrier Absorption

FEP – Free Electron Plasma

FM – Frequency Modulation

FROG – Frequency Resolved Optical Gating

FWHM – Full Width Half Maximum

GDD – Group Delay Dispersion

GLS – Gallium Lanthanum Sulphide

GSAM – Graphene based Saturable Absorber Mirror

GSOC – Graphene coated Saturable Output Coupler

GVD – Group Velocity Dispersion

HR – Highly Reflective

HIP – Hot Isostatic Pressing

HWU – Heriot Watt University

IR – Infrared

KLM – Kerr-lens Modelocking

MIIPS – Multiphoton Intrapulse Interference Phase Scan

MOPA – Master Oscillator Power Amplifier

MPI – Multiphoton Ionisation

NA – Numerical Aperture

NLO – Nonlinear Optics

OC – Output Coupler

OPO – Optical Parametric Oscillator

ORC – Optoelectronics Research Centre

OSA – Optical Spectrum Analyser

PRF – Pulse Repetition Frequency

QCL – Quantum Cascade Laser

QML – Q-switched Modelocked

ROC – Radius of Curvature

SA – Saturable Absorber

SESAM – Semiconductor Saturable Absorber Mirror

SHG – Second Harmonic Generation

SLM – Spatial Light Modulator

SPIDER – Spectral Interferometry for Direct Electric-field Reconstruction

SPM – Self-phase Modulation

TI – Tunnelling Ionisation

TM – Transition Metal

TM:II-VI – Transition Metal doped II-VI semiconductor

TOD – Third Order Dispersion

ULI – Ultrafast Laser Inscription

WDM – Wavelength Division Multiplexer

YAG – Yttrium Aluminium Garnet

List of Publications by the Author

Journal Papers

1. S. McDaniel, **F. Thorburn**, A. Lancaster, R. Sites, G. Cook and A. K. Kar, "Operation of Ho:YAG ultrafast laser inscribed waveguide lasers," Applied Optics **56**(12), 3251-3256 (2017).
2. **F. Thorburn**, A. Lancaster, S. McDaniel, G. Cook and A. K. Kar, "5.9 GHz graphene based q-switched modelocked mid-infrared monolithic waveguide laser," Optics Express **25**(21), 26166-26174 (2017).
3. **F. Thorburn***, Y. Wang*, R. A. McCracken, S. McDaniel, G. Cook, A. K. Kar, P. Laporta and G. Galzerano, "Ultrafast hot-isostatic-pressed Cr:ZnSe laser at 2.4 μm," (Under Preparation).

Conference Papers and Posters

1. G. Demetriou, **F. Thorburn**, A. Lancaster, C. Craig, E. Weatherby, D. W. Hewak and A. K. Kar, "Fluorescence in Erbium Doped Gallium Lanthanum Sulphide: Potential for mid-IR Waveguide Laser," in *CLEO: 2015,* OSA Technical Digest (online) (Optical Society of America, 2015), paper STh1G.2.
2. **F. Thorburn**, A. Lancaster, S. A. McDaniel, G. Cook and A. K. Kar, "5.9 GHz Q-Switched Mode-locked Mid-infrared Waveguide Laser," in *Conference on Lasers and Electro-Optics,* OSA Technical Digest (online) (Optical Society of America, 2017), paper SM1I.5.
3. S. McDaniel, A. Lancaster, R. Stites, **F. Thorburn**, A. K. Kar and G. Cook, "Cr:ZnSe guided wave lasers and materials," Proc. SPIE 10082, 100820D (2017).
4. **F. Thorburn** and A. K. Kar, "5.9 GHz Graphene Based Q-Switched Mode-locked Mid-Infrared Monolithic Waveguide Laser," Institute of Photonics & Quantum Sciences Symposium 2017, Heriot Watt University, May 2017, poster.
5. **F. Thorburn** and A. K. Kar, "5.9 GHz Graphene Based Q-Switched Mode-locked Mid-Infrared Monolithic Waveguide Laser," 2nd International Symposium on Doped Amorphous Chalcogenides and Devices, Grasmere, May 2018,poster.
6. S. McDaniel, **F.Thorburn,** C. Liebig, J. Evans, M. Coco, G. Cook and A. K. Kar, "Mid-IR Ultrafast Laser Inscribed Waveguides and Devices," in *2019 IEEE*

Research and Applications of Photonics and Defense Conference (RAPID), (IEEE, 2019).

Chapter 1. Introduction

1.1 Motivation

The demonstration of the first laser was reported in 1960 by T. H. Mainman, it was a flashlamp pumped Ruby laser which emitted visible red light at 694 nm [1]. As a result of this invention, the rate at which coherent light source potential applications have been uncovered has grown rapidly. This has justified the need for persistent research into the development of continually improving laser sources. Laser technology has become very well established throughout the modern world with applications ranging from everyday uses such as Blu-ray players, barcode scanners and fibre optic broadband to much more specialised uses in laser eye surgery [2], laser welding [3] and numerous military/defence applications [4]. Following this laser demonstration the range of gain materials utilised grew very quickly with dye, gas, solid-state and fibre crystals/glasses and semiconductors all proving as useful gain media in the years to follow.

Laser Gain Medium	Emission Wavelength
AlGaN	~350 nm
GaInN	375-440 nm
Argon Ion	515 nm (green), 460 nm (blue)
HeNe	633 nm (red)
Ti:Al_2O_3	~650-1100 nm
InGaAs/GaAs	~915-1050 nm
Yb:YAG	1030 nm
Nd:YAG	1064 nm
Pr:fibre	1300 nm, 635 nm
Er:fibre	~1530-1620 nm
Tm:YAG	~1.7-2.1 μm
Er:YAG	2.9 μm
CO_2	10.6 μm

Table 1.1. Table of some of the most common laser gain media researched and developed in the ~50 years following the first laser demonstration and wavelengths they emit at.

Five decades after Mainman's report there existed a broad range of laser types with varying capabilities spanning much of the electromagnetic spectrum. Some of the most commonly used and well-researched gain media during this time are shown in Table 1.1, as well as the corresponding emission wavelengths. Much of the successes during

this time focused on the visible and infrared (IR) spectral regions. The IR in particular has attracted substantial attention due to communications wavelength applications. In more recent years, one spectral region which has emerged as a particular area for further research is the mid-infrared (mid-IR); ranging from 2-5 μm. Previously, there had been an absence of sources which emit in this region as there are few semiconductor materials which allow for efficient emission compared to the IR and visible spectral regions. Subsequently, there has been significant effort and funding invested to discover and develop new sources emitting here which can satisfy the specific requirements for the vast array of applications. The motivation behind this work is to explore new mid-IR laser source systems which are compact, robust and furthermore, have the potential ability for the generation of ultrafast pulses with GHz pulse repetition frequencies (PRFs). Hence, they would overcome many of the challenges associated with the commonly used sources at present – these will be discussed further later in this section.

1.2 Mid-infrared Sources of Emission

The need to continue developing new laser sources in the mid-IR is driven by the sheer number of applications in this spectral region. This is because this spectral range contains a number of atmospheric transmission windows; this can be seen in Figure 1.1.

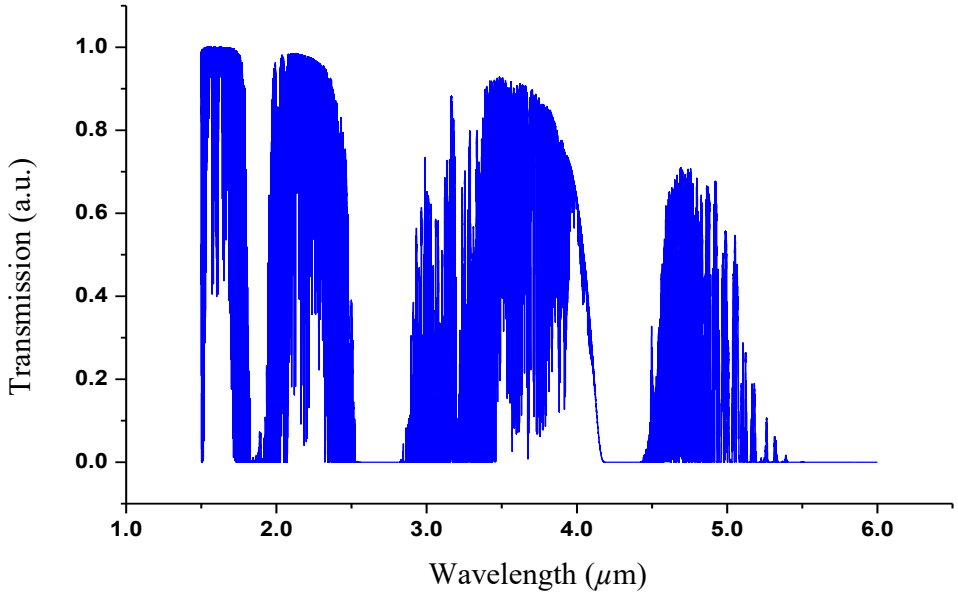

Figure 1.1. Simulated transmission spectra of the atmosphere. Data was simulated using the Atmospheric Transmission Software Tool (ATRAN) which uses the Philips Research Laboratories High-Resolution Transmission molecular absorption database (HITRAN) [5]. The data was sampled at a lower than the software output resolution to avoid very large output files.

A number of characteristic molecule absorption lines lie in this mid-IR spectral band, hence there are a great many opportunities for environmental monitoring and sensing using these sources [6]. Other applications of mid-IR laser sources include medical diagnostics and treatment [7], military countermeasures [8] and spectroscopy [9] to name but a few. Until the early 90s there was limited choice in the field of mid-IR laser sources, the area was mainly dominated by the lead salt semiconductor laser [10] and some gas lasers. These included HeNe which demonstrates emission at 3.39 μm [11], as well as Hydrogen Fluoride and Deuterium Fluoride emitting at ~ 2.8 μm and 3.9 μm respectively [12]. CO lasers have output in the higher end of the mid-IR window at ~ 4.6 – 8.7 μm, whereas CO_2 is useful for emission into the far IR at 9 – 11 μm [13, 14]. The invention of the Quantum Cascade Laser (QCL) in 1994 [15] and subsequent rapid development meant it quickly replaced the lead salt laser as the dominant source on the market in this wavelength range. QCLs have emission spanning 3 – 300 μm [16], performing at their optimum with wall plug efficiencies of up to 53%, at around 5 μm [17]. Initially they were predominantly cryogenically cooled to boost performance. Developments made in latter years have facilitated continuous wave (CW) operation at 4.9 μm with output powers of up to 5.1 W to be realised at room temperature with a wall plug efficiency of 21%, this is further increased to 27% for pulsed operation [18].

The disadvantages of QCLs lie in the fact that the output beams tend to be highly divergent resulting in limited irradiances if one cannot gather the output efficiently, and also they suffer from limitations in the transverse beam quality due to their multimode nature, diffraction and self-focusing effects [19]. QCL's which operate at room temperature with high power capabilities at 2-3 μm only cover a small range of wavelengths per emitter; thus have limited tunability. However, progress continues to be made in this area [20]. For many applications pulsed emission may be preferred over CW. Optical Parametric Oscillators (OPOs) find much of their use in the generation of mid-IR pulses by combining a modelocked near IR solid-state laser with an OPO [21], but they are also used for CW emission [22]. OPOs have impressive tuneable performance in the mid-IR but have the drawback of high thresholds thus requiring high pump power and relatively long coherence lengths to obtain oscillation. As a result they require a large number of free space optics and often have complex, large system set-ups associated with them, this can deem them unsuitable for many applications outside of the stable lab environment [23].

The specific parameters required from a particular laser source, that is to say; the wavelength, power capabilities, beam quality, system size, running and maintenance costs, pulse length, PRF and performance under extreme conditions including for example extremes of temperature and pressure are very much application dependent. For this reason a wide range of sources are required to satisfy the many different specifications and applications.

Two research areas which are promising as solutions to the lack of laser sources in the mid-IR are; transition metal (TM) doped II-VI semiconductors (TM:II-VI) and rare-earth (RE) doped crystals/glasses.

1.2.1 Transition Metal doped II-VI Semiconductor Lasers

TM:II-VI laser materials, examples of which are Chromium doped ZnSe, ZnS, and CdSe are attractive as laser gain media due to their wide tuneability, large gain cross section and absorption bands, ability to operate efficiently at room temperature and no excited state absorption (ESA) [24, 25]. Examples of other substrates which have been used for doping demonstrations are ZnTe and CdMnTe. Other common TM dopant ions include $Fe^{2+}$and Co^{2+} [26-28]. Laser wavelengths throughout the mid-IR from ~ 1.8 μm

to ~ 6 μm have been demonstrated with continuous tuneablity achieving CW output powers ranging from 10s of mW to > 100 W. One particular material which has been researched extensively is Cr^{2+} doped Zinc Selenide (Cr:ZnSe). Cr:ZnSe has been shown to have continuously tuneable lasing capability spanning over 1300 nm from 1973-3349 nm [29] and the maximum output power demonstrated to date in this material is 140 W with an optical efficiency of 62% [30]. For a long time, the highest output power reported was limited to approximately 14 W facilitated by a Master Oscillator Power Amplifier (MOPA) setup [25]. An impressive jump in output power from 14 W to 57 W [31] and subsequently 140 W was permitted by overcoming the inherent thermal lensing issue associated with ZnSe in these systems. The thermal lensing is due to the thermo-optic coefficient (dn/dT) of ZnSe; 70×10^{-6} K^{-1}[32]. This is relatively high when compared to the values associated with other common laser gain material substrates such as $Y_3Al_5O_{12}$ (YAG) and Al_2O_3 (sapphire), which have values of 9×10^{-6} K [33] and 12×10^{-6} K^{-1} respectively [32]. This parameter causes strong self-focusing in the crystal at high incident pump powers which results in cavity instabilities and possible optical damage, both leading to significant output power limitations. The high value of this parameter is common throughout the other II-VI semiconductor substrates with it being only slightly less in ZnS at 46×10^{-6} K^{-1} [32]. However, until fairly recently the fabrication process of high quality Cr^{2+}:ZnS crystals was lengthy and challenging, consequently investigations are continuing into how much the performance can be improved over ZnSe. The laser systems detailed in [30] and [31] overcome the thermal lensing problem by performing quick scanning of the pump beam and laser mode over the laser material at a speed high enough to minimise the instantly absorbed pump power over the crystal to a level so that effectively thermal lensing does not occur.

Another solution to the thermal lensing issue, whilst retaining a compact cavity, is to utilise a waveguide geometry. This can significantly reduce instabilities which occur as a result of thermal lensing. Cr:ZnSe waveguide lasers have been extensively studied over the past few years [34-38]. The first demonstration was reported in 2013 by McDonald et al. [34], in which depressed cladding channel waveguides were fabricated by the technique of Ultrafast Laser Inscription (ULI) and demonstrated an output power of 18.5 mW. However, in the years that followed the performance was greatly improved resulting in a maximum output power of 5.1 W [38]. As mentioned previously, being a TM:II-VI material, Cr:ZnSe is well-known to have a widely tunable emission range. Investigations into the tuneable range of a ULI waveguide CrZnSe

laser resulted in successful laser emission through 700 nm from 2077-2777 nm [37], this is the widest tuning range demonstrated in a waveguide laser to date.

1.2.2 Rare-earth doped Solid-state Lasers

Another major field which is also being researched for mid-IR emission is RE doped crystals/glasses. This is a vast research field with a huge amount of output in terms of laser demonstrations and papers, I will give a brief introduction to RE doped lasers concentrating predominantly on the relevance this field has in the development of mid-IR sources. The wavelength emitted by an RE doped laser material is determined by the radiative transitions which are available between the energy levels in the RE ions, which themselves are dependent on the host substrate material. This is due to Stark splitting of the energy levels of dopant ions which is a result of the local electric fields of the host material [39, 40]. There are seventeen RE elements in the periodic table; many of these are particularly useful in the IR and mid-IR due to many of their emission wavelengths lying in this window of the EM spectrum. As mentioned, there is a vast array of laser demonstrations in this field including one of the first solid-state laser demonstrations, the Nd^{3+}:YAG laser in 1964 at ~ 1 μm [41], which is still commercially manufactured and used widely today. The other most commonly used ions for emission in the IR are: Yb^{3+}, also for emission at around 1 μm [42], Pr^{3+} and Er^{3+}, with emission at 1.3 µm [43] and 1.5 μm [44] respectively – these lie in two very important telecommunications wavelength bands so are used widely for this. With regards to the mid-IR the most important RE dopants utilised to date have been Er^{3+} for its emission around 2.9 μm, Ho^{3+} for emission at 2.1 μm and Tm^{3+} which emits around 1.9-2 μm and so bridges the IR and mid-IR regions of the spectrum [45-47].

There also exists a very large number of host crystals and glasses which can be doped with these ions, I will focus solely on the ones that have been used in this work, specifically YAG, Gallium Lanthanum Sulphide (GLS) and ZnSe. The most important features of a host material among others are; its ability to accept the dopant ions, high optical quality with minimal defects, good thermal and mechanical properties and transparency throughout the mid-IR. Another sought after feature for a host material is low phonon energy. A phonon is a quantised vibration by which an electronic energy level in an atom/ion can decay. Multiple phonons are usually needed for the transition from one energy level to a lower one, as one single phonon would typically not have

enough energy to match the energy gap. The lifetime of an upper energy level can be greatly reduced by material which supports a high phonon energy. The reason for this is that the rate of the multiphonon transitions decreases exponentially with a rising number of phonons needed to match the difference in energy levels. Hence, if the phonons have low energy, a greater number of them are required and the multiphonon transition rate is kept low. For emission in the mid-IR spectral range, the energy gap between levels is small compared to emission in the visible and IR and we seek to keep the lifetime of the upper lasing level as long as possible. As a result, materials which have a low phonon energy are desirable as this ensures that this level cannot be reduced by phonon transitions and therefore the decay is radiative [48].

GLS is an emerging chalcogenide glass laser material which exhibits a relatively low phonon energy of 425 cm^{-1} [49] compared to other glasses, for example silica which has phonon energy 1150 cm^{-1} [50]. It is the first chalcogenide to have a rare earth ion as a main component, as a result it is readily acceptant of RE ions making GLS ideal for doping. Chapter 3 will discuss in depth work, that has been carried out using GLS doped with the RE ion Er^{3+} [41].

YAG is a very useful and widely established host crystal in the fabrication of solid-state laser materials. It exhibits a medium phonon energy of 700 cm^{-1} [51] and is readily acceptant of both RE and TM dopant ions – as a result, it has been used to develop a wide range of lasers in the visible, infrared and mid-infrared. Chapter 5 will discuss this material further and present results of the first Holmium doped YAG ULI waveguide laser.

1.3 Bulk vs. Waveguide Lasers

There are many different types of lasers including solid-state bulk material, optical fibre, semiconductor laser diodes, gas, dye and chemical – this is by no means an exhaustive list, there are many other types. The type of laser used is very much application dependent, as all types have their advantages and disadvantages. The research undertaken during this work focuses on two types of laser: bulk and ULI waveguide.

1.3.1 Bulk Lasers

This was the first type of laser to ever be demonstrated [1]. Generally, in the case of bulk lasers the beam propagates in free space between the gain material and other components in the cavity such as lenses and mirrors. The beam is not confined while propagating through the gain medium meaning that the size of the beam within the material is dependent on the resonator design, for which there are many options. These include a plane-plane cavity, a plane-concave cavity, concentric and x and z-fold cavities. These cavities tend to be relatively easy to set up in a laboratory setting and so can be useful for a "proof of lasing principle test" of a new material before optimising it for other laser types. The free space in the cavity between optics gives the cavity flexibility for the addition of other optical elements, for example; filters for wavelength selectivity, gratings/prisms for tuneability and dispersion compensation elements in the case of modelocking. A further advantage of the free space propagation, specifically in the case of modelocking, is that it is straightforward to increase or decrease the cavity length very quickly compared to fibre lasers where cutting/splicing may be required. In addition, one can design the resonator to implement a large effective mode area in the gain medium, this allows the generation of very high peak energies and powers for both modelocking and Q-switching operation. [52]. The shortest pulses are usually achieved using a bulk setup [53, 54].

1.3.2 Waveguide Lasers

An optically pumped waveguide laser can provide a platform to utilise the main advantageous properties of a solid-state bulk laser and a fibre laser. By implementing a waveguide geometry, a high degree of overlap between the pump mode and the laser mode can be achieved due to the confinement. In addition, a small laser mode area is achieved compared to a bulk system. The combination of these effects results in a system which can be very efficient in converting energy from pump to laser and obtaining low lasing thresholds. In comparison to a bulk system, the beam divergence is effectively removed within the gain material mitigating adverse thermal effects such as thermal lensing, this can result in a much higher quality beam mode even at high output powers [55, 56]. Depending on the method of waveguide fabrication, waveguides with propagation losses of ~ 0.1 $dBcm^{-1}$ can be achieved [57]. This is typically low in comparison to the losses associated with optical fibres considering a

much longer length of fibre is usually used. As a result of these combined effects waveguide lasers can generally achieve particularly high gain values per unit length and so can potentially operate above laser threshold at lengths on a mm to cm scale [55, 58]. A waveguide laser cavity can be easily lengthened or shortened by simply increasing or decreasing the free space length of the cavity respectively. This allows for the straightforward addition of extra cavity components as well as direct control of the PRF while operating in the pulsed regime. To summarise, a waveguide laser exploits the advantages of bulk and fibre systems simultaneously. What this means is that a waveguide laser cavity is robust in nature and also removes the beam divergence. This results in a highly compact system with high power and efficiency capabilities as well as good beam quality. It should also be noted that the compact design of waveguide laser systems can be particularly useful when the laser is used in modelocked operation where a very high PRF (multi GHz) is required as per some applications. This will be discussed in greater detail in chapter 5.

1.4 Thesis Outline

Chapter 2 provides an overview of the technique of Ultrafast Laser Inscription detailing the underlying absorption processes that facilitate waveguide fabrication. The choice of inscription geometry, the various inscription parameters and types of waveguides possible will be discussed.

Chapter 3 investigates the potential for mid-infrared laser emission from ULI waveguides in Erbium doped GLS glass. This is a relatively new host material with favourable properties for mid-IR emission. Fluorescence at 2.75 μm is detected from ULI waveguides pumped with a 980 nm source, thus demonstrating their potential for a compact mid-IR emission source. An IR ~ 1.5 μm waveguide amplifier is demonstrated with gain a of 5.4 $dBcm^{-1}$, this result is utilised to provide suggestions as to how the material and setup should be modified to facilitate laser emission into the mid-IR.

Chapter 4 details the background theory of pulsed lasers and also the techniques required to characterise the pulses. The formation of ultrafast pulses through modelocking of lasers is discussed before detailing the methods employed to achieve this. The concept of dispersion control to produce the shortest pulses is also introduced.

Finally, the autocorrelation based techniques and other methods used to measure ultrafast pulse durations are discussed.

Chapter 5 presents a CW and Q-switched modelocked Holmium doped YAG ULI waveguide laser. Depressed cladding channel waveguides are fabricated and characterised. Single transverse mode CW laser operation with output powers up to 1.78 W at 2.1 μm is initially demonstrated. Subsequently, Q-switched modelocked emission is demonstrated at a PRF of 5.9 GHz with up to 170 mW of average output power.

Chapter 6 presents a room temperature modelocked Cr:ZnSe bulk laser in which the laser crystal has been treated by hot isostatic pressing (HIP). An overview of TM doped II-VI semiconductors for laser operation in the mid-IR is given with particular attention on ultrafast pulse emission capabilities. The HIP technique and its consequences are also detailed before presenting the bulk cavity arrangement employed. A Kerr-lens modelocked Cr:ZnSe laser with a PRF of 182 MHz and average output power of 140 mW is demonstrated. Pulse durations down to 37 fs are achieved by exploiting intracavity chirped mirrors for dispersion control. This result represents the shortest pulse duration demonstrated to date in Cr:ZnSe. The reasons that the HIP process has facilitated this record result are discussed.

Chapter 7 details the conclusions achieved from the work presented in this thesis. It also discusses the possible future work that will pave the way for the development of novel compact, high PRF, ultrafast mid-IR emission sources, as this is the ultimate goal of this work.

1.5 Summary of Thesis

The comprehensive aim of the work undertaken in this thesis was to develop novel laser sources in the mid-IR with cavity designs that allow for very robust and compact systems which in turn have the potential for the generation of ultrafast pulses with multi GHz PRFs. It is the goal of the author that these may overcome many of the current disadvantages and limitations which are common to many of the mid-IR sources used at present. This section has introduced the various materials and techniques which have been utilised over the course of the research in an attempt to meet this aim.

During this work the relatively new chalcogenide glass GLS has been used as the host for Erbium as a dopant. ULI was used to inscribe waveguides in this material and mid-IR fluorescence was observed at 2.73 μm, the waveguides were also used to develop a high gain optical amplifier at 1538 nm and work continues in the field of doped GLS for laser emission. The success of ULI waveguide inscription in Ho:YAG has led to the development of the first waveguide laser in this material. Furthermore, the compact cavity has allowed for the generation of laser pulses with a high PRF of 5.9 GHz . A sub-40 fs modelocked Cr:ZnSe x-fold cavity bulk laser has been demonstrated in which the crystal has been treated with HIP. The result of the treatment is that the CW laser emission linewidth is reduced from typically 10's of nm wide to sub-nm level. This, to our knowledge, is the shortest pulse width demonstrated to date from polycrystalline Cr:ZnSe, indicating that HIP treatment is beneficial for ultrafast pulse generation.

Chapter 2. Ultrafast Laser Inscription

2.1 Introduction to ULI

The most prevalent example of a waveguide is the optical fibre, this technology is at the centre of the modern telecommunications market. As the demand for high-speed internet soared it became apparent that copper wire was undoubtedly insufficient to sustain requirements. The solution came in the form of optical fibre which provided a means for high speed, long distance communications which far out-performs copper wire. The reason for this lies in the low loss values achievable in fibre; propagation loss as low as 0.14 $dBkm^{-1}$ at 1560 nm have been reported in silica based optical fibres [59]. Thus, fibres with losses < 0.2 $dBkm^{-1}$ are now routinely produced and are available to purchase from Corning Inc. ensuring repeatable high-speed performance. However, this was not always the case; when optical fibres were beginning to emerge as an important technology in the early 1980s, the theorised losses were much closer to 20 dB/km^{-1} [60]. These high losses tended to be due to large numbers of impurities in the bulk glass and hence came a great push to research and develop much higher quality fibres with inherently low loss values. As a consequence of the advances in optical fibres came the development of the Erbium doped fibre amplifier (EDFA) paving the way for an all optical amplification system [61]. Despite the many positives that came with the development of optical fibres, one challenge imposed by them is due to the parameter of minimum bend radius. This tends to be of the order of ~ 3-8 cm [62] and as a consequence the compactness of any device utilising fibres them is limited by this parameter. Using a fibre while breaching this limit can diminish the performance significantly and fibre damage can occur. The full system used for high-speed internet telecommunications has other vital components; examples of these include arrayed waveguide gratings, optical splitters and Mach-Zehnder modulators [63]. Minimising the physical size of these devices is paramount and so fibres tend to be inadequate for these devices. As a consequence, advances in the technology of photonic integrated circuits have occurred simultaneously to that of fibres. The basis behind many devices is the guiding of light in low loss waveguides on a compact chip. There are a number of well-established techniques used during the fabrication of thin film waveguide structures, namely; RF and magnetron sputtering, Chemical Vapour Deposition and Pulsed Laser Deposition. Techniques such as ion exchange and implantation are used in the fabrication of channel waveguides. These techniques are often used alongside

lithography and annealing processes [64]. The disadvantage common to all these fabrication methods is that they are limited to the development of only 2D structures.

During the past two decades a new method has emerged for the fabrication of photonic waveguides which has the advantage of producing buried 3D structures. This technique is called Ultrafast Laser Inscription (ULI). The premise of ULI, is to tightly focus ultrafast laser pulses below the surface of a dielectric material which is transparent to the laser wavelength, if the laser parameters are chosen correctly, this can result in a localised permanent change in the dielectric material properties within the focal volume of the focused laser beam. The first demonstration of a permanent change in the refractive index was carried out by Davis et al. in 1996 [65], since then it has grown to be an effective tool for creating waveguides and other photonic devices. In the focal region of the focused pulses various energy transfer processes can occur between the pulses and the dielectric material, these processes are of a highly complex nature. Therefore I will attempt to give a summarised version of those which occur to result in the fabrication of 3D optical waveguides which are used in this work. It is vital that nonlinear light absorption processes occur at the focus for ULI to be effective, so it is important to understand how to induce these over linear absorption. For this reason, the differences between the two will first be discussed.

2.2 Linear Absorption Processes

In any non-metallic material there exists a bandgap energy, E_g, which is defined as the energy difference between the highest filled electron energy level – the valence band and the next energy level – the conduction band. If a beam of light is incident upon the dielectric material, for a single photon to be absorbed and excite an electron from the valence band into the conduction band, the energy of that photon, E_p, must be greater than or equal to E_g. This condition is summarised in equation (1) and is true for all incident electromagnetic (EM) radiation whether pulsed or CW .

$$E_p = h\nu \geq E_g \tag{1}$$

In the case of a metal, the conduction band is already partly occupied by electrons and so photons can also be absorbed through free-carrier absorption (FCA). During FCA an

electron can move to one of the closely spaced higher energy levels in the conduction band by gaining energy and momentum through absorption of a photon and interacting with a lattice vibration (phonon) respectively. There is also the potential for electron transitions between the conduction band itself and higher energy bands. Furthermore, material ablation is possible if the incident light has adequate energy [66, 67].

2.3 Nonlinear Absorption Processes

Dielectric media are used as the substrate for ULI. The wavelength of the inscription laser must be chosen so that the photon energy is not sufficient to induce linear absorption over the bandgap of the dielectric in question, in other words E_p must be < E_g. In an ideal dielectric material under normal conditions, photons with this energy would simply propagate through the material without experiencing any absorption. In ULI, ultrafast pulses are used so that the high peak powers which are tightly focused in space sufficient to generate e-fields in the focal region. In turn, the e-fields generated are great enough to excite electrons over the bandgap via the nonlinear excitation processes; tunnelling and multiphoton ionisation [67].

Multiphoton ionisation (MPI) can occur if the energy condition above is met, during this process several photons are absorbed simultaneously and the combined energy is sufficient to promote an electron over the bandgap energy into the conduction band. The probability that MPI will occur is dependent on the generated e-field at the focus of the incident light and this process dominates at high laser frequency and low irradiance. Whereas, at high irradiance, tunnelling ionisation (TI) tends to dominate, this process is not influenced by the laser frequency. Under normal conditions, electrons are bound to their atoms nucleus by the coulomb potential attracting opposite charges. During tunnelling ionisation the e-fields generated by the inscription laser are sufficient to inhibit the coulomb potential and allow electrons to tunnel through the decreased barrier into the conduction band [66, 67]. The probability of this occurring is proportional to the strength of the generated e-field. It was presented by Keldysh that MPI and TI are in fact two different limits of the same process, this is outlined in [68]. He showed that the type of ionisation which dominates is dependent on the bandgap energy and incident photon energy and can be specified in terms of the Keldysh parameter, γ, which is calculated using (2).

$$\gamma = \frac{\omega}{e}\sqrt{\frac{m_e c n \varepsilon_0 E_g}{I}} \tag{2}$$

In equation (2) ω is the laser angular frequency, e and m_e are the electron fundamental charge and mass respectively, c is the speed of light, n is the material linear refractive index, ϵ_0 is the permittivity of free space, $E_g$is the bandgap energy and finally, I is the laser intensity at the focus. If the result of (2) is that γ is much greater than 1.5, MPI dominates, conversely if γ is much smaller than 1.5, TI dominates. For instances where $\gamma \sim 1.5$ both processes occur approximately equally. The Keldysh parameter for the fabrication of waveguides within dielectric materials is typically ~ 1, as a result one can say that the photoionisation occurring is a combination of MPI and TI [67].

When an electron has been promoted into the lowest level in the conduction band by either MPI or TI it has a number of available states above it. The electron will continually absorb photons from the incident laser, this absorption is mediated by phonons to satisfy the preservation of momentum. The electron will repeatedly absorb more photons until it reaches a point at which it has enough energy to impact ionise an electron which is lying in the top of the valence band. The impacted electron is therefore excited into the conduction band. This process is called Avalanche Ionisation (AI). It recurs throughout the time that the laser is incident and as a consequence, the Free Electron Plasma (FEP) density in the conduction band exponentially increases during this time [66]. Each of the discussed processes are demonstrated in Figure 2.1.

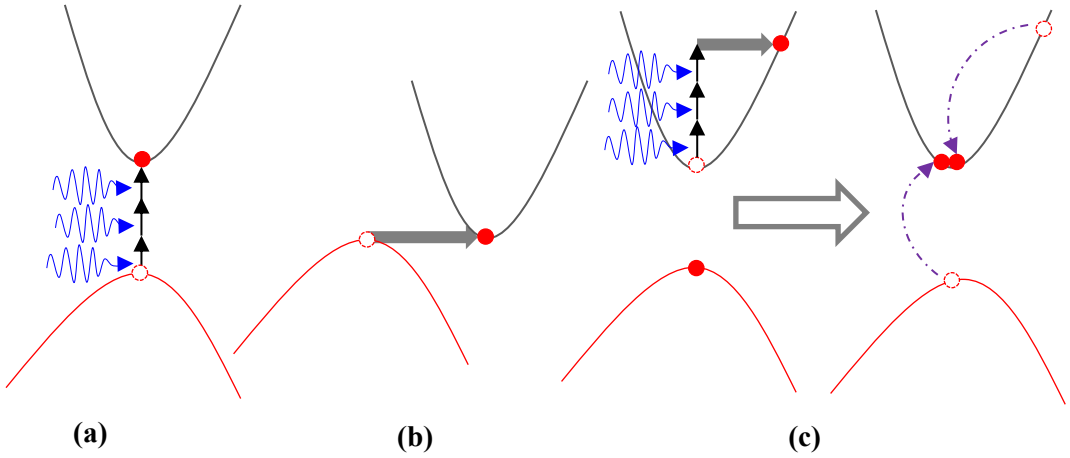

Figure 2.1. Nonlinear photoionisation processes which can occur during ULI. (a) Multiphoton ionisation, (b) Tunnelling ionisation, (c) Avalanche ionisation. Reproduced from [69].

For the AI process to occur some electrons must already exist in the lowest energy level of the conduction band, this condition can be satisfied through MPI and TI so one can say that these two processes seed the AI which results in the high density FEP. If only the nonlinear photoionisation were the only absorption processes occurring, there would be a large variation in the optical breakdown threshold for different materials because of the very different bandgap energies. Both MPI and TI seed the AI process and it repeats continuously, thus it becomes the most prominent process for increasing the electron density in the conduction band. The AI process depends linearly on the laser intensity, therefore the optical breakdown threshold is actually only loosely dependent on the bandgap energy. As a result of this there is a huge variety of dielectric materials that ULI can be used to successfully fabricate waveguides in [67, 69] . The FEP induced by the incident laser pulses oscillates with a resonant plasma frequency given by equation (3):

$$\omega_p = \sqrt{\frac{Ne^2}{\varepsilon_0 m_e}} \tag{3}$$

where N is the number of electrons per unit volume and the other parameters are the same as for (2). This value increases with increasing FEP density until it matches the frequency of the inscription laser itself, at this point the plasma oscillation is driven resonantly by the laser and much of the rest of the pulse is absorbed by the plasma. As

the pulse then leaves the focal volume the plasma starts the transfer of energy to the cold lattice. The point of resonance is referred to as the critical density of free electrons and for a ~ 1 μm inscription laser, it occurs when the density of electrons in the conduction band reaches levels of the order ~ 10^{21} cm^{-3}. When this resonance is achieved at the critical density it is assumed that optical breakdown begins in the material [69] .

2.4 Energy Transfer

The transfer of energy to the cold lattice is achieved through the scattering of phonons. This process is induced on two different timescales. On a ps timescale scale is it induced due to electron-ion collisions which occur until thermal equilibrium is reached at a temperature of approximately 10^5 K. It is also induced on a ns timescale due to the recombination of electrons with ions [70]. Therefore, the heating which actually occurs during the pulse is negligible for ultrafast fs pulses as the absorbed energy is transferred to the lattice for some time after the pulse has left the focal volume. The ultrafast pulses are able to induce a situation in which minimal energy is required to reach optical breakdown; hence a very dense FEP exists within a relatively cold surrounding lattice. This allows for very efficient heating in the material within the focal volume meaning highly precise modification is possible and damage to the surrounding area is kept to minimum as thermal diffusion to outside of the focal volume is low [69]. This is the ideal condition for ULI to induce refractive index modification for the fabrication of waveguides. Whether this condition is met or not is highly dependent on the inscription laser pulse length. If the pulse duration is longer than 10-100s of fs, i.e. picosecond to nanosecond, then the energy transfer to the cold lattice occurs on the same time scale as the pulses length. In this situation thermal diffusion out of the focal volume is the process by which energy is transferred to the lattice. This significantly diminishes the heating efficiency in the focal volume compared to case of incident pulses with sub-ps durations. Furthermore, the AI which is required to create the FEP is seeded in this case by defect states and some concentration of impurities in the conduction band, this is because the incident intensities achieved is not high enough to induce MPI and TI processes. As a result, minor fluctuations in the number of seed electrons can significantly affect the ability of the plasma to reach the critical density [67].

Conversely, if pulses which are too short are used, which is of the order of 10s of fs in most materials, this can result in the photoionisation processes becoming predominant over AI and therefore themselves inducing a FEP which is able to directly cause damage to the material. Ideally, one will select a pulse duration which lies in between these two limits ensuring that AI dominates the photoionisation processes and thermal diffusion outwith the focal volume is minimised [67, 69].

As previously discussed, the transfer of energy to the lattice from the dense FEP induces efficient heating of the material in the focal volume. This heating can result in one of the following possible outcomes; no modification occurs, the material in this region melts or the material is driven into a plasma or gas phase. If the latter two occur, the heat subsequently diffuses out from the material and it solidifies with a permanently altered structure. Thus far, ULI has been used to induce three different structural modification regimes in bulk glasses and crystals; 1) a refractive index which has a smooth variation, 2) nano-gratings which cause a birefringent change in the refractive index and 3) formation of voids of decreased material density. The specific mechanisms which are responsible for these structural modifications are not yet fully understood and are still debated in the literature and can be explored further in [63, 69, 71].

2.5 Index Modification by ULI

ULI has previously been shown to be useful in the modification of many material parameters leading to the three regimes named in the last section, they include thermal conductivity, optical absorption, chemical etch rate and most notably for this work the refractive index; for this reason this is the regime which will be concentrated on and discussed fully in the next section.

By definition, a waveguide is a structure which confines and directs the propagation of electromagnetic radiation. One method to achieve this is to create a continuous track of material which has increased refractive index compared to the surrounding material. To fabricate this type of structure with ULI, the ultrafast laser beam must be focused beneath the surface of the material and then translated through it. It is actually more practical to have a fixed position inscription laser and then fix the substrate on an xyz

stage which can be translated through the laser focus. With fine and accurate control of the inscription parameters, one can simply translate the substrate straight through the focus once to induce a region of increased refractive index resulting in a waveguide with a step profile, this is generally the simplest case. For more complex structures in which the waveguide size must be very accurately controlled or a negative change in refractive index is desired, the process is a little more complicated and the translation stage must have nm precision to achieve this [69].

2.5.1 Inscription Geometry

There are two geometries which can be used to implement ULI; longitudinal and transverse.

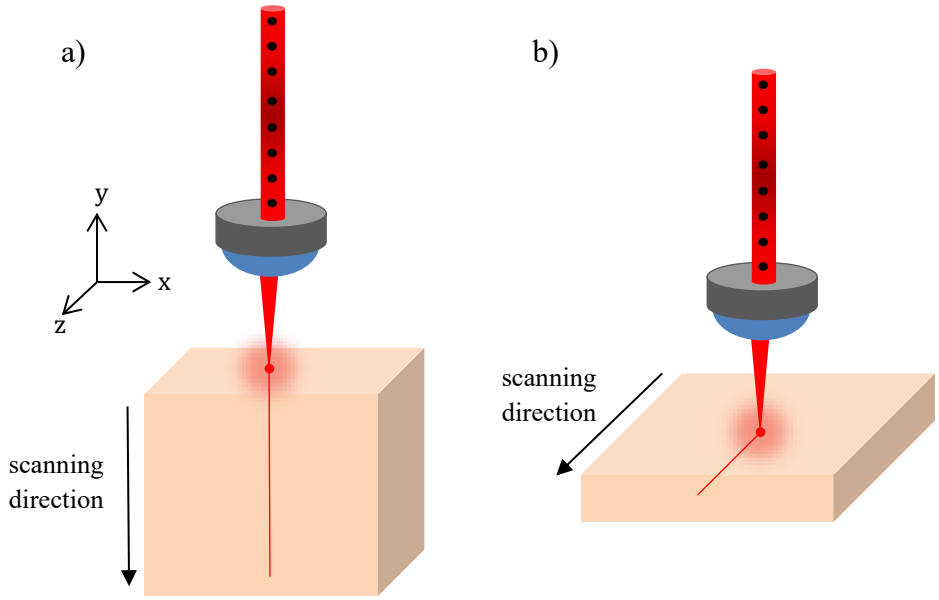

Figure 2.2. Geometries which can be used for ULI, (a) longitudinal and (b) transverse.

In the longitudinal geometry the substrate is translated in the direction parallel to the incident laser beam as shown in Figure 2.2 a). The advantage that this holds, is that the cross section will be circular and symmetrical which is usually desired. However, the length of waveguide is severely restricted by the working distance of the focusing lens used, in ULI high Numerical Aperture (NA) lenses are usually utilised to ensure tight focusing and these inherently have working distances limited to only a few mm. Generally, in the case of fabricating waveguides for lasers, it would be required to,

initially at least, write waveguides longer than this and so it is not suitable. In attempts to overcome this limitation there have been cases where lenses with lower NA values have been used to focus the laser beam. However, to meet the required intensity to induce the necessary photoionisation processes, high laser peak powers are required. These high peak powers induce the formation of a Kerr-lens self-focusing effect. During the ULI process, this self-focusing effect has been shown to cause the formation of long filaments of refractive index change [72] . Therefore it can be exploited for the formation of long waveguides overcoming the working distance limitation of the lens. However, the drawback of this process is that the formation of a waveguide takes a long time compared with that of transverse geometry methods which are discussed later. As an example, in silica glass it took 10 minutes to inscribe single filaments between 120-200 μm long with a 0.1 NA lens [73]. Whereas, transverse geometry inscription methods can inscribe the same waveguide length in typically a few tenths of a second [74]. Thus the working distance limitations can be overcome, but writing speed is drastically reduced. A different method to overcome the length limitation of the longitudinal geometry is to use a Bessel beam rather than a Gaussian beam shape. An axicon lens can be used to achieve this as reported in [75], the authors used this technique to write waveguides in BK7 glass. This method does, however, complicate matters further as the inscription is depth dependent so fabricating a consistent structure throughout the length can be challenging.

In the transverse case the substrate is translated in the direction perpendicular to the propagation direction of the inscription laser beam, this is demonstrated in Figure 2.2 b). This allows for the fabrication of waveguides of potentially any length limited only by the maximum stage translation as the lens working distance is no longer an issue. The disadvantage of this geometry is that the fabricated waveguide has an asymmetric cross section. This is due to the difference in the beam waist diameter and the confocal parameter at the focus, this is detailed in equations (4) and (5).

$$2w_0 = \frac{2f\lambda}{\pi w(f)} = \frac{2\lambda}{NA\pi} \tag{4}$$

$$b = 2z_0 = \frac{2\pi n w_0^2}{\lambda} \tag{5}$$

In equations (4) and (5) w_0 is the focused beam waist radius, $w(f)$ is the beam radius at the lens, f is the focal length of the lens, NA is the numerical aperture of the lens, λ is the laser wavelength in free space, n is the refractive index of the substrate and b is the confocal parameter which is twice the Rayleigh length: z_0. From these equations it is clear that $2w_0$ and b will only be close and so result in a near symmetrical waveguide, if the beam waist radius w_0 is $\sim \frac{\lambda}{n\pi}$. This can only be achieved if the focusing lens used has an NA which is approximately equal to the refractive index of the substrate. However, creating waveguides this small can have a very detrimental effect on the confinement of the waveguide with the $10^{-2} \sim 10^{-3}$ refractive index modification which is usually induced by ULI [76]. As a result, a single scan waveguide inscribed with ULI which exhibits suitable confinement for a guided mode will generally be elongated in the direction parallel to the beam axis as will be shown later. A symmetrical waveguide is more suitable for many application requirements. For this reason it has been necessary to investigate techniques for manipulation of the waveguide cross section and shape of the inscription beam, to achieve a high degree of waveguide symmetry. Several of these methods are discussed in the next sub-section.

2.5.2 Beam Cross Section Manipulation Techniques

Astigmatic Beam Shaping

The first method which can be employed to control the cross section of the resultant waveguide is astigmatic beam shaping (ABS). It was first demonstrated in 2002 by Cerullo and Oseallame et al. in 2003 [77], the experimental setup is shown in Figure 2.3.

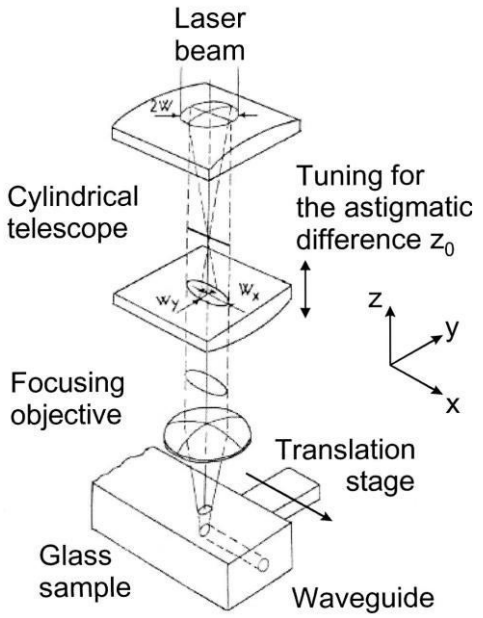

Figure 2.3. Experimental setup of astigmatic beam shaping technique. Reproduced from [77].

The basis of this method is to create an effective reduction in the Rayleigh length in the z direction at the focus, which will result in equations (4) and (5) having a much smaller difference and therefore a near-symmetric cross sectional modification occurs at the focus. The Rayleigh length is reduced by altering the distance between two lenses which form a cylindrical telescope prior to the focusing objective; this can be seen in Figure 2.3 The substrate is fixed in an x-y plane, with sample translation along x-axis and beam propagation direction in z-axis. The astigmatism which causes different focused beam sizes in the x and y planes can be tuned suitably to guarantee tight focusing in the x-z plane. This minimises the asymmetry and so leads to the fabrication of near-symmetric circular cross section waveguides. This technique was successfully employed a number of times but its use was quickly overshadowed by the development of simpler ones; the following Slit method being an example of this.

Slit Method

In this method a thin slit is simply placed before the focusing lens, the aim is to place the slit at a distance such that the incident beam fills the lens in one axis and under fills it in the other. Hence, the lens induces a different NA for each axis and the specific distance from the lens to the slit can be tailored to control the focal volume shape and adjust for asymmetry. Although this is the simpler technique compared to the ABS

method, it is limited by the fact that it only applies manipulation of the beam size in one dimension. This can be an issue if the desired device requires bends/inscription in another direction as the slit would have to be adjusted for this which would complicate the process. This technique, and that of ABS, presented two particular difficulties for the fabrication of some desired waveguide structures. The first being a lack of flexibility; the cross section of a waveguide is constant and cannot be readily altered either between concurrent waveguides or in a particular waveguide. The second is that both techniques allow manipulation in only one dimension, so the cross section of waveguides which include bends would vary along the length.

In more recent years an important development was made to overcome these limitations. New techniques involved the use of computer controlled active optics before the focusing lens to shape the laser beam. These include the use of a deformable mirror and a spatial light modulator (SLM).

Active Optics Techniques

The setup used when applying the method of a deformable mirror is shown in Figure 2.4. It was first demonstrated in 2008 by Thomson et al [78]. The idea is to project the light on to a very thin 2D membrane referred to as a "deformable mirror". This membrane is hung over the top of a series of electrode actuators, an applied voltage can cause the membrane to be pulled towards and away from the actuators effectively deforming its shape and so the shape of the reflected beam. In this way the focal volume distribution is controlled in the substrate. As the whole process can be computer controlled this has the advantage over using the standard Slit Method that more complex patterns with bending structures can be easily inscribed.

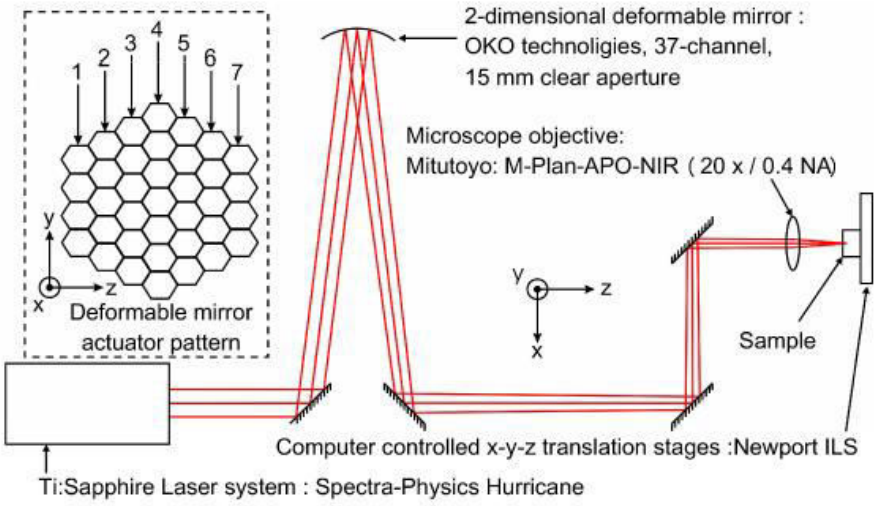

Figure 2.4. Experimental setup of deformable mirror technique for beam cross section manipulation. Reproduced from [78].

To use the SLM technique, one replaces the slit or cylindrical telescope arrangement with an SLM. The SLM gives the user the ability to introduce a controlled astigmatism in the beam wavefront prior to propagation through the focusing optics. The amount of astigmatism can be manipulated by a computer during the inscription process as opposed to previously when the slit would have to be physically adjusted continually and so, as with the deformable mirror, devices with bends or other complex structures can be created with greater ease. This was first demonstrated by Ruiz de la Cruz et al. in 2009 [79] and the experimental setup they used in shown in Figure 2.5.

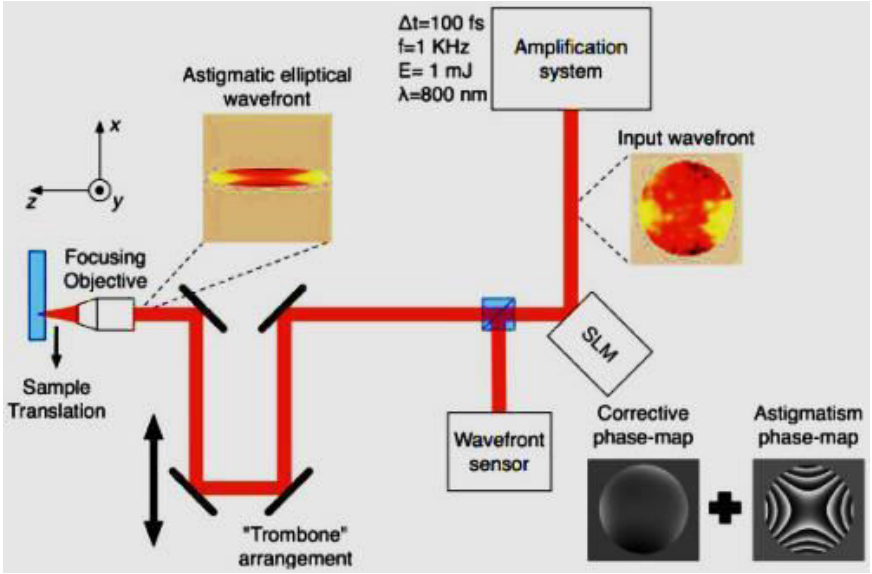

Figure 2.5. Schematic diagram of the experimental setup used to control the inscription beam cross section with an SLM. Image reproduced from [79].

Multiscan

Finally, the technique of fabricating near-symmetric structures using multiple scans to build up the waveguide will be discussed. This is the method that is used throughout this work in an attempt to control the cross section. Unlike the other methods previously mentioned, this one does not involve manipulation of the inscription beam before the objective lens. This method simply involves inscribing multiple tracks sequentially to build up a waveguide with close to homogenous modification throughout the required cross section [76].

2.6 Types of Waveguide Fabrication

Depending on the material substrate itself and the inscription parameters attainable, ULI can be used to write regions of increased or decreased effective refractive index. As a result, there are a series of inscription patterns which may be possible and these are summarised in Figure 2.6. Type I waveguides are those which are fabricated through an increase of refractive index in the modified area. A single scan of Type 1 modification is asymmetric as shown in the diagram, and directly next to this we can see a Type I waveguide; this is constructed by inscribing a series of single scans and translating the sample a small distance in the x axis in between each scan. The result is a near square shaped waveguide consisting of many overlapping scans.

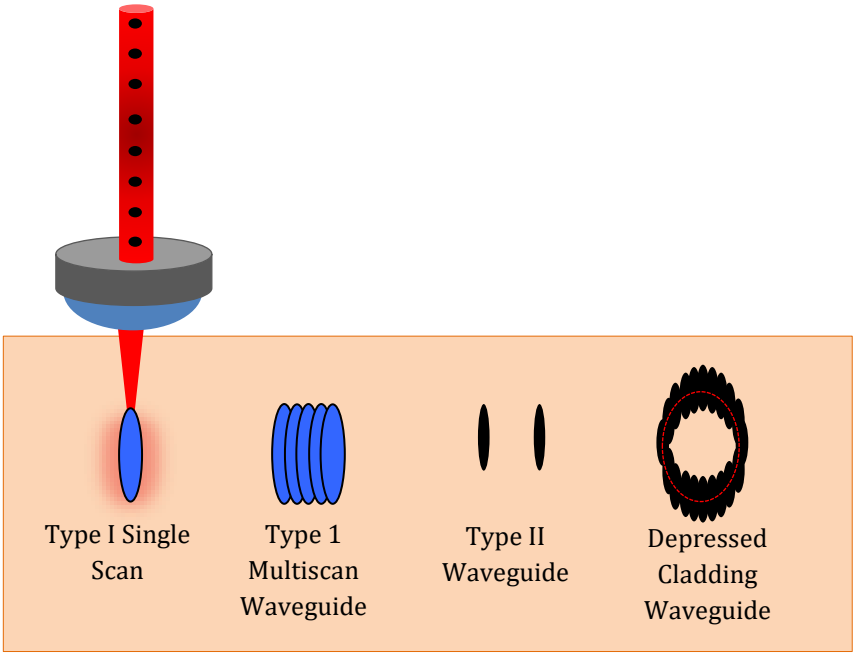

Figure 2.6. Schematic diagram of the types of waveguides which can be fabricated using ULI as viewed from the end facet of a substrate. blue: localised increase in refractive index, black: effective reduction in refractive index.

For many materials, especially crystalline structures, Type 1 modification is often very difficult to achieve with the standard available inscription parameters, however it is possible to write tracks of what are referred to as damage lines and induce a region of reduced refractive index by making use of the strain-optic effect. In this case it is not the directly modified region which has the useful index change but the volume surrounding the modification. A Type II waveguide is formed by inscribing 2 parallel tracks and the light is confined to the centre region by the overlapping strain fields induced by the inscribed region. In this case the core i.e. the guiding region is unmodified material and the strain overlap required is achieved by inscribing damage lines which are essentially regions of decreased refractive index compared to the surrounding bulk material. Guiding light down an unmodified core can be advantageous over Type I guiding in situations where knowledge/understanding of the fundamental material parameters are vital to the application as these can change during type I inscription. The last waveguide type in the figure and one which has proven particularly useful for efficient guiding in the mid-IR is called a Depressed Cladding Waveguide. This structure is made by arranging Type II elements in a ring-shaped fashion and was first successfully demonstrated in Nd:YAG material by Okhrimchuk et al. [80]. The reason these depressed cladding structures are particularly useful for the confinement and propagation of mid-IR light is that scaling waveguides in size from 10

μm to 300 μm can be achieved relatively easily without the need for increasing the inscription laser pulse energy and therefore potentially causing unintended damage and cracking in the sample. This range of sizes has been found to be optimum for propagation at this wavelength. This is not the case for Type II waveguides, their height is limited by the ablation threshold of the substrate material and substrates can be easily damaged if this is reached in attempts to increase the waveguide size.

The multiscan method is a very useful tool which allows for quick fabrication of many waveguides in a substrate during one inscription run. This is advantageous over other waveguide fabrication techniques particularly in the development of a waveguide laser. The user can write and test many waveguides very quickly once suitable initial inscription parameters are identified and so the process of optimising the laser can be very efficient. The properties of the resultant waveguide structures which are a result of ULI are dependent on a variety of inscription and material parameters. The following section describes these parameters and their role in the inscription process.

2.7 Inscription Parameters

Pulse Duration

The pulse duration has important implications for the outcome of the modification which have been discussed in some detail above. It controls to a degree the extent at which the nonlinear effects occur, because it alters the peak powers generated at the focus for a given pulse energy. This parameter has also been shown to have an effect on the propagation loss of the inscribed waveguide [81]. The authors varied the pulse duration and investigated the resultant waveguide propagations losses; they found that particular windows of pulse duration were optimum for low loss waveguide fabrication. However, the exact mechanisms responsible for the behaviour exhibited are not yet understood.

Pulse Energy

The value of the pulse energy is critical to the ULI process as it dictates how much energy is transferred to the material. Control of this parameter is vital to induce the type of modification desired.

Pulse Repetition Frequency

This parameter is also one of the most important to consider when performing ULI due to the associated thermal implications. At very high PRFs, thermal accumulation of pulses can occur as the material is not permitted sufficient time to cool in between pulses. For as long as the pulses are incident, the material undergoes melting. When the pulses have exited the focal volume, heat diffuses from the focal region in all directions equally, this results in a larger modified region which has a more symmetric cross section. Whereas, at low PRFs, each pulse interacts with cold material and thermal accumulation does not occur at all. The spatial distribution of the modified region in this case is governed by the spatial distribution of the FEP induced by each pulse and the effect of heat diffusion away from the modified region is negligible. Therefore, the PRF can play a pivotal role in determining the size of the modified material volume and hence the waveguide cross section [69].

Laser Wavelength

Again, this is one of the most important inscription parameters. As the process relies on the nonlinear processes discussed, the wavelength must be chosen to satisfy the condition for MPI, as a result the chosen wavelength depends on the substrate material bandgap energy [69].

Translation Velocity

Similar to the laser PRF, this parameter can determine if subsequent pulses overlap and to what degree and therefore how much, if any, thermal accumulation occurs. This in turn can be used to control the cross section and guiding region of the inscribed waveguides particularly at high repetition rates [69].

Polarisation

Several studies have demonstrated that the polarisation of the incident laser beam has significant ramifications on the resultant magnitude of the refractive index change in various media. For example, in fused silica, it has been shown that linearly polarised incident laser radiation results in a greater refractive index modification when compared to circularly polarised light. The authors attempt to explain this by suggesting that there is a polarization dependence of the photoionisation rates in this material [82].

Objective Lens NA

This parameter directly controls the peak irradiance that can be achieved in the material. As can clearly been seen from equation (4), it also has a crucial role in determining the cross section of the modified region.

2.8 Chemical Etch Rate Modification

Although this description has been heavily focused on the use of ULI for writing waveguides as this is what it has been used for in the presented work, it should also be noted that this technique has also been successfully used for its ability to locally increase the chemical etch rate of some materials [69]. Unlike the refractive index modification which has been demonstrated in a range of different crystals and glasses, this effect has only been shown to work in a select few, including fused silica. This is because, as opposed to the refractive index modification which is loosely dependent on the bandgap energy, the mechanism by which the chemical etch rate is changed is heavily dependent on the substrate material parameters. It has been reported that the increase in etch rate in inscribed regions is due to induced reductions in the bond angles which are then more easily broken by Hydrofluoric acid [83]. It has also been reported that another reason for the etch rate increase is that ULI generates nano-cracks in the substrate which the HF can infiltrate much more easily compared to the un-irradiated material [84].

As a result of the successes in changing the refractive index and chemical etch rates using ULI a number of useful devices have been reported in addition to waveguide

lasers. These include a microfluidic cell sorter, photonic lantern, multicore fibre couplers and wavelength division multiplexers to name but a few. For details of many of the other devices fabricated by ULI processes see [69].

2.9 Summary

The technique of ULI has been introduced in this chapter; it has been shown to be a versatile tool for the fabrication of 3D channel waveguides in dielectric media. The underlying physical processes and mechanisms of ULI which lead to refractive index modification in a substrate have been detailed. The geometries which can be used have been presented. The challenges posed by the different geometries have been discussed as well as various methods which can be employed to overcome these. It is concluded that utilising a transverse geometry setup with adequate control of the laser inscription parameters can be an effective way to fabricate waveguides which support the confinement of IR and mid-IR radiation. This is pivotal to the project of building compact mid-IR waveguide lasers.

Chapter 3. ULI Waveguides in Er^{3+}:GLS for Mid-Infrared Emission

3.1 Spectroscopy of Erbium doping for Lasers

This chapter presents the results obtained during investigations into the use of the relatively new chalcogenide glass GLS which has been doped with Erbium, with a view to demonstrate a compact waveguide source emitting on the ~ 2.9 μm line associated with this dopant. The wavelength emitted by an RE doped laser material is based on the radiative transitions which are available between the energy levels of the RE ions. The energy levels themselves, and so the specific wavelength of the emitted radiation, depend on the local electric field in the particular host material as this causes Stark splitting of the dopant ion [40, 85]. An example which illustrates this point in the mid-infrared is Erbium, it is most well-known for lasing at 2940 nm in the host material YAG [45, 86-88]. However it has also demonstrated lasing at 2797 nm, 2821 nm [88] and 2716 nm [89] in other host materials. The trivalent Erbium ion, Er^{3+}, is chosen for use as a dopant ion because of its emission potential in several useful spectral regions. The basic energy level structure of the Er^{3+} is shown in Figure 3.1.

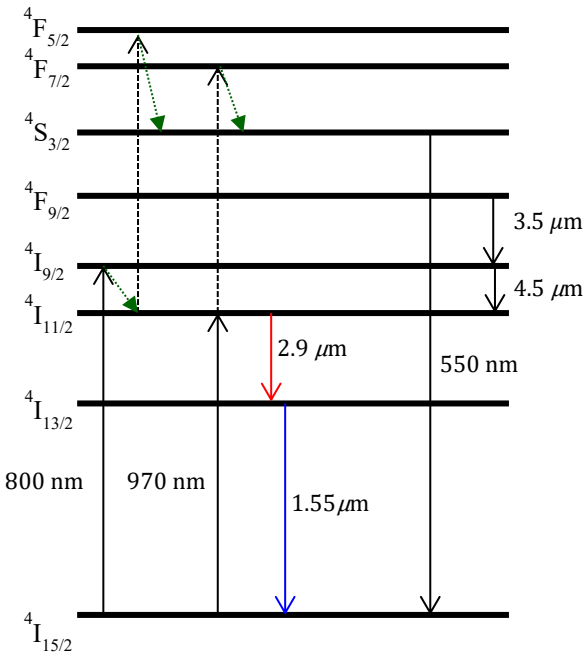

Figure 3.1. Energy level diagram of Er^{3+} ion. The transitions highlighted are those which are important for laser operation. Green dashed arrows represent fast non-radiative decay, black dashed arrows indicate a sequential pump absorption process and the solid arrows represent radiative transitions and absorption. The diagram was produced using information from [90-93].

The laser transition which has been the most extensively used and developed is that from energy level $^4I_{13/2}$ to energy level $^4I_{15/2}$ at ~ 1.55 μm, this is because it lies in the telecommunications C-Band window from 1528-1561 nm [94]. The most common setup to activate this laser transition is to use a pump source at ~ 970 nm to excite electrons into the $^4I_{11/2}$ level, these quickly decay into level $^4I_{13/2}$ and with suitable mirrors to create a resonator, lasing operation occurs from $^4I_{13/2} \rightarrow {}^4I_{15/2}$. This emission is demonstrated by the solid blue arrow in Figure 3.1. Laser action is initiated because the lifetime of the $^4I_{11/2}$ level is short compared to level $^4I_{13/2}$, hence a population inversion can easily occur on this transition through pumping into the $^4I_{11/2}$ level. In-band pumping schemes have also been demonstrated in which pump wavelengths in the absorption peaks which range 1450-1490 nm [95, 96] and 1520-1550 nm [96-98] can be used. In-band pumping is possible due to the splitting of each energy level into several Stark sublevels. For the application of in-band pumping, one option can be to excite electrons from the ground state into a particular energy level which radiatively decays directly into a higher energy sublevel of the ground state, which in this case is the lower lasing level. Another configuration employed is to pump electrons into a particular energy Stark sublevel, from here the electrons can decay non-radiatively to another nearby sublevel then lase between this Stark manifold and the ground state. These in-band pump schemes can be useful for emission in line with the L-Band communications window, 1561-1620 nm [94] and beyond, which is largely increasing in use. In-band pumping is also beneficial for overcoming efficiency limitations associated with the 970 nm pumping scheme. As already discussed in chapter 2, the development of ultra-low loss silica optical fibre transformed the field of telecommunications. This fibre is found to experience these remarkably low loss values for wavelengths in the region of 1.55 μm [59] thus justifying the subsequent development of sources in this spectral area, in particular the EDFA which has demonstrated gain greater than 50 dB [99]. Er^{3+} has been doped into many other materials and shown to successfully lase on this transition. Examples include Er^{3+}:tellurite glass [100], Er^{3+} doped bismuthate glass [101] and phosphate glass co-doped with Er^{3+} and Yb^{3+}, in which the Yb^{3+} presence increases the pump absorption efficiency and transfers the absorbed energy to the Er^{3+} [102]. Er^{3+} has also been utilised to demonstrate the operation of upconversion lasers for the generation of visible green light in materials including fluorozirconate [103, 104] and others [90-92]. An upconversion laser is one in which the emission wavelength is shorter than the pump wavelength i.e. the energy of the lasing photons is greater than the pump energy.

The processes which are responsible for the operation of these upconversion lasers are covered in detail in sub-section 3.5.1.

3.1.1 Mid-IR Emission from Er^{3+} doped Media

As this work is focused on mid-infrared source emission, it can be seen from Figure 3.1 that there are relevant potential laser transitions not only at ~ 2.9 μm as represented by the solid red arrow, but also at ~ 4.5 μm and 3.5 μm. Whilst laser emission has been demonstrated on the latter transitions previously [105-107], the ~2.9 μm transition has received the most attention and research. This is most certainly driven by the applications in medicine and dentistry in this spectral region; these specific applications are due to the fact that dental enamel consists of 85% volume hydroxyapatite, and 12% volume water, both of which experience strong absorption coefficients at wavelengths in the region of 2.9 μm [108, 109]. This wavelength is therefore also strongly absorbed by the high water content in tissue, resulting in the ability to perform microsurgery very accurately with minimal thermal damage in the localised area [110]. Er^{3+} lasers emitting at 2.9 μm also find some use in remote sensing [111] through the small atmospheric transmission bands within close range of this wavelength which can be seen in Figure 1.1. As previously stated, the specific allowed energy transitions in an RE doped material are dependent on the substrate material structure [49]. As a result, lasers emitting on the $^4I_{11/2} \rightarrow {}^4I_{13/2}$ transition have been observed spanning the range 2.7-2.94 μm in a number of different host materials. Perhaps the most well-known combination is Er^{3+} doped into YAG crystal. This is mainly due to the superior thermo-mechanical properties associated with YAG over other hosts which are desirable for high output power performance. Er^{3+}:YAG lasers at this wavelength are now widely available commercially and have demonstrated CW Watt-level output powers [45]. The mentioned properties and a detailed discussion of YAG as a dopant host is presented in chapter 5. Demonstrating lasing action from the $^4I_{11/2} \rightarrow {}^4I_{13/2}$ emission level in Er^{3+} brings with it the challenge of generating a population inversion when the upper lasing level has a much shorter lifetime than the lower lasing level. Generally a ~ 970 nm pump is used to pump electrons directly into the upper lasing level $^4I_{11/2}$ and various methods can be employed to induce the required population inversion, a number of these methods are explored more fully in section 3.7.

From the discussion in the previous section it is concluded that the wavelengths emitted from RE doped laser solid-state media are heavily dependent on the host material parameters. Two of the principal parameters to consider when identifying potential host media are the material transparency and the phonon energy, these determine which possible radiative transitions are allowed to occur. As presented in chapter 1, a phonon is defined as a quantised vibration by which an electronic energy level in an atom/ion can decay. For emission in the mid-IR it is desirable to use a material substrate with a low phonon energy to maximise the upper lasing level lifetime. In materials which support a low phonon energy, more phonons are necessary to bridge the gap between energy levels. The chance of this multiphonon process occurring is low, thus ensuring that the decay is radiative. To summarise, an optimum host for potential emission in the mid-IR will be transmissive throughout the mid-IR spectral region, have a low phonon energy and is readily acceptant of RE dopant ions [49].

3.2.1 GLS Fundamental Properties

GLS is a chalcogenide glass which has relatively recently emerged as a potential mid-IR laser material exhibiting the aforementioned properties. Figure 3.2 displays a graph of Transmission vs. Wavelength through a 1 mm sample of GLS with 1 mm and Table 3.1 summarises some of the important parameters of this glass.

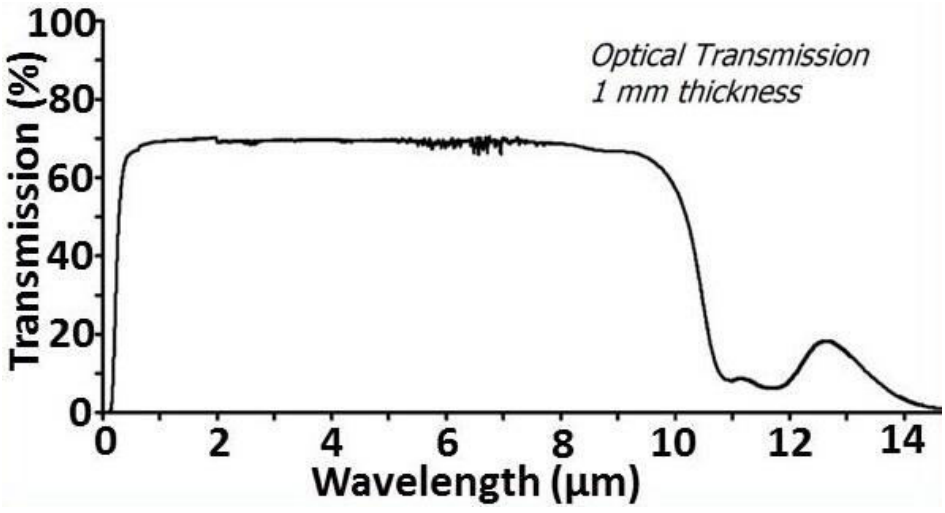

Figure 3.2. Transmission vs. Wavelength measured through a 1 mm thick sample of GLS.

Material Property	Value
Optical transparent range	0.5-10 μm
Zero material dispersion wavelength	3.61 μm
Refractive index @0.589 um	2.493
Thermo-optic (dn/dt)	$75 \times 10^{-6} K^{-1}$
Glass Transition Temp.	853 K
Phonon energy	425 cm^{-1}
Thermal conductivity	0.43 W cm^{-1} K^{-1} @ 273 K

Table 3.1. A table summarising some of GLS glass key material parameters, information contained in table has been gathered from [49, 112, 113] and datasheets provided to us by the glass manufacturers/suppliers, which are continually updated.

Unlike standard crystalline semiconductors which show a sharp absorption edge, in a disordered glass material it is expected that the absorption coefficient has an exponential dependence on the photon energy when the incident radiation has energy below the optical band gap energy. The observed decrease in transmission as absorption increases can typically span 10s of microns in wavelength before transmission reaches zero. This has the appearance of a tail and so is referred to as the Urbach tail, after Franz Urbach initially observed it in 1953 [114]. It occurs as a result of interband-gap states between extrinsic impurities and intrinsic defects which can be accessed through multiphoton absorption processes [115, 116]. In GLS, the Urbach tail reduces to zero at approximately 2.6 eV; in terms of wavelength this is equivalent to ~ 477 nm, hence the deep orange appearance of the glass.

From Table 3.1 it can be seen that the phonon energy for GLS is 425 cm^{-1}, which is significantly lower compared to that of other commonly used glasses such as silica and phosphate, which have values in the 1100-1200 cm^{-1} range [117, 118]. It is also slightly lower than that of fluoride based glasses at ~ 500 cm^{-1} [119]. Before GLS was formed, it was widely accepted that chalcogenide materials were not suitable for use as a host of RE ions because of their inherent low solubility of these ions. However, the first formation of GLS was to be pioneering in this field as low RE solubility was not the case with this glass, this is because Lanthanum itself is an RE ion [49]. This was the first time a chalcogenide glass compound existed with an RE ion as a main constituent, the Lanthanum ions can be relatively easily replaced with any RE ion, rendering it ideal for this type of doping. Since its discovery by Flahaut et al. in 1973 [120], GLS has attracted much attention and has been extensively studied for its potential use as an emission substrate material.

GLS possesses several other advantageous qualities over other chacognides. It is a chemically stable, non-toxic material and it has a relatively high glass transition temperature of 853 K. This means that the fabrication and the correct handling procedure of GLS is much simpler compared to other chalcogenides which tend to contain Arsenic or another toxic element such as Se or Te [121]. In addition, one can apply high power incident radiation on the glass with minimal thermal damage compared to, for example As_2S_3, which has a glass transition temperature of 426 K. Furthermore, it will suffer less from temperature fluctuations in the environment which could otherwise have a detrimental effect on the glass structure [49]. An additional advantage of the high glass transition temperature of GLS is that fibre geometry can be exploited which can benefit many applications over a bulk glass. Crystallisation often occurs during the fibre pulling process of other chalcogenides. It occurs as a result of the high temperatures required to pull fibres, but the higher transition temp in GLS means it can endure these without the risk of crystallisation occuring [122]. Despite the favourable properties that GLS exhibits for the application of mid-IR laser emission, it does suffer from a high thermo-optic coefficient and poor thermal conductivity which are shown in Table 3.1. When pumping with significantly high power a thermal lens will be induced in the material due to the high thermo-optic coefficient. The low thermal conductivity will result in poor heat distribution away from the laser mode which is causing the thermal lens [49]. The laser output would be detrimentally affected and consequently, attempts at power scaling laser devices may be limited. Previously, GLS has proven to be a useful host material for doping with Nd ions resulting in successful laser emission in the near-IR ~ 1 μm in both fibre [123] and bulk [124] configurations. The aim of this work was to attempt exploit the favourable parameters of GLS, particularly the low phonon energy, for emission at higher wavelengths into the mid-IR by using Erbium as the dopant.

3.2.2 GLS Fabrication Procedure

The fabrication method described here is that developed by the suppliers of all glass samples used throughout this work – the Optoelectronics Research Centre (ORC) in Southampton University.

The process begins with Gallium Sulphide and Lanthanum Sulphide in powder form, which are assembled together in molar ratios which range from $58Ga_2S_3$:$42La_2S_3$ to

$72Ga_2S_3$:$28La_2S_3$ dependant on what the glass is to be used for. For instance, a melt with a higher Lanthanum Sulphide concentration has a higher refractive index which can be used as the core in a fibre. The powders are melted together in a vitreous carbon boat which is put into a silica tube inside a furnace. The mixture is melted at a high temperature of 1423 K for around eight hours and then the carbon boat is moved along the silica tube and out of the furnace where a flow of water is directed around the tube quenching the melt into a glass. The next stage is to anneal the glass in a furnace at a lower temperature of around 800 K for typically twenty four hours. It is annealed at 800 K because at this temperature the internal stresses in the glass are relieved which results in a much more durable glass that is ideal to cut, shape and polish. During the melting, a continuous flow of Argon is directed around the melt in an attempt to reduce glass impurities. More recently the ORC have introduced reactive atmosphere melting where instead of Argon, Hydrogen sulphide/Sulfur hexafluoride are used. This further reduces Oxygen and Hydroxide impurities in the glass and more importantly, it counteracts sulphur loss which can occur during fabrication. This update to the process has resulted in a much higher quality glass produced in higher quantities [49, 125]. For doped glasses part of the Lanthanum Sulphide is replaced in the powdered form of the desired dopant ion, it is usually a molecule which is added in, for example Er_2O_3, Pr_2S_3 etc.

3.3 Laser Schemes in Er:GLS

The absorption spectrum as a function of wavelength for Er^{3+} doped GLS glass is shown in Figure 3.3, it also shows the atomic energy level diagram and the corresponding approximate energy level radiative lifetimes. From here on Er^{3+} doped GLS will be referred to as Er:GLS for simplicity.

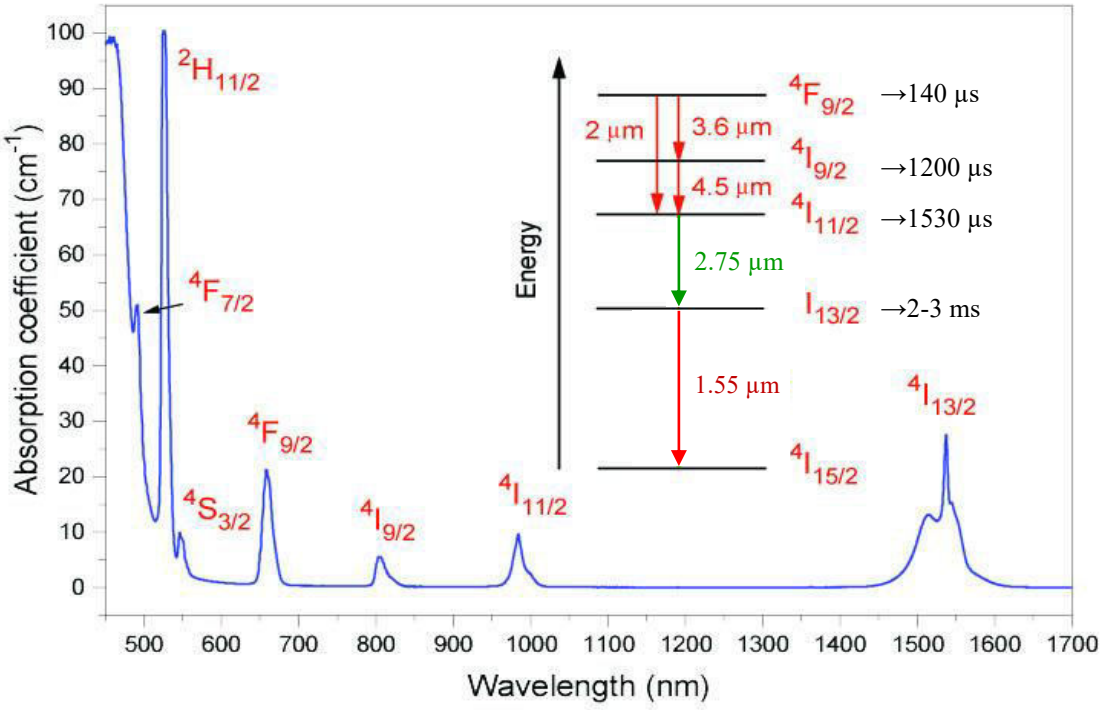

Figure 3.3. Atomic energy level diagram and absorption spectrum of Er:GLS. Diagram and annotated lifetime values reproduced from [125].

Initially, research efforts were concentrated on the demonstration of laser action between the $^4I_{11/2}$ and $^4I_{13/2}$ levels. This transition is highlighted in green in Figure 3.3 and has an expected emission wavelength of 2.75 μm. This is the mid-IR transition in other Erbium doped material which has shown the most success in previous work compared to the ~ 3.5 and 4.5 μm transitions [45, 87, 88, 126-128]. Sources at 980 nm are required for pumping directly into the $^4I_{11/2}$ level to induce a three level laser system, these are readily available in diode form. Pumping directly into the upper lasing level is preferable here because non radiative transitions which cause quick decay into the upper lasing level as with a four level system cannot be relied upon in this type of low multiphonon energy glass, as covered in detail above. It is desirable to have a situation in which the upper lasing level has a longer lifetime than the lower lasing level so that the population inversion generation required for lasing can be achieved with little difficulty [129]. However, in situations where this is not the case, as is here, there are some potential solutions which can be employed to overcome this issue and these will be further detailed in section 3.7.

3.4. Inscription of Mid-IR Waveguides in Er:GLS

ULI waveguides were fabricated in GLS for the first time by Hughes et al. [130] at the ORC in Southampton. However, to fabricate low loss waveguides using ULI in any substrate that has not been used in a particular inscription setup, an in-depth investigation must be carried out initially to identify the optimum inscription parameters offered by the system for that substrate. Such an experiment was carried out by a previous member of the Nonlinear Optics (NLO) group at Heriot Watt University (HWU) in undoped GLS. The detailed analysis and characterisation of the resultant low loss waveguides fabricated by the NLO group ULI system can be found in [131]. The author found at this time he was unable to establish a regime in which ULI could be used to induce a negative change in refractive index in GLS that could be utilised for the fabrication of depressed cladding like structures or Type II waveguides. However, suitable inscription parameters were identified which resulted in the fabrication of high quality Type I waveguide structures with propagation losses measured using the cut-back technique to be as low as ~ 0.6 $dBcm^{-1}$.

It is now generally accepted that a ULI induced positive refractive index change in GLS is caused by means of stress in the substrate material imposed by the incident laser [132] and densification [133]. The origins of the propagation losses associated with the waveguides are not yet entirely established, as a result research continues in the field to fully understand them. However, it has been reported that scattering is responsible for a considerable proportion of the loss [134, 135]. Broken chemical bonds, extended defects and laser induced colour centres which are a result of the ULI process are thought to be responsible for the significant scattering present [136, 137]. Radiation from leaky modes in the waveguide core are thought to be responsible for another portion of the loss – the evidence for this is most apparent when a small index change is induced and thus the confinement of guided light is rather weak [138].

Silica has been used extensively in the study of ULI and as a result waveguides inscribed in this glass have reported propagation losses as low as ~ 0.1 $dBcm^{-1}$ [57, 139]. However, the lowest propagation loss measured in a waveguide fabricated by ULI is 0.027 $dBcm^{-1}$, this was demonstrated in Gorilla glass [140]. This puts into context the 0.6 $dBcm^{-1}$ loss value observed in GLS glass and although higher than these values it is slightly lower than the lowest loss reported to date in GLS, which was

measured to be 0.8 $dBcm^{-1}$ by Arriola et al. [141] . It is thought that with further investigation possible with a wider parameter range, beyond the scope of our system, improved losses could be achieved. Previously ULI has been used to inscribe Type I waveguides in a number of doped glass substrates which have been developed into effective waveguide lasers. Some examples include a Tm^{3+}:fluorogermanate glass which demonstrated lasing action at 1.91 μm with an output power of 32 mW and a slope efficiency of only 6% [142], a Yb:Bismuthate glass, lasing at a wavelength of ~ 1 μm with a maximum output power of 163 mW and a remarkable slope efficiency of > 78% [143]. Further examples are the Nd doped silicate ULI waveguide laser demonstrated by Ramsay et al. with an output power and slope efficiency of 7.5 mW and 15% respectively [144] and a co-doped Er:Yb:phosphate glass waveguide laser with maximum output power of 50 mW and a slope efficiency of 21% [145]. These examples display a range of different dopant and substrate glasses which have been successful in the realisation of a Type I ULI waveguide laser thus demonstrating the versatility of this technique in glass materials for this purpose.

3.4.1 ULI Setup at Heriot-Watt University

The laser inscription setup used by George Demetriou in his initial GLS inscription parameter investigation as well as the subsequent waveguide inscription in the Erbium doped GLS samples covered in this work will now be described. The ultrafast laser was an IMRA μJewel D400, this is a Yb:fibre, chirped pulse MOPA system. The laser operated with circular polarisation at a central wavelength of 1043 nm. The pulse width was ~ 359 fs with a PRF of 500 kHz, the maximum pulse energy available was 2.5 μJ. The system operated in the transverse geometry setup described in sub-section 2.5.1. The system is computer controlled. The user is able to control the sample position by mounting it on air bearing XZY Aerotech stages with the capability of nm precision. The other parameters which can be varied by the user are the average power, the speed of the translation stage through the focused beam and how tightly the beam is focused below the substrate surface by careful selection of the focusing lens. To build up the Type 1 multiscan structures described in section 2.6 one can specify both the number of scans to inscribe and the separation between scans from the control PC, in this way the user has control over the width of the waveguide. This is important because it gives the user a high degree of control over the emission output mode profile.

The optimum output for an initial lasing demonstration is a single transverse Gaussian mode. This is because this condition ensures maximum overlap between the pump and signal within the waveguide resulting in the lowest lasing threshold [146].In addition to this, higher coupling efficiencies are achievable for single mode profiles if the NA of the waveguide can be matched to the coupling optics. Furthermore, multimode waveguides, in general, tend to exhibit higher propagation losses because they will experience more combined internal reflections, between the core and cladding, than one single mode. Practically, this is not always the case with ULI waveguides as the smaller inscribed waveguides that are required for single mode operation can have higher propagation losses, but this is due to the inscription process and parameters which the user will attempt to optimise. Transverse single mode output also has a number of advantages for applications involving the output beam. It is more straightforward to optically manipulate a single mode beam with lenses and such compared to a multimode beam. It can be focused to smaller spot sizes and the resulting higher irradiances are useful for many applications [146]. It also is essential if one should wish to use the laser in the modelocked regime.

3.4.2 Type I Waveguide Inscription in Er:GLS

The Er:GLS samples used throughout this work were fabricated by our collaborators at the ORC in Southampton University. To begin with, the samples available were a series of 20x10x2 mm bulk glasses with the following molar composition:

1) $65Ga_2S_3:34La_2S_3:1Er_2O_3$
2) $65Ga_2S_3:33La_2S_3:2Er_2O_3$
3) $65Ga_2S_3:30La_2S_3:5Er_2O_3$

Hence, these samples will be labelled 1%Er:GLS, 2%Er:GLS and 5%Er:GLS for simplicity form here on. The ULI system described above was used to fabricate a series of Type I waveguides in a sample of 1%Er:GLS in an attempt to find the optimum parameters to achieve single mode propagation for the emission of the transition corresponding to 2.75 μm, see Figure 3.3 for clarity. With a base knowledge of the range of parameters that give a successful positive index change from previous work done [131], the important parameter to vary to execute that aim was the waveguide diameter. The separation between each scan contributing to a waveguide and the

number of scans per waveguide were varied; the result was a series of waveguides with diameters ranging from 8.4 – 13.26 μm. A 0.4 NA lens was used to focus the laser pulses to a depth of 150 μm below the GLS surface, the sample was then translated perpendicularly to the direction of the laser beam. The effect of the pulse energy and sample translation speed were also investigated by using values ranging from 40 to 80 nJ and 4 to 16 mms^{-1} respectively. Figure 3.4 is a transmission microscope of the Type I multiscan waveguides in a 1%Er:GLS sample. After inscription, the end facets were polished to a high optical standard which can be seen in this image.

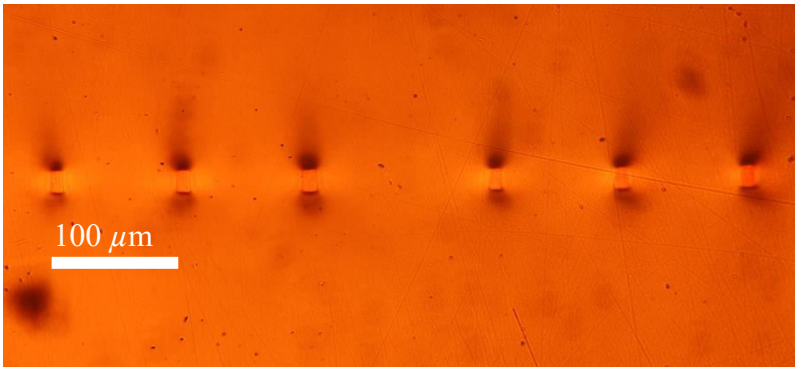

Figure 3.4. Microscope image of the end facet of the 1%Er:GLS sample with ULI waveguides inscribed.

3.4.3. Mid-IR Waveguide Characterisation and Fluorescence Measurements

The sample was then used in the experimental setup shown in Figure 3.5 for waveguide characterisation.

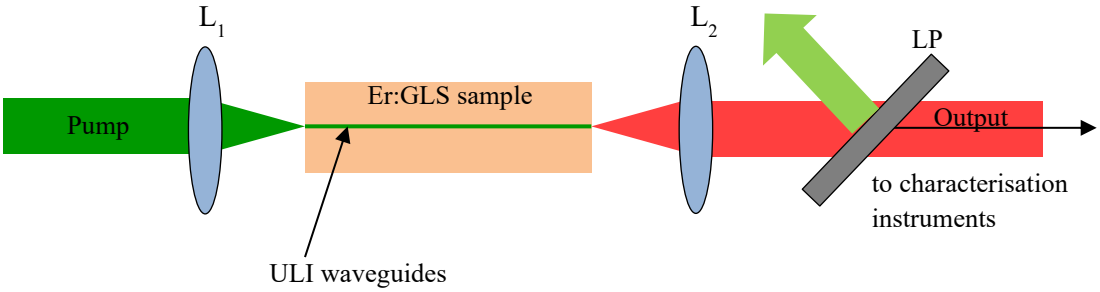

Figure 3.5. Schematic diagram of the experimental setup used to characterise Er:GLS waveguides.L_1 and L_2 are aspheric plano-convex lenses AR coated at 652 – 1050 nm. LP is a 2 µm long pass filter.

The pump laser used was a 980 nm fibre coupled diode with a maximum output power of 1 W. The 980 nm fibre output was collimated with a 10X magnification aspheric lens. L_1 is the incoupling lens which couples the pump light into each waveguides for testing, a variety of plano-convex aspheric Newport lenses were used maximise

coupling into each waveguide, these lenses were Anti-reflection (AR) coated from 625 – 1050 nm. For optimum coupling, the NA of the incoupling lens should be matched to that of a single mode waveguide. However, as this was not possible with the lenses available, the lens which resulted in maximum coupling of pump light for each waveguide was selected. L_2 is a lens used to collimate the output for testing and it was a plano-convex BK7 lens with a 50 mm focal length. LP represents a 1 μm long pass filter used to filter out any unabsorbed pump light, an LP 2 μm filter was also used to filter out any 1550 nm fluorescence when the higher wavelength emission was being investigated.

Initially the output mode profiles from the waveguides were viewed on a mid-infrared camera to inspect the transverse mode profiles. The camera is an SC7000 model manufactured and sold by FLIR which has an InSb detector and operates over a spectral range from 1.5 – 5.1 μm. With the 2 μm LP filter in the setup it was found that waveguides wider than 12.5 μm were multimode for 2.75 μm emission. Fluorescence was also detected at ~ 1.55 μm, this was found to be multimode in all the waveguides. This is not unexpected. If a step-index contrast is assumed in the waveguides the V number parameter can be calculated to estimate the number of allowed modes in the waveguide. This parameter is given by equation (6).

$$V = \frac{2\pi}{\lambda} aNA \tag{6}$$

In which a is the waveguide radius, and NA is the numerical aperture. If V is calculated to be < 2.405, the waveguide has only one allowed propagation mode per polarisation direction. For values higher than this, the waveguide can propagate multiple modes [147]. From equation (6) it can be seen that this value is inversely proportional to the wavelength, as a result for the lesser wavelength of 1550 nm, the V number will be greater than that for 2750 nm and so it is likely, that at this wavelength multiple modes are allowed to propagate.

Examples of the output beam profiles are shown in Figure 3.6.

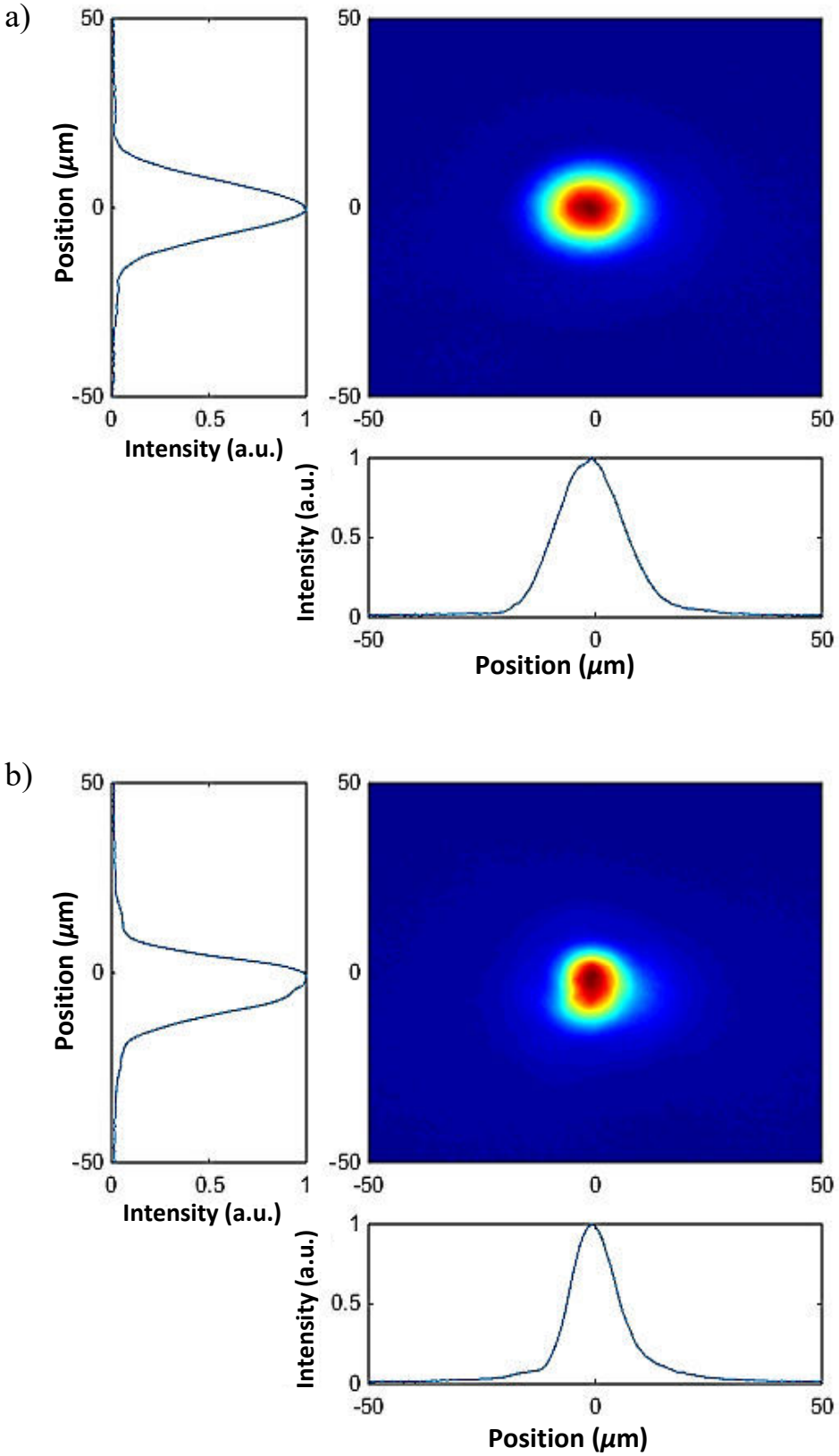

Figure 3.6. FLIR camera images of a) single mode output profile of ~2.75 μm emission and b) multimode output profile of ~ 1.5 μm emission from 8.7 μm wide waveguide in 1%Er:GLS sample.

These particular mode profiles were collected from an ~ 8.7 μm diameter waveguide which was inscribed with a pulse energy of 58 nJ at a sample translation speed of 4mms^{-1}.

To verify what was being viewed on the camera was indeed fluorescence at the wavelengths expected, the emission was measured with a spectrometer. The spectrometer used was a Yokogawa AQ6376 optical spectrum analyser used in 1 nm resolution mode. Two peaks were detected in the spectrum, one at 1550 nm and a peak of much lesser intensity was detected at 2730 nm – this is slightly blue-shifted compared to the expected wavelength. This is explained due to a hole in the atmospheric absorption at 2730 nm, the 2750 nm radiation is absorbed by water vapour in atmosphere before it reaches the spectrometer and what is actually detected is a side band of this peak. Therefore one can logically assume that the emission at 2750 nm actually has greater intensity than what is actually detectable in this setup.

The inscription process was repeated in the 2% and 5%Er:GLS samples using the identified waveguide widths for single mode propagation at the 2750 nm emission wavelength. The beam profiles of the emission were viewed on the camera to select the optimum waveguide, and the fluorescence emission was again measured. Each sample was pumped with the same incident power of 1 W. All measured spectral peaks are shown in Figure 3.7. A 1550 nm fluorescence peak could not be detected from the 5%Er:GLS sample so there is no data displayed for this sample in Figure 3.7 a). The span for Figure 3.7 a) was 150 nm and for 3.7 b) is 80 nm. These spans were used for clarity and to avoid very long measurement times. The data in each case has been normalised in the intensity scale. Concentrating, firstly on the 1%Er:GLS emission spectra, the peak detected at 1550 nm has much greater intensity than that at 2730 nm. This implies that the stimulated emission is occurring to a much greater degree in the transition from $^4I_{13/2} \rightarrow {}^4I_{15/2}$ than $^4I_{11/2} \rightarrow {}^4I_{3/2}$. There is a clear increase in the intensity of the 2730 nm emission when the samples with increased dopant levels are pumped with the same pump power. As the inscription parameters used where unchanged for each sample it is assumed that the waveguide propagation losses, and also coupling losses, are relatively similar. Therefore, it can be sensibly assumed that the intensity increase in the emission spectra is a direct result of the higher Er^{3+} concentration. The higher dopant level results in increased absorption of pump light. With increased absorption,

more electrons are excited into the $^4I_{11/2}$ level, this in turn means there are more electrons likely to decay into the $^4I_{13/2}$ level and hence emit photons.

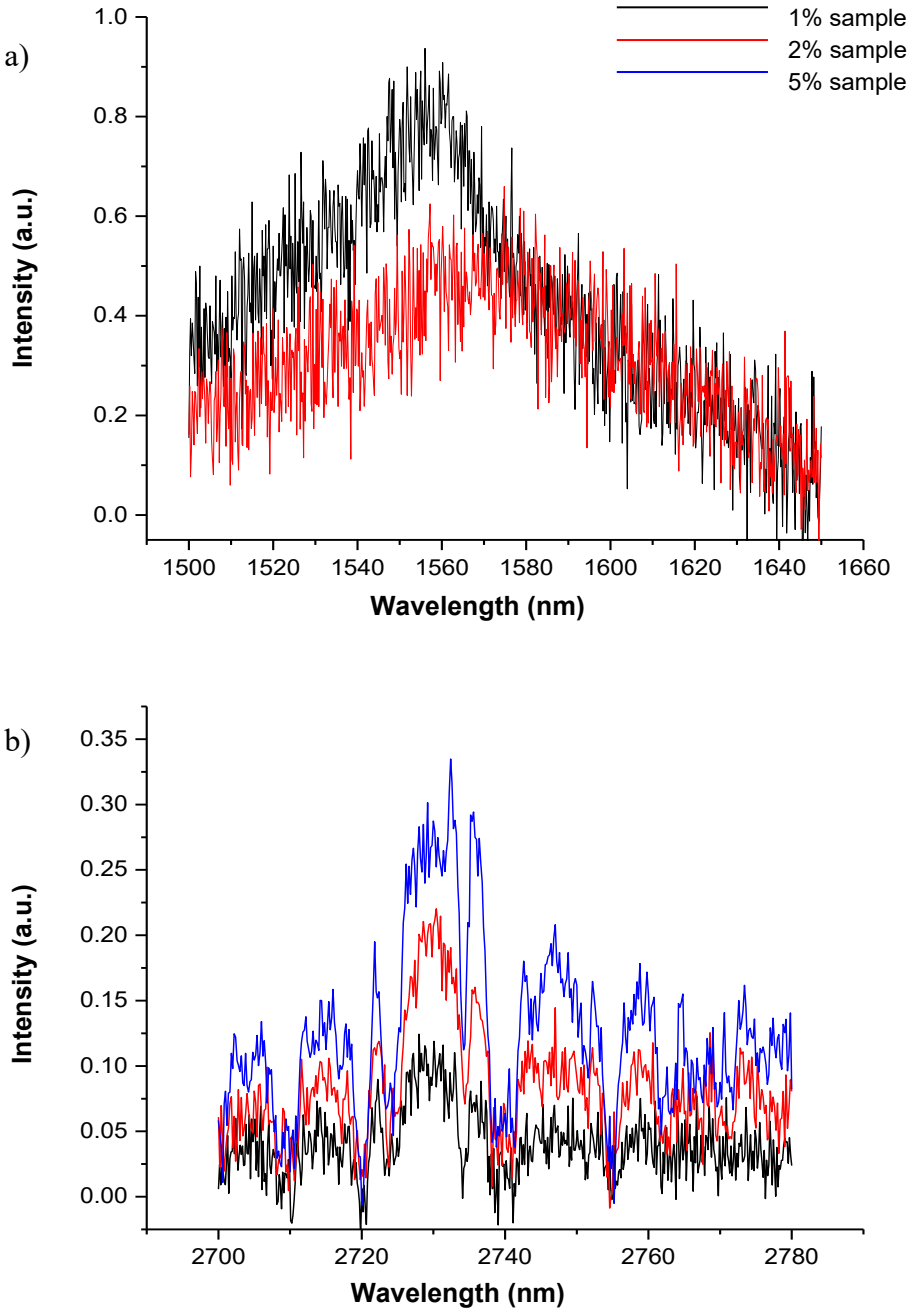

Figure 3.7. Fluorescence spectra of a) 1550 nm and b) 2730 nm peaks detected from ULI waveguides inscribed in 1, 2 and 5% doped Er:GLS samples.

In addition, there is an observed decrease in intensity of the detected 1550 nm signal as the dopant level is increased from 1 to 2%. This suggests that concentration quenching occurs for a higher dopant concentration which causes a reduction in the lifetime of level $^4I_{13/2}$ and so also the radiation emitted. This is corroborated by the fact that a 1550

nm emission peak could not be detected from the 5%Er:GLS sample, although it is likely there is emission at 1550 nm, the intensity of it has decreased so much so that the spectrometer does not have the sensitivity level required to detect it at this low level. The quenching of the lifetime of an energy level can occur through upconversion processes which are much more likely to occur with the higher dopant concentration present or, due to the high doping, there is a greater probability of an electron in an excited state encountering a quenching centre in which the excitation is deactivated via a non-radiative transition [148]. In Er^{3+} it has been demonstrated that upconversion processes due to higher dopant concentrations are responsible for lifetime quenching of the $^4I_{13/2}$ level, these processes recycle ions from this level back into the laser cycle [149, 150]. The lower lifetime level is advantageous in this case as it could potentially lead to the generation of the population inversion required for lasing from the $^4I_{11/2} \rightarrow {}^4I_{13/2}$ transition.

3.5 Er:GLS Laser Investigation

3.5.1 Resonator Arrangement

The 5% sample was subsequently chosen for lasing investigations. It was used in a compact resonator setup of which an image can be seen in Figure 3.8.

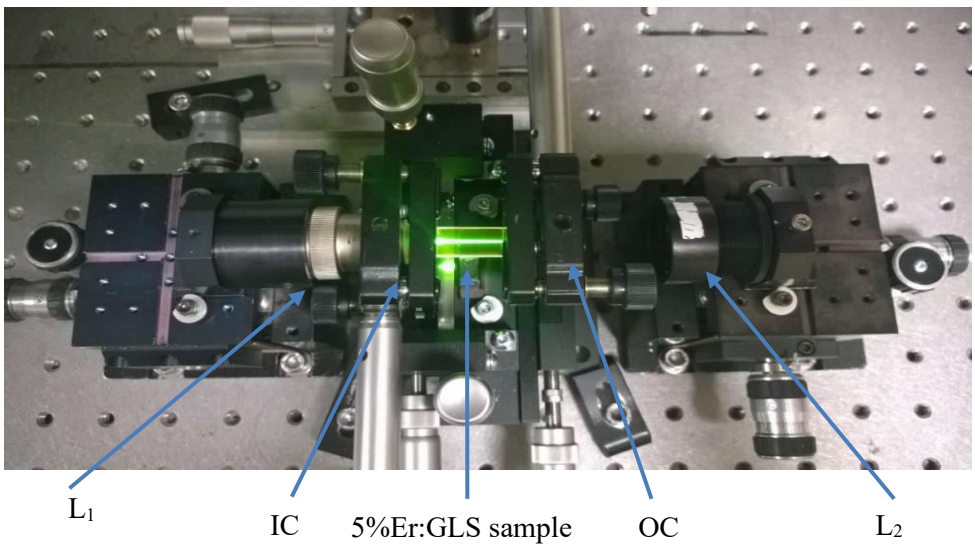

Figure 3.8. Photograph image of the laser resonator built around the 5%Er:GLS sample. L_1 and L_2 are aspheric plano-convex lenses. IC and OC are the input coupler and output coupler respectively.

In Figure 3.8. L_1 and L_2 are the same lenses used for the fluorescence investigations in Figure 3.5, IC is the input coupler which is AR coated on the rear side thus is > 99% transmissive for the pump light at 980 nm and Highly Reflective (HR) coated, > 99%, on the front face for ~ 2750 nm. OC is the output coupler which is 95% reflective from 2600-3100 nm. Despite the increase in 2730 nm fluorescence with the higher dopant value, no lasing action was demonstrated from the 5%Er:GLS sample in the laser cavity. Various possible reasons that lasing could not be demonstrated have been proposed and will now be discussed.

The first reason proposed is that doping process may be initiating much higher losses in the bulk glass, this could be due to a higher number of defects and imperfections which occur during fabrication of the RE doped glass as opposed to undoped GLS. This would, consequently, increase the propagation losses of the waveguides themselves, the effect may be sufficient to inhibit lasing. The second possible reason proposed is that a significant amount of pump light is being wasted to upconversion. In Figure 3.8. a distinct bright line of green fluorescence is observed along the length of the waveguide while 980 nm pump light is coupled into a waveguide. This is due to upconversion transitions, which as previously stated; result in the emission of light with higher photon energies than the pump light which has caused the transition. Upconversion occurs most commonly through the mechanisms of ESA or through energy transfer processes between different ions [103, 151]. The latter usually occurs in particularly high doped samples but can also be caused in even low doped samples due to dopants clustering together [152]. In the case of Er^{3+}, some possible configurations for upconversion processes to occur are shown in Figure 3.1. As shown, multiphoton absorption of pump photons can occur for wavelengths both ~ 800 nm and 980 nm. In the former, case pump photons are absorbed causing the resulting excitation of electrons into energy level $^4I_{9/2}$ which then subsequently decay very quickly and non-radiatively via the emission of phonons into the $^4I_{11/2}$ level. Further absorption of 800 nm pump photon re-excites the electrons into the $^4F_{5/2}/^4F_{3/2}$ levels, these levels also have a short lifetime which very quickly and non-radiatively decays into level $^4S_{3/2}$. Radiative decay subsequently takes place from this level into the ground state with the emission of photons at wavelengths around 550 nm; in the green visible spectral region [91, 92, 103]. For the case of 980 nm pump as in this experiment, the system is similar, however in this case the absorption of two pump photons can directly excite an electron into the $^4F_{7/2}$ level which non-radiatively decays through phonons into the $^4S_{3/2}$ level as with the

800 nm pump case [90, 103]. For either choice of pump wavelength suitable mirrors can be chosen to create a resonator for the green emission wavelength. It is possible to develop these upconversion lasers and, in the case of erbium this can be particularly useful for the generation of green visible radiation. However, in many cases with this one included, upconversion is detrimental to lasing as pump energy is being lost to generating these transitions rather than the sought after lasing transition. The third reason proposed, for the inability to lase, is that though the fluorescence has increased at 2730 nm and so lifetime quenching is occurring on the $^4I_{13/2}$ level, these effects have not been sufficient to generate the population inversion required. The fact that laser operation could not be demonstrated could be a result of any or a combination of the reasons discussed. Consequently the losses of the waveguides were tested.

3.5.2 Waveguide Propagation Loss Measurements in 5%Er:GLS

The well-known cutback method [153] was used to measure the propagation loss. A 1047 nm fibre coupled Nd:YLF laser source was butt coupled into the waveguide to be tested – the waveguide tested was that in the 5% sample for which the emitted fluorescence is shown in 3.7 b). The output was collected with a large core fibre and recorded, the sample was then diced into two smaller pieces and the same process repeated with one of the small samples. In this case a 5.5 mm length of sample was diced from the original 2 cm long sample. Assuming the other losses in the setup are constant the outputs recorded for the two different waveguide lengths can be used to calculate the propagation loss for the length of sample that has been cut off. The loss value is calculated using equation (7).

$$Loss(dB) = 10\log_{10}\left(\frac{P_L}{P_S}\right) \tag{7}$$

In which P_L is the power output from the original sample and P_S is the power output from the short sample after cutback. Ideally, to most accurately measure the propagation loss contributing to the 2750 nm resonator total loss, a laser source close to this wavelength but outwith any peaks in the material absorption spectrum would be utilised. However, a source of this wavelength was not available at this time and as a result an available 1047 nm source was used as it is outside any of the absorption peaks of Er:GLS. The 1047 nm source was set to output 3 mW and the length of sample that was cut away was 5.5 mm. The coupling from the 1047 nm source to the waveguide is

inefficient for this butt coupling experimental setup but this is not problematic provided this loss is kept constant for each sample, this was ensured as much as possible using the index matching fluid.

The power output from the original long 2 cm and short cut-back sample with 5.5 mm removed were measured to be 1.3 and 1.64 mW respectively. Using equation (7) the propagation loss for 5.5 mm of length was calculated to be -1.01 dB resulting in a propagation loss of -1.83 $dBcm^{-1}$. This value is notably higher than that of the minimum losses measured in undoped GLS. Using the same inscription laser at HWU discussed in 3.4.1, Demetriou quoted the loss in waveguides fabricated in undoped GLS to be 0.6 $dBcm^{-1}$ [131], this indicates that the process of doping does increase the overall loss of the glass. Relative to other ULI waveguide lasers, which have been demonstrated, this value is generally higher but not particularly high. Although higher than some values reported [142-145] it is comparable to the total propagation losses reported in other ULI waveguides lasers including for example 3.5 $dBcm^{-1}$ reported in Cr:ZnSe by Macdonald et al. [34] and 2.0 $dBcm^{-1}$ reported by Beecher et al. in Er:Bismuthate glass [101]. It is entirely possible that the maximum pump power available is not sufficient to induce a total gain in the system which is greater than the total losses. The processes leading to the evident upconversion which is occurring are in effect wasting a significant amount of the pump light.

Investigations could be carried out attempting to initiate lasing with a much higher pump power source however it is thought that for this level of doping, lasing from the 2750 nm transition would likely not occur. The reason that this was concluded will be fully discussed in section 3.7.

In an attempt to further understand why laser operation could not be initiated it would be useful to explore the behaviour of the $^4I_{13/2} \rightarrow {}^4I_{15/2}$ transition. In addition, although not in the mid-IR and so outwith the objective of this work, Er:GLS lasing/amplifying on this transition with an emission wavelength of ~ 1550 nm may find applications in optical telecommunications as discussed in 3.1. Furthermore, it may also contribute to overall further understanding of the quality of the produced glasses and so assist the manufacturers in their ongoing investigations into improving the fabrication procedures. For these reasons the following experiment into this emission line from waveguides in Er:GLS was carried out.

3.5.3 Infrared Waveguide Amplifier in 1%Er:GLS

Initially, attempts were made to lase at 1550 nm from the $^4I_{13/2}$ energy level using each of the samples. The set-up employed was the same as represented in Figure 3.8. The same input coupler was utilised but it was quoted to be only 85% reflective at ~ 1550 nm and a range of output couplers were tested with reflectivity at 1550 nm ranging 70 – 95%. Again, lasing operation could not be initiated. It was expected that the 1% sample would have the highest gain at ~ 1550 nm as indicated by the fluorescence measurements and as attempts to lase failed, an amplifier setup was utilised to measure the small signal gain at this wavelength. To ensure maximum efficiency of pumping for 1550 nm emission new waveguides were fabricated with narrower waveguide widths to ensure the propagation of a single mode at this wavelength. ULI was used to inscribe waveguides with widths ranging from 2.1-4.68 μm in a 1 cm long 1%Er:GLS sample. Pulse energies of 56-62 nJ and sample translation speeds ranging 4 mms^{-1} – 12 mms^{-1} were used to find an optimum combination. With the input lenses available, limited pump light could efficiently be coupled into many of the waveguides and this was observed clearly on the camera. For this reason, the signal and pump sources were butt coupled via fibre to the sample. Index matching fluid was used to minimise the coupling loss. The waveguide amplifier experimental setup is shown in Figure 3.9.

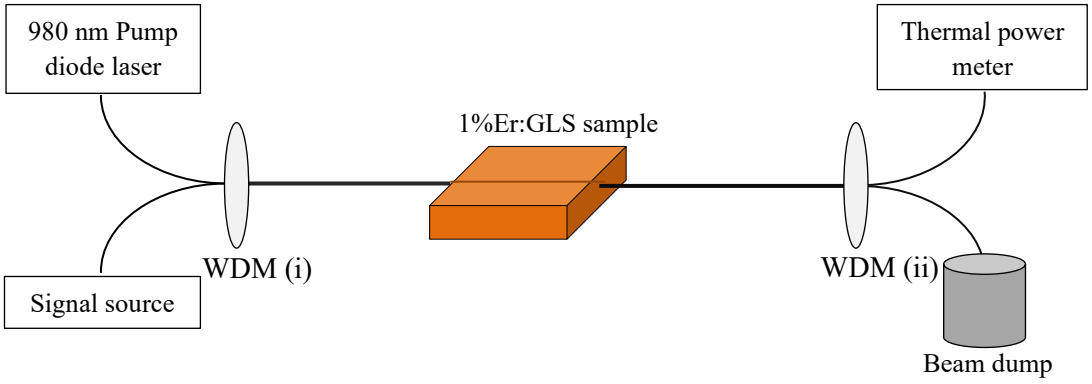

Figure 3.9. Diagram of experimental setup used to measure internal gain of ULI waveguides in 1%Er:GLS. WDM (i) and (ii) are wavelength division multiplexers.

The signal source was a 1550 nm fibre coupled tuneable laser with a maximum power output of 6 mW, the model name/number was Anritsu MG9638A. Before aligning the output fibre in the setup, the 1550 nm tuneable signal source was used to view the

output beam profiles from the waveguides on the camera. Waveguides with widths > 3 μm were found to be multimode. The gain measurements were carried out on the 2.31 μm wide waveguide inscribed with 56 nJ of pulse energy at a translation speed of 4mms^{-1}. This waveguide appeared to exhibit the optimum combination of good single mode beam quality at 1550 nm and efficient coupling of the pump and signal light from the fibre end. The two wavelength division multiplexers (WDMs) labelled (i) and (ii) in Figure 3.9 were used for simultaneous coupling of the pump and signal light into the waveguide and splitting the output signal from any unabsorbed residual pump light respectively. The method used was to couple in the signal from the tuneable source and measure the output on a Spectra-physics thermal power meter with model number 407. First, the power output from the waveguide was measured with no applied pump power, the pump was then increased in regular increments whilst recording the measured power of the output signal on the power meter. The internal gain was then calculated using equation (8).

$$Gain(dB) = 10\log_{10}\left(\frac{P_P}{P_O}\right) \tag{8}$$

In which P_P is the peak waveguide output power observed on the power meter for a given pump power and P_O is the peak power measured from the waveguide with no incident pump light. This process was repeated for signal wavelengths ranging 1516-1580 nm as this was the maximum range of the tuneable source. The maximum pump power applied to the system was 500 mW. This is because the butt coupling system used is not an ideal setup as the sample and fibre end can be damaged very easily. To protect both of these and for safety from stray reflections in the event of damage, the power was limited to this maximum. Ideally the setup would use a lens to couple in both the pump and signal light, optimising the coupling efficiency as much as possible for both. The signal would then be measured before the waveguide with no pump applied and then after with the pump applied, these values would then be used to calculate the gain. However, as this was not possible the butt coupling setup was utilised, resulting in rather poor coupling of both the pump and signal at the input facet of the waveguide. Although this system is not an ideal one and could largely be improved with the availability of the most suitable incoupling lens, we concluded it would still be valid to give an indication of the behaviour of this transition which would be sufficient to aid our understanding of why attempts to demonstrate lasing on the 2.75 μm emission spectral line had not been successful.

Using this setup the maximum gain achieved was 5.4 dBcm^{-1} at a wavelength of 1538 nm. P_O and P_P were measured as 1.02 μW and 3.53 μW respectively. The optical conversion efficiency for this gain was extremely low. A maximum pump power of 500 mW was applied resulting in this gain, and so the optical efficiency is < 1%. However, this very low value is largely explained due to the extremely poor coupling efficiency. To quantify how poor this is, the output from fibre 1 was measured to be 4.5 mW, then this light was coupled directly to fibre 2 by simply bringing the fibre ends together, applying index matching fluid and maximising the signal on the power meter. This was measured to be 2.63 mW. P_O was recorded to be only 1.02 μW. The implication from these measurements was that the coupling losses are particularly high - this largely explains the very small conversion efficiency. It should be noted here that a check was carried out to ensure that the high signal loss was not due to absorption of the signal. The 1%Er:GLS used in the fluorescence measurements in sub-section 3.4.3 was inserted into the setup. The signal was coupled into the 8.7 μm diameter waveguide and an output signal of 2.43 mW was recorded – this proves that the sample is not highly absorbing the ~ 1550 nm signal. This confirmed that the high losses observed in the 1%Er:GLS sample with the 1550 nm single mode waveguides are primarily due to very inefficient coupling into the much smaller waveguides.

It was also discovered that ~ 37% of the incident pump power was measured at the output of fibre 2 indicated by the beam dump in Figure 3.9. This also, in part, accounts for the low conversion efficiency as over a third of the pump light is simply not being absorbed by this length of sample. Furthermore, as previously discussed, a portion of the pump light which is absorbed is wasted in that it is being used in upconversion processes resulting in the emission of visible green light.

Despite the problems identified with the experimental setup that has been used to measure the internal gain, it does give a clear indication that there is gain and therefore a population inversion occurring on the $^4I_{13/2} \rightarrow {}^4I_{15/2}$ transition. The value of gain measured, 5.4 dBcm^{-1}, is greater than that measured in the same doped glass by Franz et al [112]. The authors realised a net gain of 2.8 dBcm^{-1} in waveguides fabricated through sputtering. As a result of the relatively high gain observed on this transition, it is evident that a population inversion is not occurring on the 2.75 μm transition therefore inhibiting lasing operation. We note here that in spite of the population inversion induced, as stated previously, lasing operation was not observed for this transition

either. However, the pump mirror available was custom coated for operation at 2750 nm and although quoted at approximately 85% reflective at ~ 1550 nm, this is not optimum for lasing at this wavelength. Investigations with a suitable pump mirror would be required before drawing conclusions about the reasons lasing was not observed in this case – at this time such a mirror was not available.

Although the fluorescence measurements presented in 3.5.3 indicate that the higher doped sample, 5%, has an increased population in level $^4I_{11/2}$ it is unlikely that it is sufficient to generate a population inversion between $^4I_{11/2} \rightarrow {}^4I_{13/2,}$ this was concluded from an extensive review of the literature concerned with lasing from this spectral emission line in Erbium which is covered in the next section.

3.6 Lasing from the 2.9 μm Transition in Erbium

Continuous wave lasing from the 2.9 μm line in Erbium doped materials for example Er^{3+}:YAG, has been found to be only possible with very high pump powers as well as high dopant concentrations, ~ 50% [45, 88]. This is due to large lifetime quenching of the $^4I_{13/2}$ level. Large quenching occurs because of the high dopant which recycles population through upconversion, this is only guaranteed to happen continuously and maintain the population inversion with significantly higher dopant levels than was used in these experiments. Another solution which may lead to laser operation is to use pulsed pumping. This method ensures that the laser medium is pumped quickly enough to build the population inversion before the electrons decay and emit photons, and as a result the laser output is also pulsed [154]. Another potential modification that could be made in attempts to lase is to co-dope the glass with Yb. This is a commonly used method to increase the efficiency of absorption of the pump light [102, 145, 155-159] and may be useful for lasing from the 2750 nm or the 1550 nm transition in Er:GLS. The absorption of pump light is increased because Yb has much stronger absorption peak around 980 nm than Er^{3+}. The Yb ions therefore can absorb much more of the pump light and they release this energy to the Er^{3+} ions by energy transfer [156]. Another co-dopant which has been used successfully with Er^{3+} to quench the $^4I_{13/2}$ level is Pr [160], this could also be explored for use in Er:GLS

An extensive study of the literature concerning lasing from this transition in the Er ion particularly in YAG, revealed that a great deal of investment of funding, time and resources has been made to make this possible. Therefore we reached the conclusion that using the current samples, lasing from this transition in this relatively new glass material would likely not be possible. Consequently discussions were held with our collaborators at the ORC to discuss the manufacture of glasses with much higher concentrations of Erbium. Currently, when concentrations of even as low as 15% are attempted, the optical quality of the glass is substantially reduced and work is ongoing at the ORC to manufacture highly doped glasses while retaining the quality levels. The manufacture of co-doped Er:Yb:GLS is also being explored.

3.7 Summary

ULI has been used to fabricate Type I waveguides in samples of Er:GLS with differing dopant concentrations; 1, 2 and 5%. The results from previous works carried out concerning ULI in GLS were utilised to fabricate single transverse mode waveguides for the propagation of ~ 2.75 μm light. The cross sections of the waveguides were controlled by exploiting the multiscan technique described in section 2.5. The inscribed waveguides were then pumped with a 1 W 980 nm fibre coupled diode laser, a variety of plano-convex aspheric lenses AR coated for the pump wavelength were investigated to optimise the coupling of the pump light into the waveguides. The output modes from the pumped waveguides were viewed on a camera after transmission through a 2 μm long pass filter to identify the optimum single mode waveguides in each sample. The fluorescence of the output modes was measured with a spectrometer. It was found that there was an emission peak from each sample at ~ 2.73 μm, the intensity of the fluorescence was found to increase with increasing dopant concentration. A peak at ~ 1.55 μm was detected from the 1 and 2% samples with decreasing intensity respectively. The detected peaks at 2.73 μm are slightly blue shifted from the expected emission from this material which is 2.75 μm. This shift is explained due to water absorption in the atmosphere in this spectral region, there is hole in the absorption band at ~ 2.73 μm hence what is detected is the side band of the emission. The intensity increase of this peak is due to the higher Er^{3+} concentration in the sample, leading to greater pump absorption and subsequently more emission at this wavelength. The observed decrease in the 1.55 μm emission peak from the 1 to 2% samples indicates

concentration quenching is occurring, decreasing the upper lifetime of this transition. Emission at this wavelength is not detectable from the highest doped sample, 5%, providing further evidence of this concentration quenching.

Attempts were made to lase through the waveguide in the 5% sample but this was not achieved. As a result the cutback technique was used to measure the propagation loss of these waveguides. It was found to be ~ 1.83 $dBcm^{-1}$, which is not particularly high compared to other ULI waveguides which have successfully demonstrated lasing. The required population inversion to lase from the ~ 2.75 μm line in Er:GLS may be difficult to achieve due to the short lifetime of the upper lasing level with respect to the lower lasing level. Consequently, attempts were also made to lase at 1.55 μm using the 1% sample, this also proved not possible with the current setup. However, it was possible to successfully demonstrate a waveguide amplifier exhibiting a maximum gain of 5.4 $dBcm^{-1}$ at 1538 nm. The fact that gain was observed suggests the mirrors utilised for the lasing attempts may not be suitable.

Multiple reasons for the inability to lase at 2.75 μm were explored. These include; a significant portion of pump light being wasted to upconversion and, although concentration quenching is occurring for the 5% sample, it is not sufficient to generate a population inversion. An extensive literature review of lasing from this emission line in Erbium has been carried out, from this it has been concluded that with the current samples and available pump source, lasing will not be possible. Solutions to successfully initiate lasing have been proposed, these include; pulsed pumping, higher Erbium concentrations whilst sustaining the high quality of the glass and the possibility of co-doping to induce much higher pump absorption.

These investigations and subsequent discussion have shown Er:GLS to be a promising candidate in the future as a material for laser emission in the mid-IR, as a result this work is ongoing to achieve the glass modifications required to achieve this.

Chapter 4. Theory of Pulsed Laser Operation

4.1 Introduction

This chapter details the background theory of pulsed lasers and also the techniques required to characterise the pulses. There are various methods which can be employed to generate pulsed laser sources, the choice is generally dependent on the required output pulse characteristics including for example; the PRF, the output power capabilities and the maximum pulse energy availability. Another important parameter to consider is the pulse duration required for a specific application; the pulse generation technique utilised directly effects the values it can take. The term "Q-switching" refers to techniques which result in high energy laser pulses emitted on a micro to nanosecond time scale through manipulation of the cavity quality factor, Q. Q is defined as the ratio of the energy stored in the resonator divided by the losses per oscillation. The process of Q-switching is demonstrated in Figure 4.1. Initially the active gain medium acquires energy through optical pumping while the Q factor is kept low to prevent the laser reaching threshold. Consequently, a large population inversion builds up due to energy storage in the gain medium. The Q factor is then abruptly switched to allow laser action and the high amount of energy accumulated is released in the form of an energetic pulse. The process is repeated periodically resulting in the emission of a stable train of Q-switched pulses [161].

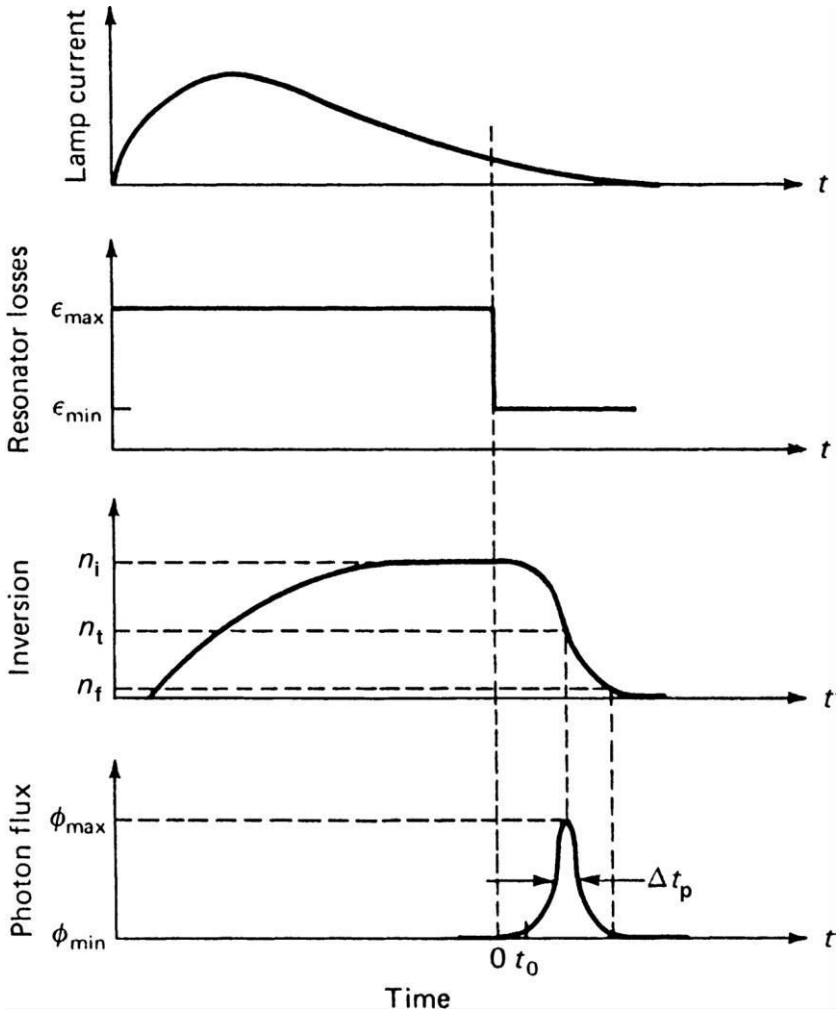

Figure 4.1. Evolution of a pulse generated in a Q-switched laser. The plots from top to bottom are; the flashlamp pump output, the resonator losses, population inversion and emitted photon flux. All are plotted as a function of time. Diagram has been reproduced from [161].

In the specific case of doped solid-state lasers, to ensure high energy pulses are produced, the gain medium implemented is required to have a long upper state lifetime and sufficient dopant ion concentration. This is so that it can efficiently store energy from the incident pump. However, if the pump-to-signal gain efficiency of the medium is too high, it can be challenging to induce the low Q factor needed initially to prevent lasing. In addition, a gain which is too high results in high levels of amplified spontaneous emission and so inhibits the energy storage capability. The Q-switching ability of a laser is therefore dependent on the specific gain medium properties [162]. Q-switched lasers find use in many applications particularly when high pulse energy is preferred; such as tattoo removal [163], range finding [164] and micro-machining applications [165]. However, many applications require much shorter pulse durations on the scale of picoseond to femtosecond, these are often referred to as ultrafast pulses.

The term “modelocking” encompasses a number of techniques that result in the emission of ultrafast pulses with durations ranging from ps to fs. In the general case of a single transverse mode free running CW laser, there are multiple discrete frequency components called longitudinal modes oscillating in the cavity with a random phase relationship. The longitudinal modes which are permitted to oscillate depend in part on the cavity length and the difference in frequency between two adjacent longitudinal modes is given in equation (9).

$$\Delta v = \frac{c}{2nL} \tag{9}$$

In equation (9) c is the speed of light, n is the refractive index of the medium the modes oscillate in and L is the cavity length. It can be seen from equation (9) that a cavity can have potentially thousands of longitudinal modes depending on the cavity length, but whether a particular mode is allowed to lase or not also depends also on the gain bandwidth and gain saturation of the active medium [166]. This is summarised in Figure 4.2.

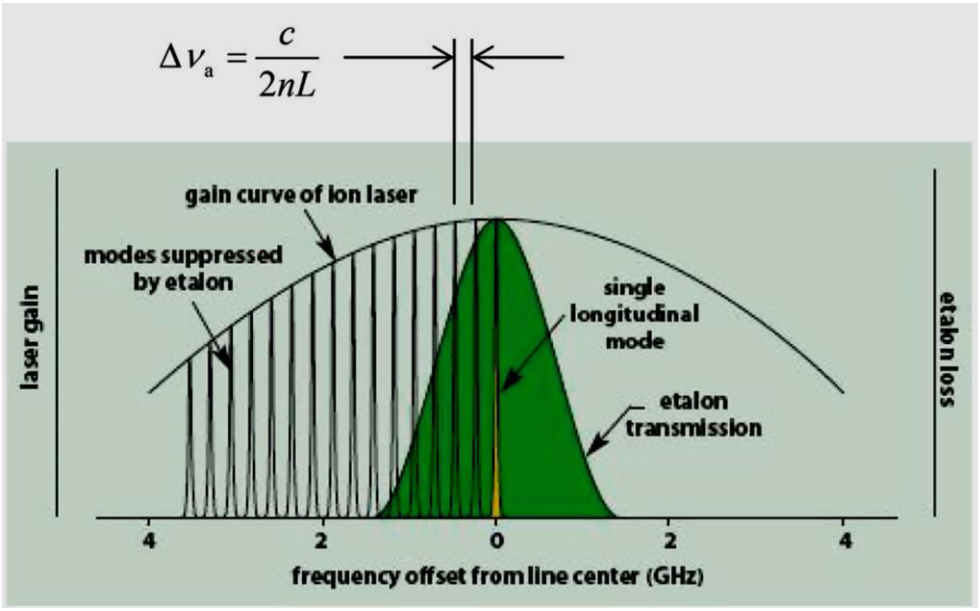

Figure 4.2. Diagram showing the longitudinal modes allowed to oscillate in a CW laser. As can be seen, the gain bandwidth can be greater than the spacing of the modes and so those closer to the edges of the gain bandwidth are supressed by resonator losses. Diagram has been reproduced from [166].

The permitted modes resonate independently constantly interfering with each other. Any fluctuations in the emitted laser signal as a result of this random interference are

averaged over time and so the signal appears as a continuous stable output. The term modelocking originates from the fact that these techniques force the longitudinal modes in the cavity to oscillate in phase, hence the modes are said to be "locked in phase" together. By forcing this fixed phase relationship, at a certain point in time, the modes will all constructively interfere generating an intense pulse [167]. This constructive interference occurs periodically, at all other times the interference is destructive resulting in a stable train of pulses which is demonstrated in Figure 4.3.

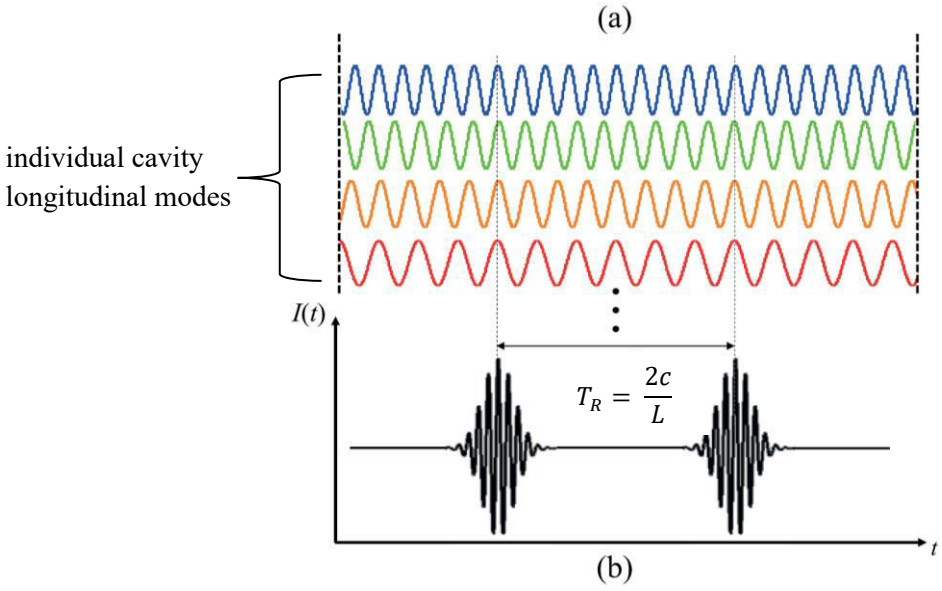

Figure 4.3. Diagram demonstrating interference of the longitudinal modes in a modelocked laser. The top part (a), shows the oscillation of separate modes in a cavity. These modes constructively interfere periodically resulting in a train of intense laser pulses as seen in the bottom graph (b). Diagram has been reproduced from [168].

When a laser is successfully modelocked the resulting steady state emission in the temporal and frequency domains are shown in Figure 4.4 a) and b) respectively.

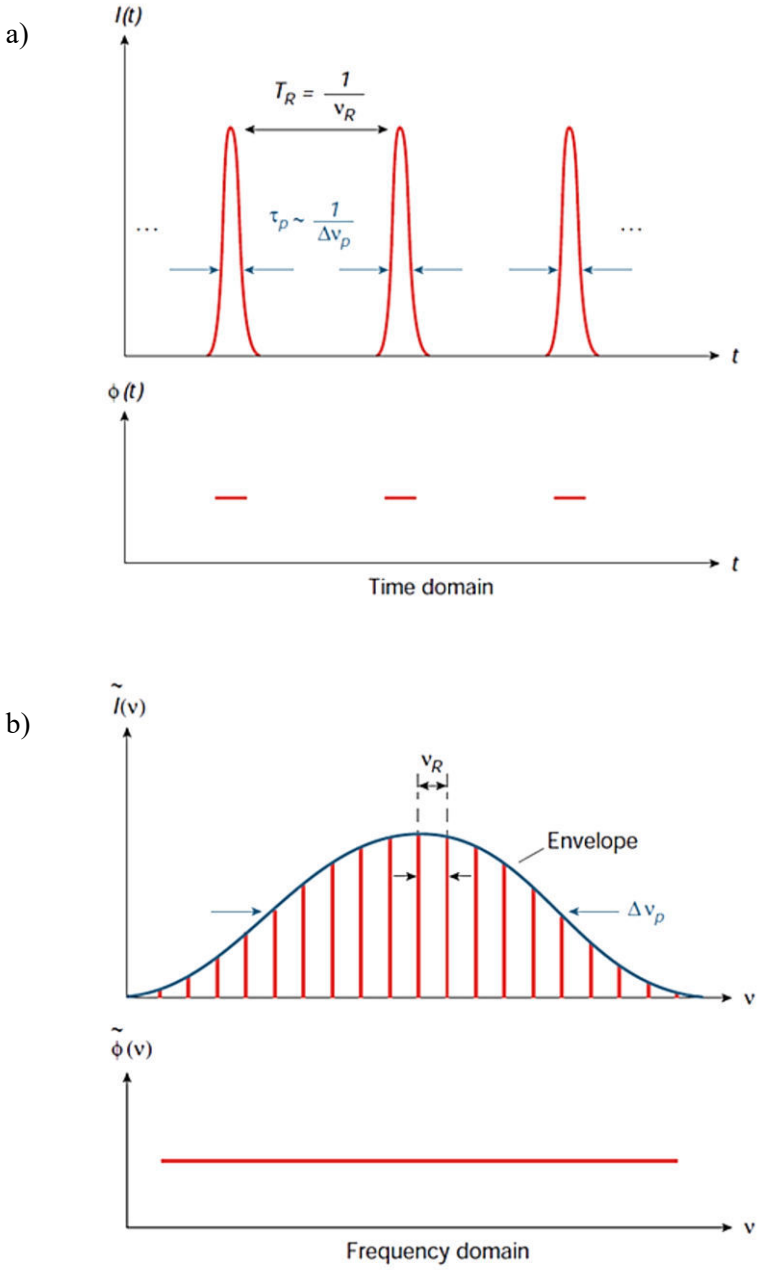

Figure 4.4. Schematic of modelocked laser emission in the a) time and b) frequency domains where I is the intensity and φ is the phases. Diagram has been reproduced from [169].

In Figure 4.4 a) we can see a steady output train of pulses which are equally spaced in time by the cavity round trip time $T_R = \frac{2nL}{c}$, this is also demonstrated in Figure 4.3 for the case of $n = 1$. The PRF is hence the reciprocal of this roundtrip time [167]. In the frequency space presented in Figure 4.4 b) the emission appears as a frequency comb of equally spaced modes which are phase locked. The purpose of this chapter is to provide an overview of both modelocked operation and modelocking techniques. A comprehensive mathematical description of the development and evolution of modelocked pulses can be found in [170].

The techniques by which a laser can be modelocked are split into two categories: active and passive. Both are based on the same premise of introducing a variable loss mechanism into the cavity as shown in Figure 4.5.

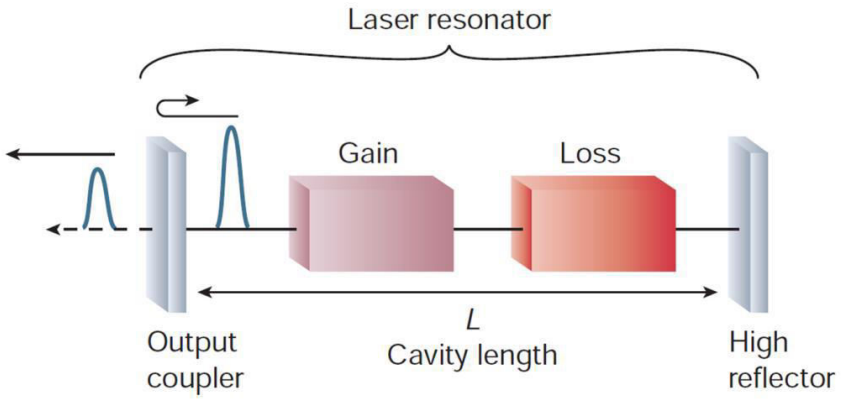

Figure 4.5. Simplified laser resonator design showing the components required for modelocked emission. Diagram has been reproduced from [169].

4.2 Active Modelocking

In the case of active modelocking, an external driving signal is applied to either modulate the intracavity losses directly - amplitude modulation (AM), or modulate the intracavity phase – frequency modulation (FM). The external signal is usually provided by an Acousto-optic (AOM) or electro-optic (EOM) modulator. The applied signal modulates the loss of the cavity in a sinusoidal fashion. The cavity is designed such that the saturated gain exceeds the loss at the minima of the applied signal. This is shown in Figure 4.6.

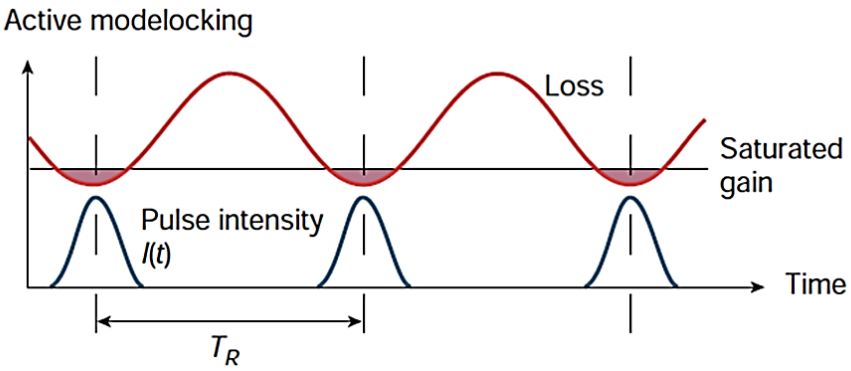

Figure 4.6. A graph demonstrating how the loss is modulated in an active modelocked laser. The signal has modulation frequency equal to the round trip time of the cavity T_R. Diagram has been reproduced from [169].

This Figure also shows how the signal is chosen to have a modulation frequency equal to the cavity mode spacing of the resonator causing energy from each mode to be coupled coherently to the adjacent modes, this results in the required fixed phase relationship for modelocking. Active modelocked cavities tend have minimum lengths limited to around ~ 1 m, therefore restricting the maximum attainable PRFs to ~ 150 MHz. This is because of the typical sizes of the modulators incorporated in the cavity. The minimum pulse durations obtainable in active modelocking are also limited, the electronic nature of the driving signal means that they tend to be confined within the ps range [169, 171].

4.3 Passive Modelocking

Passive modelocking techniques do not apply an external modulation; instead the laser contains a component called a saturable absorber (SA) which introduces a nonlinear loss mechanism into the cavity. For the case of high intensity incident radiation, the absorption of the SA material becomes saturated, hence it exhibits low loss and the light is permitted to propagate. For low intensities the loss introduced is significantly higher because in theory the SA can absorb all the incident radiation, thus it cannot propagate. In practice however, SAs do have a nonsaturable loss value which for commercially available SESAMs from, for example, BATOP GmbH; can anywhere range between <1% – ~ 25%. The result of this is a self-modulating amplitude in which the peak of a high intensity pulse is permitted and experiences gain but the lower intensity pulse wings are supressed. The process is ideally self-starting due to random noise fluctuations in the cavity which can be sufficient to saturate the absorption of the SA. In

some cases it is not self-starting but a noise spike can be initiated by simply tapping one of the cavity end mirrors. The induced noise spike grows in intensity with each round trip, whilst simultaneously the circulation of any lower intensity pulses occurring due to interference is inhibited as they experience high loss, upon reaching steady state the laser emits a high intensity pulse train [167, 169, 171]. Passive modelocking techniques can modulate the intracavity losses much faster than any applied external signal because the nonlinear response is much faster than any signal electronics can produce; consequently they are able to generate shorter pulses than active methods [169, 171] This is demonstrated in Figure 4.7, it is evident that the SA loss recovers much faster compared to the sinusoidal signal in the case of active modelocking shown in Figure 4.6.

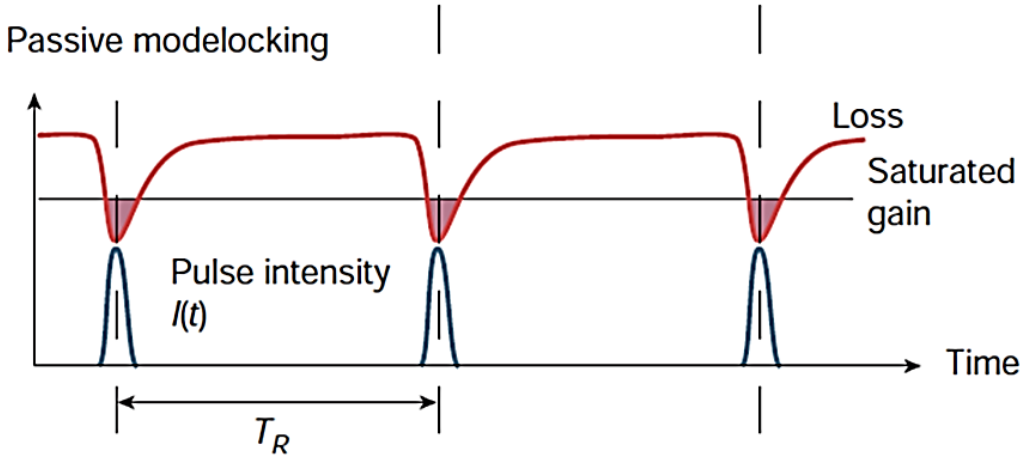

Figure 4.7. Graph which demonstrates the loss modulation in a passively modelocked laser. Periodically the absorption/loss of the SA is saturated by a high intensity pulse, which is therefore allowed to circulate experiencing high gain. Diagram has been reproduced from [169].

4.3.1 Characterisation of Saturable Absorbers

SA's for passive modelocking are characterised by a number of parameters. Three of the most important are the modulation depth, the saturation fluence and the recovery time. The modulation depth is the maximum change in the SA nonlinear loss and saturation fluence defined as the incident pulse fluence which reduces the loss by 1/e of the total modulation depth. The recovery time is a measure of how long it takes for the loss/absorption to recover after saturation by a high intensity incident pulse [172]. "Fast absorbers" have a recovery time much smaller than the pulse duration itself, whereas "slow absorbers" have one which is much greater [171].

For a fast SA, when the absorption becomes saturated, this introduces a window where the gain exceeds the loss and a pulse can be sustained, this is demonstrated in Figure 4.8 a). As the recovery time is less than the pulse duration, the SA attenuates both the leading and the trailing wings of the pulse. For a slow SA, saturation of both; the SA absorption and the gain of the active medium are required. In this case the intense pulse signal in the cavity saturates the lasers population difference which acts to temporarily reduce the small signal gain. During the time taken for the SA loss to recover there exists a small time window in which the gain is greater than the loss and a pulse is supported, this is shown in Figure 4.8 b) [171, 173]. A slow SA can only continuously supress the leading edge of the pulse, so fast SAs should theoretically generate the shortest pulse durations. However, slow SAs have been shown to support pulses with durations much shorter than the recovery time [174, 175]. Such short pulses are possible if soliton modelocking is implemented through careful balancing of the self-phase modulation (SPM) and group delay dispersion effects in the cavity [173, 176]. In this scenario the resultant pulse duration is dominated by the balancing of these effects rather than the net gain window, this regime is shown in Figure 4.8c).

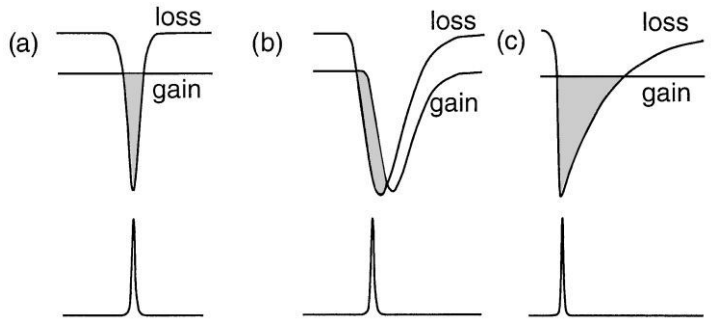

Figure 4.8. The gain and loss dynamics which support pulse propagation in lasers modelocked by a) a fast SA, b) a slow SA and c) slow SA with soliton formation. Diagram has been reproduced from [173].

Even though the theory of modelocked pulse generation is very well understood, the practical implementation can be somewhat challenging. When a laser generates ultrafast pulse of equal intensity as shown in Figure 4.4 a), it is said to be purely CW modelocked. However, a common issue encountered in modelocking is that the laser produces pulses with varying intensities, thus it is not CW modelocked. This is generally an undesirable effect and detrimental to the laser performance. It is important to understand how these intensity instabilities originate so they can be mitigated if

necessary. The next section will describe this as well as discussing the particular cases where the instabilities can be useful to generate high energy ultrafast pulses.

4.3.2 Q-switching Instabilities

The first lasers showing evidence of modelocking were reported in the mid-1960s [177-179]. However, in these demonstrations the output pulses did not exhibit constant pulse energy. Instead the modelocked pulses were emitted with intensities modulated by an overlying Q-switched envelope. This mode of operation is therefore named Q-switched modelocking (QML) and it is demonstrated in comparison to CW modelocking in Figure 4.9.

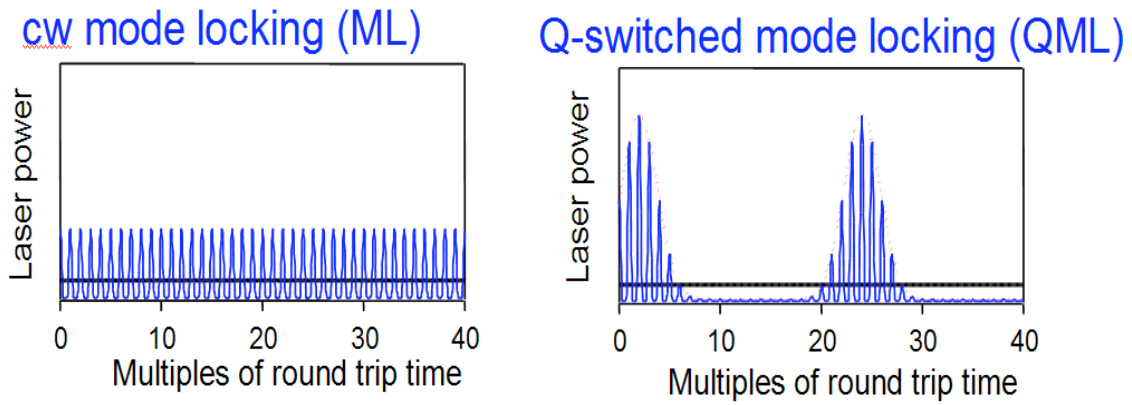

Figure 4.9. Graph showing the laser power vs time for a laser operating in the Q-switched modelocked regime on the right compared to the CW modelocked regime on the left. The blue and black lines represent the instantaneous and average laser power respectively. Diagram has been reproduced from [180].

For the majority of applications constant pulse energy is essential so efforts are made to supress any Q-switching instabilities. However, in the QML regime there is potential for a vast amount energy to be stored within in the Q-switch envelope, as a result the output has much higher peak pulse energy capabilities than that of purely CW modelocked lasers. Thus the advantage of QML lies in its use as a source for subsequent amplification. The delay between groups of pulses emitted during QML allows for appreciable energy storage in an amplifier, leading to very high power pulse generation. Conversely, pure CW modelocking often requires “pulse pickers” to isolate single pulses or groups of pulses in order to realise appreciable gain in later amplifier stages [181].

The first modelocked lasers exhibited QML behaviour as the available SAs at this time did not possess the optimum parameters required to escape this regime so as to emit pure CW modelocked pulses. With the subsequent rapid development of semiconductor technology the accessible SA parameters improved resulting in the first purely CW modelocked stable pulses from a solid-state laser [174]. The technology has continued to advance resulting in countless demonstrations of CW modelocked lasers with semiconductor based SAs [169, 175].

Whether or not a specific laser will experience QML instabilities depends on a number of both laser and SA properties. This can be expressed in the form of a stability criterion which gives an estimation of the intracavity pulse energy required to escape the QML instabilities, this criterion is given in equation (10). The criterion and following explanation have been reproduced from [180].

$$E_{P,c} = \left(E_{sat,L} E_{sat,A} \Delta R\right)^{1/2} \tag{10}$$

In equation (10) the critical pulse energy $E_{P,c}$ is defined as the minimum intracavity pulse energy required to establish stable CW modelocking, therefore for pulse energies below this value, the laser will exhibit this QML instabilities. $E_{sat,L}$ is the saturation energy of the laser gain material and is given by equation (11).

$$E_{sat,L} = \frac{F_{sat,L}}{a_L} \tag{11}$$

where a_L is the effective laser mode area inside the gain medium and $F_{sat,L}$ is the saturation fluence of the laser gain material. It is calculated using equation (12):

$$F_{sat,L} = \frac{E_{ph}}{N(\sigma_e + \sigma_a)} \tag{12}$$

where E_{ph} is the photon energy, σ_e and σ_a are the emission and absorption cross sections respectively at the signal wavelength. N is the number of time a photon passes through the gain medium in one round trip of the cavity.

$E_{sat,A}$ in equation (10) is the saturation energy of the SA in question, it is calculated using equation (13).

$$E_{sat,A} = \frac{F_{sat,A}}{a_A} \tag{13}$$

where $F_{sat,A}$ is the saturation fluence of the SA, this is fixed design parameter which is usually quoted on fabrication and a_A is the effective laser mode area incident on the SA. This parameter can be controlled by means of focusing optics in the cavity. Finally, ΔR in equation (10) is the maximum modulation depth of the SA. The intracavity pulse energy, E_P, of the laser is calculated using equation (14).

$$E_P = \frac{P_{Avg}}{f_{rep} T_{OC}} \tag{14}$$

in which P_{Avg} is the laser average output power, f_{rep} is the PRF and T_{OC} is the transmission of the OC. E_p can be directly compared with the critical pulse energy $E_{P,c}$ to identify if the laser has sufficient intracavity energy to avoid Q-switching instabilities.

The stability limit estimation presented here originates from the theory of ps lasers presented by Kaertner et al. [182], however a series of assumptions are made in order to arrive at the simplified version shown in equation (10). These include the following; it is assumed that the full modulation depth is exploited when the laser is operating in the purely CW modelocked regime, this means that the SA is bleached and for this to occur it is estimated that the pulse fluence incident on the SA must be 5 × the SA saturation fluence. It is also assumed that the reflectivity of the SA for high incident pulse fluence is 100%, in other words the nonsaturable losses are zero/negligible. A further assumption made is that the stability limit is independent of the gain materials upper state lifetime, which is generally valid because most modelocked lasers operate well above the laser threshold. The full derivation of this estimated stability criterion can be found in [180]. It is important to note that these assumptions mean that a laser which satisfies this simplified condition in equation (10) will always satisfy the stricter stability criterion without these approximations. It is therefore very useful to apply equation (10) to a laser emitting in the QML regime as it gives a clear indication of the modifications needed to change to CW modelocked operation if this is preferred. It

should also be noted that for simplicity this criterion ignores gain filtering and nonlinear effects which can have consequences for the pulse bandwidth. These are important to consider for soliton-like pulses with femtosecond durations and the extensions required to account for these can be found in [180].

The suppression of QML instabilities can be very challenging for modelocked lasers with GHz PRFs because of their relatively low pulse energies compared to those achievable with longer cavities. The properties of an SA are therefore very limited for the emission of CW modelocked, high PRF pulses.

4.3.3 Types of Saturable Absorbers

An SA can take the form of a physical component which introduces the nonlinear loss mechanism, or it can already exist within the cavity but is only activated when sufficient intensity is reached.

Semiconductor saturable absorber mirrors (SESAMs) are one of the most commonly used physical SAs. SESAM devices are based on semiconductor material technology. The physical structure of a typical SESAM device is shown in Figure 4.10.

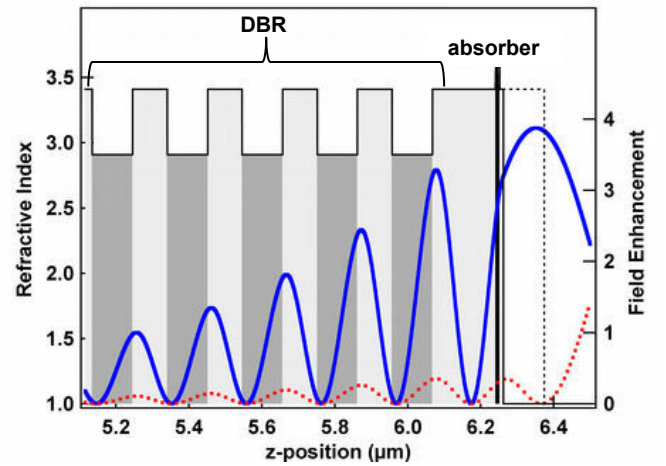

Figure 4.10. Typical physical structure of a Semiconductor saturable absorber mirror. The quantum well absorber layer is grown on top of a distributed Bragg reflector. Diagram has been reproduced from [183].

The absorber layer is constructed of a quantum well layer. In this layer the saturable absorption takes place due to transitions between the heavily populated valence band and the conduction band. A higher modulation depth can be achieved by increasing the

number of quantum wells in this layer [184], a high modulation depth generally generates shorter pulses but it can also increase the chance of QML instabilities [185], as can be seen by equation (10). However, SESAMs also tend to have low saturation fluence values which reduces the chances of these instabilities, as can be seen in equations (10) and (11). The layers behind the absorber construct a Distributed Bragg reflector (DBR) which can be seen in Figure 4.10. This is effectively a highly reflective mirror, the layer materials are chosen to have bandgaps higher than that of the quantum well to ensure no absorption occurs in them. The very thin layers involved in SESAM fabrication are grown directly on the substrate, often a GaAs wafer, to provide a robust supportive platform for the SA [172, 175]. Due to the advancement of semiconductor technology, the fabrication techniques of SESAMs have advanced to produce high quality devices with few defects that allow flexibility in the SESAM design properties and self-starting modelocking. SESAMs have had great success in the near IR spectral range [186] supporting the generation of sub-100 fs pulses [187, 188]. However, their use at longer wavelengths into the mid-IR has been limited, as broader operational bandwidths than most current SESAM materials can offer are required to produce such short pulse durations. Despite showing some success [189-191], research is ongoing to optimise SESAM technology for this spectral range.

Graphene based SA mirrors (GSAMs) have recently emerged as useful alternatives to SESAMs due to their intrinsic broadband operation. Graphene, which is a 2D sheet of sp^2-hybridised carbon atoms bound in a hexagonal honeycomb lattice, has been the subject of a vast amount of research for countless applications due to its remarkable optical, electronic and mechanical properties. It can also be arranged in the form of zero-dimensional fullerenes, 1-D Carbon Nanotubes or stacked in the form of 3-D Graphite. 1-D nanotubes have been utilised extensively as SAs with great success [192, 193]. Although postulated for many decades previous, the 2D layer form of graphene was only demonstrated for the first time in 2004 by Geim and Novoselov [194]. So important would this discovery prove, it won them the Nobel prize in 2006.

Two different research groups first demonstrated that graphene could be used as an SA almost simultaneously in 2009: Hasan, et al. [192] and Bao et al. [195]. These groups both reported modelocked fibre lasers with emission centred at ~ 1.56 μm and pulse widths of ~ 800 fs. Over the last decade since then GSAMs have attracted a great deal of attention in the development of ultrafast pulsed laser sources. This is because they

can have very broad operational bandwidths compared with other types of SAs. This is motivated by the unique band structure of graphene which in effect demonstrates a band gap of zero [195]. This zero band gap structure and the saturable absorption processes involved for a single layer of graphene are demonstrated in Figure 4.11.

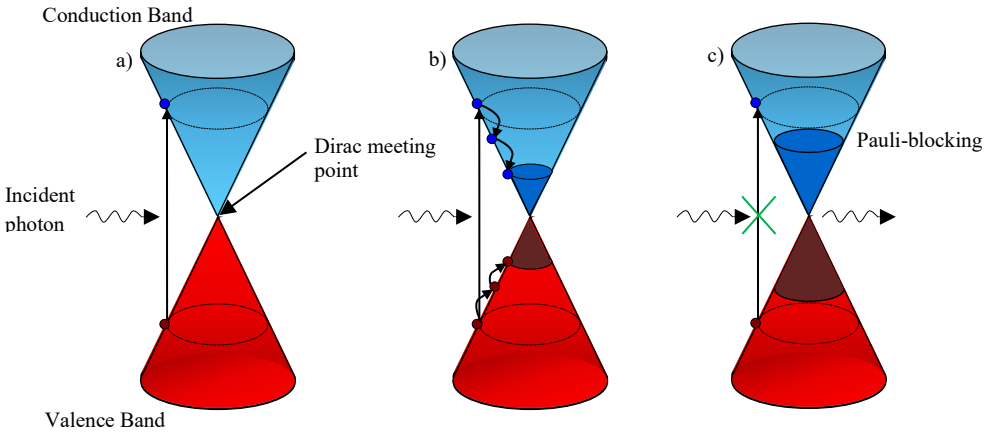

Figure 4.11. Saturable absorption process in graphene. In a) an electron is excited from the conduction band to the valence band by an incident photon. The absorbed electron loses energy by intraband decay into lower energy levels, a similar process occurs for holes in the valence band, this is depicted in b). It allows room for other electrons to be excited to where the first electron initially existed in the conduction band and the process repeats. The lower energy states become filled in both bands in the form of a Fermi-Dirac distribution. In c) high intensity incident light has caused the energy levels to become filled, hence no more electrons are allowed to be absorbed and the absorption has become saturated.

In graphene, at particular points, the conduction band meets the valence band in terms of energy. This meeting of these energy bands actually occurs at the 6 points of the hexagonal lattice in reciprocal space and these points are called Dirac points. Thus at these meeting points the bandgap is effectively zero. An example of such a point and the absorption processes involved for a single layer of Graphene are demonstrated in Figure 4.11. One consequence of the zero bandgap is that the material has broadband absorption as a photon of any wavelength can be absorbed from the valence (red) to the conduction (blue) band. How the absorption becomes saturated is shown sequentially in a) to c). High intensity incident photons excite electrons into the conduction band as shown in a), very quickly after excitation - on the scale of 100 fs, the thermally excited electrons lose energy by cooling. The electrons initially collide with other carriers then with the lattice, and as a result decaying to lower energy levels. Intraband decay also occurs similarly for holes in the valence band. The result is the forming of a Fermi-

Dirac distribution, shown in b). In the normal case of low intensity incident light, after some time electron – hole recombination would occur restoring the equilibrium and allowing continuous absorption. However, in the case of high intensity incident light, energy states of both the bands become filled therefore not permitting any more electrons being allowed to exist in the absorbed state, this can be seen in c). This effect is called Pauli-blocking, it allows the peak of the high intensity light to be transmitted [195]. In the visible to IR spectral range, a single layer of graphene has been measured to absorb ~ 2.3% of incident light, this absorption is proportional to the number of layers in the limit of few layers, < 10 [192]. This value is higher in comparison to for example a 10 nm GaAs quantum well, common in the SESAM structure, which is around 1%, giving graphene its characteristically low saturation fluence [192, 195, 196]. Graphene is also generally characterised by two recovery times, one faster of the order of 100 fs which is associated with intraband carrier scattering processes and a slower one of the order of a few ps dependant on the number of layers. This is associated with the interband carrier relaxation through the release of phonons [197].

In summary, graphene exhibits many ideal characteristics for use as an SA in the development of ultrafast laser sources. These include, ultrafast recovery times, low saturation fluence and conceivably, most significant compared to other SAs such as SESAMs; intrinsic broadband operation. A single layer/multiple layers of graphene can be coated with some ease onto a standard reflective OC resulting in a graphene coated saturable output coupler (GSOC). Therefore, graphene has emerged as a useful alternative to SESAMs which have complex fabrication procedures and are often bandwidth limited [193]. Furthermore, the use of a partly tranmissive GSCO as an SA in a waveguide laser, allows for extremely compact cavity design which is a fundamental requirement for high PRFs. Consequently, graphene has been utilised as an SA in the modelocking investigation of a ULI Holmium doped YAG waveguide laser presented in chapter 5 of this thesis.

So far only physical SA components have been discussed, however, arguably the most effective technique for generating the shortest fs pulses is Kerr-lens modelocking (KLM) which exploits a virtual SA present in a laser cavity. Its discovery came in the early 1990s after some confusion over results presented by Spence et al. [198], in which a Titanium doped Al_2O_3 (most commonly referred to as Ti:sapphire) laser was seen to produce ultrafast pulses apparently without the addition of an SA. It was soon explained

that the modelocking was actually the result of a strong self-focusing effect which occurs due to the nonlinearity of the Ti:sapphire gain medium [199, 200]. This effect is now known as KLM and it has led to the generation of extremely short sub-10 fs pulses [53, 54, 201, 202].

KLM is given this name because the Optical Kerr effect is exploited. This is a third order nonlinear process which occurs because the refractive index, n, exhibited by a material is dependent on the intensity, I, of incident radiation. This refractive index can be expressed as a Taylor expansion, the first term is thus proportional to I as shown in equation (15) [203].

$$n = n_0 + n_2 I \tag{15}$$

where n_0 is the materials linear refractive index for weak intensity incident radiation and n_2 is the second order refractive index, this has a value dependent on the material, for example Sapphire has $n_2 = 3 \times 10^{-20}\ m^2W^{-1}$ [204]. Hence, the change in refractive index induced by incident radiation of high intensity, I, is given in equation (16):

$$\Delta n = n_2 I \tag{16}$$

Assuming an incident radiation beam with a Gaussian intensity profile, the change in refractive index induced will therefore be greater in the centre and decrease in magnitude towards the outer wings of the beam. As a result, the centre of the beam propagates with a reduced phase velocity compared to the wings creating an intensity dependent lensing effect. A significantly strong noise spike in a laser cavity can induce this self-focusing effect in the laser gain medium, this can be exploited for modelocking by designing the cavity in such a way that the noise spike sees less loss than the oscillating CW mode. The spike can therefore experience gain and grow with each round trip, ultimately reaching a steady state of modelocked pulse emission [205, 206]. The cavity can be designed to favour the pulsed operation by addition of a hard or soft aperture. In the former case, a physical aperture is placed in the cavity which is tailored to inhibit the larger mode area CW light from resonating, whilst simultaneously allowing the pulses to propagate. This situation is demonstrated in Figure 4.12 a). The more commonly used method of soft aperture KLM modelocking is shown in Figure 4.12 b). In this method the size of the pump beam is carefully controlled to ensure that

only the pulsed mode can experience high gain, as a result the larger mode area CW light dies out [207].

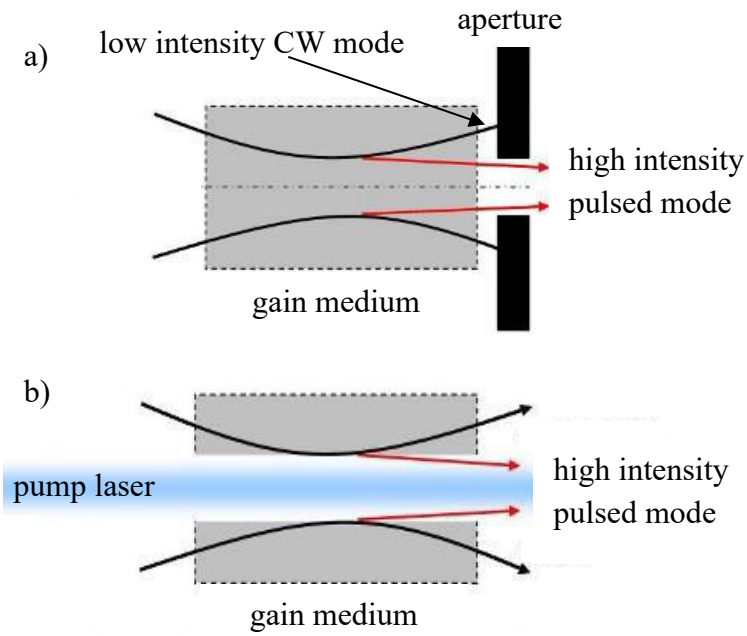

Figure 4.12. Schematic of laser cavity designs to initiate a) hard aperture and b) soft aperture Kerr-lens modelocking. Diagram has been reproduced from [207].

The major advantages of a Kerr-lens virtual SA are its very short recovery time and inherent broad operational bandwidth, which is wider than any physical SA due to its non-resonant nature. A further advantage of KLM is that SPM is generated in the gain medium, this occurs as a result of a temporal phase shift induced by the optical Kerr effect and can lead to spectral broadening of the pulses. These benefits of KLM alongside effective dispersion compensation described in section 4.4 has allowed for the demonstration of extremely short pulses [205]. This has been exploited particularly well in Ti:sapphire lasers which have achieved 2 optical cycle pulses with pulse durations ~ 5-6 fs and up to 300 mW of output power [201, 202].

However, there are some drawbacks; identification of the ideal cavity alignment for stable modelocking is not straigthforward. The position of the intracavity mirrors at which KLM can be experimentally achieved lie in close proximity to the edge of the lasers CW stability regions as the aim is to supress the CW operation. A detailed review of the identification of these regions can be found in [203]. Very compact and stable translation stages are required to successfully align to these specific positions. In addition, the process is not self-starting, but a sharp tap applied to one of the cavity

mirrors can be enough to induce a sufficiently intense noise spike which will initiate the Kerr effect [169]. Self-starting has also been achieved by using a SESAM in conjunction with KLM [201], or an AOM with KLM as in some commercial Ti:sapphire lasers currently manufactured by Spectra-Physics®.

In spite of the drawbacks discussed, KLM has proven to be the most effective modelocking technique for generating the shortest pulses, this has been particularly successful in Ti:sapphire lasers generating pulses in the near-IR spectral range. With regards to the mid-IR KLM has also had great success in generating ultrafast pulses from TM:II-VI materials [208-214]. As with Ti:sapphire, this is owed to the nonlinearity of host materials such as ZnSe and ZnS. This will discussed in greater detail in chapter 6 where results of a new type of KLM Cr:ZnSe laser is presented.

4.4 Material Dispersion and Compensation Methods

4.4.1 Effect of Dispersion on Modelocked Lasers

All dielectric media are inherently chromatically dispersive, this means they have a wavelength dependent refractive index $n(\lambda)$, therefore the phase velocity of light propagating in such a material is dependent on its wavelength. In terms of a propagating optical pulse, it travels with group velocity which is a function of the wavelength dependent group refractive index. This group velocity dispersion (GVD) effect leads to deformity of the temporal shape of the pulse caused by cavity components such as lenses, mirrors, filters and the active gain media itself [215]. The GVD of an optical element is related to the second derivative of $n(\lambda)$, this is typically expressed as the Sellmeier dispersion formula, the most general form of this is given in equation (17):

$$n^2(\lambda) = 1 + \sum_i \frac{B_i \lambda^2}{\lambda^2 - C_i} \tag{17}$$

where B_i and C_i are the experimentally determined Sellmeier coefficients of different optical materials [216]. The GVD can then be evaluated at the wavelength of interest in units of time per unit length by using the second derivative of $n(\lambda)$ in equation (18):

$$GVD = \frac{\lambda^3}{2\pi c^2}\frac{d^2 n}{d\lambda^2} \tag{18}$$

Therefore the total group delay dispersion (GDD) experienced by a pulse is then the product of the GVD and the propagation length in that material [217]. Media which have positive GVD exhibit normal dispersion. A pulse propagating in a normally dispersive medium becomes "positively" or "up-chirped" in which the instantaneous frequency of the pulse increases with time as the higher frequency components of the pulse are forced to travel slower than the lower frequencies. The majority of laser gain media are normally dispersive in the visible spectral region, with increasing wavelength into the IR/mid-IR spectral ranges many materials cross their zero-dispersion wavelength point and exhibit anomalous dispersion. In the case of anomalous dispersion, the opposite situation occurs. The GVD is negative imposing a negative or down-chirp on the pulse, in which the instantaneous frequency decreases with time and this is the way in which the pulse is temporally broadened [218]. In a modelocked laser, a net GDD value of zero is optimum to sustain the emission of ultrafast pulses therefore efforts must be made to compensate the total GDD of the various cavity elements[203]. Note that this ignores the effects of SPM which also needs to be accounted for in practice in addition to the material/component contributions to the dispersion, for obtaining the minimum pulse duration in the femtosecond regime.

It should be noted that the higher orders terms of the dispersion in equation (17) have been neglected for simplicity, however for very short ~ sub 30 fs pulses in which the range of frequencies emitted under the pulse envelope is large, these higher order dispersion terms become increasingly significant and must also be managed effectively [219].

There are a number of methods that can be employed in a laser cavity to control the net intracavtiy dispersion which will be discussed now.

4.4.2 Dispersion Compensation Methods

Neglecting the effects of SPM for simplicity in this discussion, if the total dispersion induced by all optical elements in a laser cavity is well defined, one can simply add a material into the cavity which has a dispersion equal in value but opposite in sign to the

total dispersion, resulting in a net dispersion or extremely close to zero. In the case of modelocked fibre lasers a dispersive fibre can be spliced onto the gain material fibre of appropriate length depending on its GVD value at the central wavelength of the laser [220]. Similarly, for a bulk laser, a piece of material with the correct GVD value and length can fully compensate the cavity dispersion, the loss induced is minimised by aligning the material at Brewster's angle. In this case it is more challenging to achieve the length of material required as bulk material is more difficult to dice accurately than fibre. Alternatively material windows can be stacked together to achieve the desired thickness, but in either case, it is difficult to obtain the exact desired total material length and therefore minimum pulse duration [211]. One solution to this problem has been the use of a pair of wedged windows; aligning at Brewster's angle minimises the loss. Fine control of the wedge positions and hence the thickness of material the pulse propagates through, allows for very accurate control of the dispersion the pulse experiences [203].

The use of a prism pair is another method of employing very fine control over a modelocked laser intracavity dispersion [53, 211, 221, 222] . Rather than making use of only material dispersion as above, this method introduces geometric dispersion in the cavity beam path as demonstrated in Figure 4.13. The basis of this method is to manipulate the beam paths of various wavelengths within the pulse to ensure all wavelengths have equal round trip times.

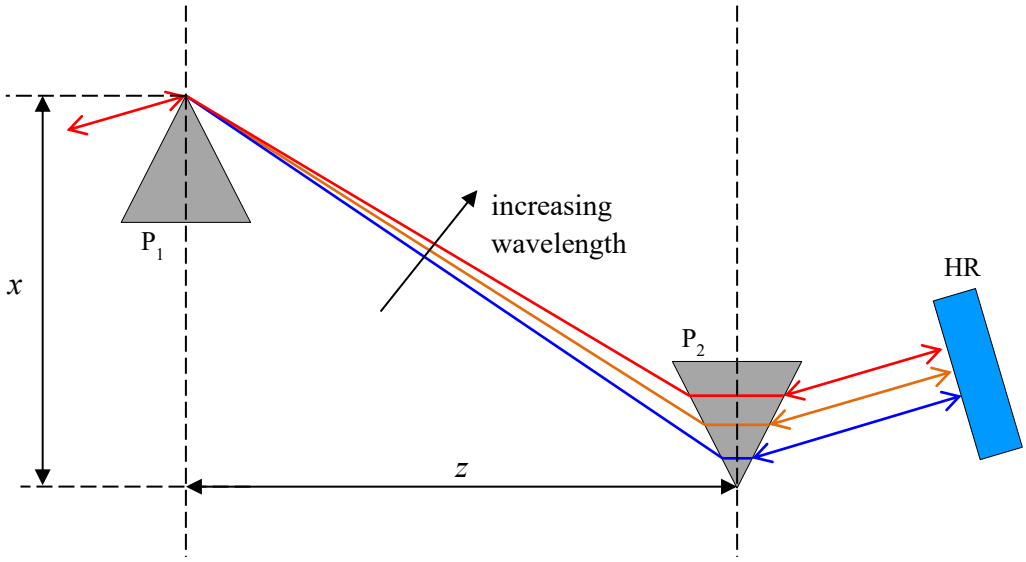

Figure 4.13. Prism pair arrangement for dispersion compensation in a modelocked laser. Diagram has been reproduced from [203].

In Figure 4.13 prism P_1 spatially splits the incident pulse wavelengths. Then, P_2 refracts the separated wavelength components such that they then propagate in parallel on exiting the prism. In this way the GDD can be tuned to either positive or negative values through appropriate positioning of the prism pair to manipulate the path length and thus the phase of the separated wavelengths. As the prism pair is usually integrated into the laser cavity, it is designed to induce half the total dispersion required, in a single pass. The light is reflected back through the prism pair by the highly reflective mirror, HR, and thus acquires half the total dispersion value again whilst also being spatially recombined. This method is particularly useful for control of extremely short pulse lengths as the separation of the prisms, z, and the penetration distance into the second prism, x, can be separately controlled allowing for independent tuning of the GDD and third order dispersion (TOD) [223]. Brewster angle prisms of the selected material are often used to minimise the losses in the system [203, 224].

Another well-established method for dispersion compensation in ultrafast modelocked lasers is the use of chirped mirrors. Chirped mirrors consist of a mirror substrate coated with a series of dielectric layers, followed by an AR coating layer to minimise the losses, this design is shown in Figure 4.14. The various wavelength components of the pulse penetrate to different layer depths within the dielectric stack as demonstrated in the figure. Longer wavelength components are reflected by the layers deeper within the stack and hence accumulate a larger group delay giving rise to anomalous dispersion [203]. Chirped mirrors are designed for a certain wavelength region and quoted to have a specific GDD value in fs^2 per bounce.

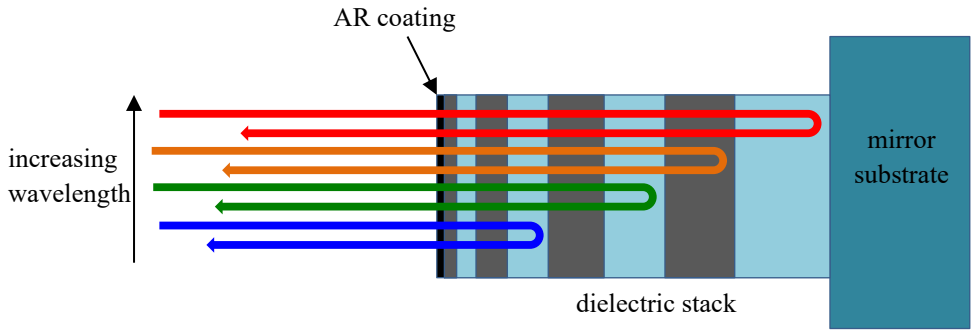

Figure 4.14. Structure of chirped mirrors for dispersion compensation.

The disadvantage of using chirped mirrors lies in that they have a GDD which is absolute and finite, this only allows for obtainable compensating values which are an

integer number multiplied by their quoted GDD value, i.e. the product of this and the number of bounces in the cavity from the chirped mirrors. As a result of this, they are often used in combination with other methods such as wedged windows or prism pairs to allow much finer tuning of the net GDD. However, the disadvantage of this, which is also common to all dispersion compensation methods is that they all complicate the cavity to a certain extent. This often requires the cavity to be lengthened to fit in the mechanical mounts needed for the components. This is particularly unfavourable when the goal is to generate ultrafast pulses with high PRFs, therefore often a compromise must be made between the shortest pulse duration and highest PRF attainable [203]. However, chirped mirrors have had a great deal of success in producing very short pulse lengths in the mid-IR as reported in [208, 212, 225]. Therefore they have been utilised in the KLM modelocking investigation of Cr:ZnSe in chapter 6 of this thesis, and have allowed us to successfully demonstrate sub-40 fs pulses.

4.5. Measurement of Ultrafast Pulses

This chapter has thus far concentrated on the theory as well as methods of generating Q-switched and modelocked laser pulses. Measuring the duration of Q-switched pulses can be done with a high speed photodetector, but the measurement of much shorter modelocked pulses, < a few ps, is not so straightforward. As a result various techniques have been developed to accurately measure such ultrafast pulses; this section will discuss some of the most commonly used techniques.

Ultrafast pulses are emitted on a timescale much shorter than that achievable by even the most modern electronics. As a result, this poses a real challenge when it comes to quantifying these pulse durations because photodetectors with adequately fast rise times and dynamic ranges do not exist. This is particular notable in the mid-IR where there is a lack of photodetectors in general compared to, for example, the IR and visible spectral regions. To illustrate this point further, the fastest photodetectors commercially available to date for wavelengths in the mid-infrared $> \sim 2.1\ \mu$m have a rise time of the order of a few ns, for example the VIGO detector which is utilised in chapter 6 of this work has a rise time of ~ 2 ns. Extended InGaAs based detectors can detect wavelengths up to ~ 2.1 μm have demonstrated significantly faster rise times of ~ 30 ps. An example of such a detector is the Newport photodiode used in chapter 5 of this work, it quotes a

rise time of 28 ps. However, this is still not fast enough for the direct measurement of fs pulses. Even in the near–IR and visible spectral regions where there is a much greater range of fast photodetectors available, the rise times are limited to a minimum of a number of ps. This justifies the need for alternative techniques that can resolve the temporal properties of ultrafast pulses.

4.5.1 Autocorrelation

Arguably the most common technique to measure ultrafast pulses is that of autocorrelation, it was one of the first methods developed to measure ultrafast pulse durations [226]. The basis of an autocorrelation measurement is to use the pulse to measure itself; this is achieved by splitting the pulse in a interferometer, then overlapping the two pulses temporally and spatially in a nonlinear medium. Such an arrangement is shown in Figure 4.15.

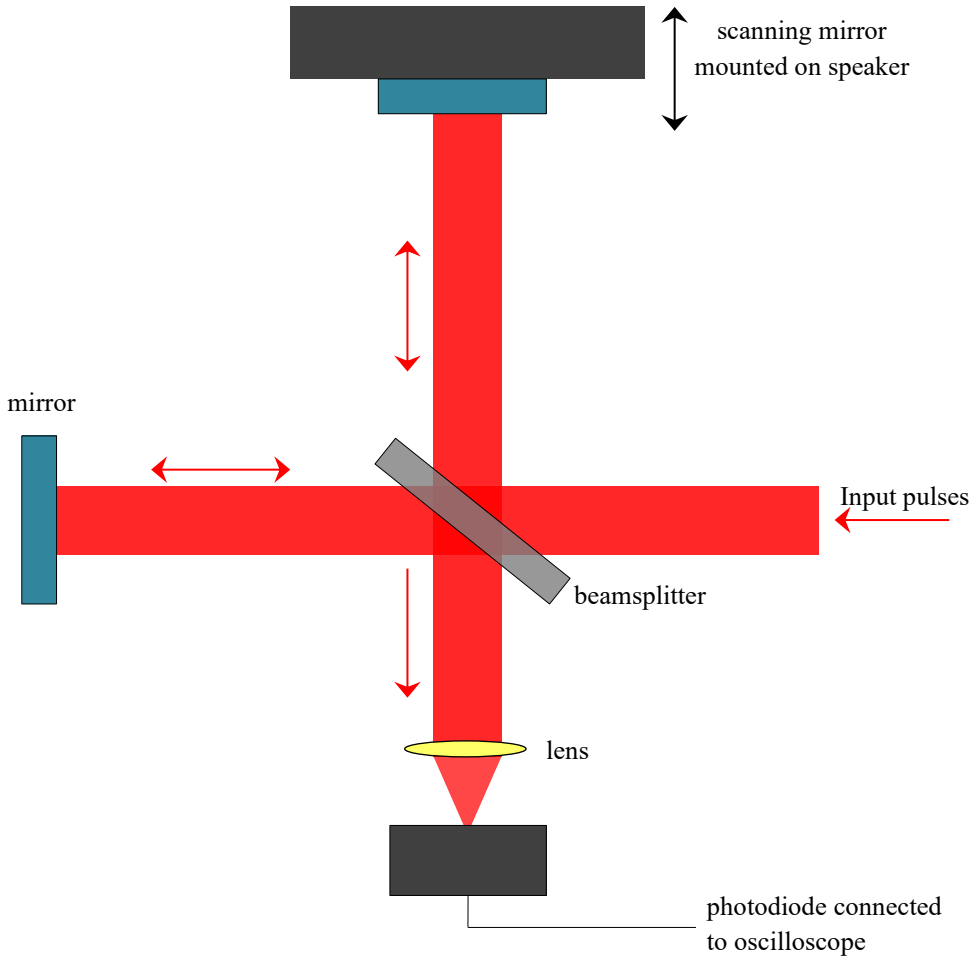

Figure 4.15. Schematic diagram of an interferometric autocorrelator.

This setup contains a Michelson interferometer which initially splits the incoming pulse into two replicas. The separate pulses propagate along the two arms of the interferometer onto the mirrors where they are reflected back toward the beamsplitter. The scanning mirror continually vibrates with a set frequency, introducing a temporal delay, τ, between the replicas as a function of the arm length difference. This means the electric field amplitudes of the two separate pulses can be expressed as $E(t)$ and $E(t-\tau)$. Subsequently, the pulses recombine spatially and are focused by the lens onto the photodiode. The overlapped pulses induce 2-photon absorption in the semiconductor material of the photodiode producing a measured frequency doubled intensity signal, of the form shown in equation (19) [227].

$$g_2(\tau) = \frac{\int_{-\infty}^{\infty} |\{E(t) + E(t-\tau)\}^2|^2 dt}{2\int_{-\infty}^{\infty} |\{E(t)\}^2|^2 \ dt} \tag{19}$$

This signal is a fringe pattern called the interferometric autocorrelation trace which has fringe spacing of $\frac{\lambda}{c}$, where λ is the central laser wavelength and c is the speed of light. An example of such a signal is demonstrated by the blue curve labelled 'experimental data' in Figure 4.16; this autocorrelation trace was measured from the modeolocked laser reported in [101]. For scanning mirror positions which give a delay of 0 and thus perfect constructive interference at the photodiode, the signal has amplitude double that of a single pulse and so an intensity which is 4 × greater. Then due to the frequency doubling the resultant signal has 16 × the intensity of a single pulse. When there is no overlap between the pulses on photodiode, there is no 2-photon absorption and the signal has intensity twice that of a single pulse. To put it another way, for limits of $\tau=0$ and $\tau \rightarrow \pm\infty$ $g_2(\tau)$ reduces to 16 and 2 respectively. Therefore, the indication of a correctly aligned interferometric autocorrelator is a characteristic ratio of 8:1 from the peak to the wings of the trace; this can be clearly seen by the scale in Figure 4.16.

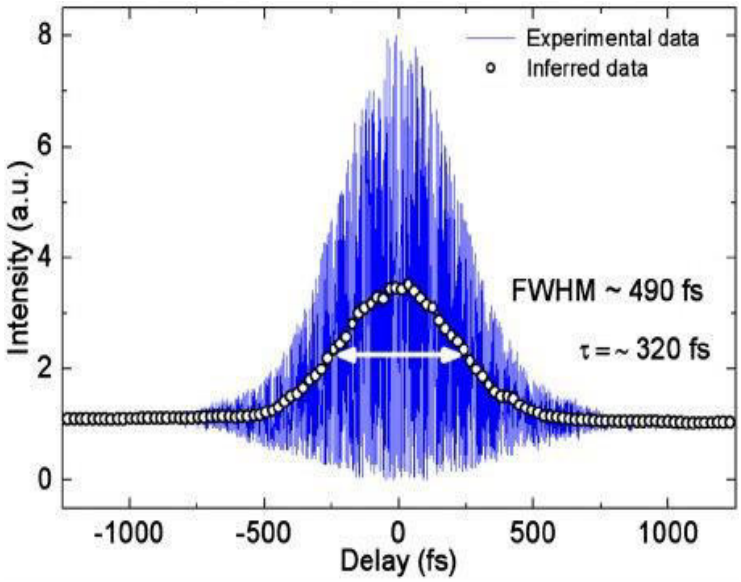

Figure 4.16. Example of experimental interferometric and inferred intensity autocorrelation traces demonstrating the peak to wing ratios in each case. These results were observed from the 320 fs modelocked Er:bismuthate waveguide laser demonstrated by Beecher at al. in [101] and the diagram has been reproduced from this report.

If the photodetector has insufficient bandwidth to resolve the interference fringes the resultant signal function in this case is shown in equation (20) [227].

$$G_2(\tau) = 1 + \frac{2\int_{-\infty}^{\infty} I(t)I(t-\tau)dt}{\int_{-\infty}^{\infty} I(t)^2 dt} \tag{20}$$

$G_2(\tau)$ is a time-averaged function called the intensity autocorrelation in which $I(t)$ and $I(t-\tau)$ are the intensity functions of the separated pulses. An example of this measurement is shown by the curve labelled 'inferred data' in Figure 4.16. For the limits of $\tau = 0$ and $\tau \rightarrow \pm\infty$, equation (20) simplifies to 3 and 1 respectively so the characteristic ratio for a correctly aligned system is 3:1. As the function $G_2(\tau)$ depends on the intensities of the pulses and the intensity itself is a function of only the magnitude of the electric field amplitude, all phase information is lost. Therefore, the disadvantage of the intensity autocorrelation is that no information about the phase is conveyed in the detected signal. Whereas, in the interferometric autocorrelation trace some observed distortion in the fringes indicates that a pulse has an additional chirp, an example of a chirped pulse autocorrelation trace is shown in Figure 4.17. A distortion of the trace envelope can be observed in the wings of the pulse compared to the ideal trace shape demonstrated by the blue curve in Figure 4.16 indicating the pulse is chirped.

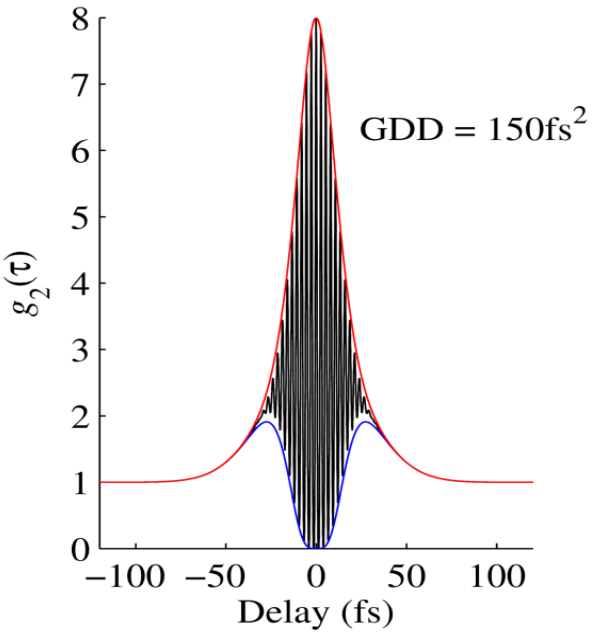

Figure 4.17. Interferometric autocorrelation of a chirped 10 fs Gaussian pulse with a central wavelength of 800 nm. An additional GDD value of 150 fs^2 has resulted in distortion of the pulse envelope in the wings. This diagram has been reproduced from [228].

The trace cannot identify whether the pulse is "up-chirped" or "down-chirped", it only indicates the magnitude of the chirp, but this can be useful when fine tuning the dispersion. The pulse duration, $\tau_{p,}$ can be directly obtained from an autocorrelation trace by measuring the full width half maximum (FWHM), τ_{FWHM}. They are related by a deconvolution factor k as shown in equation (21) [224, 227].

$$\tau_{FWHM} = k\tau_p \tag{21}$$

The appropriate choice of k depends not only on the type of the autocorrelation trace but also the pulse shape in question. The profile of an ultrafast pulse is commonly approximated as having a temporal shape which described by either a sech^2 or a Gaussian function. For the interferometric autocorrelation technique the relevant k values are 1.697 and 1.897 for Gaussian and sech^2 pulse profiles respectively. In the case of the intensity autocorrelation the k values are 1.414 and 1.543 [224, 227, 229]. The pulse shape can be verified using the time bandwidth product. For bandwidth-limited pulses with a Gaussian or sech^2 profile, this product is 0.44 and 0.315 respectively.

It should be noted that in original autocorrelator setups the recombined pulses were focused into a nonlinear crystal to induce second harmonic generation (SHG), the photodiode then detects this SHG signal from the crystal. The simpler 2-photon arrangement shown in Figure 4.15 can offer broader detection compared to using a nonlinear crystal as the frequency doubling does not rely on phasematching nor does it have any polarisation dependence [230]. This setup has therefore been chosen as the pulse measurement method for the modelocked laser that will be presented in chapter 6.

4.5.2 Alternative Pulse Measurement Techniques

Although an interferometric autocorrelation can provide some information about the phase of the measured pulses, in that one can determine the magnitude of a chirp on the pulse, it does not allow for the measurement of the phase across the pulse. Furthermore, the distortions which can be enforced upon the autocorrelation trace lead to errors in the calculation of the pulse duration from the observed FWHM. Latterly, as the ability to produce extremely short pulses has grown, there has also been a desire to reliably completely characterise the pulses in terms of both; the duration and the absolute phase. A variety of powerful techniques have emerged which accomplish this, most notably Frequency Resolved Optical Gating (FROG). FROG allows measurement in both the time and frequency domain simultaneously. It is essentially a method of measuring the signal spectrum versus the intruded time delay. This eliminates the requirement to make assumptions about the pulse. Like autocorrelation, FROG uses the pulse to measure itself, the equipment required is similar in that the beam is split by an interferometer arrangement. However, in this case, a spectrometer is used to view the output from the nonlinear crystal in place of a photodiode. The resultant trace is called a spectrogram which can be analysed with the use of a phase-retrieval algorithm which allows precise calculation of both the phase and pulse duration [227, 231]. A FROG measurement is not altered by any dispersion introduced after propagation through the nonlinear crystal because the spectral domain is unaffected by this. There exist a number of other techniques which have been explored and used successfully in the characterisation of ultrafast pulses, including, for example, Spectral Interferometry for Direct Electric-field Reconstruction (SPIDER) [227] and Multiphoton Intrapulse Interference Phase Scan (MIIPS) [232]. However, FROG has essentially become the standard for ultrafast pulse characterisation and is coming to replace autocorrelation. It is extremely versatile

allowing the precise measurement of pulses with durations ranging from sub-fs to ns scale.

In spite of this, autocorrelation measurements are still widely utilised and presented in journal papers particularly for the characterisation of mid-IR pulses. This is because the linear arrays which are required for use in FROG in this spectral region are still fairly limited in availability and expensive, and may require cryogenic cooling further complicating the experimental setup. The alternative pulse characterisation methods mentioned here will be explored no further as they are beyond the scope of this work, but it is necessary to include them in this theory section to provide a complete overview of the field of ultrafast pulse characterisation.

4.6 Summary

This chapter has introduced the operation of pulsed lasers as opposed to CW by describing the different techniques of Q-switching and modelocking to achieve pulse generation, highlighting that the latter can result in ultrafast pulse generation. The differences between active and passive modelocking techniques have been discussed. It was shown that passive techniques can achieve much shorter pulse durations. As a result, the effective passive modelocking techniques of SESAMs, graphene based SAs and KLM have been discussed in detail with particular focus on their capability for emission in the mid-IR. The concept of intracavity GDD was then introduced as it has a large impact on the minimum pulse duration obtainable by a modelocked laser, several methods for effectively managing this parameter were subsequently presented. Finally, the challenge of accurately measuring modelocked pulses was presented. Modern photodetectors are not fast enough to resolve ultrafast events justifying the requirement for alternative measurement methods. The last section has discussed the most commonly employed ultrafast measurement methods with specific attention paid to that of interferometric autocorrelation, as that is the technique which has been utilised during experiments in this thesis.

Chapter 5. CW and Pulsed Emission of a ULI Ho:YAG Waveguide Laser

5.1 Introduction

The $Y_3Al_5O_{12}$ crystal, more commonly known as Yttrium Aluminium Garnet or just YAG, has long been established as an ideal laser gain host medium. This is owed to its many favourable thermo-mechanical and optical properties for laser operation. It is an optically isotropic, chemically stable and robust material which is readily acceptant of RE ion dopants. The trivalent Yttrium ions can be directly substituted for trivalent RE ions meaning that charge compensation is not necessary [233, 234]. In addition to this, the cubic nature of the YAG structure supports narrow fluorescence bandwidths from the dopant ions which tend to favour low laser threshold and high gain values. Furthermore, this crystal structure is continually stable from low temperatures right up to its extremely high melting point of ~ 2213 K [235]. As a consequence it is particularly useful for the development of high powered emission sources as it can withstand the high pump powers required which can be in the range of 10s of kWs [236, 237]. It can also be be cryogenically cooled with no issues which can be beneficial for laser emission in some cases – this will be discussed in greater detail later in this section. Another important property is its optical transparency ranging ~ 0.2-5.2 μm [238], thus it is suitable for use throughout the visible and IR spectral ranges.

The advantageous properties discussed have led to Nd^{3+}:YAG becoming the world's most widely used, well-known solid-state laser gain material . This laser emits at 1064 nm and has demonstrated impressive multi-kW CW output power capabilities [237, 239] as well as few ps pulses in modelocked operation [240] . Various other dopants have been successfully utilised for laser emission spanning a range of wavelengths. A summary of these lasers and their emission wavelengths are provided in Table 5.1.

Dopant	Laser Emission Wavelength
Nd^{3+}	946 nm, 1064 nm, 1.3 μm [241] & 1.8 μm [242]
Tm^{3+}	~2 μm [243]
Er^{3+}	1.6[96] & 2.9 μm [87]
Cr^{4+}	1.35-1.55 μm [244]
Yb^{3+}	1.03 & 1.05 μm [245]

Table 5.1. A table summarising the elements commonly doped in YAG for laser emission as well as the wavelength they emit at.

Another dopant which has not been mentioned yet and is the focus of this chapter is the trivalent Holmium ion: Ho^{3+}. For simplicity, from here on Ho^{3+} doped YAG will be referred to as Ho:YAG. This ion is of particular interest for its transition which emits in the mid-IR at ~ 2.1 μm. Laser sources in this wavelength region find use in a variety of applications including for example surgery [7] and defence [8]. They also find use in wind velocity monitoring [246] and the detection of greenhouse gases such as N_2O [247]. The first Ho:YAG lasers demonstrating emission at 2.1 μm were co-doped with other RE ions including Er, Yb, Cr and Tm to optimise the absorption of incident pump energy [248, 249]. Subsequent energy transfer processes occur from the co-dopant ions to the Ho ions populating the upper lasing level sufficiently to create a population inversion and thus initiate lasing. The first Ho:YAG lasers to demonstrate lasing action on this 2.1 μm transition were reported in 1965-66 by Johnson et al [250, 251]. They were co-doped with Tm, Yb and Er demonstrating a maximum slope efficiency of ~ 5%. With the development of high power ~ 800 nm diode lasers, Tm emerged as the most popular choice of co-dopant for Ho:YAG laser operation. This wavelength is ideal for pumping Tm ions, thus the high powered diodes facilitated very efficient energy transfer from the Tm to the Ho ions, greatly improving the performance of lasers emitting on the 2.1 μm transition [252, 253].

The next major step in the development of Ho:YAG lasers came with improved performance of 1.9 μm Tm doped lasers demonstrating good beam quality. This facilitated laser emission from singly doped Ho:YAG crystal through in-band pumping at 1.9 μm. The first demonstration of this was reported in 1992 by Stoneman et al. [254] and the pumping scheme exploited is shown in Figure 5.1.

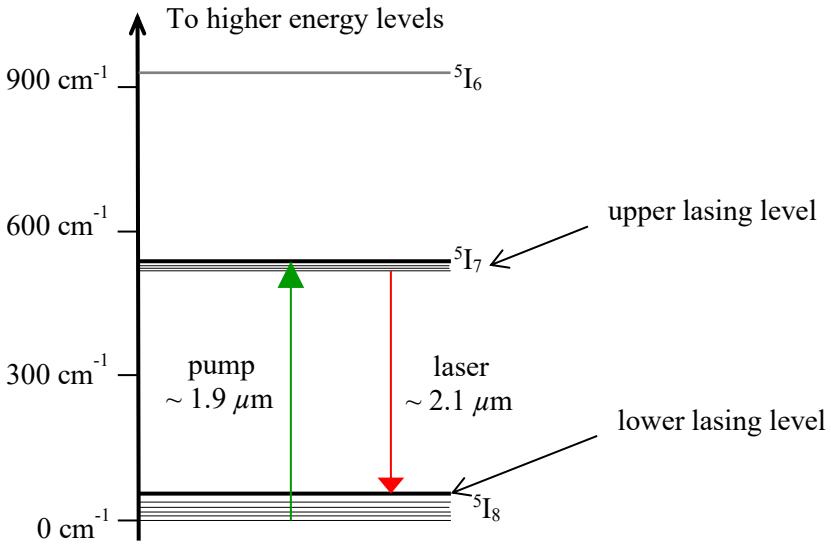

Figure 5.1. Energy level diagram of the Ho^{3+} ion with important transitions for in-band pumped laser action at 2.1 μm highlighted. Diagram was produced using information from [255].

This direct pumping of the Ho ions is made possible due to the Stark splitting of the ground state – energy level $^5I_8$, this can be seen in Figure 5.1. As shown, the 1.9 μm pump is absorbed exciting electrons into the $^5I_7$ energy level. The 2.1 μm emission occurs when an electron in this excited state decays into one of the Stark level manifolds of the ground state which are thermally populated, with the emission of a photon. The released photon has a wavelength slightly larger than the pump because the Stark levels into which the electrons decay have slightly higher energies than the zero energy ground state. As a result this is referred to as a quasi-three level laser scheme [256]. Both the ground state and the excited energy level $^5I_7$ experience considerable Stark splitting in Ho:YAG; more specifically 11 sublevels spanning energies 0 – 535 cm^{-1} and 14 sublevels spanning energies 5228 – 5455 cm^{-1} respectively [257]. When Tm co-doping is exploited, regardless of how efficient the energy transfer processes from the dopant Tm ions to the Ho ions are, the probability of upconversion processes which populate the $^5I_6$ and the higher $^5I_5$ levels as well as the thermally induced stress are significantly higher than in singly doped Ho crystals. A direct result of these processes is that the energy storage lifetime of the upper lasing level is strictly limited to be shorter than the theoretical lifetime of this level in Ho, the extent of which depends on the co-dopant concentration. These effects inhibit the laser's efficiency and power capabilities [254, 258] . As a result of this, there was a great deal of interest in exploiting an alternative pumping scheme such as that shown in Figure 5.1.

Other than negating the disadvantages associated with co-doping, another benefit of in-band pumping is that of a particularly low quantum defect and hence the potential for very high pump-to-signal lasing efficiencies. However, quasi-three level laser systems generally require high pump power levels to reach threshold. At such high incident power levels detrimental thermal effects common to the material, including a low thermal conductivity at room temperature, around 11 $Wm^{-1}K^{-1}$, are more apparent. This means that heat dissipation within the material is inefficient thus limiting the laser performance and increasing the potential for thermal damage. Consequently, much of the work done in Ho:YAG crystal lasers utilises cryogenic cooling, usually with liquid nitrogen, to operate them at temperatures approaching ~ 77 K. When the material is cooled to this low temperature, the population in the lower lasing level which is a Stark manifold is reduced by transfer to another of the Stark levels, the laser, thus, in effect behaves like a near four level system [255]. This greatly reduces the laser threshold when compared to room temperature. Cryogenic cooling in YAG has also been shown to increase the thermal conductivity of the material; the induced temperature gradients are therefore reduced resulting in more uniform cooling throughout the material. Simultaneously both the thermal expansion coefficient and the thermo-optic coefficient are reduced. These augmented properties are significantly more favourable material parameters for lasing and have therefore allowed the demonstration of up to 100 W of CW output power and thresholds < 1W. [46, 259, 260].

Despite cryogenically cooled bulk Ho:YAG lasers exhibiting high power output capabilities, the complex equipment required for effective cooling deemed them very expensive and unsuitable for many applications. As a result a significant amount of research has been done latterly to optimise the performance of Ho:YAG lasers for near room temperature operation with great success. However, these systems are generally quite large bulk cavities because this type of setup can aid effective heat dissipation in the crystal. For example the high power systems reported in [261-263] demonstrating power capabilities of 30-100 W have cavity lengths ranging of 1-2.4 m. These large systems often containing many mechanical components can be unsuitable for many "real world" applications in which compact, portable sources are required. Furthermore, the high PRF's required by some applications are not possible for these cavity lengths.

Using waveguide geometry can offer an alternative solution to these issues while also negating the need for cryogenic cooling. This is because a waveguide ensures good

overlap between pump and signal beams which can lower the laser threshold significantly and also result in high optical gain. The gain in a waveguide can be very high per unit length compared to bulk material if the ideal waveguide parameters are identified [55]. Overall, this reduces the requirement for pump powers levels which potentially cause thermal issues detrimental to the laser performance [55, 58]. This type of geometry could be employed in a fibre laser form but as discussed in Section 2, the compactness and performance of fibre lasers are limited by the inherent minimum bend radius as discussed in Section 2. A ULI waveguide laser provides an elegant solution and as a result it is possible to construct such a laser on the scale of a few mm [34, 142-145, 264], this is ideal for GHz PRF emission in the modelocked regime which is the ultimate aim of this work [265-267]. This chapter reports the first waveguide laser reported in Ho:YAG material. A full characterisation of the CW waveguide laser performance is given in section 5.2. Section 5.3 subsequently presents results from the first demonstration of a GHz PRF Ho:YAG pulsed laser which was made possible due to; the compact, high-gain and single mode nature of the ULI fabricated waveguides.

5.2 Continuous Wave ULI Ho:YAG Waveguide Laser

For this investigation the Ho:YAG substrate in question was fabricated by Blue Ridge Optics. It was doped with 0.5 at. % Ho and had dimensions of 5 × 5 × 14 mm. The waveguides were inscribed in the 14 mm length of the sample to maximise the attainable gain.

5.2.1 Waveguide Fabrication in Ho:YAG

In Ho:YAG, successful inscription of waveguides has been reported previously by Rodenas et al. [268] , in this work a positive refractive index change was induced in the material, but no lasing action was demonstrated. However, lasing operation has been reported in YAG hosts doped with Nd [80, 269] and Tm [270] facilitated by depressed cladding waveguides [80, 269, 270]. In addition to this, the inscription method for depressed cladding structures allows for very fast and precise fabrication of waveguides 10s of μm's in diameter – this tends to be the suitable scale for propagation of mid-IR wavelengths. As a result, depressed cladding waveguide structures were chosen for the Ho:YAG waveguide laser reported here.

The same Yb:fibre inscription laser system described in sub-section 3.4.1 was used for the waveguides fabricated in this section. The laser has a central wavelength of ~ 1043 nm with a pulse width of ~ 359 fs and is circularly polarised. For these waveguides it was operated with a PRF of 500 kHz and pulse energy of 250 nJ. The pulses were focused below the surface of the Ho:YAG crystal using a 0.4 NA lens with focal length = 6.2 mm, resulting in a focal spot of ~ 2 μm at an approximate distance of 250 μm below the material surface. The substrate was translated on the Aerotech stages at 10 mms^{-1} through the laser focus to create annular structures with diameters ranging from 30-80 μm. The number of inscription elements was also varied. An example of the resultant waveguide structures are displayed in Figure 5.2.

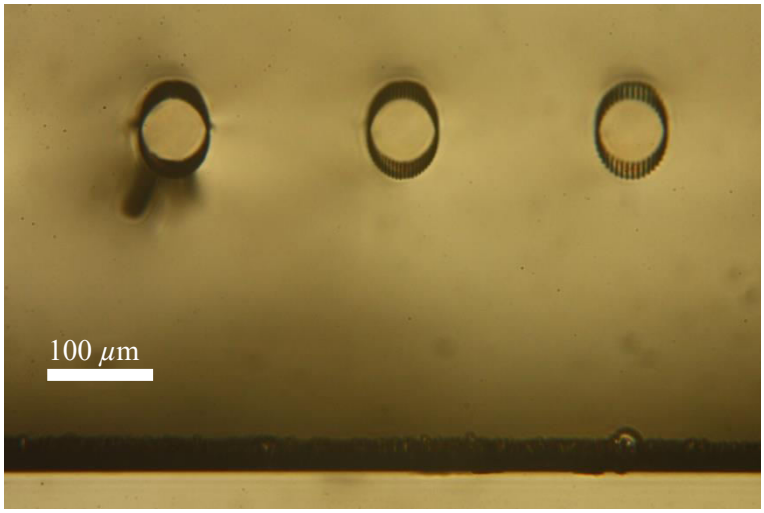

Figure 5.2. Transmission microscope image of the end facet of ULI depressed cladding waveguide structures fabricated in Ho:YAG.

The number of inscription elements tends to be dependent on the diameter of the waveguide; for the larger diameter waveguides more inscription elements are required to ensure the strained region of the inscribed cladding surrounds the entire core. However, the number of elements parameter can also be varied for waveguides of the same diameter to identify a regime for both low loss and tight confinement. This is demonstrated in Figure 5.2, each of the waveguides has a 60 μm core diameter but the number of elements decreases from left to right. Visible cracking/damage has occurred for the largest number of elements which has an adverse effect on the waveguide losses, but if too few elements are used the confinement can be ineffective. The aim was to find the optimum number.

5.2.2 Single Mode Ho:YAG Waveguide Laser

The ULI waveguides were then investigated for transverse mode propagation and laser performance in the cavity setup shown in Figure 5.3.

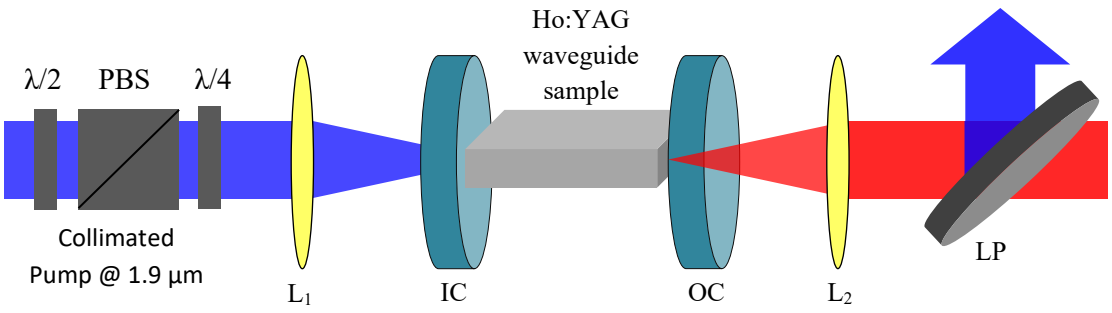

Figure 5.3. Cavity configuration of the Ho:YAG ULI waveguide laser. L_1 and L_2 are plano-convex lenses with 40 and 50 mm focal lengths respectively, both are AR coated for 1.65 – 3 µm. IC is the input coupler, OC is the output coupler and LP is a 2 µm long pass filter. PBS, is a polarising beam splitter, λ/2and λ/4 are half and quarter wave plates respectively.

L_1 and L_2 are lenses chosen to optimise the coupling of pump light into the waveguides, their AR coating allows maximum transmission of the pump and laser output. The input coupler, IC, is HR coated on the front side adjacent to the sample, at 99.9% for 2.05 – 2.43 μm and AR coated on the rear side for 1.7 – 2.0 μm to allow maximum transmission, > 99%, of the pump. OC represents the output coupler, four different output couplers were utilised to characterise the laser performance. Three had reflectivity values of 60, 70 and 80% from 1.7 – 2.7 μm, giving rise to a double pass of the pump at 1.9 μm. The other OC was coated for 97% reflectivity for 2-2.4 μm. These output couplers will be referred to as 60% R OC, 70% R OC, 80% R OC and 97% R OC from here on. The 2 μm long pass filter, LP, filtered out any unabsorbed residual pump light before measurement of the laser output characteristics. The Ho:YAG substrate was fixed with thermal paste to a copper mount which was passively water cooled to a fixed temperature of 15°C.

The pump source utilised was a linearly polarised CW Tm doped fibre laser with emission wavelength 1908nm, a maximum output power of 20 W and beam diameter of ~ 4.1 mm. It was manufactured by IPG photonics; the model number is TLR-20-1908-LP. To prevent potentially damaging feedback into the pump laser due to Fresnel

reflections from the sample surface itself and other cavity components, a beam splitter/wave plate arrangement was setup prior to the transmission through L_1 which can be seen in Figure 5.3. PBS represents a polarising beam splitter, λ/2 and λ/4 represent half and quarter wave plates respectively. The PBS is aligned to allow for maximum transmission of the pump light which is polarized horizontally, on propagation through λ/4 the beam becomes circularly polarised. Back reflections from optics in the laser waveguide laser set-up will therefore be circularly polarised in the opposite direction and thus emerge from λ/4 with linear polarisation in the opposite direction to the pump. The beam is subsequently prevented from propagating back toward the pump laser by the PBS, in this way the set-up acts as an optical isolator. A prior member of the NLO group had carried out beam quality M^2 measurements on this laser and it was shown to vary between 1.4 and 2.4 dependent on the diode current applied. These results can be found in [271]. The M^2 value was shown to increase for particularly high and low applied diode current and found to be stable if operated in between those limits. The M^2 parameter definition will be explained in detail later in this section; here it is important to know that the increase in its value at high and low diode current was detrimental to the laser performance. The PBS and wave plate arrangement allowed an alternative means of fine pump power control through rotation of the half wave plate, as opposed to changing the diode current, whilst simultaneously minimising the feedback. The resultant pump beam was circularly polarised with a maximum power of 12 W.

A total of 36 waveguides were inscribed in an attempt to identify the optimum inscription parameters for a waveguide laser. The initial inscription parameters were identified by analysis of the previous ULI work in YAG material, carried out in the NLO group. The inscription beam was focused using a 0.4 NA objective lens; this resulted in the set of waveguides being fabricated at a depth of ~ 250 μm below the substrate surface. The other inscription parameters were varied to fabricate waveguides with combinations of the following: diameters ranging from 30 – 60 μm, inscription translation speeds from 8 – 12 mms^{-1} and average powers 120 – 130 mW. As the ultimate aim was to develop a high PRF pulsed source, the waveguides were first investigated for transverse single mode propagation. The reasons that transverse single mode is optimum for laser operation has previously been presented in sub-section 3.4.1. It was found that waveguides greater than 50 μm in diameter were all multimode. The single mode waveguides were then operated in a laser cavity and it was found that none

of 30 μm diameter waveguides could demonstrate lasing action. The laser output power from the remaining waveguides was then measured as a function of pump power with the 80% R OC to identify the most efficient waveguide. The optimally performing waveguide in terms of output power capability was found to have a diameter of 50 μm comprised of 60 inscription elements and was inscribed with an average power of 125 mW at 12 mms^{-1}. The end facet of this waveguide is shown in Figure 5.4.

Figure 5.4. Transmission microscope image of the end facet of depressed cladding single mode waveguide structure in Ho:YAG.

A full characterisation of this waveguide was then performed, the results of which are presented here. Prior to investigating the laser performance, the refractive index difference between the unmodified core and the inscribed cladding regions of the waveguide was estimated. The method to do this involved the measurement of a laser beam width and divergence angle, the standard methods of measuring these parameters are defined in the ISO Standard 11146. The experimental procedure implemented will now be described with reference to this standard and Figure 5.5:

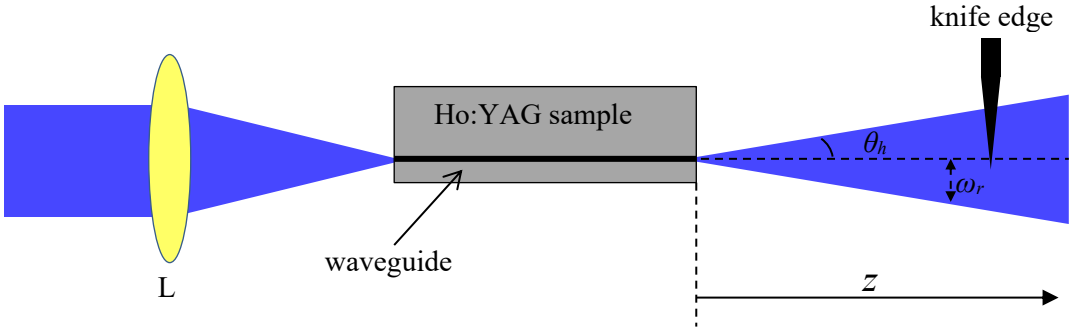

Figure 5.5. Schematic diagram of the experimental setup for the measurement of the refractive index difference between the core and cladding of a depressed cladding waveguide. L is a 40 mm focal length plano-convex lens.

Pump light is focused into the waveguide with the 40 mm focal length lens, L, and a knife edge measurement is then utilised to evaluate the radius of the output beam emerging from the waveguide as a function of distance from the output facet, z. The knife edge method consists of aligning a knife edge on a micrometer translation stage

perpendicular to the propagating beam. The knife edge is initially outside of the beam path, it is then translated through the beam whilst monitoring the output power after the knife edge. The distance that the knife edge travels between obstructing 10% and 90% of the total beam, ΔX_{90-10}, is measured, this is then used in equation (22) to calculate a value for the Gaussian beam radius.

$$\Delta X_{90-10} = 1.28\omega_r \tag{22}$$

in which ω_r is the Gaussian beam waist radius indicated in Figure 5.5. A full derivation of equation (22) is found in [272] which fully explains the origin of the calibrating factor 1.28 For the diverging beam emerging from a waveguide, the knife edge method described is utilised to evaluate several values of the beam waist as a function of the distance from the output facet. Using these values one can estimate a value of the half divergence angle of the beam θ_h shown in Figure 5.5. This angle is subsequently used in the standard formula for the NA of a waveguide which is given in equation (23)

$$NA = n_0 \sin\theta_h = \frac{1}{n_0}\sqrt{(n_{core})^2 - (n_{cl})^2} \tag{23}$$

where n_0 is the index value of the material surrounding the substrate which in this case is 1 and n_{core} and n_{cl} are the indices of the waveguide core and cladding respectively. If the refractive index of the unmodified core is known, one can calculate the value of the refractive index of the cladding with equation (23) and hence the difference between the two indices.

For the waveguide in Figure 5.4, a set of knife edge measurements were performed in the horizontal dimension, these returned a half divergence angle θ_h of approximately 1.87º. The refractive index of the Ho:YAG substrate material is ~ 1.802 at the signal wavelength. By inserting these values into equation (23) a value of ~ 1.8017 was calculated as the index of the cladding material, resulting in a refractive index difference between core and cladding of Δn = 0.0003. It is expected that the index difference should be particularly small for single mode propagation, for reference, the multimode waveguides returned an index difference of Δn = 0.01.

The waveguide was then pumped in the cavity configuration shown in Figure 5.3, the waveguide laser output power was recorded at several intervals as a function of the pump power incident on the crystal, both were measured with a thermal power meter – Spectra-Physics model 407. The Ho:YAG substrate has not been AR coated on the end facets, therefore light incident on it will experience Fresnel reflections which for this material are ~ 8%. This loss was accounted for by it subtracting it from the measured incident pump powers. Therefore, the pump power values quoted are the maximum power available to be coupled into the waveguide. The laser output power vs pump power measurements were repeated for each of the four available output couplers and the results are presented in Figure 5.6. Table 5.2 summarises the resultant slope efficiencies and maximum waveguide laser output powers observed.

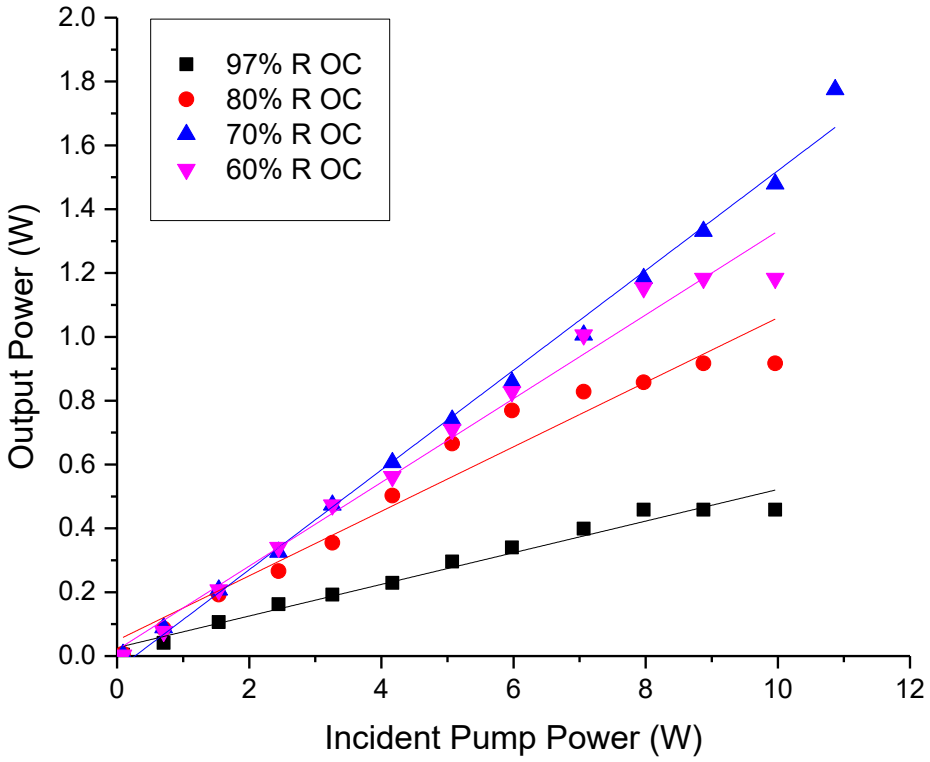

Figure 5.6. Output power characterisation of Ho:YAG waveguide laser for four different reflectivity values of output coupler. The key in the top left corner identifies the symbols which represent each OC.

OC Reflectivity (%)	Maximum Laser Output Power (mW)	Slope Efficiency (%)
97	458	5
80	917	10
70	1775	16
60	1183	13

Table 5.2. A table summarising the Ho:YAG waveguide laser maximum output power and slope efficiency for each of the 4 OC's.

The 70% R OC resulted in the highest laser output power possible with this pump source. Furthermore, with this OC, unlike with the other three, thermal rollover was not observed for the higher pump powers. From Figure 5.6 it can be deduced that the laser threshold for each OC is typically < 50 mW. These threshold values are the lowest demonstrated to date in this material and are attainable due to both the high degree of overlap between pump and signal and the small radius sustained over a relatively long distance. These are both direct results of the tight confinement provided by ULI waveguide.

The propagation loss of the waveguide fundamentally dictates the output power cability of a waveguide laser. A source at the signal wavelength of ~ 2.1 μm is required to make a direct measurement of the propagation loss but such a source was not available at this time. However, both Findlay-Clay [273] and Caird [274] analysis are alternative methods to provide an estimate of the loss. Findlay Clay analysis is suited to estimating the round trip loss of a 4 level laser system. However, for a quasi-three level system in which the round trip losses can be dominated by re-absorption losses, a Caird analysis provides a more accurate estimate of the propagation loss [275]. The plot in a Caird analysis is based on equation (24).

$$\frac{1}{\eta} = \frac{1}{\eta_0} + \frac{L}{\eta_0}\frac{1}{T_{OC}} \tag{24}$$

In equation (24), η is the laser slope efficiency, η_0 is the intrinsic slope efficiency or in other words the theoretical maximum of the slope efficiency, T_{OC} is the transmission value of the OC and L is the round trip propagation loss. By plotting a graph of $1/\eta$ versus $1/T_{OC}$, the intrinsic slope efficiency can be calculated from the y intercept and the propagation loss can be estimated from the slope efficiency of the plot. This process

was performed for the slope efficiency data obtained from the Ho:YAG waveguide laser, the resultant plot is shown in Figure 5.7. The data point for the 97% R OC has been neglected as the Caird analysis is only valid under the assumption that the laser wavelength is the same for all OCs [274, 276]. It is shown in Figure 5.10 that the laser wavelength is red shifted with the 97% R OC.

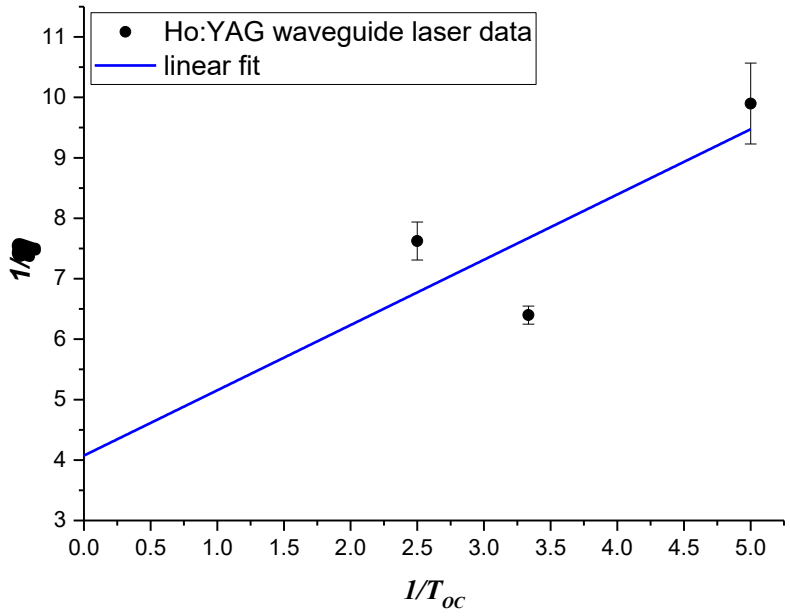

Figure 5.7. Caird plot of the ULI Ho:YAG waveguide laser.

The intrinsic slope efficiency η_0 can be obtained from the linear fit of the Caird plot by calculating the inverse of the y intercept. For the plot in Figure 5.7, the y intercept is 3.96 thus η_0 is calculated to be ~ 25.3%. The cavity loss is then estimated from the slope of the linear fit resulting in L = 28.0%. Therefore, for the cavity length of 14 mm the loss is 1.43 dB which translates to a waveguide propagation loss of 1.02 dBcm^{-1}. This is comparable to the propagation losses recorded by Ren et al. in [266]. The authors report a propagation loss of 0.77dBcm^{-1} for a Tm:YAG ULI depressed cladding waveguide laser, in a similar spectral range to our laser at around 2 μm. This estimation would be improved by recording a greater number of slope efficiencies for OCs with different T_{OC} values, which all result in very similar spectral emission. However, such OCs were not available so the estimation was made with the data obtained, and is valid in demonstrating the low loss nature of the fabricated waveguides supported by the low threshold values recorded.

The transverse mode profiles from many of the waveguides were initially viewed on a mid-IR camera (FLIR model SC7000) to identify the single mode waveguides. As the waveguide in question appeared to propagate a single mode, a beam quality measurement was carried out to verify this. The laser beam profile as viewed on the camera is shown in Figure 5.8.

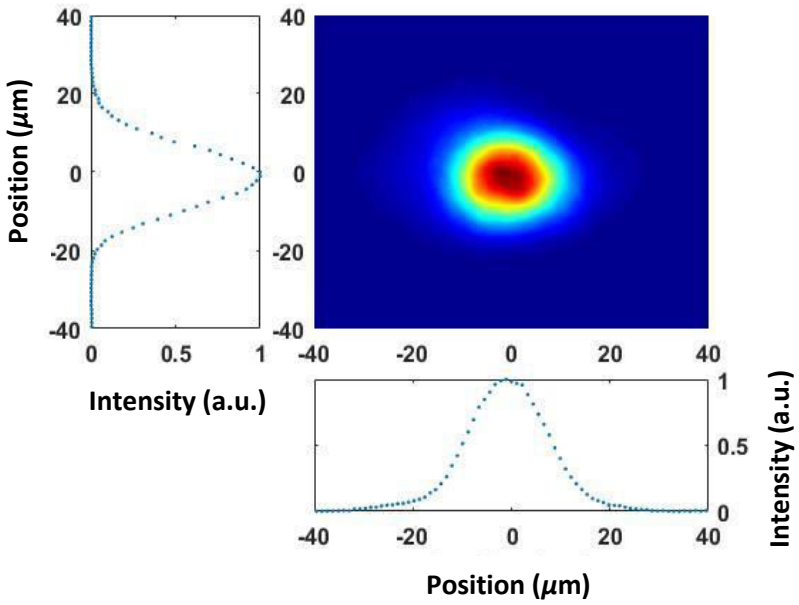

Figure 5.8. Beam profile of the ULI HoYAG single mode waveguide laser output.

The parameter indicative of the mode quality is the M^2 factor which is defined in the ISO Standard 11146 as shown in equation (25).

$$\theta = M^2 \frac{\lambda}{\pi \omega_0} \tag{25}$$

In equation (25), θ is the half-angle beam divergence, ω_0 is the beam waist radius at the focus of the 10 cm lens and λ is the emission wavelength. Hence to obtain a value for M^2 both θ and ω_0 must be evaluated. The procedure for this measurement was as follows; a 10 cm focal length lens was used to focus the collimated laser beam emitted from the Ho:YAG waveguide laser and the $1/e^2$ beam diameter was measured at several positions as a function of the propagation distance, *z*. The beam diameter was measured using a beam profiler (manufactured by DataRay with model number WinCamD-IR-BB). These measurements were carried out in both the horizontal and vertical directions

using the 70% R OC as this demonstrated the most stable output in terms of power over time. To obtain values for θ and ω_0, a numerical fit of the measured data was made to equation (26) [277] allowing for calculation of the M^2 factor.

$$(\omega(z))^2 = [\theta^2]z^2 + [-2\theta^2 z_0]z + [\omega_0^2 + \theta^2 z_0^2] \quad (26)$$

In equation (26) $\omega(z)$ is the measured beam radius, i.e. the beam diameter evaluated by the beam profiler divided by 2, and z_0 is defined as the propagation distance of the beam at the focus. As defined in the ISO standard 11146, M^2 cannot be < 1 and is equal to 1 for a perfect Gaussian single mode, for increasingly multimodal structures, the M^2 factor increases from 1. A Matlab script was used to perform the numerical fit of the measured data by means of the least squared curve fitting tool. The graphs in the horizontal and vertical direction for the z position values versus the $1/e^2$ radius measurements squared are shown in Figure 5.9 and a) and b) respectively with the numerical fit applied.

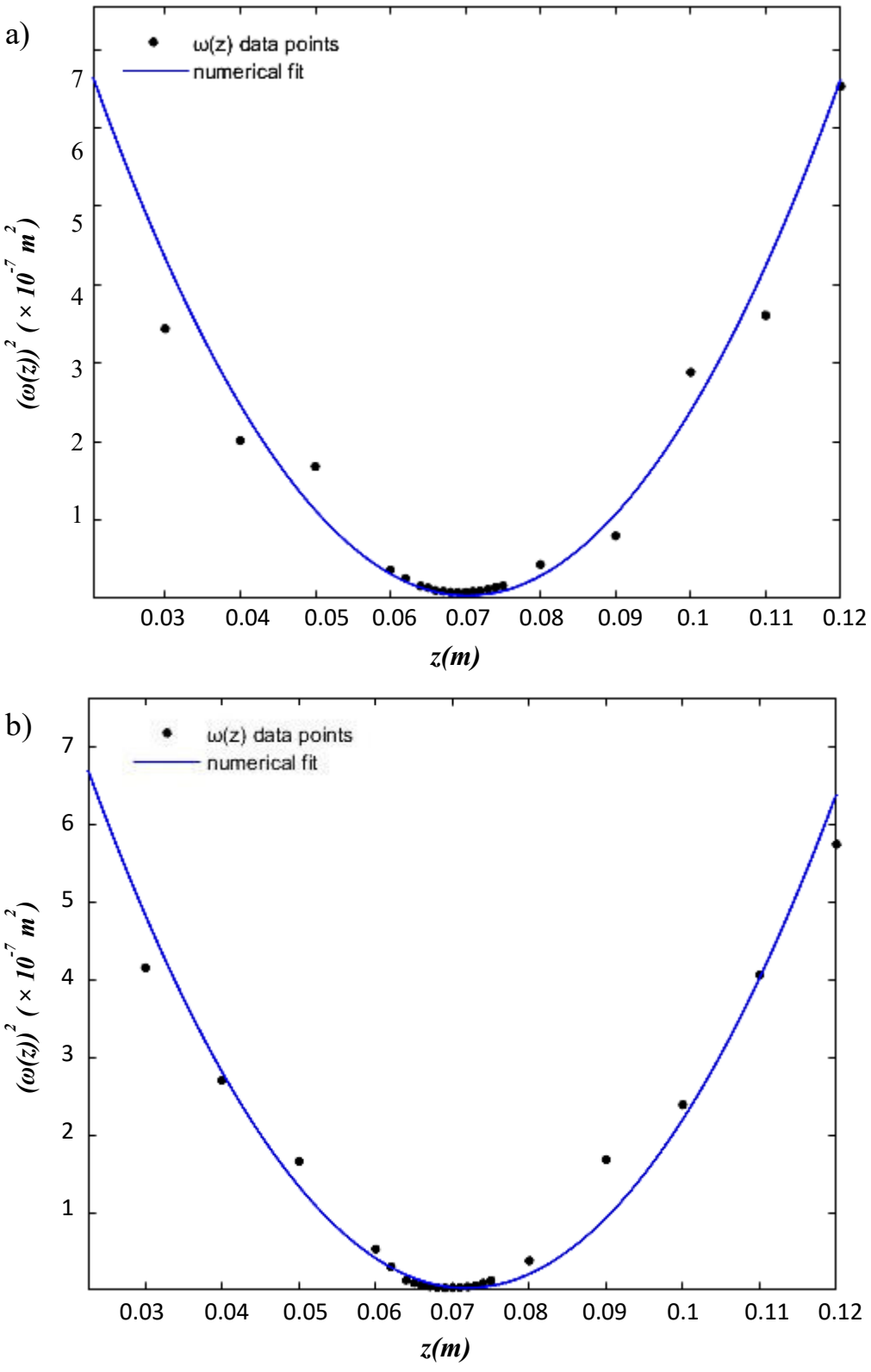

Figure 5.9. Plot of Ho:YAG laser $(\omega(z))^2$ values as a function of propagation distance, z, when the collimated laser beam is focused with a 10 cm focal length lens. Plots shown for both a) horizontal and b) vertical directions.

The Matlab script used the fit of the data to calculate values for the beam waist radius at the focus, ω_0, and the half-angle beam divergence, θ. It then uses these values in equation (25) to calculate M^2 factors of 1.48 and 1.75 in the horizontal and vertical directions respectively. This indicates that the waveguide is asymmetrical and so not a perfect Gaussian single mode, however it was decided that it was sufficiently close to be considered as a promising candidate for modelocking investigations at this stage.

In addition to the power performance and beam profile analysis, the laser spectral output with each OC was characterised with a Thorlabs Optical Spectrum Analyser (OSA) that has model number OSA205, it operates a resolution of 0.1 nm at the laser wavelengths. The normalised intensity spectra vs wavelength results are displayed in Figure 5.10 a) and b).

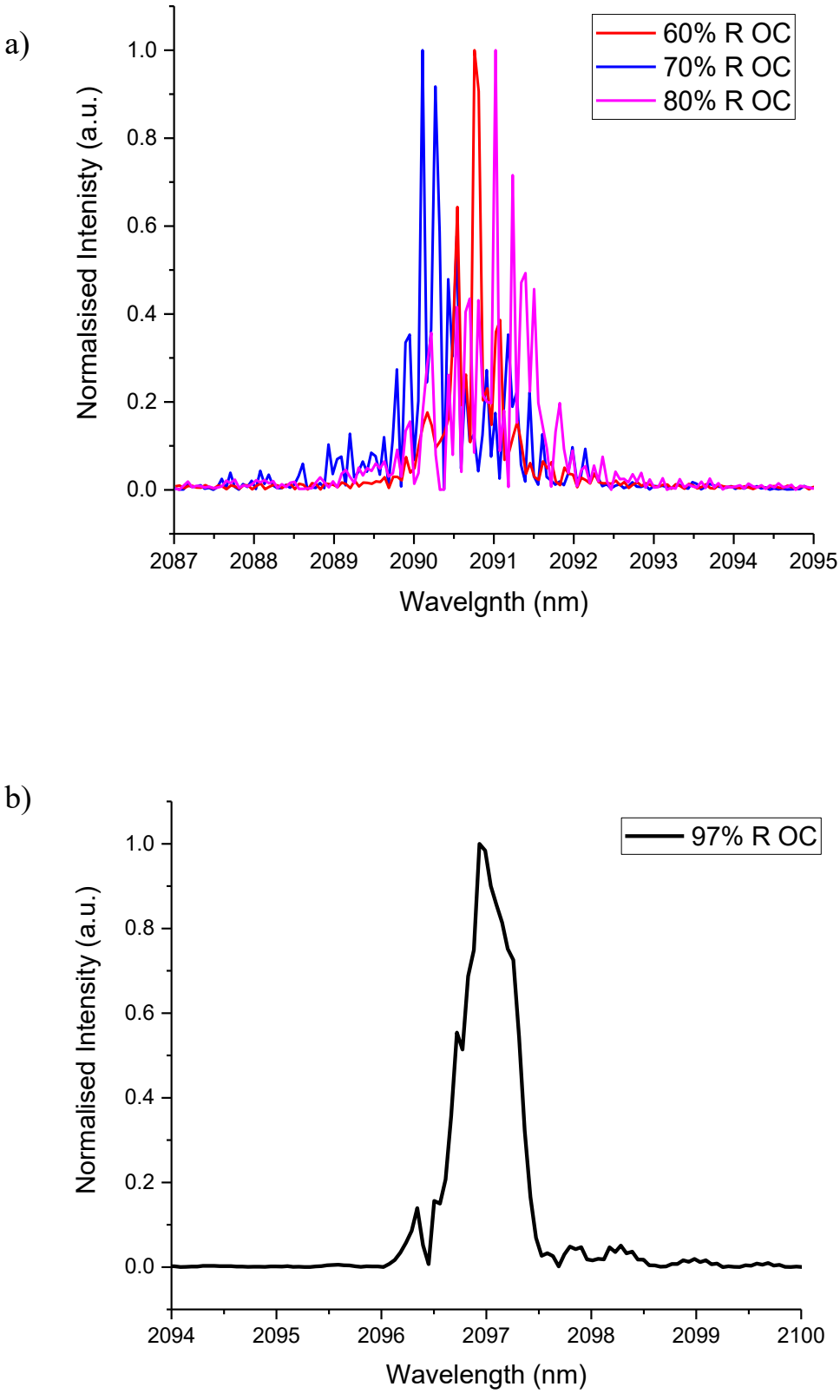

Figure 5.10. Normalised Spectral output of Ho:YAG waveguide laser for 4 different reflectivity values of output coupler. a) displays the output spectra for the 60, 70 and 80% R OCs and b) displays the 97% R OC spectrum which is red-shifted in comparison to the other three.

The three lower R OCs demonstrated laser emission wavelengths centred around 2090 – 2091 nm shown in Figure 5.10 a), the 97% R OC red-shifts the operating wavelength to ~ 2097 nm as can be seen in Figure 5.10 b). A laser emits at the wavelength which experiences the lowest losses and hence minimum threshold. The particular point at which this occurs is dependent on both the material emission cross section and the OC mirror reflectivity coating. The three lower reflectivity output couplers have broadband similar coatings whereas the 97% R OC has a different coating. This can be attributed to the combined effects of a different reflectivity coating on the 97% R OC and reabsorption loss. The latter is a common effect in this type of quasi-3 level laser in which the gain spectrum is dependent on the population inversion ratio. The value of this ratio is clearly dependent on the significant reabsorption which occurs due to the nature of the pumping scheme. For the higher reflectivity OC, the population inversion is relatively small and so there is less depletion of the inversion. As a result, the net gain peak can occur at wavelength substantially red-shifted from the peak of the emission cross-section. At the lower reflectivity OC values the required inversion to reach threshold increases and this in turn depletes the ground state and reduces the reabsorption occuring. Thus, the peak of the gain shifts back towards the peak of the emission cross-section [278].

5.2.3 Power Scaling of CW Ho:YAG Waveguide Lasers

This work has been carried out in collaboration with colleagues based at the Air Force Research Laboratory (AFRL) situated within the Wright-Patterson Air Force Base in Ohio, USA. Whilst the work at HWU concentrated on efficient single mode laser operation, research efforts at AFRL were concerned with the high power operation of Ho:YAG waveguide lasers. Bulk Ho:YAG lasers have routinely produced output powers in the region of 10s – 100 W with slope efficiencies in the 50-80% range at room temperature [255, 261, 262, 279, 280]. The performance of the ULI waveguide laser presented here is far inferior in comparison, this is due to a number of factors: the gain crystal utilised was very short, only 14 mm, for the objective of generating high repetition rate pulsed output, thus the active volume is small in comparison to the bulk arrangements. In addition, the cooling system for effective dissipation of heat away from the crystal is limited by this size. Furthermore, the propagation loss of the waveguide introduced another loss element compared to the bulk setups. Therefore the research team at the AFRL concentrated on improving the power performance of the

waveguide laser scheme. They have had some success in demonstrating a Ho:YAG crystal fibre waveguide laser fabricated through adhesive free bonding of a Ho:YAG core to an undoped YAG cladding. This laser performed with a maximum CW output power of 500 mW and slope efficiency of 17%, Q-switching pulsed operation was also observed [281]. However, a ULI waveguide laser exhibited superior power performance; a maximum slope efficiency of 29 % and output power of ~ 1.9 W were observed from an 80 μm diameter waveguide. This increased performance level was demonstrated at the cost of reduced beam quality as the output was highly multimode with an M^2 factor of ~ 5. The results of both the single and multimode waveguide laser performance have been published in Applied Optics [282]. For completeness it must be included that this paper also presents results of an experiment performed at AFRL utilising a Ho:YAG waveguide sample co-doped with Yb. The aim was to exploit energy transfer from the Yb to the HoYAG potentially allowing high-powered diode pumping at 940 nm. However, lasing action could only be achieved with in-band pumping and attempts to lase with a 940 nm diode pump were not successful as the crystal cracked under stress due to the thermal load. Although investigations are ongoing to optimise the ULI parameters in an attempt to reduce the stress in the co-doped material, we conclude that as this time in-band pumping is optimal for ULI waveguides in Ho:YAG. Although these efforts have demonstrated some improvement in terms of power performance compared to the single mode waveguide presented, research is ongoing to optimise the waveguides themselves and the cavity for much higher performance comparative to bulk lasers.

After completing the full CW characterisation of ULI Ho:YAG waveguide lasers, the single mode waveguide was then investigated for high PRF modelocked pulse generation.

5.3 Graphene based Q-switched Modelocking of Ho:YAG Waveguide Laser

5.3.1 Introduction

Although some general applications of lasers emitting at ~ 2.1 μm have previously been discussed, there are a number of specific applications which require the use of very high, > 1 GHz, PRFs. Examples include high speed optical communication as well as

optical frequency combs for precision metrology. Often, multiple GHz range PRFs are required to obtain the high level of precision and resolution required for these types of applications [169, 210, 283] and therefore justify the need to develop high repetition rate pulsed sources in this spectral range.

SESAMs have shown some success in the generation of modelocked pulses at ~ 2.1 μm [189, 284], but as detailed in sub-section 4.3.3 they have complex fabrication procedures and tend to be bandwidth limited in this spectral range [285]. Attempts have also been made to modelock a Ho doped fibre laser using black phosphorus as an SA resulting in 1.3 ps pulses [286]. Black phosphorus is a relatively new SA material exhibiting a wide operational bandwidth suited for the emission of ultrafast pulses in the mid-IR up to ~ 4 μm [287]. To date it has not yet demonstrated capabilities at 2.1 μm to rival that of graphene which has successfully emitted sub-200 fs pulse from a Ho fibre laser [288], but as it is a new material investigations are ongoing to uncover its full potential. Another method which has been exploited for pulse generation at this wavelength is that of a modelocked solid-state laser combined with an OPO for widely tunable pulsed operation [21]. These setups require a number of free space optics resulting in complex and relatively large system which can often lead to issues with sensitivity to the surrounding environment and deem them unsuitable for some applications. As a result, there remains a real need to develop compact and robust systems which not only overcome the challenges associated with alternate methods, but also have the ability to generate ultrafast high PRF pulses in the mid-IR.

With regards to modelocking the laser emission from active Ho ions in YAG crystal to obtain pulses centred at ~ 2.1 μm, co-doped schemes have been demonstrated with some success. 800 ps pulses were produced utilising an active modelocking technique in the form of an acousto-optic modulator from a Cr,Tm,Ho:YAG crystal pumped by a Kr-ion laser [289]. Passive modelocking in the form of a SESAM resulted in 21 ps pulses from a diode pumped Tm,Ho:YAG [189]. However, the disadvantages associated with these co-doped schemes, which have been discussed at length in section 5.1, limit their capability. Despite becoming a widely established laser material that has been thoroughly researched there have been few demonstrations of singly doped Ho:YAG modelocked lasers with ultrafast pulse widths and none to date with a high PRF in the multi GHz range. The shortest pulse width demonstrated from this material until two years ago was 2.1 ps exhibiting an average output power of 230 mW [284]. The laser

was passively modelocked with a slow GaSb based SESAM. Due to the high saturation fluence of many of the type of SESAMs which operate at this wavelength, > 400 μJcm^{-2}, focusing optics are required to saturate the SESAM. This, in addition to the type of bulk cavity exploited here, leads to an inherently long cavity length and hence a PRF which is limited to the MHz range. The first sub ps Ho:YAG oscillator was demonstrated in 2017 emitting pulses with a pulse width of 220 fs [290], the full results were published the following year in [291]. The authors reported an average output power of 18 W for the 220 fs pulses, which increased slightly to 270 fs during power scaling to 25 W of average output power. Such high power levels were achievable through the use of a thin-disk oscillator. This resonator arrangement allows for very effective cooling of the laser gain medium therefore significantly reducing the thermal issues often encountered at high pump power values in the range of ~ 100 W [290, 291]. However, these type of thin disk lasers generally have characteristically long cavity path lengths because multiple passes through the gain medium are required for the sought after high power output, again limiting the PRFs achievable.

Employing a waveguide geometry provides an elegant solution to obtain the short cavities required to achieve GHz PRFs. This is because tight confinement achieved in the waveguide ensures good overlap between the pump and signal beams, this combined with a small laser mode area results in low lasing thresholds and high gain over short material lengths. The cavity mirrors can be aligned directly at the end facets of the waveguide resulting in cavity lengths as short as a few mm. Here we demonstrate a QML Ho:YAG waveguide laser in which the laser outputs passively modelocked short pulses under the envelope of a Q-switch. The advantages and disadvantages associated with this QML regime have been discussed in sub-section 4.3.2. QML has been demonstrated in the past from ~ 2 μm waveguide lasers modelocked with a bismuth telluride based SA [292] and also a Graphene based SA [266]. The SA which has been utilised here is a Saturable Output Coupler coated with a few layers of Graphene. Sub-section 4.3.3 fully presents the application of Graphene as an SA, as a result of its characteristic low saturation fluence together with the waveguide cavity exploited, it has been placed directly at the end facet resulting in a cavity on the scale of a few mm and hence a high PRF greater than 1 GHz.

5.3.2 Fabrication of Graphene coated Saturable Output Coupler

Graphene was coated onto a standard output coupler which is 80% reflective in the wavelength range from 1.7 to 2.7 μm, this results in a double pass of the 1908 nm pump signal as 80% of it is reflected back into the cavity. The deposition of the graphene was performed by our collaborators based at the AFRL in Ohio, USA. It was carried out via transfer from commercially available graphene coated copper foil. The graphene-Cu foil was also coated with a layer of PMMA; this is to prevent any graphene being removed in error during the process. The copper itself was dissolved in diluted ferric chloride and then the graphene/plastic was placed on to the mirror surface after being rinsed with methanol and water. Finally the plastic was dissolved with acetone. This resulted in the mirror being coated with multiple layers of graphene; typically less than 10 layers at any place on the surface. A detailed description of the process used to produce the GSOC is given in [293]. The nonlinear transmission of the GSOC has been measured with an optical parametric amplifier operated at 2.1 μm which generated 100 fs pulses at a PRF of 1 kHz. The GSOC was placed in the path of the incident beam and the nonlinear transmission was calculated through the measurement of the transmitted power as a function of the input pulse fluence. The result is shown in Figure 5.11.

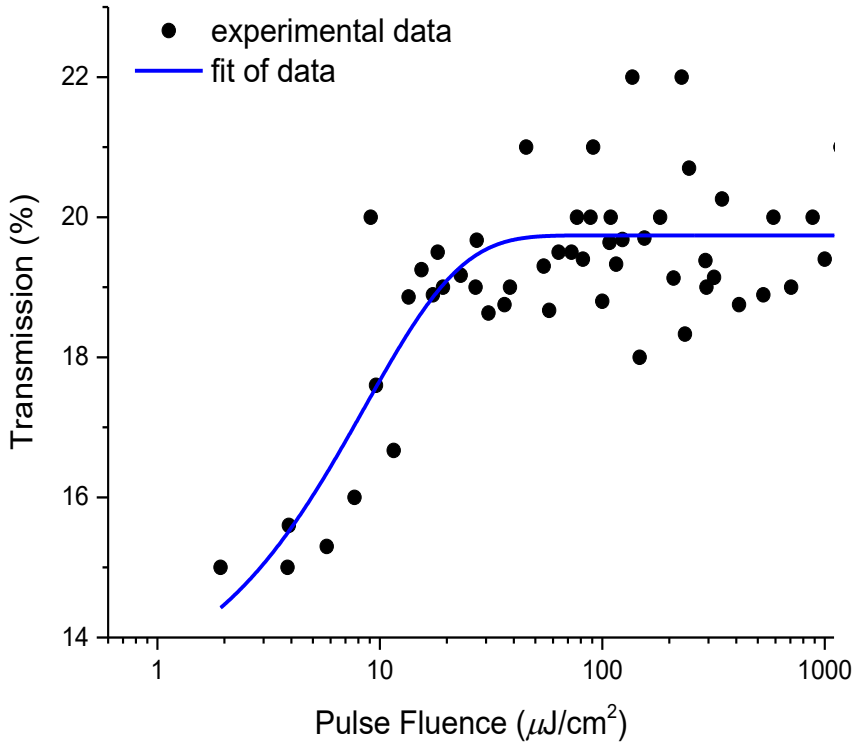

Figure 5.11. Graph of Nonlinear Transmission vs Pulse Fluence at 2.1 μm for 80% Reflective Graphene coated Saturable Output coupler.

From the fit applied to the data a value of the modulation depth of the GSOC is deduced to be ~ 6.6% and the nonsaturable loss is read from the graph as ~ 19.7%. The modulation depth is set by the thickness of the Graphene so can be controlled in this manner [195]. The nonsaturable loss value as read from the graph also accounts for the transmission of the output coupler and so it not an accurate representation of the nonsatruable losses of the Graphene coating itself. This is common to this type of Graphene coated SA mirror [265]. The GSOC has a measured saturation fluence of ~ 8.6 μJcm$^{-2,}$ which is typically lower compared to typical SESAMs in this wavelength region which tend to have a saturation fluence of 10-100s of μJcm^{-2} [189, 284].

5.3.3 Q-switched Modelocked Ho:YAG Waveguide Laser

The single mode waveguide presented in section 5.2 was used for this modelocking investigation. A very similar cavity to that in the CW characterisation was setup, the only difference being that the output coupler was replaced with the GSOC, maintaining the rather simple and compact nature of the resonator. A schematic diagram of it is shown in Figure 5.12.

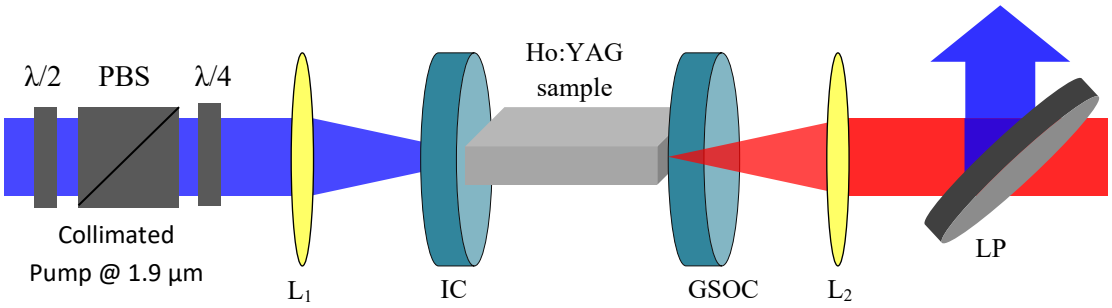

Figure 5.12. Schematic diagram of Q-switched modelocked Ho:YAG waveguide laser setup. L1 and L2 are 40 mm and 50 mm focal length lenses respectively, both AR coated for 1.65 to 3 µm. IC is the input coupler, GSOC is the Graphene coated saturable output coupler and LP is a 2 µm long pass filter.

As in the CW laser cavity, lenses L_1 and L_2 focus in the pump light and collimate the output respectively. The IC is the same as that utilised for the CW cavity, it is AR coated on the rear side for 1.7-2 μm, allowing for maximum coupling of pump light into the waveguides, and HR for 2.05-2.43 μm on the front side facing the Ho:YAG sample. The long pass filter, LP, filters out any unabsorbed pump light before measuring the laser output. As the GSOC was positioned very close to the output facet of the sample, care was taken to avoid contact with it, this is to minimise the cavity length whilst simultaneously protecting the graphene and the waveguides from damage. Precise alignment of the laser cavity, in particular the IC and the GSOC itself, resulted in pulsed operation of the Ho:YAG waveguide laser.

The RF spectrum of the laser output was observed first and is shown in Figure 5.13. It was measured using a Newport 12.5 GHz InGaAs photodetector with a quoted high speed rise time of < 28 ps, the model number is 818-BB-50. This was connected to a 13 GHz RF spectrum analyser, manufactured by Agilent with model number E4405B ESA-E. This graph indicated that there are pulses being emitted from the Ho:YAG laser with a PRF of about 5.860-5.865 GHz. With a cavity length of 14 mm and assuming a waveguide refractive index of 1.8, the theoretical value of the PRF of the cavity was calculated to be ~ 5.9 GHz, the experimentally measured value is thus in good agreement. As a number of peaks can be seen in the RF spectrum as opposed to one single narrow peak, this is the first indication that the laser is in the QML regime rather than the Continuous Wave modelocked regime.

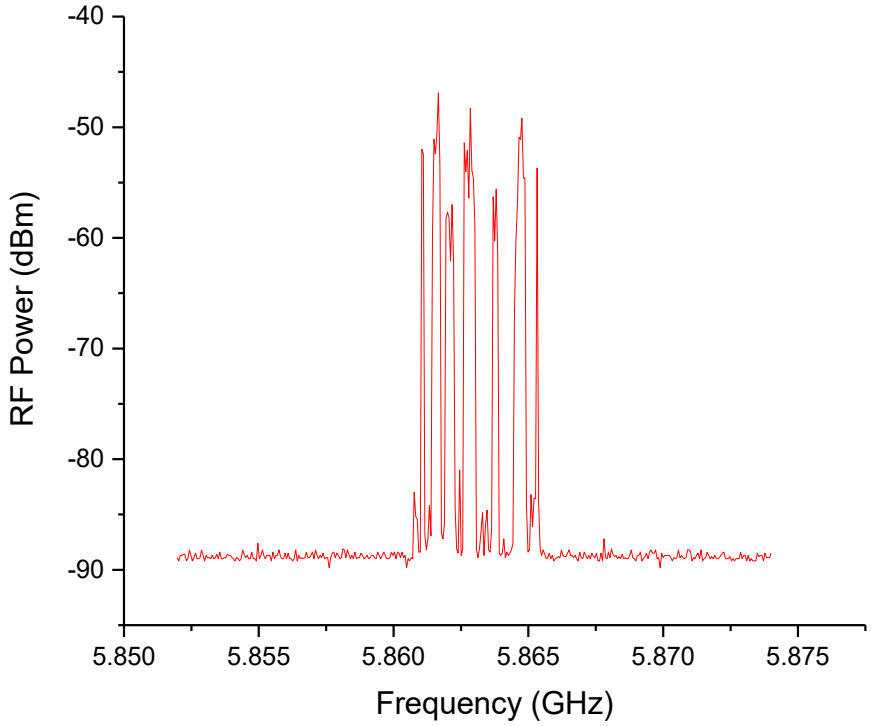

Figure 5.13. RF Spectrum of QML Ho:YAG waveguide laser; the graph has a span of 22 MHz and the measurement was taken with a resolution bandwidth of 1 kHz.

Figure 5.14 plots the average output power against the pump power. As can be seen by the linear fit in this graph the QML laser slope efficiency is 6.8% and at the highest incident pump power of 2.45 W, the maximum average power emitted was 170 mW. At a pump power of 2.7 W, damage to the Graphene was observed and as a result the damage threshold is estimated to be 1.6 μJcm^{-2}, the maximum pump power was therefore restricted to < 2.5 W to ensure the Graphene could not be damaged. There is a decrease in slope efficiency of around 3% when compared to the CW operation of this waveguide reported in section 5.2. This is most likely due to the extra loss incurred because of the gap between the GSOC and the waveguide output facet; it was found during CW investigations that the single mode waveguide produced the highest slope efficiencies when the cavity mirrors were as close to the sample as possible as this resulted in optimum alignment.

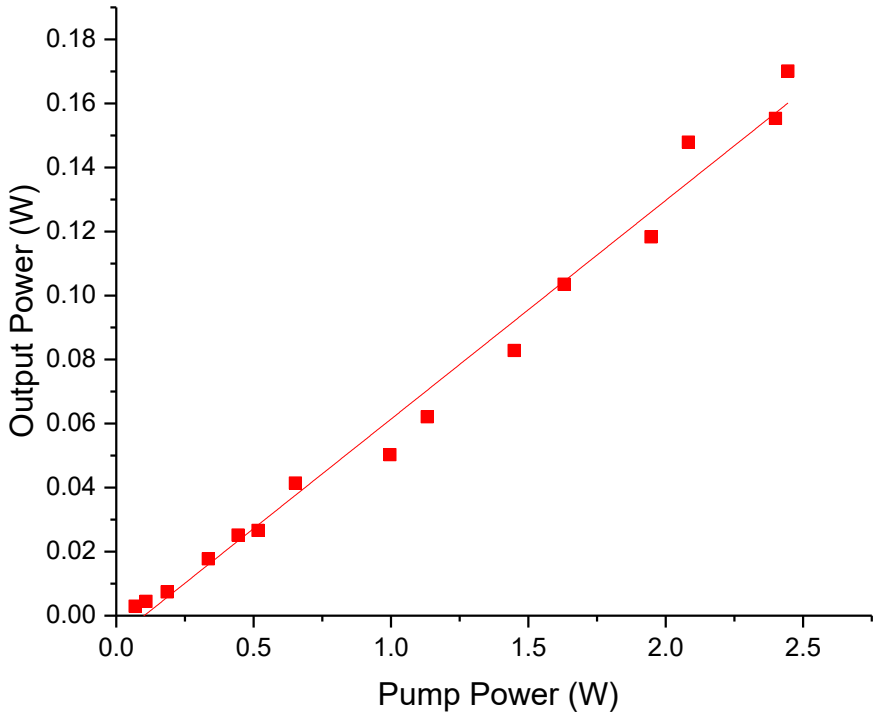

Figure 5.14. QML Ho:YAG waveguide laser average output power versus incident pump power, as in section 5.2. Fresnel reflections have been accounted for.

The Q-switched envelope is shown in Figure 5.15 on a microsecond scale of 2.0 μs per division. The repetition rate of the Q-switch is ~ 1.04 MHz resulting in a pulse energy of 0.16 μJ associated with each Q-switch envelope. The train of modelocked pulses emitted within the Q-switch envelope are shown in Figure 5.16 on a scale of 0.1 ns per division. The frequency of the pulses viewed on the oscilloscope corresponds with the peak on the RF spectrum in Figure 5.13. The pulse trains of both the modelocked and Q-switched pulses have been recorded with the Newport high speed photodetector described above and a 23 GHz Tektronix MSO/DPO72304DX oscilloscope.

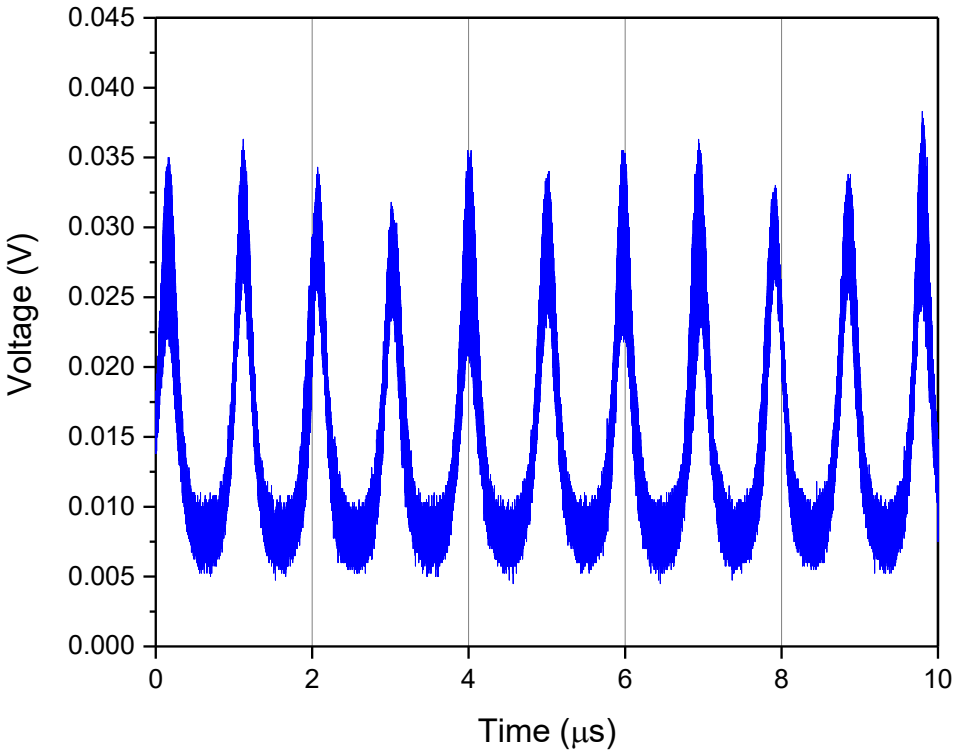

Figure 5.15. Oscilloscope trace of Q-switched pulse train emitted from QML Ho:YAG waveguide laser.

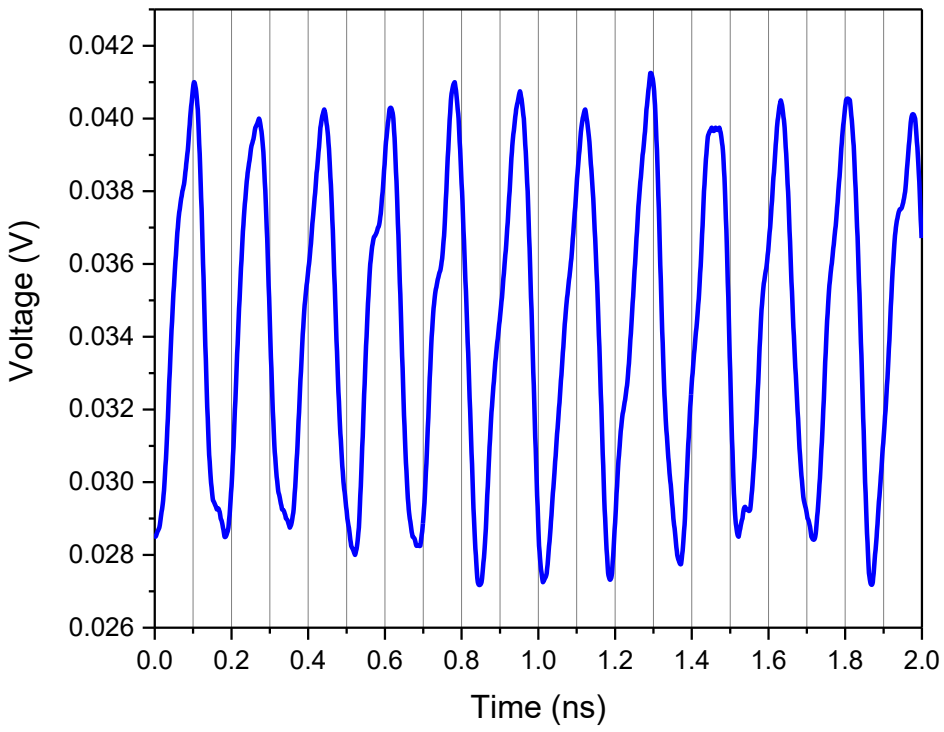

Figure 5.16. Modelocked pulse train emitted from QML Ho:YAG waveguide laser.

The laser spectral output is shown in Figure 5.17 and was measured with a Thorlabs Optical Spectrum Analyser (OSA205) with a resolution of 0.1 nm. The spectrum is centred at approximately 2090.5 nm and has a FWHM bandwidth of ~ 0.8 nm.

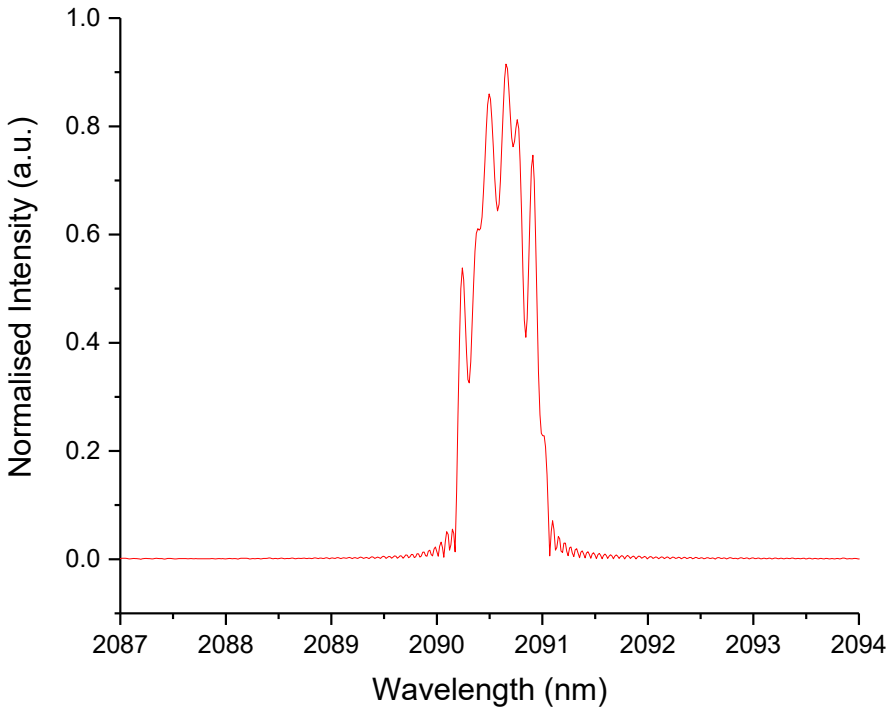

Figure 5.17. QML Ho:YAG waveguide laser spectral output.

The emission of both the pulses and Q-switch was found to be particularly stable at low powers for several hours, but if operated at high pump power > 2 W for more than ~ 30 minutes the laser became unstable with rapidly changing peak power, or in some cases it ceased to pulse at all. This is indicative of both; thermal issues due to heat accumulating inside the cavity and possible damage to the graphene itself after being irradiated for an extended time period. This suggests that the water cooling setup employed is not sufficient to dissipate the heat efficiently in the crystal for the higher pump power values. More effective cooling could be explored, for example; the sample mount could be redesigned to simply bring the flow of the coolant closer to the sample. However, it would be more beneficial to design the mount such that it surrounds the sample and provides 360º cooling rather than just underneath it, but this is challenging to implement in such a compact cavity. Another suggestion could be to investigate the use of Peltier cooling.

The QML regime behaviour observed from the laser can be verified using the stability criterion presented in sub-section 4.3.2. Equation (10) calculates an estimation of the intracavity pulse energy required to escape from the regime of Q-switching instabilities. The value of the critical pulse energy required to operate in the pure CW modelocked regime was estimated using the following procedure.

Equation (11) returns a value of $E_{sat,\,L} = 1.24\times10^{-5}$ J for the Ho:YAG material saturation fluence. In this estimation the emission and absorption cross section of this material at the signal wavelength are ~ 1.0×10^{-24} m^2 and 2.0×10^{-25} m^2 respectively, which are taken from [294]. The effective laser mode area is ~ 3.14×10^{-10} m. This value is calculated from the mode field diameter of the beam propagating in the waveguide which is estimated as ~ 20 μm from Figure 5.7. The GSOC saturation energy is calculated by equation (13) to be $E_{sat,\,A} = 2.70\times10^{-11}$ J. This is estimated using the measured saturation fluence of 8.6 μJcm^{-2} and assuming that the incident effective mode area is unchanged as it emerges from the waveguide. Although, in reality, the beam will diverge in the small distance between the end facet and the GSOC, this distance is very small so this assumption is justified for the purpose of this estimation. Finally the modulation depth was measured to be 6.6%.

Using these parameters, equation (10) estimates a value for the critical pulse energy $E_{P,c} \approx 4.70\times10^{-9}$ J. This is an order of magnitude greater than the maximum intracavity pulse energy E_P of the Ho:YAG waveguide laser which is calculated to be $\approx 1.45\times10^{-10}$ J using equation (14) implying the average output power capability of the laser would have to be some 30 × greater to escape the QML regime. This is in agreement with the experimental results as the laser output is well within the QML instabilities limit. For applications which would require the laser to be CW modelocked, strategies to cross the instability threshold include utilising a GSOC with a higher reflectivity value to increase the intracavity power attainable and also with a lower modulation depth to reduce the critical pulse energy value. Furthermore, a smaller diameter waveguide would in effect reduce the $E_{sat,A}$ and $E_{sat,L}$ parameters therefore also leading to a reduction in $E_{P,c}$. However, smaller waveguides tend to have higher associated propagation losses limiting the laser output power. In addition to this, thermal issues are encountered at much lower incident pump powers when utilising high reflectivity output couplers, therefore an optimum regime would have to be identified for the collective parameters.

To summarise, with careful tailoring of the both the ULI fabrication and GSOC parameters, the laser performance could be significantly improved to allow the cavity to reach the intracavity energies necessary to operate in the stable CW modelocked regime, whilst retaining the high PRF of the output.

It should be noted at this point that attempts were made to obtain a measurement of the pulse duration with a interferometric autocorrelation arrangement. Unfortunately, at this time it was not possible due to damage that occurred to the Graphene during this experiment. The results presented here so far do indicate that the laser is Q-switch modelocking, however, further testing is required to confirm the modelocking. Therefore, the work is continuing by optimising the design of new Graphene coated output couplers.

5.4 Summary

ULI has been utilised to fabricate several depressed cladding waveguide structures in a Ho:YAG crystal. The optimum parameters for inscription of a low loss single transverse propagating mode were identified. This waveguide was subsequently pumped in a waveguide laser resonator arrangement. The pump source was a CW 1908 nm Tm:fibre laser which was operated with circular polarisation and a maximum available power of 12 W. The CW Ho:YAG waveguide laser performance was fully characterised in terms of output power, spectral output and output mode quality. Four different output couplers where utilised in the power characterisation with reflectivity values ranging from 60-97% at ~ 2.1 μm; the emission wavelength of Ho:YAG. A maximum laser output power of ~ 1.78 W and slope efficiency of 16% was observed with the 70% R OC. A Caird analysis was performed estimating a value for the waveguide propagation loss of 1.02 $dBcm^{-1}$. The emission wavelength of the laser was centred at ~ 2090 nm for the lower reflectivity OCs and red shifted to 2091 nm for the 97% R OC as a consequence of the combined effects of the different coating of this mirror and the reabsorption effects which determine the inversion ratio dependent gain spectrum. The quality of the output laser mode was quantified by measuring the M^2 parameter in the horizontal and vertical dimensions as 1.48 and 1.75 respectively. Hence, it was concluded that this waveguide was sufficiently single mode to be utilised in modelocking investigations. Power scaling experiments of the ULI Ho:YAG waveguide laser were performed concurrently by our

colleagues based at the AFRL in Ohio, US. The result was a laser with a slightly higher output power of ~ 1.9 W and slope efficiency of 29%. However the output mode profile was multimode with an M^2 parameter of 4.88, therefore not suitable for modelocking. The CW single and multimode waveguide laser results were published in Applied Optics [282].

The single mode waveguide laser was then investigated for the generation of pulsed laser emission resulting in the first multi-GHz demonstration of a Ho:YAG laser. A thin film of Graphene coated onto a standard reflective output coupler (GSOC) replaced the regular OC in the waveguide cavity. The saturable absorption parameters associated with the GSOC were characterised by measurement of its nonlinear transmission vs incident pump fluence at 2.1 μm. With precise alignment of the laser cavity Q-switched modelocked behaviour was observed. This means that modelocked pulses were emitted under a Q-switch envelope. The short length of the resonator, 14 mm, ensured a multi-Ghz PRF of 5.9 GHz. The Q-switch operated with repetition rate of 1.04 MHz resulting in an associated energy of 0.16 μJ. The average output power from the QML laser was 170 mW measured at 2.5 W of incident pump power which was limited to this value to protect the graphene from damage. It has been presented that although the observed QML behaviour can be advantageous, in particular for subsequent amplification, in most cases it is undesirable. The QML behaviour has been verified with a stability criterion; the intracavity pulse energy required to operate in the pure CW modelocked regime was calculated to be an order of magnitude higher than that attainable by the Ho:YAG waveguide laser for the current conditions. Various methods which could result in operation in the CW modelocked regime have been discussed so that the full potential of this waveguide laser can be exploited. The results in this chapter have been published in Optic Express [295].

Chapter 6. Modelocked few-cycle, Hot Isostatic Pressed Cr:ZnSe Laser

6.1 Introduction

Transition metal doped II-VI semiconductors were introduced as active gain media in the mid-90s [24], since then they have become arguably the most favoured emission sources in not only the mid-IR, but also at longer wavelengths into the far-IR spectral region. This is because they provide a means to directly stimulate emission at wavelengths spanning 1.8-6 μm in the form of a compact solid-state laser source. Previously, emission in this spectral region tended to be dominated by rather bulky and complex, gas lasers as well as OPO setups based on down conversion of a near IR solid-state laser source. TM:II-VI lasers largely replaced these generation methods [21]. Despite laser diodes and QCLs also finding some success in this market [17, 18], they tend to be limited to small emission ranges compared to very broad bandwidths which are typical of TM:II-VI lasers. This is particularly advantageous for sensing applications as a broad tuneable source is suitable for detection of multiple substances compared to the use of many separate sources. The capability of these sources to generate ultrafast pulses is also very important as these are vital for wide-span, high powered mid-IR frequency combs which are ideal for use in the fingerprint molecular region [296]. In addition to this ultrafast, few cycle, mid-IR lasers find use in other applications including for example high harmonic/X-ray generation and high-precision material processing of semiconductors [285, 297-299].

Common examples of the type of II-VI semiconductors used as hosts for TM dopants for mid-IR emission include ZnSe, ZnS, CdMnTe and CdSe [24, 25]. These media are ideal as a choice for a host material due to their low phonon energy, wide band-gap, broad transmission range and a crystal structure which is readily acceptant of TM dopant ions [300]. The TMs are elements which lie on the periodic table between Scandium and Zinc. They are defined as having a partially filled d orbital. When doped into a crystal, the resultant spectral emissions are extremely sensitive to the local field of that host crystal. This sensitivity is a consequence of electron-phonon interactions. These interactions can occur because the outer 3d-electrons are unshielded permitting them to couple strongly to surrounding phonons. This leads to 3d-3d absorption and emission bands which are the transitions laser action is based on, the typical energy level diagram of such a crystal structure can be seen in Figure 6.1b). The strong

electron-phonon coupling also leads to the TM ions experiencing vibronic broadening of the energy transitions; the resultant broad emission bandwidths, often spanning 10s to 100s of nm, are characteristic of TM doped laser sources [301]. The most common example of such a broad emission profile from a TM doped solid-state laser is Ti:sapphire which has emission spanning ~ 680-1100 nm [302]. In the case of RE doped media, which chapters 3 and 5 of this thesis are centred on, the situation is different. The difference between TM and RE doped laser energy level transitions is highlighted in Figure 6.1.

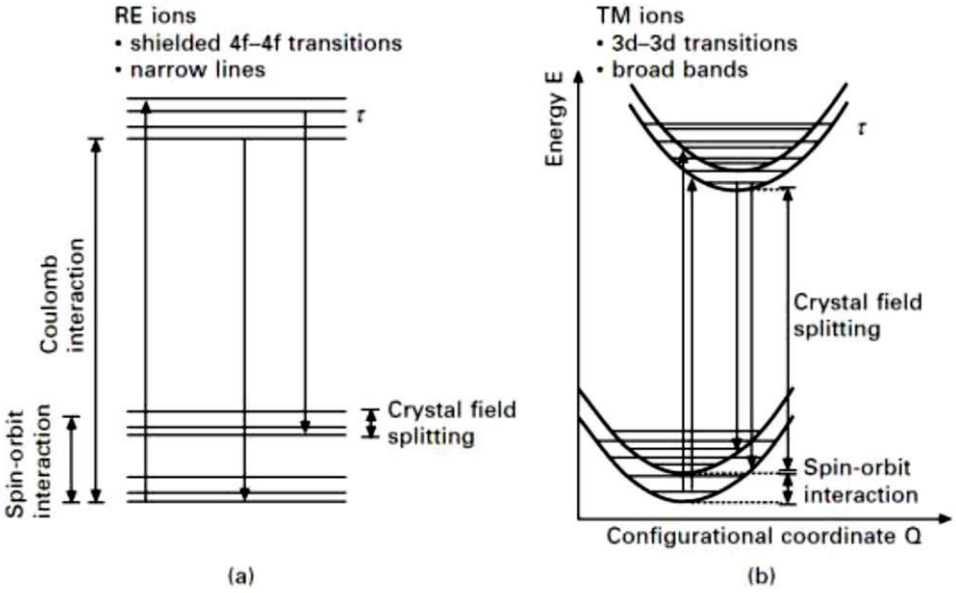

Figure 6.1. Energy level diagrams displaying the laser transitions in a) rare-earth and b) transition metal doped solid-state gain media. The electron-phonon coupling in b) is much stronger compared to a) leading to the broad emission profiles typical of TM lasers. Diagram has been reproduced from [301].

In RE doped solid-state media, shown in Figure 6.1 a) the 4d, 5s, 5p and 6s shells effectively shield the valence electrons which become excited into the 4f or 5d shells during the stimulated emission process, as a result the phonon coupling they experience is very weak relative to the case of TM ions.

When TMs are doped into the tetrahedral crystal field of an II-VI semiconductor such as ZnSe, the ^5D ground state of the dopant ion is split into a triplet $^5T_2$ level and a doublet ^5E level by crystal-field splitting. It is between these two vibronically broadened levels in which absorption/emission transitions are allowed leading to laser action, whereas transitions to higher levels are spin forbidden resulting in high gain with zero

ESA [303]. The broad emission profiles are not only due to the vibronic broadening, there is also a contribution from the Jahn-Teller effect [300]. This causes further splitting of the two electronic energy levels originating from a distortion of the crystal. The distortion itself occurs because the degenerate electronic ground state is unstable, hence the system seeks to remove the degeneracy by splitting into separate energy levels and forming a lower energy system. The full implications of the Jahn-Teller effect on TM:II-VI lasers are not fully agreed on within this field of research, but it is widely accepted that it does contribute to the broadening of energy transitions. More information on the Jahn-Teller effect on TM:II-VI media can be found in [304-306]. The combined effect of the vibronic broadening and Jahn-Teller effects discussed result in an approximate four level laser system [307].

The most well-known and commonly used combinations for laser emission in the mid-IR are ZnSe and ZnS doped with Fe^{2+} and Cr^{2+}. For simplicity these combinations are here on referred to as Cr:ZnSe and Cr:ZnS, as well as for Fe. Although Fe:ZnSe and Fe:ZnS are extremely useful for tuneable emission in the 3.4-5.2 μm range, to exploit this potential as a CW source it is necessary to cool the crystal down to ~ 150 K, otherwise they can operate as pulsed ns sources at room temperature [308]. As extensively covered in Section 5.1, cooling to such temperatures is disadvantageous as it adds considerable cost whilst also complicating the system. On the other hand Cr:ZnSe and Cr:ZnS have demonstrated excellent room temperature performance from CW to the fs regime. Furthermore, they have shown impressive tuneable performance spanning the range of 1973-3349 nm and 1962-3195 nm respectively [29]. The absorption and emission cross sections of these materials are displayed in Figure 6.2.

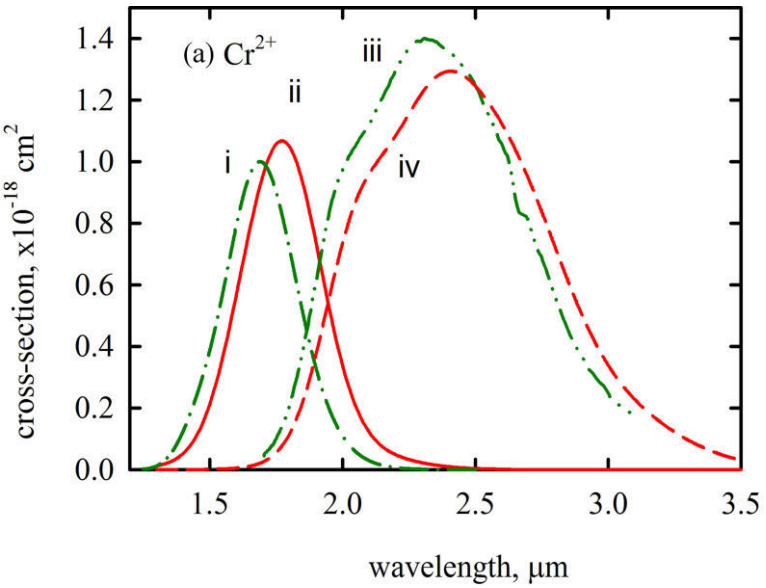

Figure 6.2. Curves i) and iii) represent the absorption and emission cross sections respectively in Cr:ZnS. Similarly ii) and iv) represent those in Cr:ZnSe. Diagram has been reproduced from [307].

This figure effectively demonstrates the broad emission/absorption profiles typical of TM:II-VI media which are due to both vibronic broadening and the Jahn-Teller effects previously discussed. The energy level splitting attributed to the Jahn-Teller effect in various Cr doped II-VI compounds has been investigated in [305]. The authors present that the ground state laser level $^5T_2$ is split by ~ 340 cm^{-1} and 300 cm^{-1} whereas the excited laser level ^5E is split to a lesser extent by ~ 40 cm^{-1} and 60 cm^{-1} in Cr:ZnSe and Cr:ZnS respectively. It can be seen from the absorption bands in Figure 6.2, for emission in the mid-IR these materials can be pumped with sources ranging ~ 1.4 – 2.1 μm. Therefore they are most commonly pumped with commercially available ~ 1.9 μm and ~ 1.5 μm Tm and Er fibre lasers, diode pumping has also shown success but these tend to have lesser beam quality limiting the efficiency in comparison [309, 310].

Despite the wide availability of suitable high powered pump sources, until fairly recently power scaling efforts were hampered by strong thermal lensing due to the large thermo-optic coefficients associated with ZnS/ZnSe. The origin of the thermal lensing issues will be detailed later in this section. However, a novel technique of scanning the coaxial laser mode and pump beam across the laser crystal at high speed has allowed for the demonstration of 140 W of CW output power with an optical efficiency of 62% from a Cr:ZnSe crystal [30]. ULI waveguides have also been exploited to mitigate the thermal lensing issue. Depressed cladding waveguide structures have been inscribed in both Cr:ZnSe and Cr:ZnS which have led to extremely compact, robust room

temperature waveguide laser sources with CW output powers up to 5.1 W [38] and 101 mW [264] respectively, where the latter was limited only by the available pump power. Cr:ZnSe waveguide lasers have also shown continual tunability from 2080-2883 nm [271], the broadest range to date demonstrated by a waveguide laser.

With regards to emission in the modelocked regime, the broadband spectral emission capability of Cr:ZnSe/ZnS has led to these crystals being considered as the "Ti:sapphire of the mid-infrared" [308]. Ti:sapphire has demonstrated the emission of pulses with durations as short as 5 fs [54], similarly should the entire bandwidth of Cr:ZnSe be used to emit modelocked pulses, there is the potential for the generation of only 6 fs $sech^2$ profile pulses. To date, no one has reported modelocking of the full bandwidth of either crystal but various SA's and modelocking techniques have been successfully implemented with these materials to result in ultrafast pulses. The first modelocked demonstration from these materials was reported in 2000 utilising an AOM to modelock a Cr:ZnSe crystal resulting in 4.4 ps pulses [311]. A summary of some of the most notable results obtained since then in Cr:ZnSe/ZnS media with the different modelocking and GDD compensation methods is presented in Table 6.1.

Saturable Absorber Type	Pulse Duration	Pulse Repetition Frequency	GDD Compensation Method	Laser Average Output Power	Reference	Year reported
Cr:ZnSe						
AOM	4.4 ps	81 MHz	none	82 mW	[311]	2000
SESAM	11 ps	100 MHz	none	400 mW	[312]	2005
SESAM	100 fs	200 MHz	Sapphire window	75 mW	[190]	2006
SESAM	80 fs	180 MHz	Chirped mirrors	80 mW	[225]	2007
Kerr-lens	100 fs	100 MHz	YAG window	300 mW	[313]	2009
Graphene based SA	226 fs	77 MHz	CaF prism pair	80 mW	[221]	2013
Combination of Graphene and Kerr-lens	116 fs	99 MHz	CaF prism pair	66 mW	[314]	2014
Kerr-lens	43 fs	83 MHz	Dispersive mirrors**	250 mW	[213]	2014
Kerr-lens	47 fs 60 fs	150 MHz 300MHz	Chirped mirrors	300 mW 250 mW	[208]	2017
Kerr-lens	45 fs	65 MHz	Dispersive mirror** and sapphire plate	500 mW	[214]	2019

Cr:ZnS						
Graphene based SA	41 fs	240 MHz	Chirped mirror and YAG wedge pair	75 mW	[315]	2014
Kerr-lens	29 fs 38 fs	100 MHz 300 MHz	Dispersive mirrors**	440 mW 700 mW	[212]	2015
Kerr-lens	41 fs	79 MHz	Dispersive mirrors **	1.9 W	[316]	2015
Kerr-lens	50 fs*	1.2 GHz	Dispersive mirrors**	120 mW	[210]	2016
* estimated pulse duration , no temporal measurement made ** dispersive mirrors is listed when the technology employed to control the dispersion value of the mirror has not been specified						

Table 6.1. A table summarising notable results in the modelocking of Cr:ZnSe/ZnS lasers with different modelocking mechanisms and dispersion compensation methods.

It is apparent from Table 6.1 that KLM coupled with optimum GDD compensation has led to generation of the shortest pulses. Until this work, the shortest pulses emitted from Cr:ZnSe were in the range 43-47 fs as reported in [208, 213, 214], whereas in Cr:ZnS a shorter pulse duration of ~ 29 fs has been demonstrated [212]. Both these resonators utilise KLM as the choice of SA and dispersive/chirped mirrors for GDD compensation. With regards to repetition rate, no GHz fs sources have been reported in Cr:ZnSe, the highest PRFs demonstrated are ~ 300 MHz and the pulse width tends to increase at higher PRFs as demonstrated by Yang et al. [208]. However PRFs of up to ~ 1.2 GHz have recently been observed from a Cr:ZnS oscillator with an estimated pulse duration of 50 fs [210] showing the potential for high PRF fs pulse generation in these materials. KLM has also facilitated improvements in the average output power with up to ~ 2 W demonstrated from Cr:ZnS [307, 316] and up to ~ 0.5 W from Cr:ZnSe [214], whereas this tends to be limited to ~ 100 mW when physical SAs such as Graphene or SESAMs are utilised. This is not unexpected as, theoretically, Cr:ZnS is favourable for high powered emission compared to Cr:ZnSe owing to its superior thermal properties. Both ZnSe and ZnS have relatively high thermo-optic coefficients of 70×10^{-6} K^{-1} and 46×10^{-6} K^{-1} respectively, compared to, for example, 7.3×10^{-6} K^{-1} in YAG. This leads to significant thermal lensing effects detrimental to laser cavity power scaling efforts. However, ZnS has a higher thermal conductivity of 0.27 $Wcm^{-1}K^{-1}$ compared to 0.18 $Wcm^{-1}K^{-1}$ in ZnSe therefore is able to distribute heat more efficiently away from the laser mode which forms the thermal lens within the laser crystal. This, together with the smaller thermo-optic coefficient value in ZnS, reduces the impact of any thermal lensing instability thus this host is preferential for high power emission. ZnS is also more suitable for power scaling due to its higher damage threshold of 1.5 Jcm^{-2}

compared to 0.5 Jcm^{-2} in ZnSe. The differences in the material properties important for lasing in each host crystal are summarised in Table 6.2.

Material Parameter	ZnSe	ZnS
Transparency range	0.5 – 20 μm	0.4 – 14 μm
Emission bandwidth (FWHM) doped with Cr (see Figure 6.2)	2.0 – 2.8 μm	1.9 – 2.7 μm
Refractive index at 2.4 μm	2.45	2.27
Thermal conductivity	0.18 $Wcm^{-1}K^{-1}$	0.27 $Wcm^{-1}K^{-1}$
Thermal expansion	7.3 $\times 10^{-6}$ K^{-1}	3.4 $\times 10^{-6}$ K^{-1}
Thermo-optic coefficient (dn/dT)	70 $\times 10^{-6}$ K^{-1}	46 $\times 10^{-6}$ K^{-1}
Damage threshold	0.5 Jcm^{-2} [317]	1.5 Jcm^{-2} [317]

Table 6.2. Material properties of ZnSe and ZnS laser crystals. Parameters gathered from [32]unless otherwise indicated.

A potential advantage that Cr:ZnSe holds over Cr:ZnS is that it emits ~ 100 nm further into the mid-IR which can be beneficial dependent on the specific application. In addition, Cr:ZnSe has a longer upper laser lifetime at room temperature, this is potentially beneficial for superior laser performance at room temperature but this is also dependent on a range of other factors in the set-up. This is demonstrated in Figure 6.3 in which the temperature dependence of the lifetime for each crystal is shown, a curve for Ti:sapphire is also included for reference.

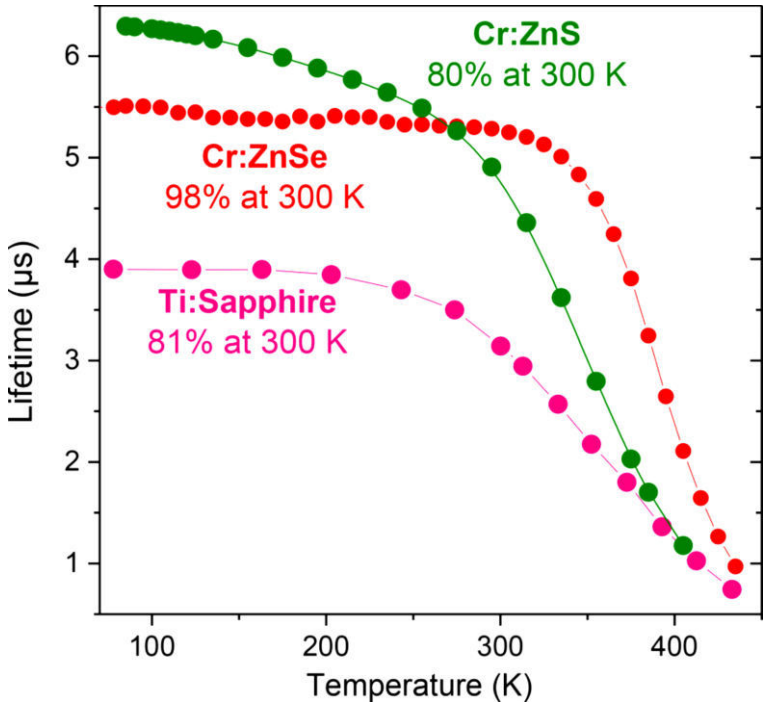

Figure 6.3. Temperature dependence upper state lifetime as a function of temperature for Cr:ZnSe, Cr:ZnS and Ti:sapphire. Graph has been reproduced from [299].

Cr:ZnS sees a 20% reduction in its lifetime at room temperature ~ 300 K and as a result exhibits a lower lifetime of 4.7 μs compared to 5.4 μs in Cr:ZnSe – this may lead to lower lasing thresholds for Cr:ZnSe [299]. Furthermore, the fast lifetime drop of Cr:ZnS beyond 300 K can present a challenge for laser operation in the event of high thermal loads. However, the success of Ti:sapphire as a laser crystal has not been hampered by having a similar drop of rate implying this should not significantly limit the performance of Cr:ZnS.

Despite Cr:ZnS exhibiting many favourable mechanical material properties over Cr:ZnSe, it can been seen from Table 6.1 and the literature that the majority of modelocking and CW investigations have been carried out in Cr:ZnSe. This is due to the fact that until the last decade or so, it has been difficult to fabricate low optical loss ZnS crystals doped with Cr [318]. This justifies why much of the research output was concentrated on Cr:ZnSe until the methods of fabricating improved quality Cr:ZnS were developed through the thermal diffusion of Cr ions into already grown high quality polycrystalline ZnS [308]. It is worth noting here that both Cr:ZnSe and Cr:ZnS are available in both single crystal and polycrystalline form, however the fabrication of high optical quality crystals with sufficient doping levels for lasing applications is difficult to achieve. In comparison, post-growth thermal diffusion doping of polycrystalline media has led to the ability to produce low loss, high quality, highly and uniformly doped II-VI semiconductor based laser gain media on a commercial scale [308]. As a consequence, the bulk of the laser application investigations in Cr:ZnSe and Cr:ZnS , have been carried out in polycrystalline materials, thus the samples utilized in all experiments presented in this Chapter are all polycrystalline. The advantages and disadvantages of both Cr:ZnS and Cr:ZnSe have been discussed here at length. It is therefore concluded at this point that it is necessary to continue research and development into both in order to fully exploit the favourable parameters of each crystal.

As ULI has facilitated the development of robust, efficient and extremely compact Cr:ZnSe laser sources which effectively eliminate thermal lensing effects, these may provide an ideal method of achieving a GHz modelocked source. Experiments exploring the use of a commercial SESAM in combination with a single mode depressed cladding Cr:ZnSe waveguide laser have been performed by a previous member of the NLO group in [271] and also partly presented by colleagues from the AFRL in [319]. The authors

claimed at this time that the waveguide laser emitted ~ 1.5 ps pulses at a PRF of 960 MHz and ~ 0.6 ps pulses at the reduced PRF of 308 MHz. The autocorrelation trace and corresponding wavelength spectrum obtained for the two different PRFs are shown in Figures 6.4 and 6.5.

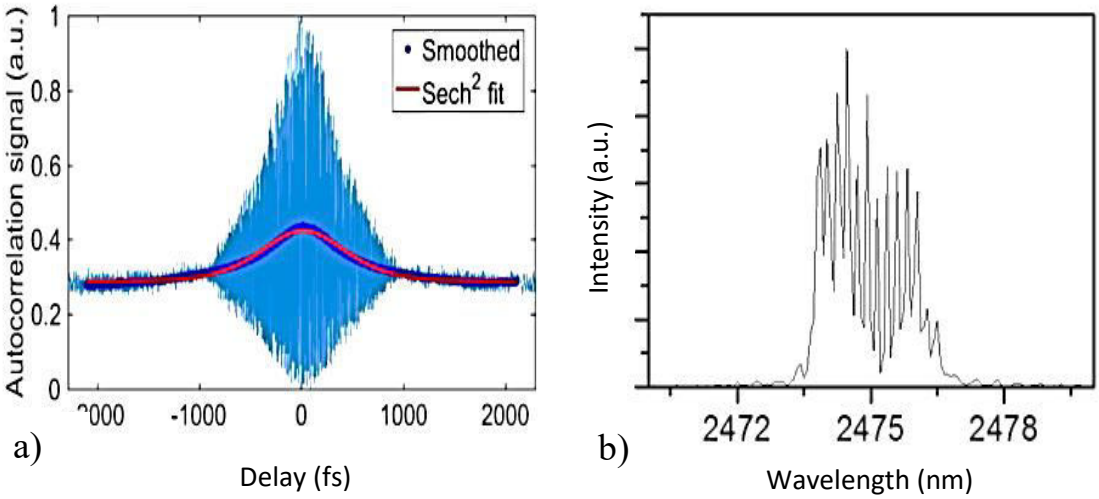

Figure 6.4. a) Autcorrelation trace and b) Wavelength spectrum obtained from SESAM modelocked Cr:ZnSe ULI waveguide laser at 308 MHz. a) measures a pulse duration of 0.6 ps. Graphs have been reproduced from [319].

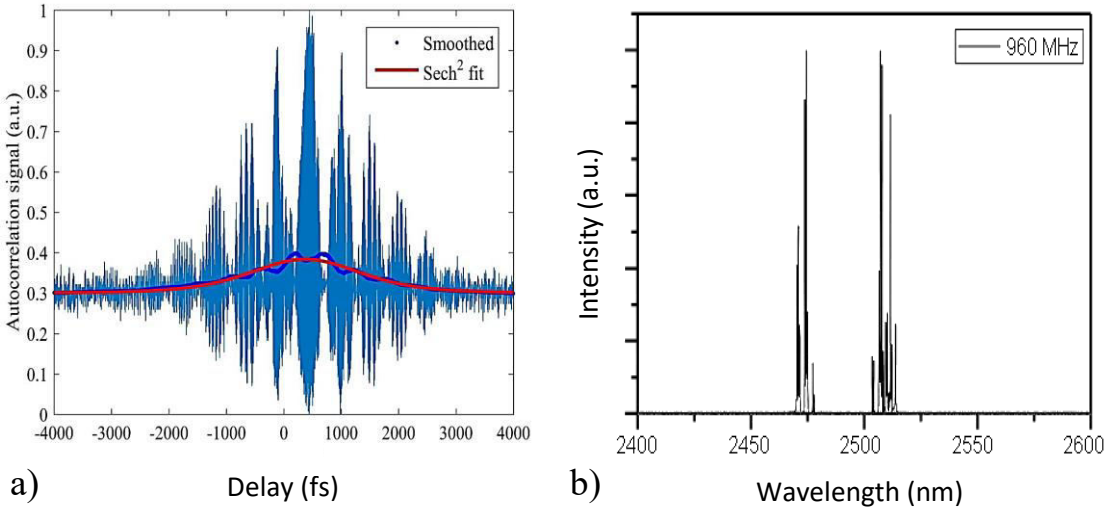

Figure 6.5. a) Autcorrelation trace and b) Wavelength spectrum obtained from SESAM modelocked Cr:ZnSe ULI waveguide laser at 960 MHz. a) measures a pulse duration of 1.5 ps. Graphs have been reproduced from [271].

It can be clearly seen from Figures 6.4 a) and 6.5 a) that in both cases the autocorrelations traces presented do not exhibit the 8:1 peak to wing ratio required as described in section 4.3.9. The trace in Figure 6.5 a) also exhibits an interference effect

not common to standard autocorrelation traces. This explained by the suggestion of interference of the two different emission bands which appear in the corresponding wavelength spectrum in Figure 6.5 b). Although these results are indicative of mode beating occurring in the cavity, further investigations are required to clarify if the laser is indeed operating in the CW modelocked regime and why the pulse measurements do not have the correct ratio.

Simultaneous to this work, our colleagues at the AFRL also reported significant results concerning the use of Hot Isostatic Pressing Treatment on TM:II-VI materials [320]. This paper presents results of utilising HIP for both the actual diffusion of the TMs into the host and as a post dopant treatment to an already diffusion doped sample. In both cases the result is that the laser spectral linewidth in a bulk resonator is reduced from spanning typically 10s of nm to sub-nm levels, this will be explained more fully in section 6.2. Consequently, efforts were aimed at inscribing ULI waveguides in HIP treated Cr:ZnSe and utilising a SESAM to compare results to the untreated material with the aim of developing a high PRF source. However, it was found that the waveguide inscription parameters for the untreated material resulted in high loss waveguides in HIP treated material. Therefore investigations into identifying the optimum parameters are ongoing. As a consequence of this, and also the recent results exploiting KLM in Cr:ZnSe shown in Table 6.1, we postulated that investigating the use of bulk HIP treated Cr:ZnSe with KLM would be useful to assess its performance for the generation of fs pulses compared to untreated bulk Cr:ZnSe. Hence this could enhance understanding of the full effect of the HIP treatment. The next two sections will present results of a HIP treated Cr:ZnSe bulk laser in the CW and KLM regimes respectively.

6.2 CW Operation of HIP treated Cr:ZnSe laser

HIP is a material treatment process in which both high temperature and pressure, typically > 100 MPa and 500ºC respectively, are applied concurrently to a material in a container designed to withstand such conditions [321]. In general, HIP treatment has been used to improve the mechanical properties of metal based materials for applications such as upgrading castings and consolidating powders [320, 321]. However, it has also found use in some optical applications for the manufacture and

preparation of ceramic laser crystals [322]. Specifically for the case of materials used in TM:II-VI semiconductors, HIP treatment has previously been shown to grow the grain sizes in undoped ZnSe [323] and latterly it was shown that it can also remove defects in Cr:ZnSe [324]. Most recently, Stites et al. published a report in which they describe the process of utilising HIP treatment to force-diffuse Cr ions which were sputtered on to a ZnSe host surface [320]. The samples were held in argon gas at 1050°C at 30,000 PSI for two hours. This ultimately results in extremely narrow, < 140 pm, linewidth laser output from a standard z-fold bulk laser cavity. They also demonstrate that the narrow linewidth occurs when a commercially bought sample of Cr:ZnSe is HIP treated, proposing that the reason for the spectral narrowing is that the HIP treatment converts inhomogeneously broadened material to homogeneously broadened material. The treatment causes this conversion by acting to remove crystalline defect centres and growing the grain size thus reducing the number of grain boundaries in the crystal. These are believed to be the sources of strong inhomogeneous broadening exhibited in commercially available untreated polycrystalline Cr:ZnSe [320]. The effect has also been demonstrated in a Fe:ZnSe bulk laser [325].

The modelocking investigation which is presented in section 6.3 has been carried out in collaboration with colleagues based in Politecnico di Milano. Prior to these experiments, a preliminary CW characterisation of a HIP treated Cr:ZnSe crystal was carried out in our labs at HWU where we have a 1.9 μm Thulium doped fibre pump laser. The results of this initial CW investigation will be presented first.

6.2.1 HIP Treated Cr:ZnSe Laser pumped at 1.9 µm

The Cr:ZnSe sample utilised in this experiment had dimensions 3 × 6 × 7 mm and a dopant concentration of 6.05×10^{18} cm^{-3}. The sample was fabricated by IPG photonics and subsequently treated with HIP. The HIP process is as follows: the sample was sealed within a chamber designed to withstand high temperatures and pressure, subsequently the temperature and pressure were raised over the course of two hours to values of 1050ºC and 30,000 PSI respectively. Inert argon gas was used as a buffer for the isostatic process. The samples were then held at these temperature and pressure for two hours before temperature reduction and gas ventilation over an additional two hours. The laser setup implemented was that of a standard linear z-fold bulk laser cavity as shown in Figure 6.6.

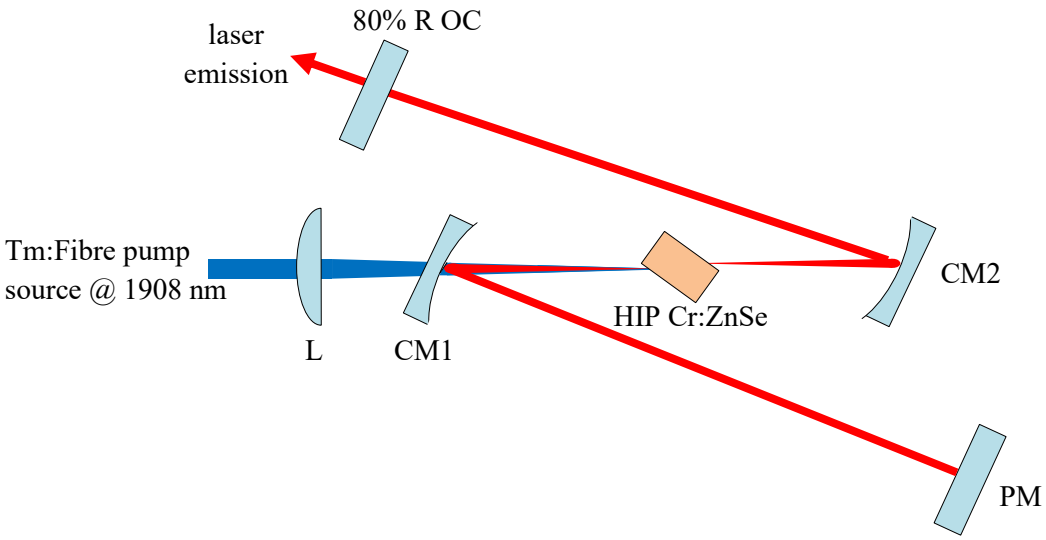

Figure 6.6. Schematic diagram of CW HIP Cr:ZnSe bulk laser pumped at 1.9 µm. L is a plano-convex 10 cm focal lens AR coated at 1.65 – 3 µm. CM1 and CM2 are plano-concave curved mirrors with 50 mm ROC and HR on the concave face for 2.3 – 2.8 µm, PM is a plane mirror HR for 2 – 3 µm and 80 % R OC is an output coupler which is 80% reflective for 1.7 – 2.7 µm

The sample was placed at Brewster's angle at the focus between the plano-concave mirrors; CM1 and CM2, propagation occurred through the 7 mm length in order to maximise the gain. CM1 and CM2 set cavity folding angles of ~ 22º as this was the experimentally estimated angle which optimally compensated for the astigmatism imposed on the cavity by the Brewster angled faces of the crystal. The pump source is the same as that used in chapter 5; a 20W linearly polarised Tm:fibre laser operating at 1908 nm. The pump entered the cavity through the rear face of the CM1 and was focused into the laser crystal by the lens, L. The distance between both CM2→OC and CM1→PM is 12.5 cm, this distance arbitrarily chosen in this initial lasing attempt. The output coupler utilized was 80% reflective for 1.7 – 2.7 μm.

A graph of the HIP Cr:ZnSe bulk laser output power versus incident pump power is given in Figure 6.7. The power values were measured with the Spectra-Physics thermal power meter (model number 407).

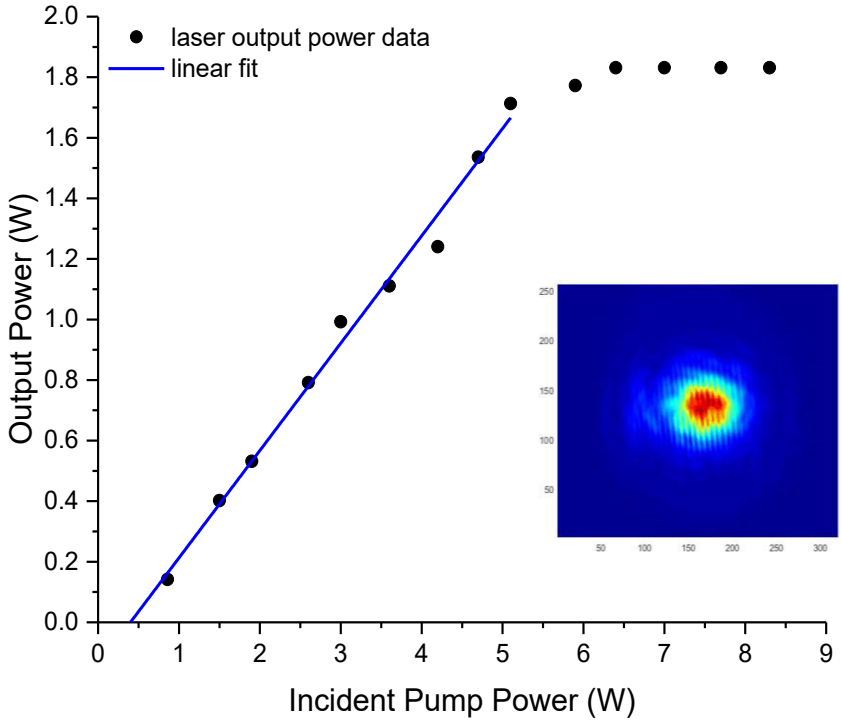

Figure 6.7. Graph of incident pump power versus output power of CW HIP treated Cr:ZnSe laser with an 80% R OC pumped at 1.9 µm. The inset image shows the far field output mode image in a 300 × 250 µm image.

The maximum output power observed was 1.83 W when pumped with 6.4 W, for output powers greater than this thermal rollover was observed as can be seen in Figure 6.7. There was no active cooling in place for the sample in the setup therefore, the addition of some cooling could improve the performance at higher pump powers > 6.4 W. Neglecting the last 5 data points in the region of thermal rollover, the laser has a slope efficiency of ~ 35.5% and lasing threshold of 399 mW. The inset image shows the far field output mode image which was observed with the FLIR SC7000 mid-IR camera to monitor the astigmatism imposed by the Brewster faces of the crystal. Note the vertical lines seen on the image are due to a stack of neutral density filters placed in the beam path to protect the camera detector from damage.

The spectral output of the HIP Cr:ZnSe laser was characterized with a Thorlabs OSA (OSA205) which has wavelength range: 1 – 5.6 μm and a resolution of 140 pm at the signal wavelength. The spectrum observed from the HIP Cr:ZnSe bulk laser can be seen in Figure 6.8, this spectrum was observed for a laser output power of 0.99 W when pumped with 3 W.

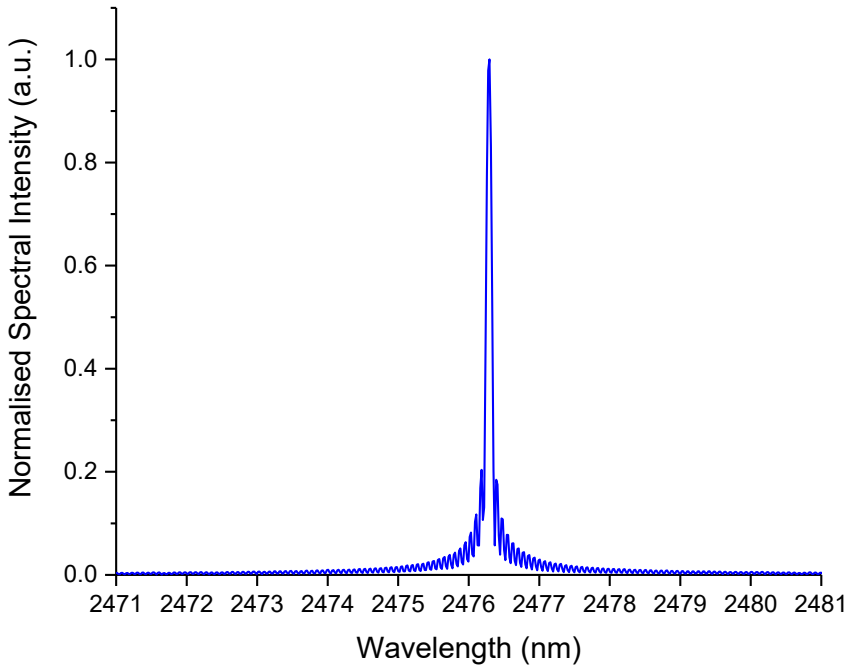

Figure 6.8. Normalised wavelength spectrum emitted by HIP treated Cr:ZnSe laser pumped with 1.9 µm. The measurement was taken at a pump power of 3 W and laser output power of 0.99 W.

The spectrum in Figure 6.8 is centred at ~ 2760.3 nm and has a FWHM linewidth of 140 pm limited by the resolution of the OSA. This linewidth is significantly narrower than the typical bandwidth emitted from free running Cr:ZnSe lasers reported in the literature. An example of the spectral emission from such a free running untreated Cr:ZnSe laser is shown in Figure 6.9. It has a FWHM linewidth spanning ~ 20 nm, thus proving the HIP treatment has significantly narrowed the spectral emission as expected by the results reported by Stites et al in [320].

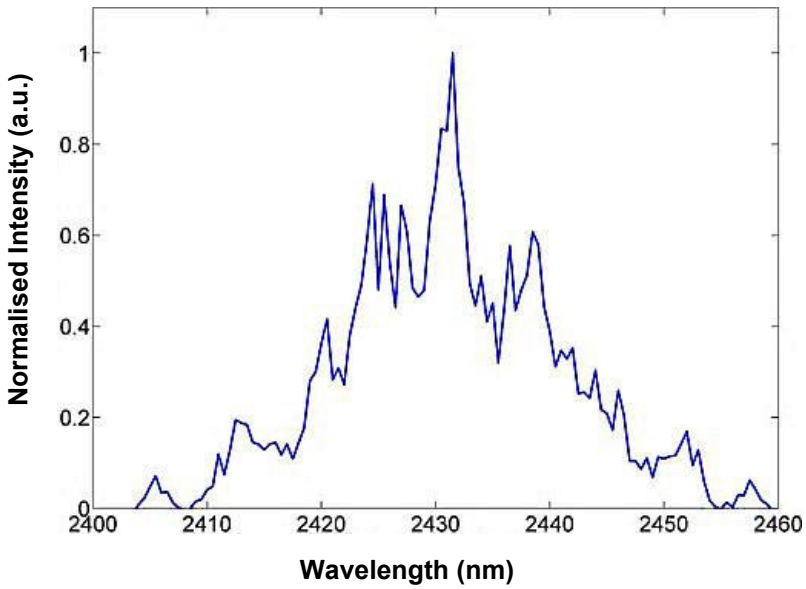

Figure 6.9. Broad spectral emission of a typical free running Cr:ZnSe bulk laser. Graph reproduced from [320].

This preliminary experiment confirmed that the HIP treatment had converted our sample from an inhomogenously to homogeneously broadened crystal. The next step of the work was to investigate HIP treated Cr:ZnSe for modelocking. This modelocking investigation which is presented in section 6.3 was carried out at our collaborators lab in Politecnico di Milano. In this lab the pump source available was a 1.57 μm Erbium doped fibre laser therefore the sample utilised for modelocking was initially characterised for CW operation with this pump. These results are presented in the following sub-section.

6.2.2 HIP treated Cr:ZnSe Laser pumped at 1.57 µm

The Cr:ZnSe sample to be investigated for modelocking had dimensions 2 × 3 × 7 mm with a dopant concentration of 1.05×10^{19} cm^{-3}, it was fabricated by IPG photonics then subsequently treated with HIP. The HIP Cr:ZnSe crystal was utilised in the linear x-fold bulk laser cavity shown in Figure 6.10. This x-shape was chosen over the z-shape utilised in the previous sub-section due to space constraints of the curved mirror mounts. For modelocking, the ultimate aim is to generate high PRFs thus we sought to minimise the cavity length by employing smaller focal length curved mirrors. The mounts would only fit to correctly compensate the astigmatism by using an x-fold shaped cavity.

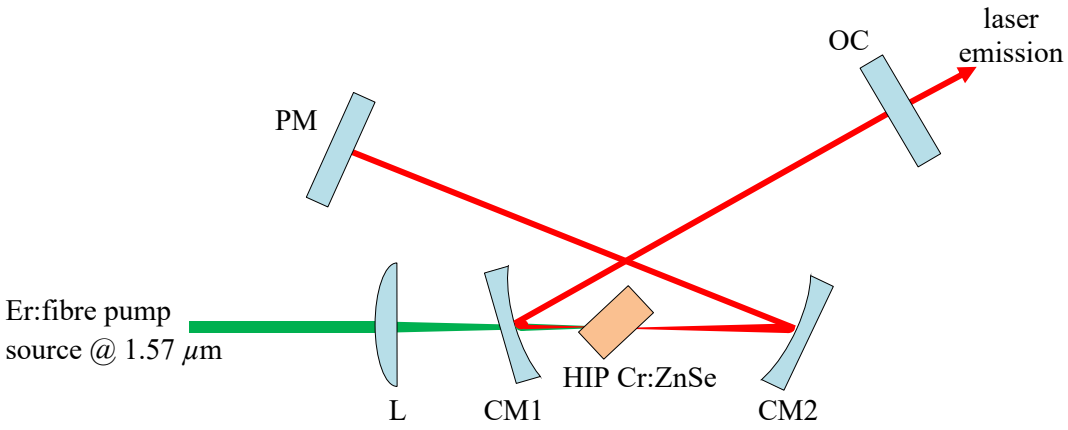

Figure 6.10. Schematic diagram of bulk laser cavity configuration for CW characterisation of HIP treated Cr:ZnSe pumped at 1.57 μm. L is a 50 mm focal length plano-convex lens AR coated for 1050 – 1700 nm, PM is a plane mirror which is HR for 2.3 – 2.6 μm and OC is the output coupler. CM1 and CM2 are plano-concave mirrors with ROCs of 30 and 50 mm respectively, both are HR for the signal wavelength.

The pump source in this case is a linearly polarised CW Er:fibre laser (IPG Photonics, ELR-LP-20), with maximum output power availability of 5.5 W. CM1 is a plano-concave mirror with a 30 mm radius of curvature (ROC) HR, > 99.5%, coated for the range 2.3 – 2.6 μm. CM2 is also a plano-concave mirror but has an ROC of 50 mm and is HR, > 99% from 2.3-2.8 μm. PM represents a plane mirror HR, >99.5%, for 2.3 – 2.6 μm and OC represents the output coupler. The sample is again placed at Brewster's angle relative to the input pump beam, at the point of focus between the plano-concave mirrors and the pump beam is focused into the crystal through CM1 with lens L. CM1 and CM2 set folding angles of 17º in both arms of the cavity, which is the angle calculated by numerical simulations, based on ABCD matrices, to compensate for astigmatism imposed on the cavity by the Brewster-angled surfaces of the crystal. The distance between CM2 →PM is 31 cm and from CM1→OC is 50 cm resulting in a total cavity length of approximately 85 cm. CM1 is not optimised for transmission of the pump wavelength through the rear face and allows transmission of 74%. This has been accounted for in the incident pump power levels quoted in the results. Propagation occurs through the 3 mm length of the crystal which was not actively cooled in this CW characterisation, therefore the pump power was limited to < 1 W to reduce any detrimental thermal effects on the laser performance. We characterised the power performance of the laser with two different output couplers: one coated for 97% reflectivity at 2.05 – 2.43 μm (97% R OC) and one for 80% reflectivity for 1.7 – 2.7 μm (80% R OC). The CW laser output power versus the incident pump power for both OCs

is displayed in Figure 6.11. Both were measured after propagation through a 2 μm long pass filter using a Thorlabs thermal power sensor with model number S401C, designed for detection in the wavelength range 0.2 – 10.6 μm.

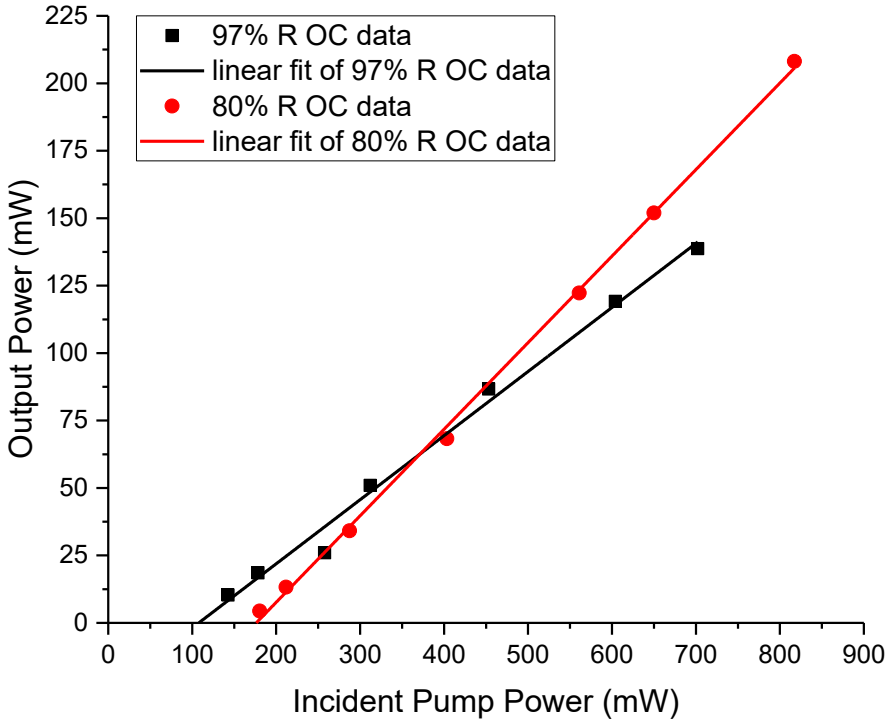

Figure 6.11. Graph of incident pump power versus output power of CW HIP treated Cr:ZnSe laser for 80% and 97% reflectivity output couplers.

With the 80% R OC the maximum output power was 208 mW measured for a pump power of 817 mW, the slope efficiency was 32% and the threshold was 177 mW. For the 97% R OC the laser threshold was 108 mW and the slope efficiency was 24%. The maximum output power obtained in this case was 139 mW for a pump power of 702 mW, it was decided not to increase pump power beyond this due to the lack of active cooling and increased intracavity power with this output coupler.

The wavelength spectrum emitted by the HIP Cr:ZnSe laser was measured with an extended InGaAs array near-IR spectrometer operating in the wavelength range from 0.9 – 2.55 μm, it was manufactured by Ocean Optics Inc. with model number NIRQuest512-2.5. The normalised wavelength spectra measured with both output couplers are shown in Figure 6.12.

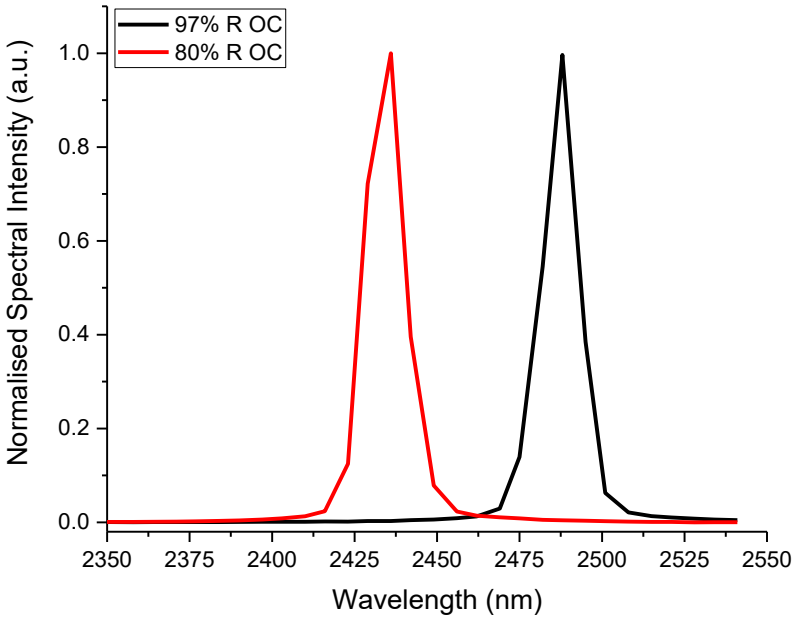

Figure 6.12. Normalised intensity wavelength spectra of HIP treated Cr:ZnSe laser pumped at 1.57 µm for 80% and 97% reflectivity output couplers.

As can be seen in Figure 6.12, the emission spectrum of the 97% R OC is centred at ~ 2488 nm, longer in comparison to the spectrum obtained with the 80% R OC which is centred at ~ 2436 nm. This shift may be due to the peak reflectivity being different for each of the coatings on the output couplers. It may also have a contribution due to the absorption of the Cr:ZnSe which extends into the emission cross section as can be seen in Figure 6.2. This means that for the higher R OC, the population inversion is lower and the peak gain wavelength is longer than the peak of the emission cross section. For the lower reflectivity OC, the ground state is less populated and thus the absorption is less, the peak gain wavelength is therefore closer to the peak of the emission cross section. The FWHM linewidth of the spectra are both ~ 14 nm which is considerably narrower than the typical bandwidth emitted from a free running Cr:ZnSe laser shown in Figure 6.9. In this case the measured spectra of the HIP treated sample are limited by the 7 nm resolution of the near-IR Spectrometer, it is expected that the true linewidth is much narrower in agreement with the sub-140 pm level demonstrated in Figure 6.8.

It is noted here that there is further evidence that the HIP conditions lead to narrowing of the linewidth in the spectral emission of TM:II-VI ULI waveguide lasers. The typical spectral emission of a Cr:ZnSe ULI depressed cladding waveguide laser is demonstrated in Figure 6.13 a), whereas the spectral output of both a Fe:ZnSe ULI waveguide laser and bulk laser is shown in Figure 6.13 b).

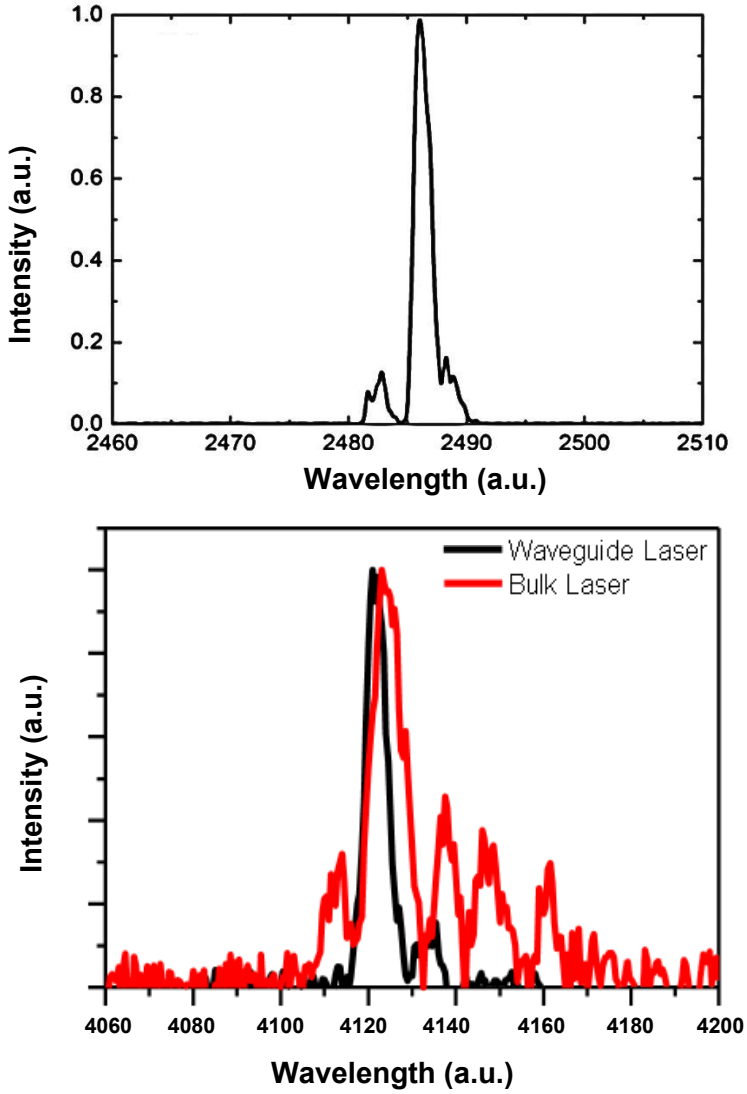

Figure 6.13 a) Typical spectral emission of Cr:ZnSe ULI waveguide laser. b) Spectral output both of Fe:ZnSe ULI waveguide laser and bulk laser. Images have been reproduced from [35] and [271] respectively.

The spectrum of the Cr:ZnSe waveguide laser in Figure 6.13 a) has a FWHM linewidth of 1.6 nm, this is a great deal narrower than the 20 nm FWMH linewidth of the free running bulk laser emission presented in Figure 6.9. Similarly, for the Fe:ZnSe lasers demonstrated in Figure 6.13 b), the 6.7 nm linewidth emitted by the waveguide laser is narrower than the bulk counterpart which consists of multiple peaks spanning ~ 50 nm. From these results it has been proposed that the ULI process results in conditions within the crystals which are consistent with HIP treatment. In fact, it has been calculated in [326] that ULI results in temperatures in excess of 1100ºC and pressures ≈ 50,000 PSI at the irradiated focal region in the substrate, similar to those utilised in the HIP treatment in [320]. Therefore, it is believed that the ULI process also removes defects in

the irradiated area of crystal hence leading to some narrowing of the spectral output [319].

After confirming that the emission from the HIP Cr:ZnSe bulk laser was spectrally narrowed as intended by the HIP treatment the laser was subsequently investigated for modelocked emission.

6.3 KLM Operation of a HIP Treated Cr:ZnSe Bulk Laser

The theory behind the technique of KLM has been presented in sub-section 4.3.3. In this sub-section it was also shown that to date KLM has found the majority of its success with Ti:sapphire as the active gain media. This has led to generation of ultrafast pulses with durations down to 5 fs in the near-IR extending over the range 600-1350 nm [54]. However, KLM is generally more difficult to achieve in the mid-IR because the Kerr effect is inversely proportional to laser mode size in the crystal, and this mode size itself is proportional to the square root of the signal wavelength. Thus at mid-IR wavelengths it is generally more challenging to induce the necessary Kerr effect for modelocking, expect for the case of sufficiently high nonlinear refractive index media [285]. For that reason Cr:ZnSe is particularly suitable for use in KLM, it has a n_2 value of ~ 7.5×10^{-19} m^2W^{-1} at 2.4 μm [327], around 25 times greater compared to $n_2 = 3 \times 10^{-20}$ m^2W^{-1} at the signal wavelength in Ti:sapphire [204]. Table 5 shows that KLM has led to improvement in the average output power demonstrated from Cr:ZnSe/ZnS as the issue of potential damage to a physical saturable absorber has been eliminated. It can also be seen in Table 5 that KLM used in combination with chirped mirrors for GDD control has facilitated the generation of the shortest ultrafast pulses from a polycrystalline Cr:ZnSe laser of 47 fs. Therefore, this is the method which has been adopted here to investigate the potential for the emission of ultrafast pulses from HIP treated Cr:ZnSe.

A schematic diagram of the KLM HIP Cr:ZnSe laser cavity is shown in Figure 6.10. Although it is similar to that of the x-fold resonator used for which the CW characterisation in Figure 6.10, in this case the dispersion of the cavity elements must be

considered.

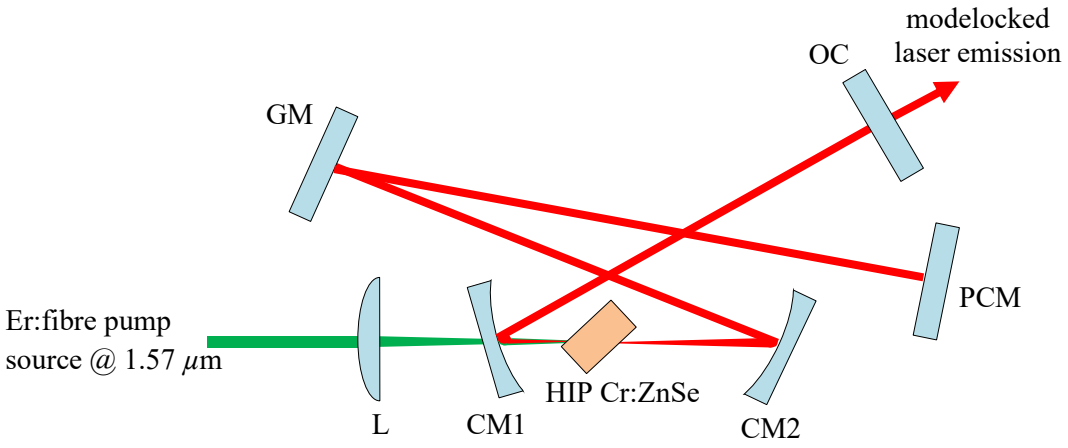

Figure 6.14. Schematic diagram of KLM HIP treated Cr:ZnSe Laser. L is a plano-convex 50 mm focal length lens. CM1 and CM2 are plano-concave mirrors with 30 mm and 50 mm ROCs respectively, both are HR for2.3 – 2.6 μm and PCM is a plane mirror with the same coating. CM1, CM2 and PCM are all chirped mirrors with GDD = ~ -250 fs^2.GM is plane gold mirror and OC is the output coupler.

L is the same 50 mm focal length plano-convex lens as in Figure 6.10. However, in this case CM1 and CM2 are plano-concave chirped mirrors with ROCs of 30 mm and 50 mm respectively. PCM is a plane chirped mirror which was mounted on a translation stage. The three chirped mirrors are coated for high reflectivity, > 99.5%, in the region 2.3-2.6 μm and have nominal GDD = - 250 fs^2. GM represents a plane gold mirror designed for low loss of typically < 2% in the mid-IR, and OC is the output coupler. The length of the cavity arms CM1→OC and CM2→GM→PCM was 36 cm and 42.5 cm respectively; resulting in a total cavity length of approximately 83 cm, as discussed further below this varies by a few mm depending on the separation of the curved mirrors which the modelocking is very sensitive to. The modelocked output was characterised utilising two output couplers with different coatings; one being 97% reflective for 2.05 – 2.43 μm (97% R OC) and the other was 99% reflective for 2.1-2.5 μm (99% R OC). In this case, the sample was actively cooled by securing on a copper heat sink held at a temperature of 20ºC. This was achieved through the use of a Peltier-electric cooler, in which the heat was distributed by passive water cooling. The laser was pumped with the same Er:fibre source as in the CW characterisation. CM1 and CM2, again, set folding angles of 17º in both arms of the cavity to compensate for astigmatism imposed on the cavity. It was decided to propagate through the 2 mm length of the crystal for modelocking. This is because with chirped mirrors available,

the GDD of the cavity could be compensated more fully through this sample dimension than the other two. In this orientation the single-pass absorption of pump light was measured as ~ 69%.

The resonator was initially aligned for CW operation. Then the position of the curved mirrors and the crystal could be finely adjusted by use of the compact micrometer stages they were mounted on. This is necessary to identify the edges of the resonator stability regions as this is where KLM can most likely be achieved, a detailed discussion of the laser stability regions can be found in [203]. KLM operation was initiated by sharp translation of the PCM. It was found that KLM operation was not particularly difficult to start and the modelocked emission was extremely stable over several hours. Various measurements were made to fully characterise the modelocked laser performance which will now be detailed.

Modelocked operation was verified by detection of the laser output with a 1 GHz extended InGaAs photodiode connected to an oscilloscope. The photodiode was manufactured by Hamamatsu with model number G8423-03SPL and designed for use in the range 1.2-2.6 μm. The spectrum of the emitted pulses was measured with a near-to-mid-IR monochromator with gratings covering 0.8-20 μm manufactured by Newport (model number 74125). The measurement was taken with a resolution of 2 nm and slit aperture 0.28 nm. An interferometric autocorrelation measurement was taken to characterise the temporal duration of the pulses, this technique has been discussed at length in sub-section 4.5.1. The autocorrelator employed was a homemade setup based on 2-photon absorption in an InGaAs photodiode with a cutoff wavelength of 1.7 μm. The modelocking threshold and average output power performance of the laser was also measured. These measurements were recorded for both the 97% and 99% R OCs, the full results will be presented in Figures 6.15– 6.21 with the discussion to follow.

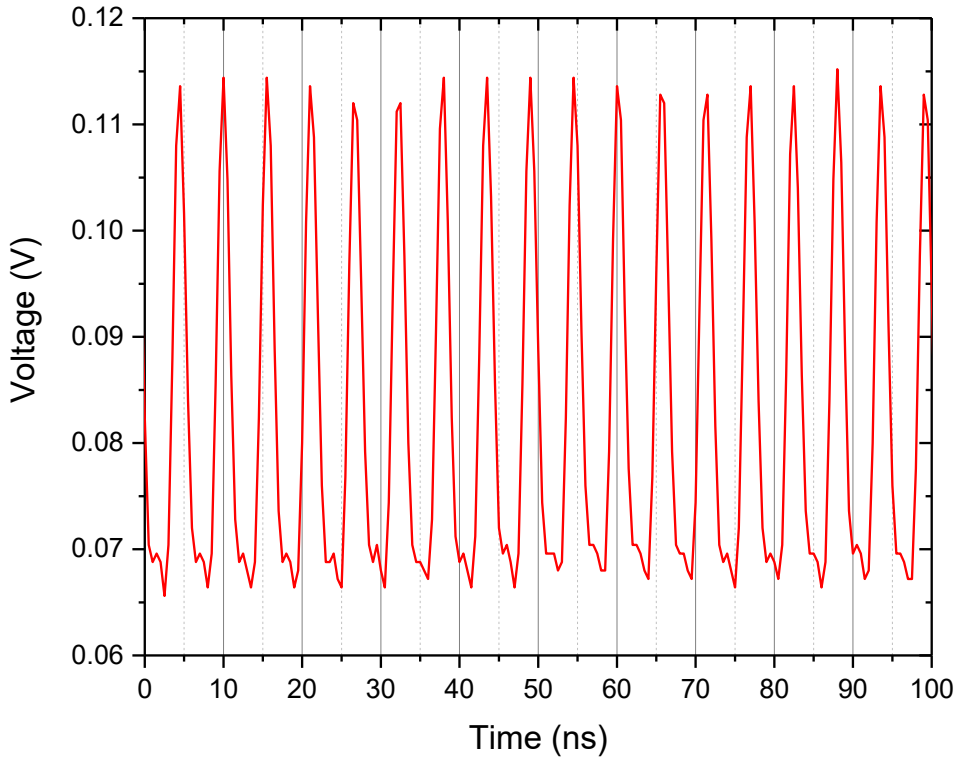

Figure 6.15. Modelocked pulse train emitted from HIP Cr:ZnSe laser with 97% reflective OC viewed with an oscilloscope.

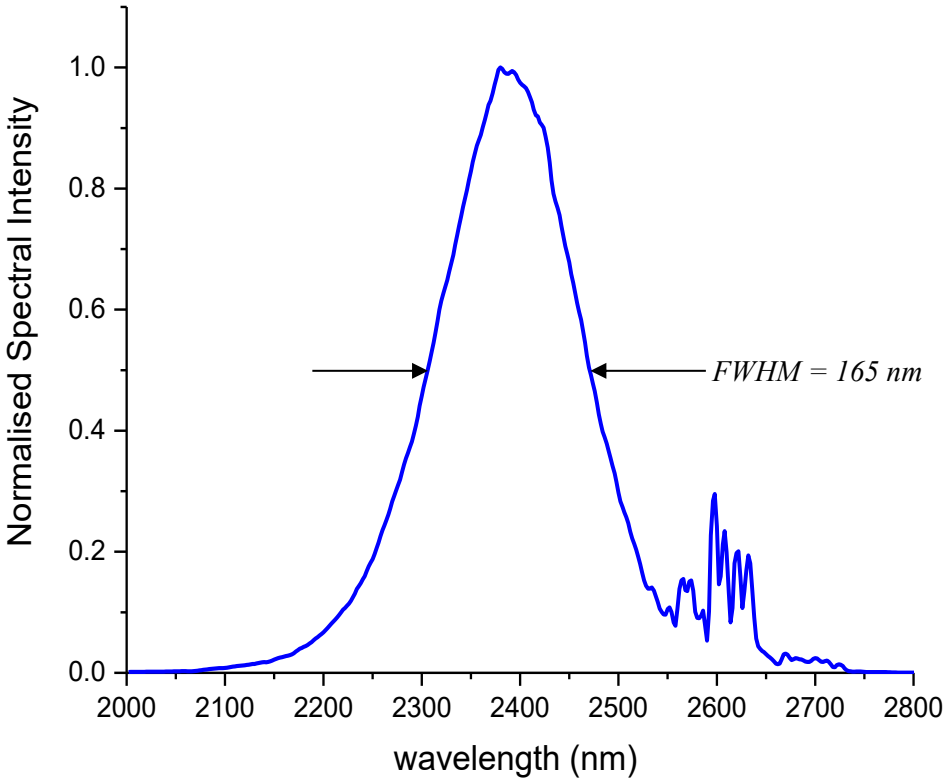

Figure 6.16. Wavelength spectrum of modelocked HIP Cr:ZnSe laser with 97% reflective OC. The spectrum is centred at 2388 nm with a FWHM of 165 nm.

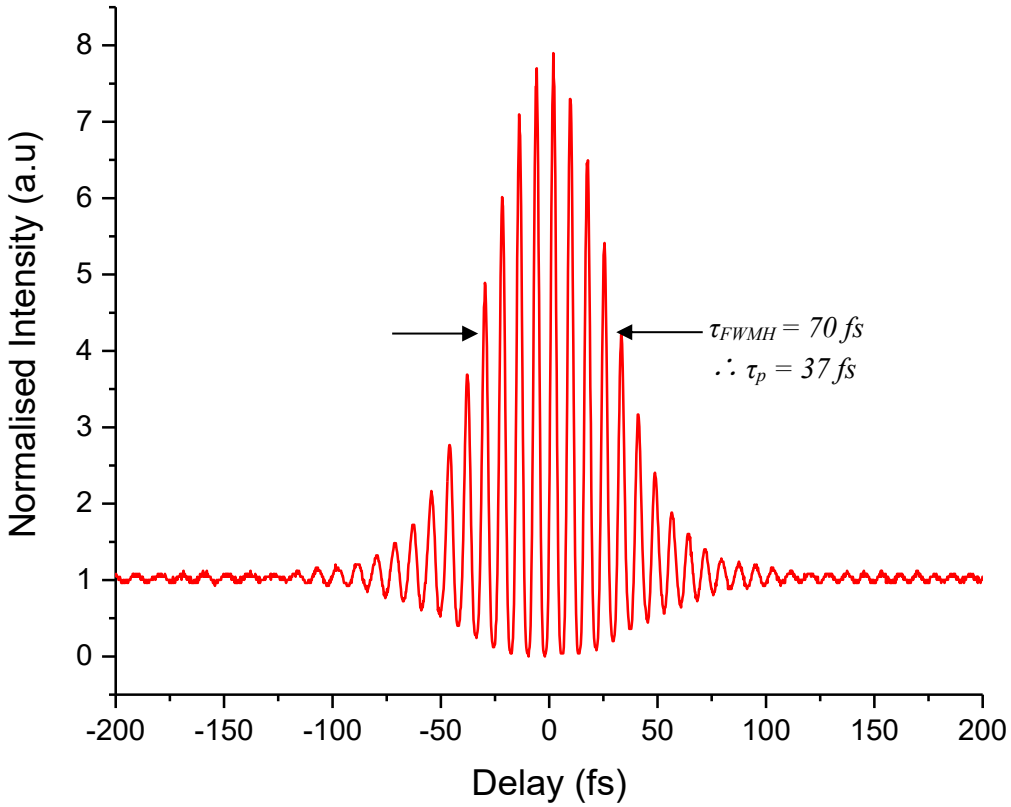

Figure 6.17. Interferometric autocorrelation trace of modelocked HIP Cr:ZnSe laser with 97% reflective OC, the FWHM of the trace is 70 fs translating to a pulse duration of 37 fs.

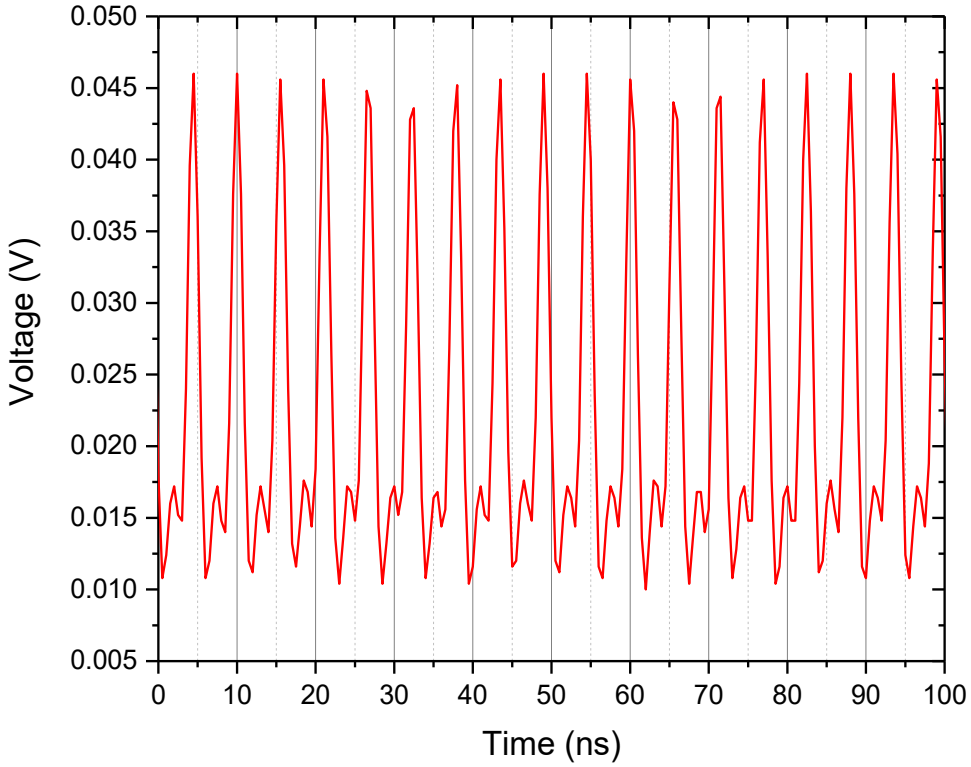

Figure 6.18. Modelocked pulse train emitted from HIP Cr:ZnSe laser with 99% reflective OC viewed on an oscilloscope.

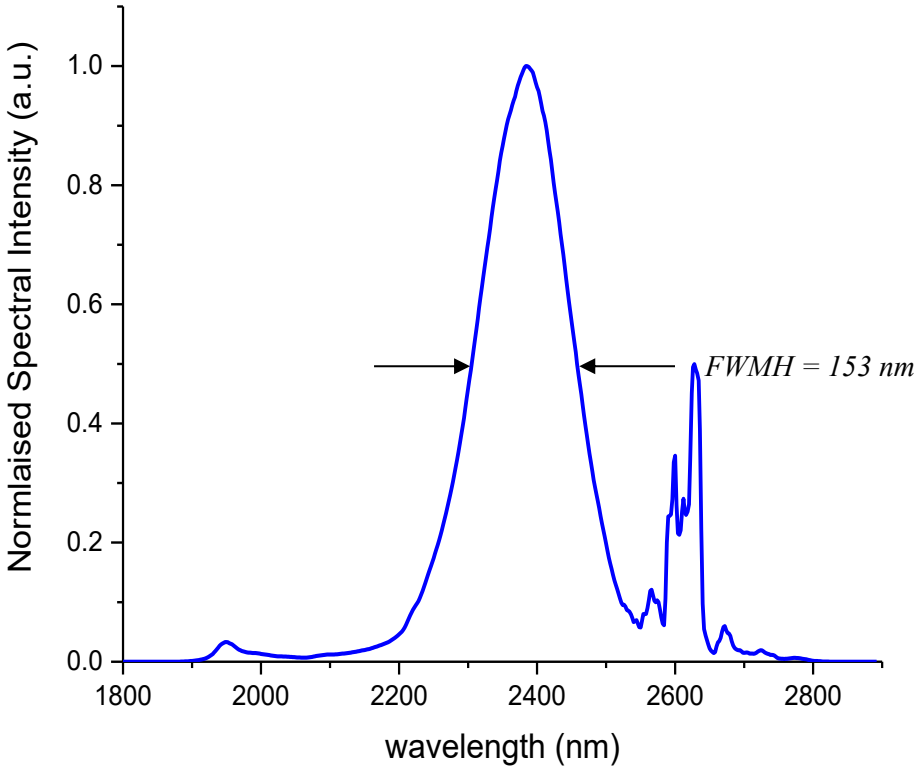

Figure 6.19. Wavelength spectrum of modelocked HIP Cr:ZnSe laser with 99% reflective OC. The spectrum is centred at 2382 nm with a FWHM of 153 nm.

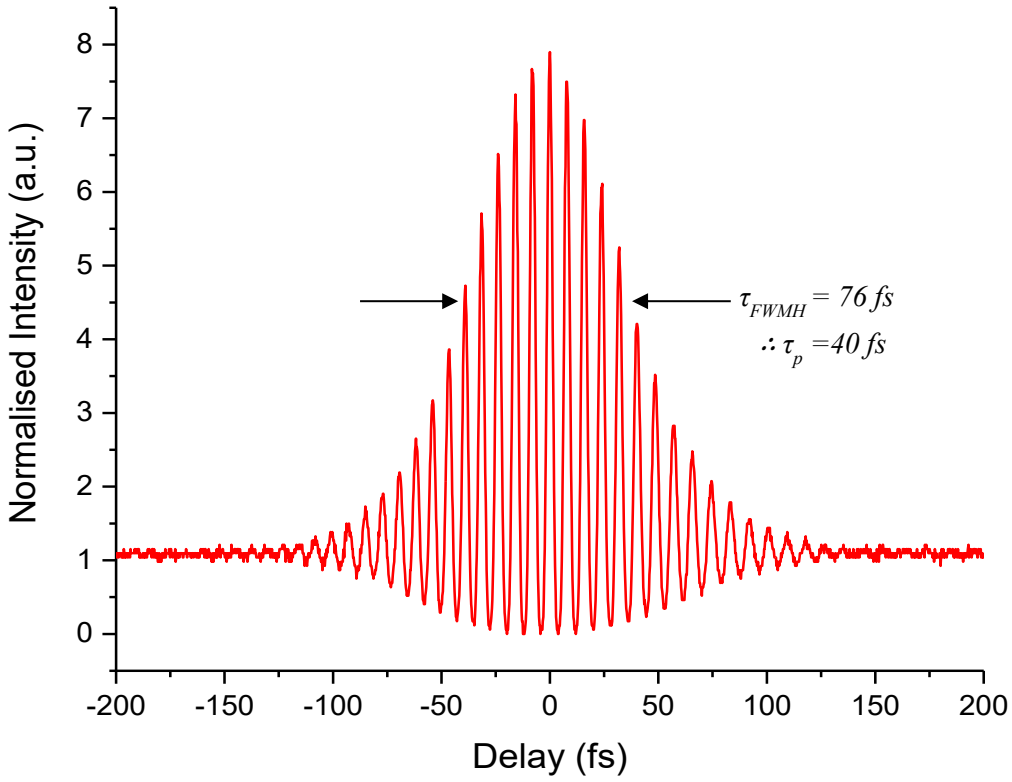

Figure 6.20. Interferometric autocorrelation trace of modelocked HIP Cr:ZnSe laser with 99% reflective OC, the FWHM of the trace is 76 fs translating to a pulse duration of 40 fs.

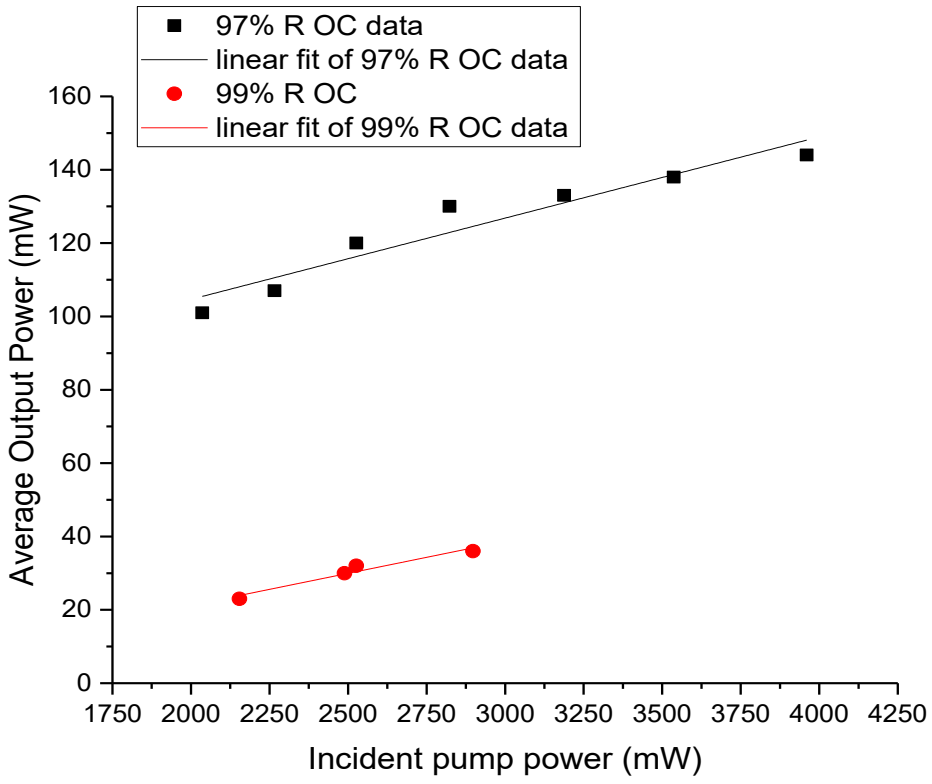

Figure 6.21. Average output power versus incident pump power of modelocked HIP Cr:ZnSe laser.

Figures 6.15 and 6.18 contain the modelocked pulse trains emitted for the 97 and 99% R OCs respectively. In Section 4.1 is was presented that the expected PRF of a modelocked laser can be estimated using $\frac{c}{2nl}$, where c is the speed of light, n is the intracavity refractive index and l is the cavity length. In the HIP Cr:ZnSe laser the index of the cavity is taken to be 1 as the majority of the propagation is in free space. The cavity length is ~ 83 cm which remained the same for both OCs, resulting in an estimated PRF of 181 MHz. As can be seen in Figures 6.15 and 6.18 the pulses are emitted with a period of approximately 5.5 ns hence a PRF of ~ 182 MHz, corresponding well with the expected value.

The wavelength spectrum obtained with the 97% R OC is shown emission in Figure 6.16, it is centred at 2388 nm with a FWHM of 165 nm. Note that there are a series of spikes observed in the long wavelength wing of the spectrum around 2.6 μm, these are due to water vapour absorption in the atmosphere common for spectra in this wavelength range in cavities which are not actively purged [316]. The corresponding interferometric autocorrelation trace for this OC shown in Figure 6.17 is characterised by the expected 8:1 peak-to-background ratio discussed in sub-section 4.5.1, and has a FWHM of 70 fs. Assuming a sech^2 pulse profile thus applying a deconvolution factor of 1.897 in equation (21), this translates to a pulse duration of 37 fs. The associated time-bandwidth product is therefore 0.321.

For the case of the 99% R OC, the wavelength spectrum is shown in Figure 6.19, it is centred at 2382 nm and has a FWHM spanning 153 nm. The spikes at ~ 2.6 μm are again present, but in this case there is also a low intensity spike at around 1950 nm which is not observed with the 97% R OC. The presence of this spike is most likely due to modulations in the reflectivity coating of this OC at ~ 1950 nm. The interferometric autocorrelation measurement obtained is shown in Figure 6.20, the trace again has the correct peak-to-wings ratio of 8:1 and in this case the FWHM is 76 fs corresponding to a pulse duration of 40 fs. The time-bandwidth product is calculated again assuming a sech^2 pulse profile, the calculated value is 0.323.

The obtained time-bandwidth products are slightly larger than the expected value of transform-limited sech^2 pulses of 0.315. This indicates there is a residual chirp in the pulses. To identify the reason for this chirps the net GDD of the cavity was estimated as

follows: Brewster's angle for the Cr:ZnSe crystal is ~ 68º resulting in a propagation length through the sample of 2.16 mm and the GVD of ZnSe at the signal wavelength of ~ 2385 nm is +209 fs^2mm^{-1} [328]. This results in a calculated total GDD of +903 fs^2 per round trip due to the laser crystal in the cavity. Data provided by the chirped mirror suppliers gives a GDD value of -220 fs^2 per bounce at the signal wavelength, thus a total round trip GDD due to the chirped mirrors is calculated to be $-220 \times 5 = -1100$ fs^2. The GDD of the gold mirror is zero, that of the atmosphere and the unknown value of the output coupler are assumed to be negligible in this estimation. From these calculations the net round trip intracavity GDD is estimated to be -197 fs^2, therefore in the anomalous dispersion regime. Furthermore, before arriving at the autocorrelator for the measurement the laser emission propagates through the 6.4 mm fused silica material of the OC and a 0.4 mm Germanium plate included in the beam path to filter out any SHG signal in the output. The GDD values for these components are ~ -1330 fs^2 for the OC and ~ +930 fs^2 for Ge resulting in an additional chirp of -400 fs^2. Therefore, there is indeed a negative chirp which acts to distort the pulse profile.

The modelocked laser average output power vs incident the pump power is displayed in Figure 6.17 for both of the output couplers. The 97% R OC results in a slope efficiency of 2.21% and the CW modelocking was found to be initiated at a minimum pump power of 2.04 W. The maximum average output power measured was 144 mW for a maximum incident pump power of 3.96 W, this is limited only by the available pump power. In the case of the 99% R OC the slope efficiency and CW modelocking threshold are 1.75% and 2.15 W respectively. The maximum average power for the 99% R OC was 36 mW measured for 2.9 W of pump power, for values greater than this the modelocking was very unstable and the average output power was observed to decrease. This is likely due to thermal issues in the crystal, more efficient cooling may improve the stability for these higher pump power values. Just below the modelocking threshold for both OC's the laser output was found to be continually switching between a Q-switched modelocked regime and CW emission with unstable output power and it was found that it could not emit stable CW emission without considerable changes to the curved mirror/crystal positions. This is not unexpected as the laser is aligned near the edges of the stability regions for KLM operation.

It may be logically expected that the higher reflectivity output coupler would result in a lower CW modelocking threshold due to higher expected intracavity energy, however

this was not the case. However, the difference in the thresholds of ~ 110 mW is relatively small compared to the pump powers applied, ranging 2-4 W. As the laser is operating on the edge of a stability region the intracavity losses are expected to be relatively high compared to in the case of operating will within the stability region. Therefore, changing the output coupling by a factor of 3 as has been done here does not have a significant effect on the intracavity energy as expected according to equation (14), accounting for the low slope efficiencies observed. To obtain a clearer view of the effect the OC reflectivity value has on the modelocking threshold, it would be useful to repeat the measurements with lower reflectivity OCs. This was attempted with a 90% reflectivity OC but it was found that this was not sufficient to initiate KLM, therefore a higher value, e.g. 95% is required, but such a mirror was not available at this time.

The emitted modelocked pulse durations of 37 fs and 40 fs corresponding to 4.6 and 5 optical cycles are the shortest observed to date from a Cr:ZnSe crystal. The 97 % R OC led to the generation of slightly shorter pulses thus a broader spectral bandwidth. This is could be due to a slightly broader bandwidth of the reflective coating on this OC compared to the 99% R OC, the reflective coatings of the two OCs would have to be analysed to confirm this. These record results indicate that the HIP treatment is advantageous for modelocking of polycrystalline Cr:ZnSe lasers. During the HIP treatment the crystal is converted from inhomogeneously to homogeneously broadened material, the reasons that this can be beneficial for ultrafast pulse generation will now be discussed. In an inhomogeneously broadened laser material, if the photon interaction time of propagating photons is less than the thermalisation time, the energy cannot be redistributed across the gain spectrum at sufficient speed, this results in any oscillating laser pulse burning a hole in the gain spectrum [329]. This reduces the overall gain and leaves much of the excited state energy inaccessible to the building laser pulse. During the initiation of modelocking whilst the pulse begins to form, if the pulse duration falls below that of the thermalisation time the pulse compression process stalls, hence the duration is limited to the equivalent of the thermalisation time. In polycrystalline solid-state crystals such as ZnSe, this is of the order of ~ 100s of fs where thermalisation is determined through the phonon spectrum, as a result the generation of few-cycle pulses can be difficult to achieve. HIP treatment of the polycrystalline material has two major effects 1) the removal of crystalline defects and 2) growth of the grains. The removal of defects means that all ions now experience the same crystal fields, thus the crystal now acts as a homogenously broadened material. In combination with this defect removal,

fewer grain boundaries reduces the phonon lifetime so even if the material is not perfectly homogeneously broadened the thermalisation time is reduced in any residual inhomogeneously broadened fraction [319, 320]. Homogenous broadening results in no such spectral hole burning and the gain profile is uniformly depleted as the pulse builds. Any residual inhomogeneously broadened component has very small thermalisation times and so the mode locked pulse can still access the full gain spectrum. Of course net intracavity dispersion also has major consequences on resultant pulse duration. However, the results presented in this section strongly suggest that the laser is operating in a regime in which the thermalisation time is less than the photon interaction time i.e. the pulse duration, and as such has allowed for the generation of record short sub-40 fs pulse durations.

The next stage of our work in this material will focus on initially testing the KLM cavity with the available 1.9 μm pump source at HWU. It is expected that this will result in improved output power performance because of the reduced quantum defect and the fact that the absorption peak in Cr:ZnSe is closer to 1.9 μm than 1.57 μm as can be seen in Figure 6.2. In addition to this, the quantum defect is reduced for a 1.9 μm also resulting in higher obtainable slope efficiencies. The cavity will subsequently be optimised for GHz PRF emission whilst maintaining the ultrafast sub-ps pulse width. This would satisfy the aim of developing a GHz PRF ultrafast mid-IR emission source which also has high power capability.

6.4 Summary

In conclusion, this chapter presents results of an ultrafast HIP treated Cr:ZnSe laser. Two different HIP treated Cr:ZnSe crystals were initially characterised for CW laser operation. These experiments were carried out separately in HWU and Politecnico di Milano utilising 1.9 μm and 1.57 μm pump sources respectively. The laser crystals were both utilised in astigmatically compensated bulk resonators and the pump powers were intentionally kept low during these measurements due to an absence of active crystal cooling. In both experiments the laser exhibited a significantly narrower spectral emission linewidth than traditional free running polycrystalline Cr:ZnSe lasers which typically span 10s of nm. The emitted FWHM linewidths were 140 pm and 14 nm when pumped with 1.9 μm and 1.57 μm respectively. In the latter case this was limited by the

spectral resolution of the different spectrometer used and it is expected that the true linewidth is sub-nm as in the former case. The spectral narrowing is a result of the HIP treatment converting the Cr:ZnSe crystals from an inhomogenously to a homogeneously broadened material as demonstrated first by Stites et al. [320]

The laser was then operated in an ultrafast pulsed regime through the technique of KLM. The cavity was similar to that for the CW experiments with the addition of chirped mirrors for management of the intracavity dispersion and plane gold mirror to control the cavity length. Modelocked emission was initiated by sharp perturbation of one of the intracvaity chirped mirrors. Stable CW-modelocked operation was observed for 97% and 99% R OCs. With the 97% R OC the temporal pulse duration was found to be 37 fs with a spectral bandwidth of 165 nm centred at 2385 nm. For the 99% R OC the pulse duration was 40 fs and the bandwidth was 153 nm centred at 2382 nm. The slightly shorter pulse duration obtained with the former is likely due to the broader bandwidth of the reflective coating on the OC. The 97% R OC also exhibited superior power performance; demonstrating an average output power of 144 mW when pumped with 3.94 W, compared to a maximum of 32 mW for the 99% R OC which could not be pumped with more than 2.9 W due to thermal instabilities. A PRF of 182 MHz was measured corresponding well with the 83 cm cavity length. These results represent the shortest pulse duration to date generated in a Cr:ZnSe laser, indicating that HIP treatment of the crystal may be beneficial for the emission for ultrafast sub-ps pulses in this medium. The next stages of this work are to characterise the modelocking performance when pumped at 1.9 μm and optimise the cavity length for GHz PRF.

Chapter 7. Conclusion and Future Work

7.1 Conclusions

The work presented in this thesis has focused on the development of novel laser sources in the 2-5 μm range which have the potential for the generation of ultrafast pulses with multi-GHz PRFs. This research topic is motivated by the disadvantages and limitations associated with many of the mid-IR sources available at present. ULI is a powerful tool for the fabrication of compact waveguide laser emission sources which are particularly suitable for GHz PRF generation. In chapter 3, the novel gain material Erbium doped GLS glass has been investigated for potential laser emission in the mid-IR from ULI waveguides. Inscribed waveguides were pumped with a 980 nm diode laser which led to the emission of fluorescence at 2.75 μm. The investigation concluded that further improvements in the glass quality and cavity design will result in laser action. Chapter 4 introduces the theory behind pulsed laser emission. One of the main topics covered in this chapter is the saturable absorption property of graphene. This makes it ideal for passive modelocking of lasers in the mid-IR as an alternative to traditional SAs such as SESAMs which are limited in this spectral range. Chapter 5 then focused on the development of a 5.9 GHz Ho:YAG ULI waveguide laser at ~ 2.1 μm which was modelocked with a graphene based SA. This result is the first GHz source demonstrated in this laser gain material. Chapter 6 has explored the use of HIP treated Cr:ZnSe to assess its capability in producing ultrafast sub-ps pulses in a Kerr-lens modelocked bulk laser cavity. The results presented surpass the minimum pulse durations reported previously in Cr:ZnSe and show potential for the development of a high PRF ultrafast laser. The following paragraphs provide a summary of these experiments and the conclusions we have reached.

Chapter 3 presents the investigation of utilising ULI waveguides in Er:GLS with the aim of developing a compact, robust solid-state emission source at 2.75 μm. A Yb:fibre chirped pulse amplifier system was utilised to fabricate Type I waveguides in samples of Er:GLS with differing dopant concentrations. The waveguides were pumped with a 980 nm diode laser resulting in the detection of fluorescence from each sample at ~ 2.73 μm. The blue-shift in comparison to the expected emission wavelength of 2.75 μm has been explained as being a result of strong water vapour absorption in the atmosphere at this wavelength. The intensity of the fluorescence was found to increase with increasing

dopant concentration. Lasing was attempted from waveguides in the highest doped sample but this was found to be not possible at this time; the reasons for this were explored. The propagation loss of these waveguides was measured to be ~ 1.83 dBcm^{-1}. This is comparable to other Type I waveguides which have succeeded in laser operation, however there is some improvement to be made compared to the 0.6 dBcm^{-1} propagation loss recorded from undoped GLS. In addition, an IR waveguide amplifier was demonstrated exhibiting a maximum gain of 5.4 dBcm^{-1} at 1538 nm. As gain was observed on this energy transition, this indicates that a population inversion does not exist on the sought after 2.75 μm energy transition. Various suggestions have been made to optimise the setup for lasing operation including; pulsed pumping, higher Erbium concentrations whilst sustaining the high quality of the glass and the possibility of co-doping to induce much higher pump absorption into the upper lasing level. This investigation concluded that Er:GLS has promising potential as a material for waveguide laser emission in the mid-IR; improvements to both the glass properties and the cavity design will maximise this potential.

Chapter 5 explores the use of a Ho:YAG ULI waveguide laser for high PRF modelocked emission at 2.1 μm. ULI was utilised to fabricate depressed cladding waveguide structures in a 0.5% at. Ho:YAG crystal which demonstrated propagation losses of 1.02 dBcm^{-1} estimated by a Caird analysis. The waveguides were pumped in a laser cavity by a CW 1908 nm Tm:fibre laser with a maximum power of 12 W resulting in transverse single mode laser emission. Initially a full CW characterisation was performed. A maximum laser output power of ~ 1.78 W and slope efficiency of 16% was observed with a 70% reflective OC. The emission wavelength of the laser was centred at ~ 2090 nm for the 60,70 and 80% reflectivity OCs and red shifted to 2097 nm for the 97% reflective OC, due to the different coating on this mirror. The beam quality of the laser mode was determined by measuring the M^2 parameter in the horizontal and vertical dimensions. This measurement was carried out by focusing the collimated output beam with a 10 cm focal length lens and utilising a beam profiler to measure the $1/e^2$ beam radius as a function of the propagation distance. These results were plotted and numerical fit applied to obtain values for the beam divergence angle and the beam radius at the focus. From these results the M^2 parameter was calculated in the horizontal and vertical dimensions as 1.48 and 1.75 respectively.

This single mode waveguide laser was subsequently investigated for the generation of pulsed emission. A graphene coated saturable OC replaced the regular OC in the waveguide cavity and Q-switched modelocked behaviour was observed. The 14 mm length of the resonator resulted in a PRF of 5.9 GHz whilst the Q-switch operated with repetition rate of 1.04 MHz. A maximum average output power of 170 mW was measured for 2.5 W of incident pump. The QML behaviour was verified applying the Q-switching stability criterion which was discussed in sub-section 4.3.2. This calculation indicated that the maximum intracavity energy in this setup is an order of magnitude smaller than required to escape QML instabilities, and thus operate in the pure CW modelocked regime. This could be achieved with tailored design of the graphene coated saturable OC. These results represent the first GHz PRF modelocked Ho:YAG laser.

Chapter 6 investigates the potential of HIP treated Cr:ZnSe for ultrafast sub-ps pulse generation in the 2-3 μm wavelength range. Initially, two HIP treated Cr:ZnSe crystals were characterised for CW laser operation separately with 1.9 μm and 1.57 μm pump sources. The laser crystals were both utilised in astigmatically compensated bulk resonators. In both cases the laser exhibited a significantly narrower spectral emission linewidth than for traditional free running Cr:ZnSe lasers which generally span 10s of nm. The FWHM linewidths were measured as 140 pm and 14 nm when pumped with 1.9 μm and 1.57 μm respectively. In the latter case this was limited by the spectral resolution of the spectrometer used and it is expected that the true linewidth is sub-nm. These spectral narrowing results proved that the HIP treatment acts to convert the Cr:ZnSe crystals from inhomogenously to a homogeneously broadened media.

The laser was then operated in the KLM regime with the addition of chirped mirrors for intracavity dispersion compensation. CW modelocked operation was observed at a PRF of 182 MHz in good agreement with the 83 cm cavity length. A maximum average output power of 144 mW was observed for 3.94 W of incident pump. The minimum pulse duration demonstrated was 37 fs assuming a sech^2 pulse profile, corresponding to ~ 4.6 optical cycles. With a spectral bandwidth of 165 nm centred at 2385 nm, this resulted in a time-bandwidth product of 0.32. A small anomalous chirp was calculated to be responsible for the deviation from the ideal time-bandwidth product of 0.315. This is the shortest pulse duration generated in a Cr:ZnSe laser to our knowledge, therefore

indicating that HIP treatment is advantageous in the generation ultrafast pulses in this medium.

7.2 Future Work

7.2.1 Compact monolithic Er:GLS Waveguide Laser

The fluorescence results recorded in chapter 3 of this thesis have shown that Er:GLS is an attractive gain medium for laser emission at 2.75 μm. More specifically, it was demonstrated that an increase in dopant level is favourable for emission from this energy transition, thus the dopant concentration must be optimised for this whilst simultaneously retaining the high optical quality of the glass. Our collaborators at the ORC have experienced challenges in producing glasses with dopant concentrations higher than 5-10% which do not compromise the glass quality. As a consequence, investigations into the glass fabrication procedures are ongoing to improve this capability. As previously discussed, creating a population inversion for CW laser operation at ~ 2.9 μm in Er:YAG is achievable with dopant concentrations, ~ 50%. Therefore, there is significant improvements to me made by the fabricators to facilitate this in Er:GLS. Another method to overcome the challenge of creating the required population inversion is to co-dope with Yb to optimise absorption of the ~ 980 nm pump radiation, the researchers at the ORC are also exploring this option and we await the results of these co-doping investigations.

The results in chapter 3 also suggested that a higher pump power source be acquired for CW lasing operation. Applying these discussed modifications could result in a compact, robust mid-IR ULI waveguide laser which in turn could then be utilised in modelocking investigations. The technology for SESAMS in this spectral range is still in its infancy, as a result there are few reports of ultrafast pulse generation with SESAMs from the 2.7 – 2.9 μm transition in Er doped lasers. However, relatively new SAs including graphene, carbon nanotubes and black phosphorus are promising candidates in the mid-IR owed to their broad operational range. Thus, these may be ideal for high PRF modelocking of an Er:GLS ULI waveguide laser.

7.2.2 CW modelocked operation of a GHz Ho:YAG waveguide laser

In chapter 5, a 5.9 GHz QML Ho:YAG ULI waveguide laser has been presented. The next stage of this work is to obtain CW modelocked operation from the laser whilst retaining the high PRF. To facilitate this, the design parameters of the GSOC must be optimised for emission in the CW modelocked regime. With reference to equation (10), this could be achieved by designing the GSOC with a reduced modulation depth. In addition, a higher reflectivity OC value could result in an increase of the intracavity energy as required by equation (14). However, a higher reflectivity OC would likely cause the average output power to reduce as shown in sub-section 5.2.2. Thus, it would be necessary to also inscribe lower loss single mode waveguides to optimise the output power capability of the waveguide laser. The optimisation of these parameters has resulted in the generation of 16 ps stable CW modelocked pulses at PRFs up to 11.5 GHz from Nd:YAG ULI depressed cladding waveguide lasers at ~ 1064 nm reported in [267] and [330]. A further example is that of the 2 ps pulses emitted at 2 GHz from a Yb:YAG ULI Type II waveguide laser in [331], in which Carbon nanotubes, the 1D from of Graphene, has provided the SA mechanism. The GDD of these waveguide lasers has been controlled by use of a small gap between the uncoated end facet of the waveguide and one of the plane cavity mirrors. This could be implemented for use with a GSOC CW modelocked Ho:YAG waveguide laser to optimise for the minimum pulse duration. The cavity design for this is shown in the diagram in Figure 7.1.

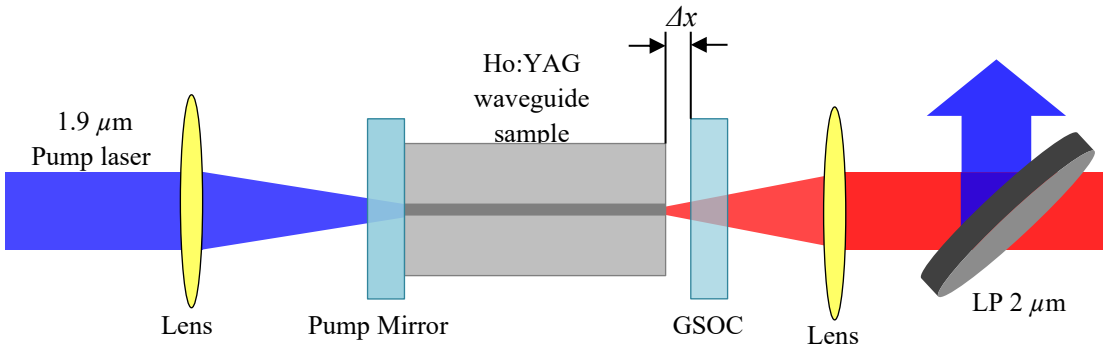

Figure 7.1. Schematic diagram of a cavity for a Ho:YAG ULI waveguide laser modelocked by a GSOC in which the GDD is controlled through adjustment of the size of the gap, Δx.

The small air gap, Δx, can create negative GVD in the form of a Gires-Tournois interferometer. Thus, careful micrometer precision adjustment of the air gap size provides a means of tuneable control of the cavity GDD. [267]. This method has also

been demonstrated for GDD control in waveguide lasers modelocked by SESAMs facilitating the generation of stable ultrafast pulses with up to 15 GHz PRFs [332-334]. Hence, this method is effective for dispersion control in a ULI waveguide laser without compromising the compact nature of the cavity. This is not the case for alternative GDD compensation methods discussed in section 4.4 which tend to require space for the components and mechanical mounts. One other modification to increase the PRF obtainable would be to simply use a shorter sample. Lower waveguide propagation loss would be advantageous to generate the necessary output powers to emit in the CW modelocked regime for a shorter sample.

7.2.3 GHz level KLM HIP treated Cr:ZnSe Laser

Chapter 6 of this thesis presented an ultrafast modelocked Cr:ZnSe bulk laser in which the laser was treated with HIP facilitating sub-40 fs pulse generation at a PRF of 182 MHz. The first stage in the continuation of this work is to attempt KLM of a HIP Cr:ZnSe crystal with the 1.9 μm pump source at HWU, as opposed to the 1.57 μm pump implemented for the cavity presented in section 6.3. The lesser quantum defect and increased absorption at this wavelength in Cr:ZnSe should lead to improved output power performance and also potentially reduced cooling requirements.

As the aim of this thesis is to ultimately develop multi-GHz ultrafast mid-IR sources, the focus will then be on attempting to increase the PRF of the laser to this level. There are two main methods which will be investigated to achieve this and they will be presented below.

1) High PRF bulk cavity

Theoretically, as the PRF is inversely proportional to the cavity length, this can be achieved by simply reducing this length. However, with reference to equation (14), an increase in the PRF of a cavity directly leads to a reduction in the intracavity energy. Applying this to the KLM cavity in section 6.3, the generation of a PRF > 1 GHz requires an increase in the current PRF by a factor of > 5 and hence would result in an > 80% reduction in the intracavity energy, assuming similar levels of average output power. The resultant setup would suffer a greater risk of Q-switched instabilities which continually increases with

larger PRF values. Therefore, the cavity design parameters, particularly, the transmission of the OC, output power capability must be carefully considered during attempts to shorten the cavity.

A practical consideration associated with reducing the cavity length is fitting in the cavity components and mounts. This can be particularly challenging for the plano-concave mirrors mounts which have to be aligned at specific angles for astigmatism compensation. Custom designed miniature mirror mounts are required to fit in curved mirrors with focal lengths as short as 5-15 mm which would be particularly useful in minimising the cavity length. Maintaining the optimum GDD compensation with chirped mirrors can also be challenging as making the number of bounces needed places a limit on the minimum cavity length that can be achieved. Thus, we are working with the company: *Ultrafast Innovations GmbH* to obtain custom designed chirped mirrors tailored for this specific cavity arrangement. The aim is to have chirped mirror sets which are tailored for use with the 1.9 μm and 1.57 μm pump sources in order to directly compare the KLM laser performance at each wavelength.

2) Compact, modelocked HIP treated Cr:ZnSe waveguide laser

An alternative method is to fabricate waveguides in HIP treated Cr:ZnSe material and exploit both the compact nature of a waveguide cavity and the advantage of the HIP treatment for the generation of GHz PRF ultrafast pulses. However, as discussed in section 6.1, there have been some difficulties in fabricating low loss waveguides in HIP treated material compared to traditional commercially available Cr:ZnSe. It was discussed in sub-section 6.2.2, that ULI induces temperatures and pressure changes in the irradiated region which are comparable to this utilised in the HIP process. Research is required into the effect this has on HIP material in comparison to untreated material and how it could be contributing to high waveguides losses. This research is still in its infancy but investigations are ongoing to optimise the waveguide inscription parameters and also retain the advantage of the HIP process. This will facilitate the development of an inherently compact laser in which the gain material is ideal for ultrafast pulse generation.

7.2.4 Ultrafast Mid-IR Cr:ZnSe Waveguide Amplifier

High average power, ultrafast 2-3 μm laser pulses are essential for various applications such as high harmonic generation, time resolved studies and the development of high power mid-IR frequency combs for sensing and spectroscopy [296, 297, 335]. The thermal limitations imposed on Cr:ZnSe crystal restrict the output power capability of this laser material as discussed at length in section 6.1. This effect becomes particularly detrimental in high PRF lasers as the application of active cooling for effective heat distribution is difficult to achieve in such small resonators. Although Cr:ZnS has better thermal properties in comparison, there have been no reports of significant improvement in the output power of this material compared to Cr:ZnSe. Therefore, in summary it is challenging to generate multi-Watt level GHz PRF ultrafast pulses from Cr:ZnSe/ZnS lasers.

One solution to this is to implement an external amplifier as reported by Vasilyev et al. [335]. The authors have demonstrated amplification of 2.4 μm 40 fs pulses with an average output power of 1.7 W, by gain of factors ~ 4.2 and ~ 1.6 in bulk Cr:ZnS and Cr:ZnSe crystals respectively. The high nonlinearity in the amplifier crystals also prompted considerable broadening of the spectrum which results in compression of the pulses to 27 fs and 33 fs in Cr:ZnSe and Cr:ZnS respectively. The experimental setup of these amplifiers is demonstrated in Figure 7.2.

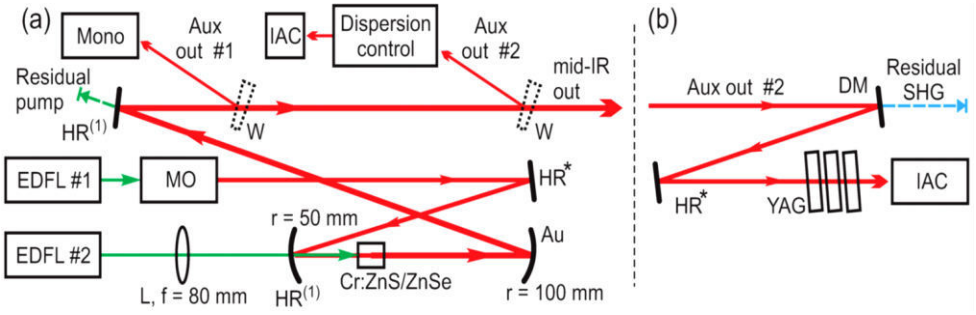

Figure 7.2. Experimental setup of (a) Master Oscillator Power Amplifier for the amplification of 2.4 μm ultrafast pulses reported in [335]. (b) optical setup for dispersion compensation of output pulses. MO – fs master oscillator (2380 nm central wavelength, 22 nJ pulse energy, 40 fs pulse duration, 79 MHz repetition rate); EDFL#1 – MO pump EDFL#2 – amplifier pump. L –focusing lens, Cr:ZnS/ZnSe –polycrystalline gain element of the amplifier, HR(1) –dispersive mirrors, HR –TOD compensator, W – CaF2 wedge; DM – dichroic mirror for SHG separation YAG – stack of plane-parallel YAG plates; IAC – interferometric autocorrelator; Mono – grating monochromator. Diagram has been reproduced from [335].*

The two curved mirrors and lens, L, optimise the overlap between the pump and signal whilst simultaneously inducing sufficient nonlinearity for spectral broadening in the amplifier crystal. As can be seen in Figure 7.2, these optics have focal lengths ranging 25 - 50 mm, meaning that the drawback of this system is that it is fairly large. An alternative method is to utilise a ULI waveguide amplifier. The implementation of a waveguide geometry guarantees a high degree of overlap between the pump and signal due to the tight confinement, resulting in a very compact and robust high gain amplifier. A single pass waveguide amplifier experiment was undertaken to explore this method. The preliminary results of this investigation will now be presented here.

Single pass ultrafast Cr:ZnSe waveguide amplifier preliminary results

Depressed cladding waveguide structures were fabricated in a 3 × 6 × 7 mm Cr:ZnSe sample by ULI, for clarity it is noted that this sample was not HIP treated. The sample was fabricated by IPG photonics with a dopant concentration of 6×10^{18} cm^{-3}. The waveguides were inscribed by our collaborators in the AFRL in Ohio, USA. The inscription laser was a Yb:fibre laser (IMRA µJewel model D1000) operating with linear polarisation at a central wavelength of 1047 nm with a pulse width of 450 fs and a PRF of 100 kHz. The pulses were focused by a 0.68 NA lens to inscribed the waveguides at a depth of ~ 200 μm beneath the surface of the sample. A set of 24 waveguides were fabricated in the 7 mm length of the sample with an average laser power of 120 mW at a translation speed of 10 mms^{-1}. The waveguide diameters decreased in increments of 5 μm between 100 – 45 μm, two waveguides were written at each diameter with 1 overscan in the first and 2 overscans in the second. These waveguides were originally fabricated to be pumped at 1.9 μm for laser emission; previous investigations had identified these as optimum parameters for this application. After inscription the input and output facets had been AR coated for 1.9 – 3 μm for the mitigation of Fresnel reflection losses. The sample was then utilised in the counter-propagating amplifier setup in Figure 7.3.

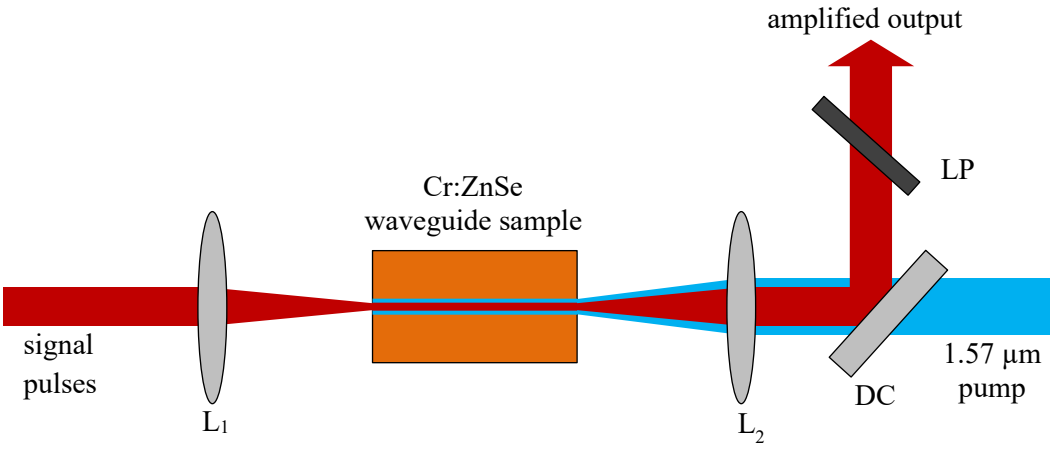

Figure 7.3. Schematic of Cr:ZnSe ULI waveguide amplifier. L_1 and L_2 are 50 mm focal length plano-convex lenses AR coated for 1.65 - 3µm and 1.05 – 1.7 µm respectively. DC is a 45° dichroic HR on the front face for 2 – 3 µm and AR on the rear for the1.57 µm pump wavelength. LP is a 2 µm long pass filter.

In the setup the ultrafast signal pulses were provided by a KLM Cr:ZnSe laser operating at 2.4 μm with an average output power of 110 mW measured behind L_1 and a PRF of 140 MHz. The input pulse duration and bandwidth are 47 fs and 160 nm respectively. The pulses were coupled into the waveguides with L_1 which is a plano-convex 50 mm focal length lens AR coated for 1.65 – 3 μm. The pump source was the same Er:fibre laser that pumped the KLM HIP Cr:ZnSe in chapter 6, the maximum power availability in this case was 10.25 W. It was coupled into the waveguides in a counter-propagating direction to the signal pulses with L_2, which is a plano-convex 50 mm focal length lens AR coated from 1050 – 1700 nm. DC represents a 45º dichroic mirror which allowed propagation of the pump light through the rear face and is HR on the front face for 2 – 3 μm. LP is a long pass 2 μm filter to remove any residual back reflected pump, as the AR coating on the end facets was not applied for this pump wavelength. Initially, the maximum pump power was coupled into each waveguide and the amplified output power was measured after the LP filter. The waveguide which resulted in the maximum amplified signal had a 90 μm diameter and was written with one overscan. The emitted signal from this waveguide with no pump power applied was measured as 80 mW. When pumped with the maximum pump power of 10.25 W at 1.57 μm, the amplified output had measured power of 430 mW. This translates to an internal gain factor of 5.375. In terms of the overall system efficiency from input to output signal, the gain factor is ~ 3.9. The spectral emission was measured with the same NIRQuest512-2.5 spectrometer that was used for the spectra taken in sub-section 6.2.2; it operates in the

range 0.9 – 2.55 μm with a resolution of 7 nm. These measurements for the case of no pump and maximum power applied are shown in Figure 7.4 a) and b).

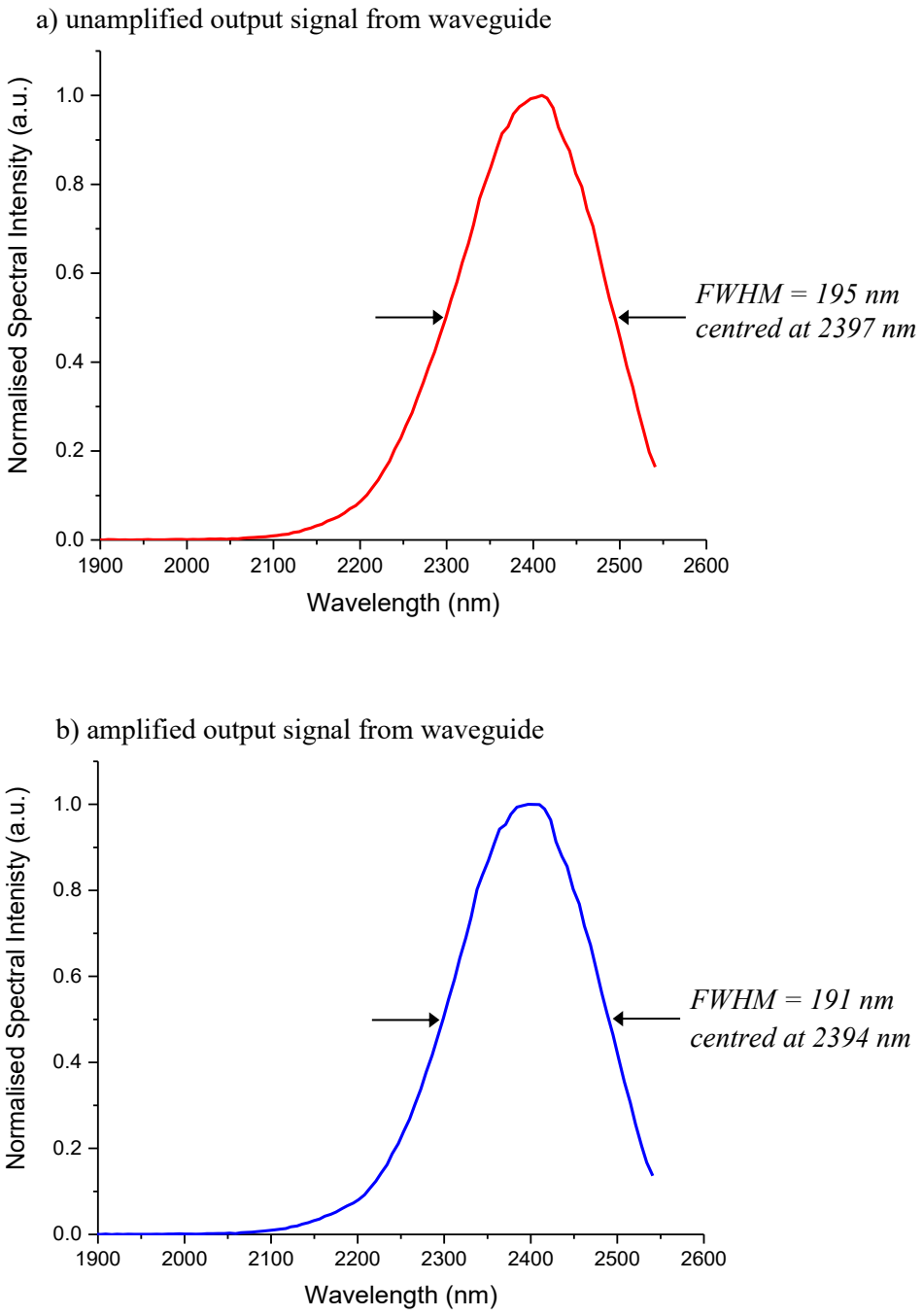

Figure 7.4. Spectral emission from Cr:ZnSe waveguide amplifier setup with a) no pump and b) 10.25 W of pump applied. The spectrum in a) is centred at 2397 with a FWHM of 195 nm, the spectrum in b) is centred at 2394 nm with a FWHM of 191 nm. The spectra cut off at 2.55 µm as this is the upper limit of the spectrometer operational range.

Figures 7.4 a) and b) indicate that the waveguide does induce spectral broadening in the pulses. The input signal pulses have a 47 fs pulse duration and a FWHM bandwidth of ~ 160 nm, which has been broadened to > 190 nm in the waveguide. Going forward, temporal pulse durations are required to confirm the implied pulse compression imposed by the waveguide. The spectral measurements also demonstrate that when the waveguide is pumped the spectral output is narrowed very slightly, by ~ 3 nm, further research is required to confirm and understand the source of this narrowing. The gain measurement was also repeated in the bulk material of the sample by simply translating the sample away from the waveguide region and optimising the lens positions for the maximum amplified output signal. The internal gain factor in the bulk was measured to be 3.8, and the overall system gain factor recorded was ~ 3. It would also be useful in the future to measure the spectral emission and pulse duration after propagation through the bulk material to provide a comparison of the nonlinearity with the waveguide. It is evident from this experiment that the waveguide amplifier is indeed advantageous in the amplification of ultrafast pulses compared to the bulk. It is expected that the gain obtained could be improved further by optimising the coupling of the pump light as this was not done in our setup.

This experiment was conducted to provide an initial indication of the amplification of ultrafast pulses in a Cr:ZnSe ULI waveguide. In summary, this preliminary investigation has shown that a Cr:ZnSe ULI waveguide is a promising candidate for the amplification of ultrafast pulses from Cr:ZnSe/ZnS lasers. Thus providing a solution to the output power limitations associated with these lasers. There is a plethora of work to be done, to further investigate and optimise the setup in terms of both output power and spectral broadening. We anticipate that tighter confinement imposed by a smaller diameter waveguide may induce larger nonlinearity in the gain medium to broaden the spectral output and thus compress the pulses. The long term goal is to implement the GHz KLM modelocked HIP Cr:ZnSe arrangements described in the previous sub-section 7.2.3 together with a waveguide amplifier. The result will be a compact, robust, mid-IR, few-optical-cycle, high PRF emission source, with Watt-level output power capability.

References

1. T. H. Maiman, "Stimulated Optical Radiation in Ruby," Nature **187**, 493-494 (1960).
2. T. Sakimoto, M. I. Rosenblatt, and D. T. Azar, "Laser eye surgery for refractive errors," The Lancet **367**, 1432-1447 (2006).
3. J. Stavridis, A. Papacharalampopoulos, and P. Stravropoulos, "Quality assesment in laser welding: a critical review," International Journal of Advanced Manufacturing Technology **94**, 1825-1847 (2018).
4. H. Kaushal and G. Kaddoum, "Applications of Lasers for Tactical Military Operations," IEEE Access **5**, 20736-20753 (2017).
5. S. D. Lord, "A new software tool for computing Earth's atmospheric transmission of near- and far- infrared radiation," NASA Technical Memorandum, 103957 (1992).
6. B. M. Walsh, H. R. Lee, and N. P. Barnes, "Mid infrared lasers for remote sensing applications," Journal of Luminescence **169**, 400-405 (2016).
7. A. P. Patel and B. E. Knudsen, "Optimizing use of the holmium:YAG laser for surgical managment of urinary lithiasis," Current Urology Reports **15**, 397 (2014).
8. A. Sijan, "Develpment of military lasers for optical countermeasuers in the mid-IR," in *SPIE Security + Defence*, 2009), 748304.
9. F. K. Tittel, D. Richter, and A. Fried, "Mid-Infrared Laser Applications in Spectroscopy," in *Solid State Mid-Infrared Laser Sources. Topics in Applied Physics*, I. T. Sorokina and K. L. Vodopyanov, eds. (Springer, 2003).
10. A. Joullié, P. Christol, A. N. Baranov, and A. Vicet, "Mid-Infrared 2-5 μm Heterojunction Laser Diodes," in *Solid-State Mid-Infrared Laser Sources, Topics in Applied Physics*, I. T. Sorokina and K. L. Vodopyanov, eds. (Springer, 2003).
11. A. L. Bloom, W. E. Bell, and R. C. Rempel, "Laser Operation at 3.39 μ in a Helium-Neon Mixture " Applied Optics **2**, 317-318 (1963).
12. R. I. Rudko, Z. Drozdowicz, S. Linhares, and D. Bua, "High-repetition-rate, recirculating hydrogen fluoride/deuterium fluoride laser," Review of Scientific Instruments **53**, 452-457 (1982).

13. A. A. Ionin, I. O. Kinyaevskiy, Y. M. Klimachev, A. A. Kotkov, and L. V. Seleznev, "Influence of multi-line CO laser focusing on broadband sum-frequency generation," Laser Physics Letters **14**, 065401 (2017).
14. R. Paschotta, "Carbon-Dioxide Lasers," in *Field Guide to Lasers* (SPIE Publications, 2008).
15. J. Faist, F. Capasso, D. L. Sivco, C. Sirtori, A. L. Hutchison, and A. Y. Cho, "Quantum Cascade Laser," Science **22**, 553-556 (1994).
16. M. Razeghi, Q. Y. Lu, N. Bandyopadhyay, W. Zhou, D. Heydari, Y. Bai, and S. Slivken, "Quantum cascade lasers: from tool to product," Optics Express **23**, 8462-8475 (2015).
17. Y. Bai, S. Slivken, S. Kuboya, S. R. Darvish, and M. Razeghi, "Quantum cascade lasers that emit more light than heat," Nature Photonics **4**, 99-102 (2010).
18. Y. Bai, N. Bandyopadhyay, S. Tsao, S. Slivken, and M. Razeghi, "Room temperature quantum cascade lasers with 27% wall plug efficiency," Applied Physics Letters **98**, 181102 (2011).
19. S. Ferré, L. Jumpertz, M. Carras, R. Ferreira, and F. Grillot, "Beam shaping in high-power broad-area quantum cascade lasers using optical feedback," Scientific Reports **7**, 44284 (2017).
20. Y. Yao, A. J. Hoffman, and C. F. Gmachl, "Mid-infrared quantum cascade lasers " Nature Photonics **6**, 432-439 (2012).
21. M. Ebrahimzadeh, "Mid-Infrared Ultrafast and Continuous-Wave Optical Parametric Osciallators," in *Solid-State Mid-Infrared Laser Sources, Topics in Applied Physics*, I. T. Sorokina and K. L. Vodopyanov, eds. (Springer-Verlang, Berlin Heidelberg 2003).
22. M. E. Klein, D. Lee, J. Meyn, K. Boller, and R. Wallenstein, "Singly-resonant continuous-wave optical parametric oscillator pumped by a diode laser," in *Technical Digest. Summaries of papers presented at the Conference on Lasers and Electro-Optics. Postconference Edition. CLEO '99. Conference on Lasers and Electro-Optics (IEEE Cat. No.99CH37013)*, 1999), 6-7.
23. A. Ciattoni, A. Marini, C. Rizza, and C. Conti, "Phase-matching-free parametric oscillators based on two-dimensional semiconductors," Light: Science & Applications **7**, 5 (2018).
24. L. D. DeLoach, R. H. Page, G. D. Wilke, S. A. Payne, and W. F. Krupke, "Transition Metal-Doped Zinc Chalcognides: Spectroscopy and Laser

Demonstration of a New Class of Gain Media," IEEE Journal of Quantum Electronics **23**, 885-895 (1996).

25. P. A. Berry and K. L. Schelper, "High-power, widely-tunable Cr^{2+}:ZnSe master oscillator power amplifier systems," Optics Express **18**, 15062-15072 (2010).
26. M. P. Frolov, Y. V. Korostelin, V. I. Kozlovsky, V. V. Mislavsky, Y. P. Podmar'kov, Y. K. Skasyrsky, and A. A. Voronov, "Laser radiation tunable within the range of 4.35–5.45 μm in a ZnTe crystal doped with Fe^{2+} ions," Journal of Russian Laser Research **32**, 528-536 (2011).
27. S. Mirov, I. Moskalev, V. Federov, D. Martyshkin, A. Martinez, M. Mirov, J. Peppers, and S. Vasilyev, "Mid-infrared lasers based on transition metal doped II-VI semiconductors," in *2nd International Conference and Exhibition on Lasers, Optics & Photonics*, 2014),
28. U. Hömmerich, J. T. Seo, A. Bluiett, M. Turner, D. Temple, S. B. Trivedi, H. Zong, S. W. Kutcher, C. C. Wang, R. J. Chen, and B. Schumm, "Mid-infrared laser development based on transition metal doped cadmium manganese telluride," Journal of Luminescence **87-89**, 1143-1145 (2000).
29. E. Sorokin, I. T. Sorokina, M. S. Mirov, V. V. Federov, I. S. Moskalev, and S. B. Mirov, "Ultrabroad Continuous-Wave Tuning of Ceramic Cr:ZnSe and Cr:ZnS Lasers," in *Advanced Solid-State Photonics* (San Diego, 2010).
30. I. Moskalev, S. Mirov, M. Mirov, S. Vasilyev, V. Smolski, Z. A, and V. Gapontsev, "140 W Cr:ZnSe laser system," Optics Express **24**, 21090-21104 (2016).
31. S. Mirov, V. Fedorov, D. Martyshkin, I. Moskalev, M. Mirov, and S. Vasilyev, "High Average Power Fe:ZnSe and Cr:ZnSe Mid-IR Solid State Lasers," in *Advanced Solid State Lasers,* (Optical Society of America, Berlin, 2015), p. AW4A.1.
32. I. T. Sorokina, "Cr^{2+}-doped II-VI materials for lasers and nonlinear optics," Optical Materials **26**, 395-412 (2004).
33. R. Wyne, J. L. Daneu, and T. Y. Fan, "Thermal coefficients of the expansion and refractive index in YAG," Applied Optics **38**, 3282-3284 (1999).
34. J. R. Macdonald, S. J. Beecher, P. A. Berry, K. L. Schelper, and A. K. Kar, "Compact mid-infrared Cr:ZnSe channel waveguide laser," Applied Physics Letters **102**, 161110 (2013).

35. J. R. Macdonald, S. J. Beecher, P. A. Berry, G. Brown, K. L. Schelper, and A. K. Kar, "Efficient mid-infrared Cr:ZnSe channel waveguide laser operating at 2486 nm," Optics Letters **38**, 2194-2196 (2013).
36. P. A. Berry, J. R. Macdonald, S. J. Beecher, S. A. McDaniel, K. L. Schelper, and A. K. Kar, "Fabrication and power scaling of a 1.7 W Cr:ZnSe waveguide laser," Optical Material Express **3**, 1250-1258 (2013).
37. J. R. Macdonald, S. J. Beecher, L. A, P. A. Berry, K. L. Schelper, and A. K. Kar, "Ultrabroad Mid-Infrared Tunable Cr:ZnSe Channel Waveguide Laser," IEEE Journal of Selected Topics in Quantum Electronics **21**, 1601405 (2015).
38. S. A. McDaniel, A. Lancaster, J. W. Evans, A. K. Kar, and G. Cook, "Power scaling of ultrafast laser inscribed waveguide lasers in chromium and iron doped zinc selenide," Optics Express **24**, 3502-3512 (2016).
39. H. Steinkemper, S. Fischer, M. Hermle, and J. C. Goldschmidt, "Stark level analysis of the spectral line shape of electronic transitions in rare earth ions embedded in host crystals," New Journal of Physics **15**, 053033 (2013).
40. K. Renk, "Solid State Lasers," in *Basics of Laser Physics* (Springer-Verland Berlin Heidelberg, 2012), pp. 279-296.
41. J. E. Geusic, H. M. Marcos, and L. G. Van Uitert, "Laser Oscillations in Nd-doped Yttrium Aluminum, Yttruim Gallium and Gadlinium Garnets," Applied Physics Letters **4**, 182-184 (1964).
42. P. Haumesser, R. Gaumé, B. Viana, E. Antic-Fidancev, and D. Vivien, "Spectroscopic and crystal-field analysis of new Yb-doped laser materials," Journal of Physics: Condensed Matter **13**, 5427-5447 (2001).
43. Y. Ohishi, T. Kanamori, and S. Takahashi, "Pr^{3+} -doped fluoride single-mode fiber laser," IEEE Photonics Technology Letters **3**, 688-690 (1991).
44. R. J. Mears, L. Reekie, S. B. Poole, and D. N. Payne, "Low-threshold tunable CW and Q-switched fibre laser operating at 1.55 μm," Electronics Letters **22**, 159-160 (1986).
45. D. Chen, C. L. Fincher, T. S. Rose, F. L. Vernon, and R. A. Fields, "Diode-pumped 1-W continuous-wave Er:YAG 3-μm laser," Optics Letters **24**, 385-387 (1999).
46. M. Ganija, N. Simakov, A. Hemming, J. Haub, P. Veitch, and J. Munch, "Efficient, low threshold, cryogenic Ho:YAG laser," Optics Express **24**, 11569-11577 (2016).

47. T. S. McComb, R. A. Sims, C. C. C. Willis, P. Kadwani, V. Sudesh, L. Shah, and M. Richardson, "High-power widely tunable thulium fiber lasers," Applied Optics **49**, 6236-6242 (2010).
48. J. Ganem and S. R. Bowman, "Use of Thulium-sensitized rare earth-doped low phonon energy crystalline hosts for IR sources.," Nanoscale Research Letters **8**, 455 (2013).
49. T. Schweizer, "Rare-Earth-Doped Gallium Sulphide Glasses for Mid Infrared Fibre Lasers," (University of Soutampton, Optoelectronics Research Centre, 2000).
50. D. C. Hanna, "Fibre Lasers," in *Laser Sources and Applications*, A. Miller and D. M. Finlayson, eds. (SUSS & Institute of Physics Publishing, Bristol and Philadelphia, 1996).
51. L. Fornasiero, E. Mix, V. Peters, K. Petermann, and G. Huber, "New Oxide Crystals for Solid State Lasers," Crystal Research and Technology **24**, 255-260 (1999).
52. T. Y. Fan, "Diode-Pumped Solid State Lasers," The Lincoln Laboratory Journal **3**, 413-426 (1990).
53. I. D. Jung, F. X. Kärtner, N. Matuschek, D. H. Sutter, F. Morier-Genoud, G. Zhang, U. Keller, V. Scheuer, M. Tilsch, and T. Tschudi, "Self-starting 6.5-fs pulses from a Ti:sapphire laser," Optics Letters **22**, 1009-1011 (1997).
54. R. Ell, U. Morgner, F. X. Kärtner, J. G. Fujimoto, E. P. Ippen, V. Scheuer, G. Angelow, T. Tschudi, M. J. Lederer, A. Boiki, and B. Luther-Davies, "Generation of 5-fs pulses and octave-spanning spectra directly from a Ti:sapphire laser " Optics Letters **26**, 373-375 (2001).
55. C. Grivas, "Optically pumped planar waveguide lasers, Part I: Fundamentals and fabrication techniques," Progress in Quantum Electronics **35**, 129-239 (2011).
56. J. Nilsson and D. N. Payne, "High-Power Fiber Lasers," Science **332**, 921 (2011).
57. K. Hirao and K. Miura, "Writing waveguides and gratings in silica and related materials by a femtosecond laser," Journal of Non-Crystalline Solids **239**, 91-95 (1998).
58. J. I. Mackenzie, "Dielectric Solid-State Planar Waveguide Lasers: A Review," IEEE Journal of Selected Topics in Quantum Electronics **13**, 626-637 (2007).
59. Y. Tamura, H. Sakuma, K. Morita, M. Suzuki, Y. Yamamoto, K. Shimada, Y. Honma, K. Sohma, T. Fujii, and T. Hasegawa, "The First 0.14-dB/km Loss

Optical Fiber and its Impact on Submarine Transmission," Journal of Lightwave Technology **36**, 44-49 (2018).

60. K. C. Kao and G. A. Hockham, "Dielectric-fibre surface waveguides for optical frequencies," IEEE J - Optoelectronics **133**, 191-198 (1986).
61. R. J. Mears, L. Reekie, I. M. Jauncey, and D. N. Payne, "Low-noise erbium-doped fibre amplifier operating at 1.54μm," Electronics Letters **23**, 1026-1028 (1987).
62. M. Z. Iqbal, H. Fathallah, and N. Belhadj, "Optical fiber tapping: Methods and precautions," in *8th International Conference on High-capacity Optical Networks and Emerging Technologies*, 2011), 164-168.
63. S. Gross and M. J. Withford, "Ultrafast-laser-inscribed 3D integrated photonics: challenges and emerging applications," Nanophotonics **4**, 332-352 (2015).
64. G. C. Righini and A. Chiappini, "Glasss optical waveguides: a review of fabrication techniques," Optical Engineering **53**, 071819 (2014).
65. K. M. Davis, K. Miura, N. Sugimoto, and K. Hirao, "Writing waveguides in glass with a femtosecond laser," Optics Letters **21**, 1729-1731 (1996).
66. L. Cerami, E. Mazur, S. Nolte, and C. B. Schaffer, "Femtosecond Laser Micromachining," in *Ultrafast Nonlinear Optics*, R. Thomson, C. Leburn, and D. Reid, eds. (Springer International Publising Switzerland, Switzerland, 2013), pp. 287-321.
67. S. M. Eaton, G. Cerullo, and R. Osellame, "Fundamentals of Femtosecond Laser Modification of Bulk Dielectrics," in *Femtosecond Laser Micromachining*, R. Osellame, G. Cerullo, and R. Ramponi, eds. (Springer Berline Heidelberg, Berlin Heidelberg, 2012), pp. 3-18.
68. L. V. Keldysh, "Ionization in the field of a strong electrmagnetic wave," Soviet Physics Journal of Experimental and Theoretical Physics **20**, 1307-1314 (1965).
69. R. Thomson and G. Cerullo, "Ultrafast Laser Inscription of Photonic Devices in Bulk Dielectrics," in *Ultrafast Nonlinear Optics*, R. Thomson, C. Leburn, and D. Reid, eds. (Springer International Publising Switzerland, Switzerland, 2013), pp. 323-350.
70. C. B. Schaffer, A. O. Jamison, J. F. García, and E. Mazur, "Structural changes induced in transparent materials with ultrashort laser pulses," in *Ultrafast Lasers: Technology and Applications* M. E. Fermann, A. Galvanauskas, and G. Sucha, eds. (CRC Press, Boca Raton, 2002), pp. 395-419.

71. C. B. Schaffer, A. O. Jamison, and E. Mazur, "Morphology of femtosecond laser-induced structural changes in bulk transparent materials," Applied Physics Letters **84**, 1441 (2004).
72. O. Caulier, D. Le Coq, L. Calvez, E. Bychkov, and P. Masselin, "Free carrier accumulation during direct laser writing in chalcogenide glass by light filamentation," Optics Express **19**, 20088-20096 (2011).
73. K. Yamada, W. Watanabe, T. Toma, K. Itoh, and J. Nishii, "In situ observation of photoinduced refractive-index changes in filaments formed in glasses by femtosecond laser pulses," Optics Letters **26**, 19-21 (2001).
74. J. E. McCarthy, H. T. Bookey, N. D. Psaila, R. R. Thomson, and A. K. Kar, "Mid-infrared spectral broadening in an ultrafast laser inscribed gallium lanthanum sulphide waveguide," Optics Express **20**, 1545-1551 (2012).
75. J. A. Dharmadhikari, R. Bernard, A. K. Bhatnagar, D. Mathur, and A. K. Dharmadhikari, "Axicon- based writing of wavegudies in BK7 glass," Optics Letters **38**, 172-174 (2013).
76. R. Thomson, N. D. Psaila, H. T. Bookey, D. Reid, and A. K. Kar, "Controlling the Cross-section of Ultrafast Laser Inscribed Optical Waveguides," in *Femtosecond Laser Micromachining* R. Osellame, G. Cerullo, and R. Ramponi, eds. (Springer Berlin Heidelberg, Berlin Heidleberg, 2012), pp. 93-125.
77. R. Osellame, S. Taccheo, M. Marangoni, R. Ramponi, P. Laporta, S. D. S. Polli, and G. Cerullo, "Femtosecond writing of active optical waveguides with astigmatically shaped beams," Journal of the Optical Society of America B **20**, 1559-1567 (2003).
78. R. R. Thomson, A. S. Bocklet, E. Ramsay, S. J. Beecher, A. H. Greenaway, A. K. Kar, and D. T. Reid, "Shaping ultrafast laser inscribed optical waveguides using a deformable mirror," Optics Express **16**, 12786-12793 (2008).
79. A. Ruiz de la Cruz, A. Ferrer, W. Gawelda, D. Puerto, M. Galván Sosa, J. Siegel, and J. Solis, "Independent control of beam astigmatism and ellipticity using a SLM for fs-laser wavegudie writing," Optics Express **17**, 20853-20859 (2009).
80. A. G. Okhrimchuk, A. V. Shestakov, I. Khrushchev, and J. Mitchell, "Depressed cladding, buried waveguide laser formed in YAG:Nd^{3+} crystal by femtosecond laser writing," Optics Letters **30**, 2248-2250 (2005).

81. H. Zhang, S. M. Eaton, and P. R. Herman, "Low-loss Type II waveguide writing in fused silica with single picosecond laser pulses," Optics Express **14**, 4826-4834 (2006).
82. D. J. Little, M. Ams, P. Dekker, G. D. Marshall, J. M. Dawes, and M. J. Withford, "Femtosecond laser modification of fused silica: the effect of writing polarization on Si-O ring structure," Optics Express **16**, 20029-20037 (2008).
83. Y. Bellouard, E. Barthel, A. A. Said, M. Dugan, and P. Bado, "Scanning thermal microscopy and Raman analysis of bulk fused silica exposed to low-energy femtosecond laser pulses," Optics Express **16**, 19520-19534 (2008).
84. C. Hnatovsky, R. S. Taylor, E. Simova, P. P. Rajeev, D. M. Rayner, V. R. Bhardwaj, and P. B. Corkum, "Fabrication of microchannels in glass using focused femtosecond laser radiation and selective chemical etching," Applied Physics A **84**, 47-61 (2006).
85. P. Urquhart, "Review of rare earth doped fibre lasers and amplifiers " IEE Proceedings J - Optoelectronics **135**, 385-407 (1988).
86. C. Ziolek, H. Ernst, G. F. Will, H. Lubatschowski, and H. Welling, "High-repetition-rate, high-average-power, diode-pumped 2.94-mm Er:YAG laser," Optics Letters **26**, 599-601 (2001).
87. R. J. B. C. E. Hamilton, S. B. Sutton, L. H. Furu, and W. F. Krupke, "1-W average power levels and tunability from a diode-pumped 2.94-μm Er:YAG oscillator," Optics Letters **19**, 1627-1629 (1994).
88. B. J. Dinerman and P. F. Moulton, "3-μm cw laser operations in erbium-doped YSGG, GGG, and YAG," Optics Letters **19**, 1143-1145 (1994).
89. L. Wang, H. Huang, D. Shen, J. Zhang, H. Chen, Y. Wang, X. Liu, and D. Tang, "Room temperature continuous-wave laser performance of LD pumped Er:Lu_2O_3 and Er:Y_2O_3 ceramic at 2.7 μm," Optics Express **22**, 19495-19503 (2014).
90. H. X. Tsao, S. T. Lin, C. L. Wang, H. C. Su, C. M. Huang, Y. W. Jhang, C. Hu, T. Y. Tsai, and J. K. Sheu, "A Green Upconversion Laser with Erbium-Doped $LiLuF_4$ Crystal by 967 nm Fiber Laser Pump," International Journal of Optics and Applications **2**, 72-75 (2012).
91. F. Heine, E. Heaumann, T. Danger, T. Schweizer, and G. Huber, "Green upconversion continuous wave Er^{3+}:$LiYF_4$ laser at room temperature," Applied Physics Letters **65**, 383-384 (1994).

92. A. J. Silversmith, W. Lenth, and R. M. Macfarlane, "Green infrared-pumped erbium upconversion laser," Applied Physics Letters **51**, 1977-1979 (1987).
93. S. M. Kirkpatrick, L. B. Shaw, S. R. Bowman, S. Searles, and B. J. Feldman, "Mid-infrared spectroscopy of erbium doped chloride laser crystals," Optics Express **1**, 78-86 (2019).
94. S. V. Kartalopoulos, "Elastic bandwidth," IEEE Circuits and Devices Magazine **18**, 8-13 (2002).
95. V. R. Supradeepa, J. W. Nicholson, and K. Feder, "Continuous wave Erbium-doped fiber laser with output power of >100 W at 1550 nm in-band core-pumped by a 1480nm Raman fiber laser," in *Conference on Lasers and Electro-Optics 2012*, OSA Technical Digest (online) (Optical Society of America, 2012), CM2N.8.
96. N. Ter-Gabrielyan, V. Fromzel, L. D. Merkle, and M. Dubinskii, "Resonant in-band pumping of cryo-cooled Er^{3+}:YAG laser at 1532, 1534 and 1546 nm: a comparative study " Optics Materials Express **1**, 223-233 (2011).
97. K. N. Gorbachenya, V. E. Kissel, A. S. Yasukevich, A. A. Pavlyuk, and N. V. Kuleshov, "In-band pumped room-temperature Er:$KY(WO_4)_2$," Laser Physics **23**, 12005 (2013).
98. D. Y. Shen, J. K. Sahu, and W. A. Clarkson, "Highly efficient in-band pumped Er:YAG laser with 60W of output at 1645 nm," Optics Letters **31**, 754-756 (2006).
99. R. I. Laming, M. N. Zervas, and D. N. Payne, "Erbium-doped fiber amplifier with 54 dB gain and 3.1 dB noise figures," IEEE Photonics Technology Letters **4**, 1345-1347 (1992).
100. A. Mori, Y. Ohishi, and S. Sudo, "Erbium-doped tellurite glass fibre laser and amplifier," Electronics Letters **33**, 863-864 (1997).
101. S. J. Beecher, R. Thomson, N. D. Psaila, Z. Sun, T. Hasan, A. G. Rozhin, A. C. Ferrari, and A. K. Kar, "320 fs pulse generatiom from an ultrafast inscribed waveguide laser mode-locked by a nanotube saturable absorber " Applied Physics Letters **97**, 111114 (2010).
102. P. Laporta, S. Taccheo, S. Longhi, O. Svelto, and G. Sacchi, "Diode-pumped microchip Er-Yb:glass laser," Optics Letters **18**, 1232-1234 (1993).
103. T. J. Whitley, C. A. Millar, R. Wyatt, M. C. Brierley, and D. Szebesta, "Upconversion pumped green lasing in erbium doped fluorozirconate fibre," Electronics Letters **27**, 1785-1786 (1991).

104. J. Y. Allain, M. Monerie, and H. Poignant, "Tunable green upconversion erbium fibre laser," Electronics Letters **28**, 111-113 (1992).
105. H. Többen, "Room temperature cw fibre laser at 3.5 μm in Er^{3+}-doped ZBLAN glass," Electronics Letters **28**, 1361-1362 (1992).
106. J. F. Pinto, G. H. Rosenblatt, and L. Esterowitz, "Continuous-wave laser action in Er^{3+}:YLF at 3.41 μm," Electronics Letters **30**, 1596-1598 (1994).
107. S. R. Bowman, S. Searles, N. W. Jenkins, S. B. Qadri, E. F. Skelton, and J. Ganem, "New mid-IR laser based on erbium activated low phonon energy crystal," in *Conference on Lasers and Electr-Optics,* (OSA Technical Digest (Optical Society of America, 2001), paper CFD2, Baltimore, USA, 2001).
108. C. Bader and I. Krejci, "Indications and limitations of Er:YAG laser applications in dentistry " American Journal of Dentistry **19**, 178-186 (2006).
109. S. Parker, "Laser/Light Application in Dental Procedures," in *Lasers in Dermatology and Medicine: Dental and Medical Applications* 1ed., K. Nouri, ed. (Springer-Verlang London, London, 2012), pp. 53-80.
110. M. H. Niemz, "Medical Applications of Lasers," in *Laser-Tissue Interactions* 1ed. (Springer-Verlang Berlin Heidelberg, Berlin Heidelberg, 1996).
111. W. Ma, X. Qian, J. Wang, J. Liu, X. Fan, J. Liu, L. Su, and J. Xu, "Highly efficient dual-wavelength mid-infrared CW Laser in diode end-pumped Er:SrF_2 single crystals," Scientific Reports **6**, 36635 (2016).
112. J. A. Frantz, L. B. Shaw, J. S. Sanghera, and I. D. Aggarwal, "Waveguide Amplifiers in Sputtered films of Er^{3+} -doped gallium lanthanum sulfide glass," Optics Express **14**, 1797-1803 (2006).
113. G. Demetriou, J.-P. Bérubé, R. Vallée, Y. Messaddeq, C. P. Petersen, D. Jain, O. Bang, C. Craig, D. H. Hewak, and A. K. Kar, "Refractive index and dispersion control of ultrafast laser inscribed waveguides in gallium lanthanum sulphide for near and mid-infrared applications," Optics Express **24**, 6350-6358 (2016).
114. F. Urbach, "The Long-Wavelength Edge of Photogrpahic Sensitivity and of the Electronic Absorption of Solids," Physical Review **92**, 1324 (1953).
115. J. S. Sanghera, L. B. Shaw, P. Pureza, V. Q. Nguyen, D. Gibson, L. Busse, and I. D. Aggarwal, "Nonlinear Properties of Chalcogenide Glass Fibers," International Journal of Applied Glass Science **1**, 296-308 (2010).
116. A. A. Popescu, D. Savastru, S. Miclos, V. Braic, M. Popescu, A. Manea, and A. Kiss, "Properties of Rare earth Ga-La-S glasses obtained by RF Inductor Heating," Digest Journal of Nanomatierals and Biostructures **6**, 341-348 (2011).

117. R. J. Amjad, M. R. Sahar, S. K. Ghoshal, M. R. Dousti, S. Riaz, and B. A. Tahir, "Optical Investigation of Sm^{3+} Doped Zinc-Lead-Phosphate Glass," Chinese Physics Letters **29**, 087304-087301 - 087304-087304 (2012).

118. D. C. Hanna, "Fibre Lasers: Low-Phonon energy glasses and upconversion," in *Laser Sources and Applications*, A. Miller and D. M. Finlayson, eds. (SUSSP Publications and Institute of Physics Publishing, Bristol, UK, 1996).

119. A. J. Stevenson, H. Serier-Brault, P. Gredin, and M. Mortier, "Fluoride materials for optical applications: Single crystals, ceramics, glasses, and glass-ceramics," Journal of Fluorice Chemistry **132**, 1165-1173 (2011).

120. A. M. Lozac'h, M. Guittard, and J. Flahaut, "Sur une nouvelle famille de combinaison soufrees, de type "mellenite"," Materials Research Bulletin **8**(1973).

121. B. Voigt and D. Linke, "Optical glasses for infrared transmittance - Synthesis and properties of chalcogenide glasses," in *Physics and Applications of Non-Crystalline Semiconductors in Optoelectronics*, A. Andriesh and M. Bertolotti, eds. (Kluwer Academic, Dordrect, The Netherlands, 1997).

122. D. H. Hewak, R. C. Moore, T. Schweizer, J. Wang, B. Samson, W. S. Brocklesby, D. N. Payne, and E. J. Tarbox, "Gallium lanthanum sulphide optical fibre for active and passive applications " Electronics Letters **32**, 384-385 (1996).

123. T. Schweizer, B. N. Samson, R. C. Moore, D. H. Hewak, and D. N. Payne, "Rare-earth doped chalcogenide glass fibre laser," Electronics Letters **33**, 414-416 (1997).

124. T. Schweizer, D. W. Hewak, D. N. Payne, T. Jensen, and G. Huber, "Rare-earth doped chalcogenide glass laser," Electronics Letters **32**, 666-667 (1996).

125. T. Schweizer, D. J. Brady, and D. W. Hewak, "Fabrication and Spectroscopy of erbium doped gallium lanthanum sulphide glasss fibres for mid-infrared laser applications," Optics Express **1**, 102-107 (1997).

126. D. Faucher, M. Bernier, N. Caron, and R. Vallée, "Erbium-doped all-fibre laser at 2.94 um," Optics Letters **34**, 3313-3315 (2009).

127. S. D. Jackson, T. A. King, and M. Pollnau, "Diode-pumped 1.7-W erbium 3-μm fiber laser," Optics Letters **24**, 1133-1135 (1999).

128. H. Yanagita, H. Toratani, T. T. Yamashita, and I. Masuda, "Diode-pumped Er3+ glass laser at 2.7 um," in 1991),

129. K. Renk, "Laser Principle," in *Basics of Laser Physics: For Students of Science and Engineering* (Springer-Verlag Berlin Heidelberg, Berlin Heidelberg, 2012).
130. M. Hughes, W. Yang, and D. H. Hewak, "Fabrication and characterization of femtosecond laser written waveguides in chalcogenide glass," Applied Physics Letters **90**, 131113 (2007).
131. G. Demetriou, "Ultrafast Nonlinear Optics of Bulk and Two-Dimensional Materials for Infrared Applications " (Heriot Watt University ROS Theses Repositry 2016).
132. V. R. Bhardwaj, P. B. Corkum, D. M. Rayner, C. Hnatocsky, E. Simova, and R. S. Taylor, "Stress in femtosecond-laser-written waveguides in fused silica," Optics Letters **29**, 1312-1314 (2004).
133. C. W. Ponader, J. F. Schroeder, and A. M. Streltsov, "Origin of the refractive-index increase in laser-written waveguides in glasses," Journal of Applied Physics **103**, 063516 (2008).
134. S. M. Eaton, W. J. Chen, H. Zhang, R. Iyer, J. Li, M. L. Ng, S. Ho, S. Aitchison, and P. R. Herman, "Spectral Loss Characterization of Femtosecond Laser Written Waveguides in Glass With Application to Demultiplexing of 1300 and 1550 nm Wavelengths," Journal of Lightwave Technology **27**, 1079-1085 (2009).
135. L. Tong, R. R. Gattas, I. Maxwell, J. B. Ashcom, and E. Mazur, "Optical loss measurements in femtosecond laser written waveguides in glass," Optics Communications **259**, 626-630 (2006).
136. S. M. Eaton and P. R. Herman, "Passive Photonic Devices in Glass," in *Femtosecond Laser Micromachining* R. Osellame, G. Cerullo, and R. Ramponi, eds. (Springer Berlin Heidelberg, Berlin Heidelberg, 2012), pp. 155-195.
137. B. McMillen, B. Zhang, K. P. Chen, A. Benayas, and D. Jaque, "Ultrafast laser fabrication of low-loss waveguides in chalcogenide glass with 0.65 dB/cm loss," Optics Letters **37**, 1418-1420 (2012).
138. D. Choudhury, J. R. Macdonald, and A. K. Kar, "Ultrafast laser inscription: perspectives on future integrated applications," Laser and Photonics Reviews **8**, 827-846 (2014).
139. Y. Nasu, M. Kohtoku, and Y. Hibino, "Low-loss waveguides written with femtosecond laser for flexible interconnection in a planar light-wave circuit," Optics Letters **30**, 723-725 (2005).

140. J. Lapointe, M. Gagné, M. J. Li, and R. Kashyap, "Making smart phones smarter with photonics," Optics Express **22**, 15473-15483 (2014).
141. A. Arriola, S. Mukherjee, D. Choudhury, L. Labadie, and R. R. Thomson, "Ultrafast laser inscription of mid-IR directional couplers for stellar interferometry," Optics Letters **39**, 4820-4822 (2014).
142. F. Fusari, R. R. Thomson, G. Jose, F. M. Bain, A. A. Lagatsky, N. D. Psaila, A. K. Kar, A. Jha, W. Sibbett, and C. T. A. Brown, "Lasing action at around 1.9 μm from an ultrafast laser inscribed Tm-doped glass waveguide," Optics Letters **36**, 1566-1568 (2011).
143. R. Mary, S. J. Beecher, G. Brown, R. R. Thomson, D. Jaque, S. Ohara, and A. K. Kar, "Compact, highly efficient ytterbium doped bismuthate glass waveguide laser," Optics Letters **37**, 1691-1693 (2012).
144. E. Ramsay, R. Thomson, N. D. Psaila, A. K. Kar, and D. T. Reid, "Laser action From an Ultrafast Laser Inscribed Nd-Doped Silicate Glass Waveguide," IEEE Photonics Technology Letters **22**, 742-744 (2010).
145. G. Della Valle, S. Taccheo, R. Osellame, A. Festa, G. Cerullo, and P. Laporta, "1.5 μm single longitudinal mode waveguide laser fabricated by femtosecond laser writing," Optics Express **15**, 3190-3194 (2007).
146. R. Scheps, "Basic Concepts," in *Introduction to Laser Diode-Pumped Solid State Lasers* (SPIE Press, 2002), pp. 7-15.
147. J. N. Downing "Charactersistics of Optical Fibers," in *Fiber-optic communications* (Thomson Delmar Learning Kentucky USA, 2004).
148. P. C. Becker, N. A. Olsson, and J. R. Simpson, "Rare Earth Ions Introductory Survey," in *Erbium-Doped Fiber Amplifiers: Fundamentals and Technology* (Academic Press, London, UK, 1999), pp. 87-130.
149. T. Jensen, A. Diening, G. Huber, and B. H. T. Chai, "Investigation of diode-pumped 2.8-μm Er:LiYF4 lasers with various doping levels," Optics Letters **21**, 585-587 (1996).
150. R. C. Stoneman, J. G. Lynn, and L. Esterowitz, "Direct Upper-State Pumping of the 2.8 μm Er^{3+} : YLF Laser," IEEE Journal of Quantum Electronics **28**, 1041-1045 (1992).
151. J. W. Kim, J. I. Mackenzie, and W. A. Clarkson, "Influence of energy-transfer-upconversion on threshold pump power in quasi-three-level solid-state lasers," Optics Express **17**, 11935-11943 (2009).

152. P. Blixt, J. Nilsson, T. Carlnas, and B. Jaskorzynska, "Concentration-Dependent Upconversion in Er $^{3+}$ -Doped Fiber Amplifiers: Experiments and Modeling " IEEE Photonics Technology Letters **3**, 996-998 (1991).

153. R. Hui and M. O'Sullivan, "Optical Fibre Measurement," in *Fiber Optic Measurement Techniques* (Academic Press, 2009), pp. 365-479.

154. W. Demtröder, "Time-Resolved Laser Spectroscopy," in *Laser Spectroscopy* (Springer-Verlag Berlin Heidelberg, Berlin Heidelberg, 2008), pp. 259-350.

155. J. E. Román, M. Hempstead, W. S. Brocklesby, S. Nouh, and J. S. Wilkinson, "Ion-exchanged Er/Yb waveguide laser at 1.5 μm pumped by laser diode," Electronics Letters **31**, 1345-1346 (1995).

156. J. T. Kringlebotn, J. L. Archambault, L. Reekie, J. E. Townsend, G. Vienne, and D. N. Payne, "Highly-efficient, low-noise grating-feedback Er3+:Yb3+ codoped fibre laser," Electronics Letters **30**, 972-973 (1994).

157. J. D. Minelly, W. L. Barnes, R. Laming, P. R. Morkel, J. E. Townsend, S. G. Grubb, and D. N. Payne, "Diode-array pumping of Er^{3+}/Yb^{3+} Co-doped fiber lasers and amplifiers," Photonics Technology Letters, IEEE **5**, 301-303 (1993).

158. Z. J. Chen, J. D. Minelly, and Y. Gu, "Compact low cost Er3+/Yb3+ co-doped fibre amplifiers pumped by 827 nm laser diode," Electronics Letters **32**, 1812-1813 (1996).

159. F. K. E. Georgiou, O. Musset, J. Boquillon, "1.65 um Er:Yb:YAG diode-pumped laser delivering 80mJ pulse enrgy," Optical Engineering **44**(2005).

160. D. S. Knowles and H. P. Jenssen, "Upconversion versus Pr-deactivation for Efficient 3 μm Laser Operation in Er," IEEE Journal of Quantum Electronics **28**, 1197-1208 (1992).

161. W. Koechner, "Q-Switching," in *Solid-State Laser Engineering* (Springer New York, New York, NY, 2006), pp. 488-533.

162. R. Paschotta, "Q Switching," in *Field Guide to Laser Pulse Generation,* (SPIE Press, Bellingham, WA, 2008).

163. S. L. Kilmer and R. R. Anderson, "Clinical Use of the Q-Switched Ruby and the Q-Switched Nd:YAG (1064 nm and 532 nm) Lasers for Treatment of Tattoos," The Journal of Dermatologic Surgery and Oncology **19**, 330-338 (1993).

164. J. F. Ready, "Distance Measurement and Dimenional Control," in *Industrial Applications of Lasers* 2nd ed. (Academic Press, 1997), pp. 256-277.

165. M. Skorczakowski, J. Swiderski, W. Pichola, P. Nyga, A. Zajac, M. Maciejewska, L. Galecki, J. Kasprzak, S. Gross, A. Heinrich, and T. Bragagna,

"Mid-infrared Q-switched Er:YAG laser for medical applications," Laser Physics Letters **7**, 498-504 (2010).

166. K. J. Kasunic, "Introduction:Laser Engineering," in *Laser Systems Engineering* (SPIE Press, 2016).
167. W. Koechner, "Mode Locking," in *Solid-State Laser Engineering* (Springer New York, New York, NY, 2006), pp. 534-586.
168. J. Jin, "Dimensional metrology using the optical comb of a mode-locked laser," Measurement Science and Technology **27**, 022001 (2016).
169. U. Keller, "Recent developments in compact ultrafast lasers," Nature **424**, 831-838 (2003).
170. H. A. Haus, "Mode-locking of lasers," IEEE Journal of Selected Topics in Quantum Electronics **6**, 1173-1185 (2000).
171. R. Paschotta, "Mode locking," in *Field Guide to Laser Pulse Generation* (SPIE Press, Bellingham, WA, USA, 2008), pp. 34-38.
172. M. Haiml, R. Grange, and U. Keller, "Optical characterization of semiconductor saturable absorbers," Applied Physics B **79**, 331-339 (2004).
173. F. X. Kärtner and U. Keller, "Stabilization of solitonlike pulses with a slow saturable absorber," Optics Letters **20**, 16-18 (1995).
174. U. Keller, D. A. B. Miller, G. D. Boyd, T. H. Chiu, J. F. Ferguson, and M. T. Asom, "Solid-state low-loss intracavity saturable absorber for Nd:YLF lasers: an antiresonant semiconductor Fabry–Perot saturable absorber," Optics Letters **17**, 505-507 (1992).
175. U. Keller, K. J. Weingarten, F. X. Kartner, D. Kopf, B. Braun, I. D. Jung, R. Fluck, C. Honninger, N. Matuschek, and J. A. d. Au, "Semiconductor saturable absorber mirrors (SESAM's) for femtosecond to nanosecond pulse generation in solid-state lasers," IEEE Journal of Selected Topics in Quantum Electronics **2**, 435-453 (1996).
176. F. X. Kurtner, J. A. d. Au, and U. Keller, "Mode-locking with slow and fast saturable absorbers-what's the difference?," IEEE Journal of Selected Topics in Quantum Electronics **4**, 159-168 (1998).
177. K. Gürs, "Beats and modulation in optical ruby masers," in *Quantum Electronics III*, P. Grivet and N. Bloembergen, eds. (Columbia University Press, New York, 1964), pp. 1113-1119.

178. H. Statz and C. L. Tang, "Zeeman Effect and Nonlinear Interactions between Oscillating Modes in Masers," in *Qauntum Electronics III*, P. Grivet and N. Bloembergen, eds. (Columbia University Press, New York, 1964), pp. 469-498.
179. A. J. DeMaria, D. A. Stetser, and H. Heynau, "SELF MODE-LOCKING OF LASERS WITH SATURABLE ABSORBERS," Applied Physics Letters **8**, 174-176 (1966).
180. C. Hönninger, R. Paschotta, F. Morier-Genoud, M. Moser, and U. Keller, "Q-switching stability limits of continuous-wave passive mode locking," Journal of the Optical Society of America B **16**, 46-56 (1999).
181. J. K. Jabczyński, W. Żendzian, and J. Kwiatkowski, "Q-switched mode locking in diode pumped lasers," Opto-electronics Review **13**, 317-323 (2005).
182. F. X. Kaertner, L. R. Brovelli, D. Kopf, M. Kamp, I. G. Calasso, and U. Keller, "Control of solid state laser dynamics by semiconductor devices," Optical Engineering **34**, 2024-2036, 2013 (1995).
183. V. Liverini, S. Schön, R. Grange, M. Haiml, S. C. Zeller, and U. Keller, "Low-loss GaInNAs saturable absorber mode locking a 1.3-μm solid-state laser," Applied Physics Letters **84**, 4002-4004 (2004).
184. A. C. Tropper, A. H. Quarterman, and K. G. Wilcox, "Ultrafast Vertical-External-Cavity Surface-Emitting Semiconductor Lasers," in *Advances in Semiconductor Lasers*, J. J. Coleman, A. C. Bryce, and C. Jagadish, eds. (Academic Press, USA, 2012), pp. 269-300.
185. R. Paschotta, L. Krainer, S. Lecomte, G. J. Spühler, S. C. Zeller, A. Aschwanden, D. Lorenser, H. J. Unold, K. J. Weingarten, and U. Keller, "Picosecond pulse sources with multi-GHz repetition rates and high output power," New Journal of Physics **6**, 174-174 (2004).
186. D. Reid and C. Leburn, "Advances in Solid-State Ultrafast Laser Oscillators," in *Ultrafast Nonlinear Optics*, R. Thomson, C. Leburn, and D. Reid, eds. (Springer International Publishing Switzerland, Switzerland 2013), pp. 73-104.
187. A. Diebold, F. Emaury, C. Schriber, M. Golling, C. J. Saraceno, T. Südmeyer, and U. Keller, "SESAM mode-locked Yb:CaGdAlO4 thin disk laser with 62 fs pulse generation," Optics Letters **38**, 3842-3845 (2013).
188. C. J. Saraceno, O. H. Heckl, C. R. E. Baer, C. Schriber, M. Golling, K. Beil, C. Kränkel, T. Südmeyer, G. Huber, and U. Keller, "Sub-100 femtosecond pulses from a SESAM modelocked thin disk laser," Applied Physics B **106**, 559-562 (2012).

189. K. Yang, D. Heinecke, J. Paajaste, C. Kölbl, T. Dekorsy, S. Suomalainen, and M. Guina, "Mode-locking of 2 um Tm,Ho:YAG laser with GaInAs and GaSb-based SESAMs," Optics Express **21**, 4311-4318 (2013).
190. I. T. Sorokina and E. Sorokin, "Femtosecond pulse generation from a SESAM mode-locked Cr:ZnSe laser," Conference on Lasers and Electro-Optics/Quantum Electronics and Laser Science Conference and Photonic Applications Systems Technologies, Technical Digest (CD) (Optical Society of America, 2006), paper CMQ2. (2006).
191. X. Bu, Y. Shi, J. Xu, H. Li, and P. Wang, "408 fs SESAM mode locked Cr:ZnSe laser," Proc. SPIE 10619, 1061903 (2018).
192. T. Hasan, Z. Sun, F. Wang, F. Bonaccorso, P. H. Tan, A. G. Rozhin, and A. C. Ferrari, "Nanotube–Polymer Composites for Ultrafast Photonics," Advanced Materials **21**, 3874-3899 (2009).
193. Z. Sun, T. Hasan, and A. C. Ferrari, "Ultrafast lasers mode-locked by nanotubes and graphene," Physica E: Low-dimensional Systems and Nanostructures **44**, 1082-1091 (2012).
194. K. S. Novoselov, A. K. Geim, S. V. Morozov, D. Jiang, Y. Zhang, S. V. Dubonos, I. V. Grigorieva, and A. A. Firsov, "Electric Field Effect in Atomically Thin Carbon Films," Science **306**, 666-669 (2004).
195. Q. Bao, H. Zhang, Y. Wang, Z. Ni, Y. Yan, Z. X. Shen, Z. X. Shen, K. P. Loh, and D. Y. Tang, "Atomic-Layer Graphene as a Saturable Absorber for Ultrafast Pulsed Lasers," Advanced Functional Materials **19**, 3077-3083 (2009).
196. B. Guo, "2D noncarbon materials-based nonlinear optical devices for ultrafast photonics [Invited]," Chin. Opt. Lett. **16**, 020004 (2018).
197. I. H. Baek, H. W. Lee, S. Bae, B. H. Hong, Y. H. Ahn, D.-I. Yeom, and F. Rotermund, "Efficient Mode-Locking of Sub-70-fs Ti:Sapphire Laser by Graphene Saturable Absorber," Applied Physics Express **5**, 032701 (2012).
198. D. E. Spence, P. N. Kean, and W. Sibbett, "60-fsec pulse generation from a self-mode-locked Ti:sapphire laser," Optics Letters **16**, 42-44 (1991).
199. U. Keller, G. W. 'tHooft, W. H. Knox, and J. E. Cunningham, "Femtosecond pulses from a continuously self-starting passively mode-locked Ti:sapphire laser," Optics Letters **16**, 1022-1024 (1991).
200. F. Salin, J. Squier, and M. Piché, "Mode locking of Ti:Al2O3 lasers and self-focusing: a Gaussian approximation," Optics Letters **16**, 1674-1676 (1991).

201. D. H. Sutter, G. Steinmeyer, L. Gallmann, N. Matuschek, F. Morier-Genoud, U. Keller, V. Scheuer, G. Angelow, and T. Tschudi, "Semiconductor saturable-absorber mirror–assisted Kerr-lens mode-locked Ti:sapphire laser producing pulses in the two-cycle regime," Optics Letters **24**, 631-633 (1999).
202. U. Morgner, F. X. Kärtner, S. H. Cho, Y. Chen, H. A. Haus, J. G. Fujimoto, E. P. Ippen, V. Scheuer, G. Angelow, and T. Tschudi, "Sub-two-cycle pulses from a Kerr-lens mode-locked Ti:sapphire laser," Optics Letters **24**, 411-413 (1999).
203. S. Yefet and A. Pe'er, "A Review of Cavity Design for Kerr Lens Mode-Locked Solid-State Lasers," Applied Sciences **3**, 694-724 (2013).
204. A. Major, F. Yoshino, I. Nikolakakos, J. S. Aitchison, and P. W. E. Smith, "Dispersion of the nonlinear refractive index in sapphire," Optics Letters **29**, 602-604 (2004).
205. O. Svelto, "Transient Laser Behaviour," in *Principles of Laser*, D. C. Hanna, ed. (Springer-Verland US, New York, USA, 2010).
206. F. J. Duarte, "Nonlinear Optics," in *Tunable Laser Optics*, F. J. Duarte, ed. (Academic Press, San Diego, 2003), pp. 157-176.
207. J. Jin and S. Kim, "Precision Dimensional Metrology Based on a Femtosecond Pulse Laser," in *Advances in Solid State Lasers Development and Applications*, M. Grishin, ed. (IntechOpen, 2010), pp. 169-194.
208. Y. Wang, T. T. Fernandez, N. Cocuccelli, A. Gambetta, P. Laporta, and G. Galzerano, "47-fs Kerr-lens mode-locked Cr:ZnSe laser with high spectral purity," Optics Express **25**, 25193-25200 (2017).
209. S. Vasilyev, M. Mirov, and V. Gapontsev, "Kerr-lens mode-locked femtosecond polycrystalline Cr2+:ZnS and Cr2+:ZnSe lasers," Optics Express **22**, 5118-5123 (2014).
210. S. Vasilyev, I. Moskalev, M. Mirov, V. Smolski, S. Mirov, and V. Gapontsev, "Kerr-Lens Mode-Locked Middle IR Polycrystalline Cr:ZnS Laser with a Repetition Rate 1.2 GHz," in *Lasers Congress 2016 (ASSL, LSC, LAC)*, OSA Technical Digest (online) (Optical Society of America, 2016), AW1A.2.
211. M. N. Cizmeciyan, H. Cankaya, A. Kurt, and A. Sennaroglu, "Operation of femtosecond Kerr-lens mode-locked Cr:ZnSe lasers with different dispersion compensation methods," Applied Physics B **106**, 887-892 (2012).
212. S. Vasilyev, I. Moskalev, M. Mirov, S. Mirov, and V. Gapontsev, "Three optical cycle mid-IR Kerr-lens mode-locked polycrystalline Cr^{2+}:ZnS laser," Optics Letters **40**, 5054-5057 (2015).

213. S. Vasilyev, M. Mirov, and V. Gapontsev, "High Power Kerr-Lens Mode-Locked Femtosecond mid-IR Laser with Efficient Second Harmonic Generation in Polycrystalline Cr2+:ZnS and Cr2+:ZnSe," in *Advanced Solid State Lasers*, OSA Technical Digest (online) (Optical Society of America, 2014), AM3A.3.

214. N. Nagl, S. Gröbmeyer, V. Pervak, F. Krausz, O. Pronin, and K. F. Mak, "Directly diode-pumped, Kerr-lens mode-locked, few-cycle Cr:ZnSe oscillator," Optics Express **27**, 24445-24454 (2019).

215. M. Rosete-Anguliar, F. C. Estrada-Selva, N. C. Bruce, C. J. Román-Moreno, and R. Orgeta-Martínez, "Calculation of temporal spreading of ultrashort pulses propagating through optical glasses," Revista Mexicana de Fisica **54**, 141-148 (2008).

216. J. W. Gooch, "Sellmeier Equation," in *Encyclopedic Dictionary of Polymers*, J. W. Gooch, ed. (Springer New York, New York, NY, 2011), pp. 653-654.

217. U. Keller, "Ultrashort Pulse Generation," in *Proceedings of SUSSP 52 - Advances in Lasers and Applications*, (Institute of Physics Publising 1999), 83-115.

218. C. del Río Campos and P. R. Horche, "Effects of Dispersion Fiber on CWDM Directly Modulated System Performance," in *Optical Fiber Communications and Devices*, M. Yasin, ed. (IntechOpen, 2012), pp. 55-76.

219. U. Keller and R. Paschotta, "Ultrafast Solid-State Lasers," in *Ultrafast Lasers: Technology and Applications* M. E. Fermann, A. Galvanauskas, and G. Sucha, eds. (Markel Dekker, Inc., New York, USA, 2003), pp. 1-285.

220. B. Jopson and A. Gnauck, "Dispersion compensation for optical fiber systems," IEEE Communications Magazine **33**, 96-102 (1995).

221. M. N. Cizmeciyan, J. W. Kim, S. Bae, B. H. Hong, F. Rotermund, and A. Sennaroglu, "Graphene mode-locked femtosecond Cr:ZnSe laser at 2500 nm," Optics Letters **38**, 341-343 (2013).

222. J. Ma, H. Huang, K. Ning, X. Xu, G. Xie, L. Qian, K. P. Loh, and D. Tang, "Generation of 30 fs pulses from a diode-pumped graphene mode-locked Yb:CaYAlO4 laser," Optics Letters **41**, 890-893 (2016).

223. Y. Shaked, S. Yefet, and A. Pe'er, "The Prism-Pair: Simple Dispersion Compensation and Spectral Shaping of Ultrashort Pulses," International Journal of Experimental Spectrscopic Techniques **1**, 007 (2016).

224. M. Wollenhaupt, A. Assion, and T. Baumert, "Short and Ultrashort Laser Pulses," in *Springer Handbook of Lasers and Optics*, F. Träger, ed. (Springer-Verlang Berlin Heidelberg, Berlin Heidelberg, 2012), pp. 1047-1094.
225. I. T. Sorokina and E. Sorokin, "Chirped-mirror dispersion controlled femtosecond Cr:ZnSe laser," in *Advanced Solid-State Photonics, OSA Technical Digest Series (CD) (Optical Society of America, 2007), paper WA7.,* (2007).
226. J. A. Armstrong, "MEASUREMENT OF PICOSECOND LASER PULSE WIDTHS," Applied Physics Letters **10**, 16-18 (1967).
227. D. T. Reid, "Measuring ultrafast laser pulses," in *Ultrafast Photonics*, A. Miller, D. T. Reid, and D. M. Finlayson, eds. (SUSSP Publications & Institute of Physics Publishing, Cornwall, UK, 2004), pp. 59-71.
228. R. A. McCracken, "Femtosecond optical parametric oscillator frequency combs for coherent pulse synthesis," (Heriot Watt University, Edinburgh, 2013).
229. K. G. Jespersen, T. Le, L. Grüner-Nielsen, D. Jakobsen, M. E. V. Pederesen, M. B. Smedemand, S. R. Keiding, and B. Palsdottir, "A higher-order-mode fiber delivery for Ti:Sapphire femtosecond lasers," Optics Express **18**, 7798-7806 (2010).
230. D. T. Reid, W. Sibbett, J. M. Dudley, L. P. Barry, B. Thomsen, and J. D. Harvey, "Commercial Semiconductor Devices for Two Photon Absorption Autocorrelation of Ultrashort Light Pulses," Applied Optics **37**, 8142-8144 (1998).
231. R. Trebino, K. W. DeLong, D. N. Fittinghoff, J. N. Sweetser, M. A. Krumbügel, B. A. Richman, and D. J. Kane, "Measuring ultrashort laser pulses in the time-frequency domain using frequency-resolved optical gating," Review of Scientific Instruments **68**, 3277-3295 (1997).
232. B. Xu, J. M. Gunn, J. M. D. Cruz, V. V. Lozovoy, and M. Dantus, "Quantitative investigation of the multiphoton intrapulse interference phase scan method for simultaneous phase measurement and compensation of femtosecond laser pulses," Journal of the Optical Society of America B **23**, 750-759 (2006).
233. W. Koechner, "Properties of Solid-State Laser Materials," in *Solid-State Laser Engineering,* 5 ed., A. L. Schawlow, T. Tamir, and A. E. Siegman, eds. (Springer-Verlang Berlin Heidelberg, Berlin Heidelberg, 1999), pp. 28-87.
234. R. C. Powell, "$Y_3Al_5O_{12}:Nd^{3+}$ Laser Crystals," in *Physics of Solid-State Laser Materials*, G. W. F. Drake, ed. (Springer-Verland New York New York, 1998), pp. 294-338.

235. J. L. Caslavsky and D. J. Viechnicki, "Melting behaviour and metastability of yttrium aluminium garnet (YAG) and YAIO3 determined by optical differential thermal analysis," JOurnal of Materials Science **15**, 1709-1718 (1980).

236. J. Yi, B. Tu, X. An, X. Ruan, J. Wu, H. Su, J. Shang, Y. Yu, Y. Liao, H. Cao, L. Cui, Q. Gao, and K. Zhang, "9 kilowatt-level direct-liquid-cooled Nd:YAG multi-module QCW laser," Optics Express **26**, 13915-13926 (2018).

237. L. Sun, Y. Guo, C. Shao, Y. Li, Y. Zheng, C. Sun, X. Wang, and L. Huang, "10.8 kW, 2.6 times diffraction limited laser based on a continuous wave Nd:YAG oscillator and an extra-cavity adaptive optics system," Optics Letters **43**, 4160-4163 (2018).

238. W. J. Tropf, T. J. Harris, and M. E. Thomas, "OPTICAL MATERIALS: VISIBLE AND INFRARED," in *ELECTRO-OPTICS HANDBOOK,* 2nd ed., R. W. Waynant and M. N. Ediger, eds. (McGraw-Hill, Inc, New York, USA, 2000).

239. A. Mandl and D. E. Kilmek, "Textron's J-HPSSL 100 kW ThinZag® Laser Program," in *Conference on Lasers and Electro-Optics* (San Jose, CA, USA, 2010), p. paper JThH2

240. J. Goodberlet, J. Jacobson, J. G. Fujimoto, P. A. Schulz, and T. Y. Fan, "Self-starting additive-pulse mode-locked diode-pumped Nd:YAG laser," Optics Letters **15**, 504-506 (1990).

241. F. Chen, X. Yu, R. P. Yan, X. D. Li, D. J. Li, G. L. Yang, J. J. Xie, and J. Guo, "Experimental investigation of a diode-pumped powerful continuous-wave dual-wavelength Nd:YAG laser at 946 and 938.6 nm," Laser Physics **23**, 055002 (2013).

242. B. Xu, Y. Wang, X. Huang, J. Lan, Z. Lin, Z. Luo, H. Xu, Z. Cai, and R. Moncorgé, "Watt-level narrow-linewidth Nd:YAG laser operating on 4F3/2 → 4I15/2 transition at 1834 nm," Optics Express **24**, 3601-3606 (2016).

243. H. Zhu, Y. Zhang, J. Zhang, Y. Zhang, Y. Duan, X. Ruan, J. Zhang, and D. Tang, "1.96-μm Tm:YAG Ceramic Laser," IEEE Photonics Journal **9**, 1-7 (2017).

244. H. Eilers, W. M. Dennis, W. M. Yen, S. Kuck, K. Peterman, G. Huber, and W. Jia, "Performance of a Cr:YAG laser," IEEE Journal of Quantum Electronics **29**, 2508-2512 (1993).

245. C. Hönninger, "Ultrafast ytterbium-doped bulk lasers and laser amplifiers," Applied Physics B **69**, 3-17 (1999).

246. N. P. Barnes and B. M. Walsh, *Tm:glass laser pumping a Ho:YAG laser*, Third International Asia-Pacific Environmental Remote Sensing Remote Sensing of the Atmosphere, Ocean, Environment, and Space (SPIE, 2003), Vol. 4893.

247. K. Naganuma and K. Mogi, "50-fs pulse generation directly from a colliding-pulse mode-locked Ti:sapphire laser using an antiresonant ring mirror," Optics Letters **16**, 738-740 (1991).

248. R. Remski and D. Smith, "Temperature Dependence of Pulsed Laser Threshold inYAG: Er^{3+}, Tm^{3+}, Ho^{3+}," IEEE Journal of Quantum Electronics **6**, 750-751 (1970).

249. M. E. Storm, "Laser characteristics of a *Q*-switched Ho:Tm:Cr:YAG," Applied Optics **27**, 4170-4172 (1988).

250. L. F. Johnson, J. E. Geusic, and L. G. V. Uitert, "EFFICIENT, HIGH-POWER COHERENT EMISSION FROM Ho3+ IONS IN YTTRIUM ALUMINUM GARNET, ASSISTED BY ENERGY TRANSFER," Applied Physics Letters **8**, 200-202 (1966).

251. L. F. Johnson, J. E. Geusic, and L. G. V. Uitert, "COHERENT OSCILLATIONS FROM Tm3+, Ho3+, Yb3+ and Er3+ IONS IN YTTRIUM ALUMINUM GARNET," Applied Physics Letters **7**, 127-129 (1965).

252. T. Y. Fan, G. Huber, R. L. Byer, and P. Mitzscherlich, "Continuous-wave operation at 2.1 μm of a diode-laser-pumped, Tm-sensitized Ho:$Y_3Al_5O_{12}$ laser at 300 K," Optics Letters **12**, 678-680 (1987).

253. S. W. Henderson and C. P. Hale, "Tunable single-longitudinal-mode diode laser pumped Tm:Ho:YAG laser," Applied Optics **29**, 1716-1718 (1990).

254. R. C. Stoneman and L. Esterowitz, "Intracavity-pumped 2.09-μm Ho:YAG laser," Optics Letters **17**, 736-738 (1992).

255. K. Scholle, S. Lamrini, P. Koopmann, and P. Fuhrberg, "2 μm Laser Sources and Their Possible Applications," in *Frontiers in Guided Wave Optics and Optoelectronics*, B. Pal, ed. (IntechOpen, 2010), pp. 471-500.

256. S. So, J. I. Mackenzie, D. P. Shepherd, and W. A. Clarkson, *High-power slab-based Tm:YLF laser for in-band pumping of Ho:YAG*, Lasers and Applications in Science and Engineering (SPIE, 2008), Vol. 6871.

257. A. A. Kaminskii, "Stark-Level Structure of Lasing Activator Ions," in *Crystalline Lasers:Physical Processes and Operating Schemes* (CRC Press, Inc, Boca Raton, Florida, USA, 1996).

258. T. Y. Fan, G. Huber, R. L. Byer, and P. Mitzscherlich, "Spectroscopy and diode laser-pumped operation of Tm,Ho:YAG," IEEE Journal of Quantum Electronics **24**, 924-933 (1988).

259. M. Ganija, A. Hemming, N. Simakov, K. Boyd, J. Haub, P. Veitch, and J. Munch, "High power cryogenic Ho:YAG laser," Optics Express **25**, 31889-31895 (2017).

260. J. W. Kim, J. I. Mackenzie, W. O. S. Bailey, L. Pearson, D. Y. Shen, Y. Yang, and W. A. Clarkson, "Cryogenically-cooled Ho:YAG laser in-band pumped by a Tm fibre laser," Lasers and Electro-optics 2009 and the European Quantum Electronics Conference. CLEO Europe - EQEC 2009. European Conference on (2009).

261. Y.-J. Shen, B.-Q. Yao, X.-M. Duan, G.-L. Zhu, W. Wang, Y.-L. Ju, and Y.-Z. Wang, "103 W in-band dual-end-pumped Ho:YAG laser," Optics Letters **37**, 3558-3560 (2012).

262. J. Zhang, F. Schulze, K. F. Mak, V. Pervak, D. Bauer, D. Sutter, and O. Pronin, "High-Power, High-Efficiency Tm:YAG and Ho:YAG Thin-Disk Lasers," Laser & Photonics Reviews **12**, 1700273 (2018).

263. I. Elder and T. Kendall, *Efficient single-pass resonantly-pumped Ho:YAG laser*, SPIE Security + Defence (SPIE, 2012), Vol. 8543.

264. J. R. Macdonald, S. J. Beecher, A. Lancaster, P. A. Berry, K. L. Schepler, S. B. Mirov, and A. K. Kar, "Compact Cr:ZnS channel waveguide laser operating at 2333 nm," Optics Express **22**, 7052-7057 (2014).

265. R. Mary, G. Brown, S. J. Beecher, F. Torrisi, S. Milana, D. Popa, T. Hasan, Z. Sun, E. Lidorikis, S. Ohara, A. C. Ferrari, and A. K. Kar, "1.5 GHz picosecond pulse generation from a monolithic waveguide laser with a graphene-film saturable output coupler," Optics Express **21**, 7943-7950 (2013).

266. Y. Ren, G. Brown, R. Mary, G. Demetriou, D. Popa, F. Torrisi, A. C. Ferrari, F. Chen, and A. K. Kar, "7.8-GHz Graphene-Baser 2-um Monolithic Waveguide Laser," IEEE Journal of Selected Topics in Quantum Electronics **21**, 1602106-(2015).

267. A. G. Okhrimchuk and P. A. Obraztsov, "11-GHz waveguide Nd:YAG laser CW mode-locked with single-layer graphene," Scientific Reports **5**, 11172 (2015).

268. A. Rodenas, A. Benayas, J. R. Macdonald, J. Zhang, D. Y. Tang, D. Jaque, and A. K. Kar, "Direct laser writing of near-IR step-index buried channel waveguides in rare earth doped YAG," Optics Letters **36**, 3395-3397 (2011).

269. P. Wu, S. He, and H. Liu, "Annular waveguide lasers at 1064 nm in Nd:YAG crystal produced by femtosecond laser inscription," Applied Optics **57**, 5420-5424 (2018).

270. Y. Ren, G. Brown, A. Ródenas, S. Beecher, F. Chen, and A. K. Kar, "Mid-infrared waveguide lasers in rare-earth-doped YAG," Optics Letters **37**, 3339-3341 (2012).

271. A. Lancaster, "Mid-IR Waveguide Lasers in Transition Metal Doped II-VI Semiconductors " (Heriot Watt University Edinburgh, 2017).

272. J. M. Khosrofian and B. A. Garetz, "Measurement of a Gaussian laser beam diameter through the direct inversion of knife-edge data," Applied Optics **22**, 3406-3410 (1983).

273. D. Findlay and R. A. Clay, "The measurement of internal losses in 4-level lasers," Physics Letters **20**, 277-278 (1966).

274. J. A. Caird, S. A. Payne, P. R. Staber, A. J. Ramponi, L. L. Chase, and W. F. Krupke, "Quantum electronic properties of the $Na_3Ga_2Li_3F_{12}:Cr^{3+}$ laser," IEEE Journal of Quantum Electronics **24**, 1077-1099 (1988).

275. A. Choudhary, "ULTRAFAST WAVEGUIDE LASERS," (University of Southampton, Optoelectronics Research Centre, Southampton, 2014).

276. P. Koopmann, S. Lamrini, K. Scholle, M. Schäfer, P. Fuhrberg, and G. Huber, "Holmium-doped Lu2O3, Y2O3, and Sc2O3 for lasers above 2.1 μm," Optics Express **21**, 3926-3931 (2013).

277. J. P. Landy, "Optical oblique -incidence reflectivity difference microscopy: Application to label-free detection of reactions in biomolecular microarrays," (University of California, Davis, 2008).

278. P. Loiko, J. M. Serres, X. Mateos, K. Yumashev, N. Kuleshov, V. Petrov, U. Griebner, M. Aguiló, and F. Díaz, "Microchip laser operation of Tm,Ho:KLu(WO4)2 crystal," Optics Express **22**, 27976-27984 (2014).

279. S. Lamrini, P. Koopmann, M. Schäfer, K. Scholle, and P. Fuhrberg, "Efficient high-power Ho:YAG laser directly in-band pimped by a GaSb-based laser diode stack at 1.9 μm," Applied Physics B **106**, 315-319 (2012).

280. T. Zhao, F. Wang, and D. Y. Shen, "High-power Ho:YAG laser wing-pumped by a Tm:fiber laser at 1933 nm," Applied Optics **54**, 1594-1597 (2015).

281. S. A. McDaniel, P. A. Berry, G. Cook, D. Zelmon, S. Meissner, H. Meissner, and X. Mu, "CW and passively Q-Switched operation of a Ho:YAG waveguide laser," Optics & Laser Technology **91**, 1-6 (2017).
282. S. McDaniel, F. Thorburn, A. Lancaster, R. Stites, G. Cook, and A. Kar, "Operation of Ho:YAG ultrafast laser inscribed waveguide lasers," Applied Optics **56**, 3251-3256 (2017).
283. D. A. Braje, M. S. Kirchner, S. Osterman, T. Fortier, and S. A. Diddams, "Astronomical spectrograph calibration with broad-spectrum frequency combs," The European Physical Journal D **48**, 57-66 (2008).
284. Y. Wang, R. Lan, X. Mateos, J. Li, C. Hu, C. Li, S. Suomalainen, A. Härkönen, M. Guina, V. Pertov, and U. Griebner, "Broadly tunable mode-locked Ho:YAG ceramic laser around 2.1 um," Optics Express **24**, 18003-18012 (2016).
285. J. Ma, Z. Qin, G. Xie, L. Qian, and D. Tang, "Review of mid-infrared mode-locked laser sources in the 2.0 μm–3.5 μm spectral region," Applied Physics Reviews **6**, 021317 (2019).
286. M. Pawliszewska, Y. Ge, Z. Li, H. Zhang, and J. Sotor, "Fundamental and harmonic mode-locking at 2.1 μm with black phosphorus saturable absorber," Optics Express **25**, 16916-16921 (2017).
287. Y. Chen, S. Chen, J. Liu, Y. Gao, and W. Zhang, "Sub-300 femtosecond soliton tunable fiber laser with all-anomalous dispersion passively mode locked by black phosphorus," Optics Express **24**, 13316-13324 (2016).
288. M. Pawliszewska, T. Martynkien, A. Przewłoka, and J. Sotor, "Dispersion-managed Ho-doped fiber laser mode-locked with a graphene saturable absorber," Optics Letters **43**, 38-41 (2018).
289. F. Heine, E. Heaumann, G. Huber, and K. L. Schelper, "Mode locking of room-temperature cw thulium and holmium lasers," Applied Physics Letters **60**, 1161 (1992).
290. J. Zhang, K. F. Mak, S. Gröbmeyer, D. Bauer, D. Sutter, V. Pervak, F. Krausz, and O. Pronin, "Kerr-lens mode-locked Ho:YAG thin-disk oscillator at 2.1 μm," in *2017 European Conference on Lasers and Electro-Optics and European Quantum Electronics Conference*, (Optical Society of America, 2017), CA_5_5.
291. J. Zhang, K. F. Mak, and O. Pronin, "Kerr-Lens Mode-Locked 2-μm Thin-Disk Lasers," IEEE Journal of Selected Topics in Quantum Electronics **24**, 1-11 (2018).

292. X. Jiang, S. Gross, H. Zhang, Z. Guo, M. J. Withford, and A. Fuerbach, "Bismuth telluride topological insulator nanosheet saturable absorbers for q-switched mode-locked Tm:ZBLAN waveguide," Annalen der physik **528**, 543-550 (2016).
293. S. Husaini and R. G. Bedford, "Graphene saturable absorber for high power semiconductor disk laser modelocking," Applied Physics Letters **104**, 161107 (2014).
294. Y. Terekhov, I. S. Moskalev, D. V. Martyshkin, V. V. Fedorov, and S. B. Mirov, "Cr-ZnSe passively Q-switched fiber-bulk Ho:YAG hybrid laser," in *SPIE LASE*, (SPIE, 2010),
295. F. Thorburn, A. Lancaster, S. McDaniel, G. Cook, and A. K. Kar, "5.9 GHz graphene based q-switched modelocked mid-infrared monolithic waveguide laser," Optics Express **25**, 26166-26174 (2017).
296. S. Vasilyev, I. Moskalev, M. Mirov, V. Smolski, S. Mirov, and V. Gapontsev, "Ultrafast middle-IR lasers and amplifiers based on polycrystalline Cr:ZnS and Cr:ZnSe " Optical Material Express **7**, 2636-2650 (2017).
297. T. Popmintchev, M.-C. Chen, D. Popmintchev, P. Arpin, S. Brown, S. Ališauskas, G. Andriukaitis, T. Balčiunas, O. D. Mücke, A. Pugzlys, A. Baltuška, B. Shim, S. E. Schrauth, A. Gaeta, C. Hernández-García, L. Plaja, A. Becker, A. Jaron-Becker, M. M. Murnane, and H. C. Kapteyn, "Bright Coherent Ultrahigh Harmonics in the keV X-ray Regime from Mid-Infrared Femtosecond Lasers," Science **336**, 1287 (2012).
298. A. H. Nejadmalayeri, P. R. Herman, J. Burghoff, M. Will, S. Nolte, and A. Tünnermann, "Inscription of optical waveguides in crystalline silicon by mid-infrared femtosecond laser pulses," Optics Letters **30**, 964-966 (2005).
299. I. T. Sorokina and E. Sorokin, "Femtosecond Cr2+-Based Lasers," IEEE Journal of Selected Topics in Quantum Electronics **21**, 273-291 (2015).
300. S. Mirov, I. Moskalev, S. Vasilyev, V. Smolski, V. Federov, D. Martyshkin, J. Peppers, M. Mirov, A. Dergachev, and V. Gapontsev, "Frontiers of mid-IR lasers based on transition metal doped chalcogenides," IEEE Journal of Selected Topics in Quantum Electronics, 08295223 (2018).
301. K. Petermann, "Oxide laser crystals doped with rare earth and transition metal ions," in *Handbook of solid-sate lasers*, B. Denker and E. Shklovsky, eds. (Woodhead Publishing, 2013), pp. 3-27.

302. W. R. Rapoport and C. P. Khattak, "Titanium sapphire laser characteristics," Applied Optics **27**, 2677-2684 (1988).
303. J. Peppers, V. V. Fedorov, and S. B. Mirov, "Mid-IR photoluminescence of Fe2+ and Cr2+ ions in ZnSe crystal under excitation in charge transfer bands," Optics Express **23**, 4406-4414 (2015).
304. H. A. Jahn, E. Teller, and G. F. Donnan, "Stability of polyatomic molecules in degenerate electronic states - I—Orbital degeneracy," Proceedings of the Royal Society of London. Series A - Mathematical and Physical Sciences **161**, 220-235 (1937).
305. M. Kaminska, J. M. Baranowski, S. M. Uba, and J. T. Vallin, "Absorption and luminescence of Cr2+(d4) in II-VI compounds," Journal of Physics C: Solid State Physics **12**, 2197-2214 (1979).
306. C. E. Housecroft and A. G. Sharpe, "*d*-Block chemistry: coordination complexes," in *Inorganic Chemistry Second Edition,* 2nd ed. (Pearson Education Limited, 2005).
307. S. B. Mirov, V. V. Fedorov, D. Martyshkin, I. S. Moskalev, M. Mirov, and S. Vasilyev, "Progress in Mid-IR Lasers Based on Cr and Fe-Doped II–VI Chalcogenides," IEEE Journal of Selected Topics in Quantum Electronics **21**, 292-310 (2015).
308. S. Vasilyev, I. Moskalev, M. Mirov, V. Smolski, S. Mirov, and V. Gapontsev, "Recent Breakthroughs in Solid-State Mid-IR Laser Technology," Laser Technik Journal **13**, 24-27 (2016).
309. E. Sorokin and I. T. Sorokina, "Tunable diode-pumped continuous-wave Cr2+:ZnSe laser," Applied Physics Letters **80**, 3289-3291 (2002).
310. A. V. Podlipensky, V. G. Shcherbitsky, N. V. Kuleshov, V. I. Levchenko, V. N. Yakimovich, M. Mond, E. Heumann, G. Huber, H. Kretschmann, and S. Kück, "Efficient laser operation and continuous-wave diode pumping of Cr2+:ZnSe single crystals," Applied Physics B **72**, 253-255 (2001).
311. T. J. Carrig, G. J. Wagner, A. Sennaroglu, J. Y. Jeong, and C. R. Pollock, "Mode-locked Cr^{2+}ZnSe laser," Optics Letters **25**, 168-170 (2000).
312. C. R. Pollock, N. A. Brilliant, D. Gwin, T. J. Carrig, W. J. Alford, J. B. Heroux, W. I. Wang, I. Vurgaftman, and J. R. Meyer, "Mode locked and Q-switched Cr:ZnSe laser using a Semiconductor Saturable Absorbing Mirror (SESAM)," in *Advanced Solid-State Photonics*, Technical Digest (Optical Society of America, 2005), TuA6.

313. E. Sorokin and I. T. Sorokina, "Ultrashort-pulsed Kerr-lens modelocked Cr:ZnSe laser," in *CLEO/Europe and EQEC 2009 Conference Digest*, (Optical Society of America, 2009), CF1_3.

314. J. Ma, G. Xie, P. Lv, W. Gao, P. Yuan, L. Qian, U. Griebner, V. Petrov, H. Yu, H. Zhang, and J. Wang, "Wavelength-versatile graphene-gold film saturable absorber mirror for ultra-broadband mode-locking of bulk lasers," Scientific reports **4**, 5016-5016 (2014).

315. N. Tolstik, E. Sorokin, and I. T. Sorokina, "Graphene mode-locked Cr:ZnS laser with 41 fs pulse duration," Optics Express **22**, 5564-5571 (2014).

316. S. Vasilyev, M. Mirov, and V. Gapontsev, "Mid-IR Kerr-Lens Mode-Locked Polycrystalline Cr2+:ZnS Laser with 0.5 MW Peak Power," in *Advanced Solid State Lasers*, OSA Technical Digest (online) (Optical Society of America, 2015), AW4A.3.

317. D. M. Simanovskii, H. A. Schwettman, H. Lee, and A. J. Welch, "Midinfrared Optical Breakdown in Transparent Dielectrics," Physical Review Letters **91**, 107601 (2003).

318. I. T. Sorokina, E. Sorokin, S. Mirov, V. Fedorov, V. Badikov, V. Panyutin, and K. I. Schaffers, "Broadly tunable compact continuous-wave Cr2+:ZnS laser," Optics Letters **27**, 1040-1042 (2002).

319. S. McDaniel, A. Lancaster, R. Stites, F. Thorburn, A. Kar, and G. Cook, *Cr:ZnSe guided wave lasers and materials*, SPIE LASE (SPIE, 2017), Vol. 10082.

320. R. W. Sites, S. A. McDaniel, J. O. Barnes, D. M. Krein, J. H. Goldsmith, S. Guha, and G. Cook, "Hot isostatic pressing of transition metal ions into chalcogenide laser host crystals," Optical Material Express **6**, 3339-3353 (2016).

321. H. V. Atkinson and S. Davies, "Fundamental aspects of hot isostatic pressing: An overview," Metallurgical and Materials Transactions A **31**, 2981-3000 (2000).

322. J. Sanghera, W. Kim, G. Villalobos, B. Shaw, C. Baker, J. Frantz, B. Sadowski, and I. Aggarwal, "Ceramic Laser Materials," Materials (Basel) **5**, 258-277 (2012).

323. H. Namba, H. Osaka, K. Kamon, and F. Higuchi, "Process for preparing ZnSe single crystal," 4,584,053 (1986).

324. M. Chen, H. Cui, W. Li, H. Kou, J. Li, Y. Pan, and B. Jiang, "Reparative effect of diffusion process on host defects in Cr2+ doped ZnS/ZnSe," Journal of Alloys and Compounds **597**, 124-128 (2014).
325. J. W. Evans, R. W. Stites, and T. R. Harris, "Increasing the performance of an Fe:ZnSe laser using a hot isostatic press," Opt. Mater. Express **7**, 4296-4303 (2017).
326. S. A. McDaniel, "MID-IR ULTRAFAST LASER INSCRIBED WAVEGUIDES AND DEVICES," (University of Dayton, Dayton, Ohio, 2017).
327. M. Durand, A. Houard, K. Lim, A. Durécu, O. Vasseur, and M. Richardson, "Study of filamentation threshold in zinc selenide," Optics Express **22**, 5852-5858 (2014).
328. D. T. F. Marple, "Refractive Index of ZnSe, ZnTe, and CdTe," Journal of Applied Physics **35**, 539-542 (1964).
329. E. Sorokin, "Solid-State Materials for Few-Cycle Pulse Generation and Amplification," in *Few-Cycle Laser Pulse Generation and Its Applications*, F. X. Kärtner, ed. (Springer-Verlag Berlin Heidelberg, Germany, 2004), pp. 3-73.
330. P. A. Obraztsov, A. G. Okhrimchuk, M. G. Rybin, E. D. Obraztsova, and S. V. Garnov, "Multi-gigahertz repetition rate ultrafast waveguide lasers mode-locked with graphene saturable absorbers," Laser Physics **26**, 084008 (2016).
331. S. Y. Choi, T. Calmano, F. Rotermund, and C. Kränkel, "2-GHz carbon nanotube mode-locked Yb:YAG channel waveguide laser," Optics Express **26**, 5140-5145 (2018).
332. A. Choudhary, A. A. Lagatsky, P. Kannan, W. Sibbett, C. T. A. Brown, and D. P. Shepherd, "Diode-pumped femtosecond solid-state waveguide laser with a 4.9 GHz pulse repetition rate," Optics Letters **37**, 4416-4418 (2012).
333. A. Lancaster, A. Choudhary, N. S. Jha, R. Mary, D. P. Shepherd, and A. K. Kar, "1.94 GHz CW Modelocked Ytterbium-Doped Bismuthate Glass Waveguide Laser," in *Advanced Solid State Lasers*, OSA Technical Digest (online) (Optical Society of America, 2015), AM5A.22.
334. A. A. Lagatsky, A. Choudhary, P. Kannan, D. P. Shepherd, W. Sibbett, and C. T. A. Brown, "Fundamentally mode-locked, femtosecond waveguide oscillators with multi-gigahertz repetition frequencies up to 15 GHz," Optics Express **21**, 19608-19614 (2013).

335. S. Vasilyev, I. Moskalev, M. Mirov, S. Mirov, and V. Gapontsev, "Multi-Watt mid-IR femtosecond polycrystalline Cr^{2+}:ZnS and Cr^{2+}:ZnSe laser amplifiers with the spectrum spanning 2.0-2.6 um " Optics Express **24**, 1616-1623 (2016).